A STUDY OF RADIATED SURFACE WAVES IN THE CONTEXT OF THE CAPTURE OF OCEAN WAVE ENERGY

A thesis submitted in partial fulfilment

of the requirements for the Degree of

Doctor of Philosophy in Engineeing

with the

Department of Mechanical Engineering

of the

University of Canterbury

by Matthew F. Wypych BE (Hons) (Mech)

2012

Table of Contents

List of Tables

List of Figures

Acknowledgements

This thesis was made possible by the help and support of many people. As the author, I'd like to acknowledge a few of those people who have made substantial contributions.

I'd like to thank Associate Professor Keith Alexander, my doctoral supervisor, for his guidance, support and everlasting enthusiasm. I'd also like to thank Dr Mathieu Sellier and Professor David Wall for their help with some of the technical issues in this thesis.

I'd like to show my appreciation for the technical and financial support offered by Industrial Research Limited and Power Projects Limited. A special thank you goes to Alister Gardner and Dr Lan Le-Ngoc for providing the robust discussions and critical analysis that helped refine many of the concepts embodied within this thesis.

I'd also like to recognise the skill and professionalism of the technical staff at the University of Canterbury. The excellent advice and workmanship offered by Scott Aimes, Dave Hurring, Jim McClean, Gerry Kirk, Julian Phillips and Eric Cox contributed significantly to the success of the radial wave generator.

This thesis would not have been possible without the love and support of my partner, Lauren Beven. Thank you for giving me the inspiration and confidence needed to take on this project. Your strength, compassion and understanding throughout this monumental task has been truly inspiring. I'd also like to thank all our family for supporting us both in our chosen endeavours.

1 Abstract

The current drive to find new low-carbon forms of electricity generation has intensified interest in capturing energy from ocean waves. The large range of devices currently proposed to fulfil this drive raises the question “What are the characteristics of an effective wave energy converter?”. This thesis explores the design of a particular type of wave energy converter (WEC), namely the point absorber, by examining the properties and interactions of different types of surface waves.

Current theory suggests that in order for a WEC to effectively absorb wave energy, it must also be an efficient wave radiator. The solutions to the Laplace equation in circular-cylindrical coordinates (known as circular waves) are used as point sources for the surface waves radiated from an oscillating body. The properties of circular waves provide guidelines with regard to the shape, movement and radiation properties required to make an effective WEC. The interactions of circular waves with plane waves also determines the theoretical optimum performance of a WEC in three-dimensional wave fields. Limitations on the theoretical size of radiated waves are identified and linked to the size of the oscillating body. This establishes the connection between a body's displaced volume and its performance as a WEC.

Practical experiments aimed at determining if the circular waves correspond to waves radiated by different oscillating bodies were completed. A method of consistently generating and measuring radial waves was developed and data recorded for a cylinder, sphere and flat plate oscillating vertically or horizontally. The results show that the circular-cylindrical models are accurate, providing the body is axisymmetric and oscillates either vertically, or horizontally with a small amplitude. The experiments also demonstrate the practical implications of radiating surface waves.

This thesis advances the understanding of point absorber wave energy converters by identifying simple design guidelines that embody the underlying physics of surface waves. It also develops new methods for generating, measuring and analysing the waves radiated from an oscillating body.

2 Introduction

This section highlights the importance of research in wave energy within a New Zealand context and provides an introduction to the parameters of the project.

2.1 The Current Climate of Wave Energy

According to the International Energy Agency the world consumed 513 exajoules of energy in 2008 [1]. Of this, 81.3% came from coal/peat, oil and gas with a further 5.8% from nuclear power generation. Carbon Dioxide has been identified as a greenhouse gas and is currently making a significant contribution to the global temperature rise. This means that if the disastrous effects of global warming are to be minimised then there must be a significant change to the way in which the human race produces and consumes energy. The alternatives (to fossil fuels) with long term sustainability are the different forms of renewable energy. Renewable energy can be broken down into several categories: Solar, Wind, Hyrdo, Geothermal, Waste and Marine.

The challenge behind renewable energy is security of supply. Wind power can vary greatly. Solar is dependant on the amount of cloud cover. Even the large hydro dams are affected by variation in rain fall and, especially valid in today's climate, the melting of glaciers. The remedy for variability in supply is the diversity of the forms of generation. For instance, a stormy overcast day favours wind power over solar and a clear calm day favours solar power over wind.

The potential resource available through ocean wave energy has been estimated to be between 1 and 10 Terra-Watt-Years [2]. This is equivalent to between 32 and 315 exajoules of energy per year, a total in the order of global energy consumption. This indicates that ocean wave energy has the potential to play a significant role in providing a renewable energy resource for the human race.

The window within which a renewable resource can be accurately predicted varies from resource to resource. For instance the forecasting window for wind is hours, for

waves it can be up to days [3] and tidal flow may be predicated years in advance. This means that wave and tidal generation can be integrated with base load power sources more easily than wind.

Like wind and hydro resources, wave energy can be viewed as a concentrated solar energy [4]. Waves are generated by wind, and the major sources of wind are extra-tropical storms and trade winds. As a result, countries that have a western coastline, situated on the eastern edge of an ocean basin in the latitudes between 30° and 60°, have a significant wave resource [2]. It is interesting to note that New Zealand fulfils all of these requirements and has one of the most energetic wave resources in the world along the south western corner of the South Island. There are various sources that provide maps of the worlds wave resource. The author recommends seeing Thies [5] for an illustrative map.

2.1.1 Wave Energy and New Zealand

In a 2010 report [6] on Oil and Gas Security, the IEA notes that New Zealand relies on imports for around half of its oil consumption and although New Zealand has been self-sufficient for natural gas, the local gas fields are already in decline. It also noted that New Zealand has no liquid natural gas terminal and therefore cannot import natural gas. New Zealand will soon have no choice but to invest in developing energy infrastructure. The question is: which technologies will New Zealand opt for? The Intergovernmental Panel for Climate Change has recommended that in order to minimise the global temperature rise, investment should be made in energy efficiency and the deployment of low greenhouse gas technologies [7].

The wave energy industry is, at the date of publishing, still in the development phase. There are no commercially available infrastructure scale wave power generators. This means that although wave energy has the potential to contribute to the New Zealand electricity grid, it is not a realistic option to fill our short term consumption needs. However, this does afford New Zealand an interesting opportunity for the future as it is in a rather uncommon position.

New Zealand has two contrary wave climates in close proximity to each other. The first is the considerable wave resource off the west coast of the South Island. Here the wave climate is among some of the most energetic in the world with figures as high as 100kW/m of wave front. The second is that of the of the less energetic east coast. Here the wave climate is rated between 20 and 30kW/m. This would allow wave device developers to prototype, design and test in relatively calm waters, and for a minimum of cost and time, transfer to the west coast to put the device through a stress test.

The challenge within New Zealand is finding the capital funding for wave energy projects. The size of proposed full scale designs, often featuring structures with dimensions between five and one hundred meters, means that the investment required to build a full scale device is considerable. The scale of costs involved can be illustrated by the installation of marine cabling at the EMEC testing centre in Orkney, Scotland. The cost, including the cable and installation, was a total of 5.5 million pounds. This did not include any wave energy conversion devices or mooring points. Indeed, raising capital is one of the major challenges facing the wave energy conversion industry world wide as the available funds are spread between the wide number of diverse solutions being offered. The dilution of funding has occurred to the extent that some observers believe this is hampering significant advancement [8].

As with all investments there is considerable concern around the risk and return on investment. Due to the limited amount of field experience and the lack of publicly available failure rate data the reliability of wave energy converters (WECs) is difficult to quantify [5]. The current development of WECs has had some significant failures. Devices have either been damaged or washed away [9] or returned lower than expected energy conversion. This means that being able to predict winners at an early stage is important.

The uncertainty in the estimation of reliability has been compounded by the changing environment. A general trend of increasing mean wave heights at a rate of around 2% per year (or between 30% and 50% over 30 years) [10] may be the cause of damage to various prototypes. For example, the multiresonant oscillating water column (MOWC)

deployed at Toftestallen was installed in 1985 and was swept off its foundation by what was considered to be a 100 year storm, despite having only been deployed for 3 years [9].

Scale prototypes are often used to lower the risk of losing invested funds. However, assuming Froude scaling, the scaling effects mean that power from a small prototype is governed by the relationship $P_{\text{prototype}} = P_{\text{full scale}} \left(\frac{L_{\text{prototype}}}{L_{\text{full scale}}} \right)^{3.5}$ [11]. To put this into context, if the full scale device is a 40m sphere with a 2MW output, then a 1/80$^{\text{th}}$ scale device results in a 0.5m sphere absorbing just 0.44W. This makes accurate characterisation of the power output of a scale prototype difficult.

Demonstrating an understanding of wave energy extraction and the strengths and weaknesses of tank testing is one of the key elements of attracting the required capital to further develop wave energy devices.

2.1.2 The Importance of Radiated Waves

One particular branch of WEC design is the point absorber wave energy converter (PAWEC). These devices have been studied intensely over 40 years due to key attributes that should offer excellent economic performance. By definition a point absorbers should have horizontal physical dimensions significantly smaller than the incident wave length [12]. This equates to a smaller physical size and, relatively, lower construction costs. There is also a theoretical phenomenon in which a point absorber has the potential to absorb more energy than would be incident on the physical extent of the device [13]. These two factors would indicate that the point absorber may have an economic advantage over either the terminator or attenuator. (see Section 5.1.1 for classifications of WEC and Section 5.3.2.5 on the maximum performance of a PAWEC).

The principal by which a point absorber removes energy from an incident wave is the principal of destructive interference between the incident wave and the waves radiated by the WEC's motion. Falnes summarised the effect as follows:

> The physical law of conservation of energy requires that the energy-extracting device must interact with the waves such as to reduce the amount of wave energy that is otherwise present in the sea. [14]

The interaction described by Falnes is the interaction between the incoming ocean wave and the waves that are scattered and radiated by the associated motion of the body. Therefore, the understanding of the effective and efficient operation of a PAWEC should be advanced by the study of waves radiated from a body, and the interaction of these waves with incident waves.

2.2 Industrial Research Limited Assistance

Industrial Research Limited (IRL) is a Crown Research Institute focusing on scientific research and development in the manufacturing and service sectors. Together with Power Project Limited they have patented and developed the WET-NZ device, a point absorber WEC [15].

IRL have provided technical and financial support for this doctoral study in conjunction with the Ministry for Science and Innovation. The support was offered with the understanding that, if possible, the WET-NZ device should be used for a case study and that the project would focus on developing the understanding of impedance matching. The contract reference is C08X0804 Wave Energy Technology. The technical support was provided in the form of regular meetings to discuss progress and emerging ideas.

2.3 Scope of Study

One of the interesting observations about the wave industry is that there is a significantly diverse range of devices currently under development. The diversity begs the question: Which devices will be successful?

Given that the antenna theory predicts that a small device can absorb a power greater than is incident upon the device (see Section 5.3.2.5) it would seem that any device that can utilise this effect must have a commercial advantage over those that do not. As this theory is based upon the concept of destructive interference between incident waves and radiated waves, a study of this interaction should provide an insight into the design constraints determined by the wave mechanics. This thesis aims to investigate the use of circular waves (see Section 4.1.4) as a model for waves radiated from a point absorbing wave energy converter (see Section 5.1.1).

The first question examined in this thesis is "Can circular wave theory be used to determine design constraints for wave energy converters?". The hypothesis is that the dynamics of the destructive interference between incident plane waves and radiated circular waves will determine a range of constraints for the characteristics of the radiated circular wave and the amount of power that can be absorbed. The study of this question takes the form of an analytical analysis based on linear wave theory. The key element that differentiates this study from the others performed by various authors is that this study will examine only the interaction of surface waves and will not incorporate the dynamics of the oscillating body. This allows the characteristics of wave power absorption to be explored without limiting the scope of study by choosing a specific form of oscillating body.

The second question examined is "Do the theoretical circular waves match the waves radiated by real-world physical bodies?". The hypothesis associated with this question is that circular waves will provide a good model for the radiated waves. This question is investigated by generating and measuring radiated waves in a controlled fashion and then matching circular waves to the recorded wave data. The importance of this

question lies in connecting the theoretical study of radiated waves with the physical realities that face wave energy converters.

Due to time constraints of the project, the experimental study was limited to three different wave radiators: a sphere, a cylinder and a vertical flat plate. These bodies provided two axisymmetric bodies for comparison and a non-axisymmetric body for contrast. All three bodies have also been closely examined theoretically and have a significant amount of supporting literature.

The final question examined as part of this thesis is "What are the limitations on the radiation of power from an oscillating body?" The hypothesis is that there will be some form of theoretical and practical limits on how much power can be radiated. This is of interest because, if the absorption of wave power is related to the size of the wave radiated by a body (see Section 5.3.1), the limits on wave radiation must also be limits on power absorption. To answer this question a study of the theoretical limitations of circular waves is compared and contrasted with the experimental results.

Overall the goal is to gain a deeper understanding of the factors that influence wave power absorption so that the design of point absorbing wave energy converters can be improved. This understanding can also be used to identify wave energy devices that are likely to be successful and which facets of the design can be improved.

In summary the three key objectives of this thesis are:

1. Determine whether or not circular wave theory can be used to identify constraints that determine the performance characteristics of WECs.

2. Determine whether or not circular waves represent experimentally measured waves radiated by oscillating bodies.

3. Determine any significant physical limitations on the radiation of wave power from an oscillating body.

3 Background Information

This chapter contains basic information fundamental to understanding this thesis. It includes an introduction to coordinate systems, terminology and notations used throughout this thesis and is largely for reference.

3.1 Coordinate Systems

Several coordinate systems will be referred to throughout this thesis and this section provides a reference for each system. For further information, *The Field Theory Handbook* by Moon and Spencer [16] provides an excellent reference. Note that t denotes time for all coordinate systems, and all dimensions are in SI units unless otherwise stated.

3.1.1 Rectangular Coordinates

The rectangular coordinate system provides the most basic frame of reference for this study. Fig 1 depicts the rectangular coordinate system. Note that $x \in \Re$, $y \in \Re$ and $z \in \Re$. Equation 1 is the Laplace transform in rectangular coordinates.

$$\nabla^2 f = \frac{\partial^2 f}{\partial x^2} + \frac{\partial^2 f}{\partial y^2} + \frac{\partial^2 f}{\partial z^2} \tag{1}$$

3.1.2 Circular Cylindrical Coordinates

The circular cylindrical coordinates will also be used extensively throughout this study. Fig 2 shows the circular cylindrical coordinate system and its relationship with Cartesian coordinates. Note that $r \in \Re$, $r > 0$, $\theta \in \Re$, $-\pi > \theta \geq \pi$ and $z \in \Re$. Conversion between the Cartesian and circular cylindrical coordinates is as follows:

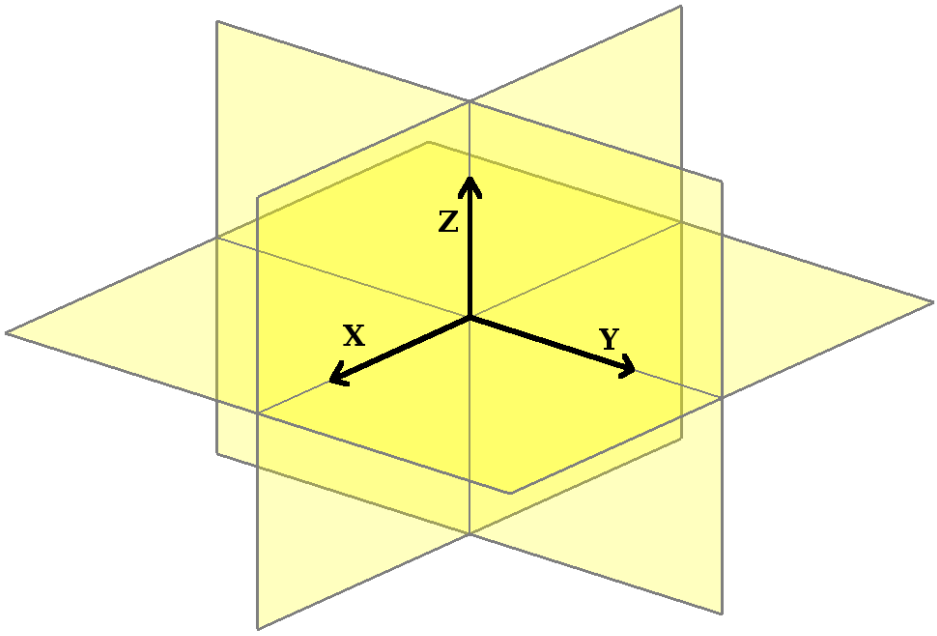

Figure 1: The Rectangular Coordinate System

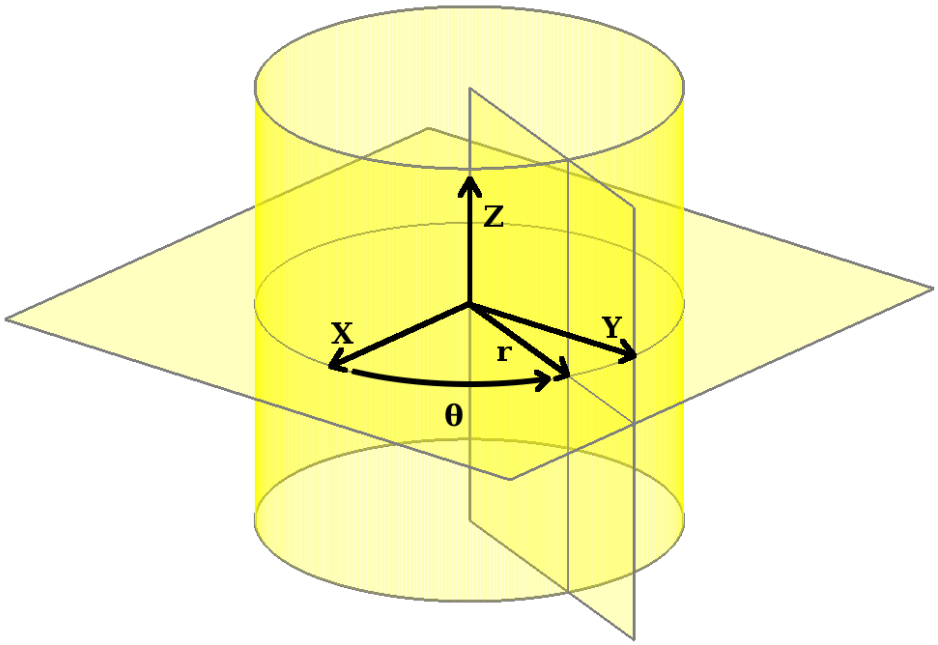

Figure 2: The Circular Cylindrical Coordinate System

$$r = \sqrt{x^2 + y^2} \tag{2}$$

$$\theta = atan\left(\frac{y}{x}\right) \tag{3}$$

$$z = z \tag{4}$$

With the reverse process being:

$$x = r\cos(\theta) \tag{5}$$

$$y = r\sin(\theta) \tag{6}$$

$$z = z \tag{7}$$

The Laplace equation may also be written in circular cylindrical coordinates:

$$\nabla^2 f = \frac{\partial^2 f}{\partial r^2} + \frac{1}{r}\frac{\partial f}{\partial r} + \frac{1}{r^2}\frac{\partial^2 f}{\partial \theta^2} + \frac{\partial^2 f}{\partial z^2} = 0 \tag{8}$$

3.1.3 Elliptical Cylindrical Coordinates

The elliptical cylindrical coordinates will be referred to on occasion. Fig 3 shows the elliptical cylindrical coordinate system and its relationship with Cartesian coordinates.

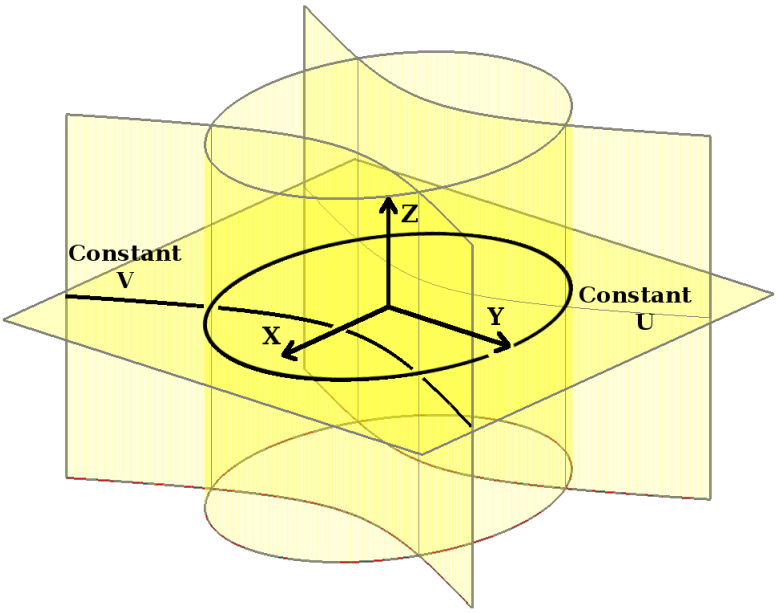

Figure 3: The Elliptical Cylindrical Coordinate System

Note that a_e is a constant, $u_e \in \Re$, $u_e > 0$, $v_e \in \Re$, $-\pi > v_e \geq \pi$ and $z \in \Re$. Conversion between the elliptical cylindrical and Cartesian coordinates is as follows:

$$x = a_e \cos(v_e) \cosh(u_e) \tag{9}$$

$$y = a_e \sin(v_e) \sinh(u_e) \tag{10}$$

$$z = z \tag{11}$$

The Laplace equation may also be written in Elliptical Cylindrical Coordinates:

$$\nabla^2 f = \frac{1}{a_e^2\left(\cosh^2(u_e) - \cos^2(v_e)\right)}\left(\frac{\partial^2 f}{\partial u_e^2} + \frac{\partial^2 f}{\partial v_e^2}\right) + \frac{\partial^2 f}{\partial z^2} = 0 \tag{12}$$

3.2 Terminology and Notation

There are several key areas that require definition before proceeding with a study of surface waves. This section provides a reference for various definitions required by this thesis.

3.2.1 Complex Notation

This thesis uses complex notation for the amplitude and phase of waves. This results in expressions in terms of complex numbers, which conserves the generality. However, wherever physical quantities are described, such as surface displacement or pressure, it is assumed that only the real components correspond to the physical solutions. Hence whenever a function for velocity ($\vec{V}$) velocity potential (ϕ) or surface displacement (η) is stated it is assumed that only the real parts of the expression are being examined i.e. For all physical functions:

$$\eta = f(x, y, z, t) \quad \textit{is equivalent to} \quad \eta = \Re\left(f(x, y, z, t)\right) \tag{13}$$

3.2.2 Body Motion Terminology

The nomenclature for body motion is defined relative to an incident wave. The three translations are heave, surge and sway, and the three rotations are yaw, roll and pitch. Fig 4 shows the body motions relative to the Cartesian coordinates.

3.2.3 Key Abbreviations

Table 1 is a reference of the abbreviations most commonly used within this thesis.

Abbreviation	Definition
OWC	Oscillating water column
PAWEC	Point-absorbing wave energy converter
RHS	Rectangular hollow section
SALWT	Small amplitude linear wave theory
SWL	Still water level
WEC	Wave energy converter

Table 1: Key Abbreviations

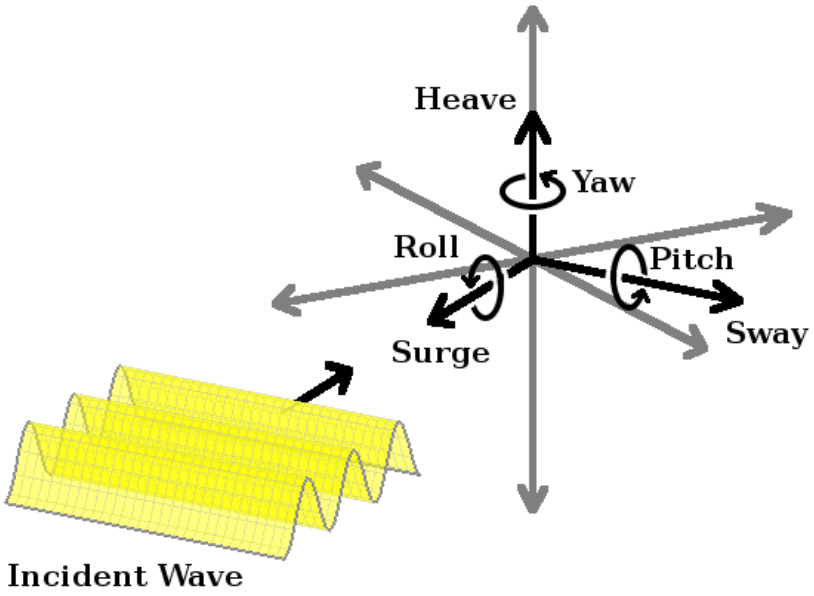

Figure 4: The Motions of a Body as Defined with Respect to an Incident Wave.

4 An Introduction to Surface Waves

This chapter provides an introduction to linear waves and scale model testing in the context of ocean wave energy. It is included largely for reference and for readers that are unfamiliar with ocean wave theory.

A surface wave is defined as the transmission of a disturbance in the interface between two fluids. In the case of ocean waves, the two fluids are water and air. Surface waves can divided into different categories depending on the physical mechanism that drives the propagation of the wave. Table 2 represents only the relevant wave types in context of this thesis. For a more complete list see Mei [17].

The waves that can be seen crashing onto beaches are typically wind waves and swell, formed by the movement of air over the water's surface. The key factors in the formation of wind waves are wind speed, wind duration and the Fetch (the distance over which the wind blows in one direction) [18]. Wind waves are usually the focus of the study for wave energy devices due to their abundance, predictability and relatively high energy density.

The gap between capillary waves and wind waves represents an area in which there is a combined gravity and surface tension effect. Falnes, for instance, limits his study of waves to wave lengths greater than 250mm (or a period of 0.4s in deep water) [19]. Falnes also notes that the spectrum of ocean waves usually lies between the limiting periods of 5 and 15 seconds. This range is suitable for an investigation into wave

Wave Type	Mechanism	Typical Period
Capillary Waves	Surface Tension	Less than $\frac{1}{10}$ of a second
Wind waves and swell	Gravity	Between 1 and 25 seconds
Tsunami	Gravity	10 minutes to 2 hours
Tides	Gravity and the Earth's rotation	12 hours to 24 hours

Table 2: Classification of Waves

energy conversion, however it is important to note that ocean waves consist of a wider range of periods including capillary, wind and swell waves.

4.1.1 Wave Nomenclature

Figure 5 depicts a plane wave and indicates the various terms used to describe a surface wave. Table 3 gives the definition of each term.

4.1.2 Linear wave theory

Linear wave theory for plane waves is well developed and documented in a range of sources. Dean and Dalrymple [20], Sorensen [21], Rahman [22], McCormick [23] and Newman [24] all have complete derivations, to name a few. It was originally recorded in its complete form by Sir George Biddell Airy and is known as Airy wave theory. A brief summary of linear wave theory is included to show the origins of important theoretical concepts. It is assumed that the reader understands the concepts of complex potential theory and that they may refer to any of the above texts for further clarification if required.

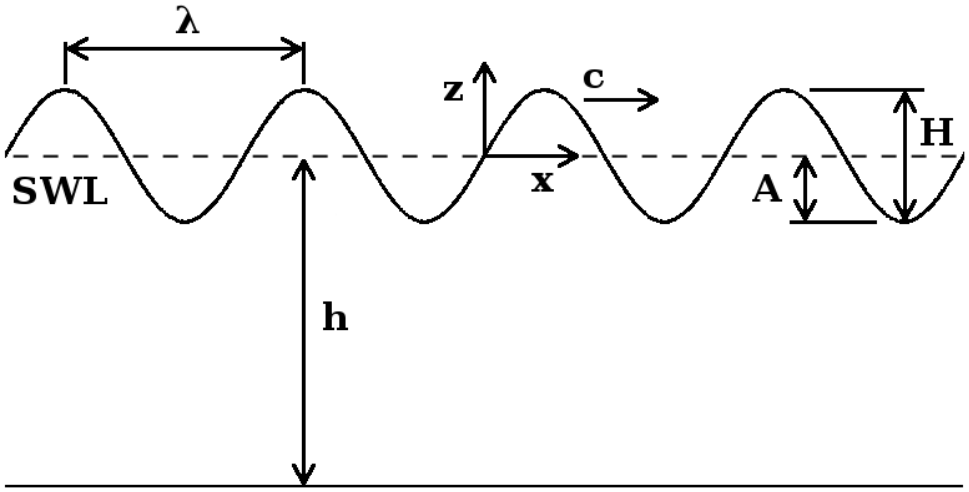

Figure 5: Basic Wave Nomenclature

Symbol	Title	Definition	IS Unit of Measure
A	Wave Amplitude	Surface displacement amplitude.	m
c	Wave Celerity	The forward speed of the wave.	m s^{-1}
h	Fluid Depth	Distance from the free surface to the bottom boundary.	m
H	Wave Height	The vertical distance between a peak and a trough on the free surface.	m
T	Wave Period	The time between two consecutive wave crests passing a stationary reference point.	s
λ	Wave Length	The distance between two successive wave crests in direction of wave propagation.	m
SWL	Still Water Level	The height of the undisturbed free surface. Assumed to be $z=0$.	-

Table 3: Wave Nomenclature

The goal of linear wave theory is to define a mathematical model that describes a wave travelling across the interface of two fluids, in this case between a body of water and a body of air. The solution is also chosen to be periodic along the free surface as well as periodic in time. The principal of superposition must also remain valid. Consideration should be given to the limitations of linear wave theory when applying it to specific situations. Section 5.7 gives a more detailed review of the limitations of linear wave theory.

Linear wave theory, also known as small-amplitude water wave theory, starts with the assumptions that water is an incompressible fluid undergoing an irrotational motion. These two assumptions and the principal of the conservation of mass leads to the continuity equation:

$$\nabla \cdot \vec{V} = 0 \tag{14}$$

where $\vec{V}$ is the velocity vector and can be described by the velocity potential, ϕ :

$$\vec{V} = -\nabla \phi \tag{15}$$

This implies that the continuity equation will be satisfied if the velocity potential, ϕ, satisfies the Laplace Equation:

$$\nabla^2 \phi = 0 \tag{16}$$

The form of the solutions to the Laplace equation depend on the chosen coordinate system. This thesis deals largely with the interactions between the solutions derived from the rectangular coordinates, or plane waves, and those derived from the circular-cylindrical coordinates, or circular waves.

4.1.3 The Rectangular General Solution

The Laplace equation in rectangular coordinates is:

$$\nabla^2 \phi = \frac{\partial^2 \phi}{\partial x^2} + \frac{\partial^2 \phi}{\partial y^2} + \frac{\partial^2 \phi}{\partial z^2} = 0 \tag{17}$$

To reduce the number of possible solutions, the process of separation of variables is applied. This defines the complex potential as the product of functions of a single variable:

$$\phi = C(x) D(y) G(z) H(t) \tag{18}$$

Combining Equations 17 and 18 and dividing through by ϕ gives:

$$\nabla^2 \phi = \frac{1}{C(x)} \frac{\partial^2 C(x)}{\partial x^2} + \frac{1}{D(y)} \frac{\partial^2 D(y)}{\partial y^2} + \frac{1}{G(z)} \frac{\partial^2 G(z)}{\partial z^2} = 0 \tag{19}$$

To simplify this example it is assumed that the spatial periodicity exists only in the x direction i.e. $D(y)$ is a constant. This does not affect the generality of the solution as the orthogonal vectors, $\hat{x}$ and $\hat{y}$, can always be rotated so that, with respect to the plane wave, the function $D(y)$ is constant. Noting that each term in Equation 19 is dependant on a single variable, it is possible to create a solution based on ordinary differential equations by making the following statements:

$$\frac{1}{C(x)} \frac{\partial^2 C(x)}{\partial x^2} = -k^2 \quad \textit{and} \quad \frac{1}{G(z)} \frac{\partial^2 G(z)}{\partial z^2} = +k^2 \tag{20}$$

Hence the solution for the the Laplace equation depends on the value of k. To obtain a solution that is periodic in x and not in z, k^2 must be real and non-zero. This leads to solutions for $C(x)$ and $G(z)$:

$$C(x)=A_c\cos(k\,x)+B_c\sin(k\,x) \tag{21}$$

$$G(z)=A_g e^{(k\,z)}+B_g e^{-(k\,z)} \tag{22}$$

As the desired result is a simple time harmonic solution, it is possible to define the time component of the velocity potential as $H(t)=A_h e^{-i\,\omega t}$ where A_h is a constant, ω is the phase velocity and t is time. Note that both t and ω have real values.

The unconstrained, rectangular general solution for the complex potential becomes:

$$\phi(x,z,t)=\left(A_c\cos(k\,x)+B_c\sin(k\,x)\right)\left(A_g e^{kz}+B_g e^{-kz}\right)A_h e^{-i\,\omega\,t} \tag{23}$$

To satisfy the periodicity requirement in the x direction there must exist a situation where $\phi(x,z,t)=\phi(x+\lambda_\infty,z,t)$ where λ_∞ is the wavelength of the wave at a great distance from the origin. The inclusion of the distance criteria for the wavelength may seem irrelevant for a wave with a constant wavelength but it is necessary for consistency with the circular-cylindrical solutions. The wavelength of the circular-cylindrical solutions to the Laplace equation changes with distance from the origin and tends to a given value (λ_∞) as r tends toward ∞. Examining the unconstrained, rectangular general solution it is possible to isolate the terms that vary with x and determine the conditions for periodicity.

$$\begin{aligned} &A_c\cos(k(x+\lambda_\infty))+B_c\sin(k(x+\lambda_\infty)) \\ &\quad=A_c\left(\cos(k\,x)\cos(k\,\lambda_\infty)-\sin(k\,x)\sin(k\,\lambda_\infty)\right) \\ &\qquad+B_c\left(\sin(k\,x)\cos(k\,\lambda_\infty)+\cos(k\,x)\sin(k\,\lambda_\infty)\right) \end{aligned} \tag{24}$$

Hence, to satisfy the condition for periodicity in the x direction for rectangular solutions to the Laplace equation, k is defined as the wave number:

$$k=\frac{2\pi}{\lambda_\infty} \tag{25}$$

4.1.3.1 Boundary conditions

The rectangular general solution can be further refined by applying three boundary conditions: the bottom boundary condition, the kinematic free surface condition and the dynamic free surface condition.

The bottom boundary condition is used to specify a surface at the lower z location of the control volume being examined. In this case it is instructive to assume a perfectly flat surface at the height of $z=-h$. This gives the condition that the velocity in the z direction at that boundary must be zero. Hence:

$$-\frac{\partial \phi}{\partial z}\bigg|_{z=-h}=0 \tag{26}$$

The kinematic free surface boundary condition states that the velocity of the fluid at the surface must be the velocity of the surface. Put another way, there exists a deformable interface at the top boundary of the fluid volume that the fluid cannot cross. The displacement of the free surface is denoted as η. The resulting condition for the rectangular coordinate system can be expressed mathematically as:

$$-\frac{\partial \phi}{\partial z}\bigg|_{z=\eta}=\left(\frac{\partial \eta}{\partial t}-\frac{\partial \phi}{\partial x}\frac{\partial \eta}{\partial x}-\frac{\partial \phi}{\partial y}\frac{\partial \eta}{\partial y}\right)\bigg|_{z=\eta} \tag{27}$$

The dynamic free surface condition determines that, providing surface tension is neglected, Bernoulli's equation must hold over the free surface specified by the kinematic free surface boundary condition, as the free surface cannot support pressure variations across its interface. Assuming the effects of surface tension are minimal means that the scope of the solution is limited to gravity waves (see Section 4). The resulting relationship is:

$$\left(-\frac{\partial \phi}{\partial t}+\frac{1}{2}\left(\left(\frac{\partial \phi}{\partial x}\right)^2+\left(\frac{\partial \phi}{\partial y}\right)^2+\left(\frac{\partial \phi}{\partial z}\right)^2\right)+g z\right)\bigg|_{z=\eta}=c(t) \tag{28}$$

Note that it is assumed that gauge pressure has been used in the formulation of this equation and that the atmospheric pressure is uniform throughout the wave field..

Other more specific boundary conditions may be applied depending on the situation being examined. For instance, it is possible to describe the solid surface of a freely moving body as a boundary condition and thereby study the dynamics of a given interaction. The mathematics quickly becomes complex and analytical solutions are rare except for highly simplified situations e.g. a two dimensional cylinder.

It is useful to note that all of the boundary conditions can be linearised with respect to x. This allows the second trigonometric x term in Equation 23 to be dropped without any loss of generality. This reduces the general unconstrained, rectangular general solution to:

$$\phi(x,z,t)=A_c\cos(k\,x)\left(A_g e^{kz}+B_g e^{-kz}\right)A_h e^{-i\omega t} \tag{29}$$

The principal of superposition and the fact that for any function, f, representing a physical property, it is automatically implied that only the real component is relevant i.e. $f(x,y,z,t)=\Re(f(x,y,z,t))$, it is possible to contract the notation further:

$$\begin{aligned}\phi(x,z,t)&=A_c e^{i k x}\left(A_g e^{kz}+B_g e^{-kz}\right)A_h e^{-i\omega t}\\ &=A_c\left(A_g e^{kz}+B_g e^{-kz}\right)A_h e^{i(k x-\omega t)}\end{aligned} \tag{30}$$

Applying the bottom boundary condition (Equation 26) to the unconstrained, rectangular general solution (Equation 29) results in:

$$\begin{aligned}-\left.\frac{\partial\phi}{\partial z}\right|_{z=-h}&=-A_c\left(A_g k e^{kz}+B_g k e^{-kz}\right)A_h e^{i(k x-\omega t)}\Big|_{z=-h}=0\\ &\Rightarrow -A_c\left(A_g k e^{-kh}-B_g k e^{kh}\right)A_h e^{i(k x-\omega t)}=0\end{aligned} \tag{31}$$

To fulfil Equation 31 the bracketed term must equal zero. Hence:

$$\begin{aligned}\left(A_g k e^{-kh}-B_g k e^{kh}\right)&=0\\ \Rightarrow\ A_g&=B_g e^{2\mathrm{kh}}\end{aligned} \tag{32}$$

Substituting Equation 32 back into Equation 29 yields:

$$\begin{aligned}\phi&=A_c\left(B_g e^{2\mathrm{kh}}e^{kz}+B_g e^{-kz}\right)A_h e^{i(k x\omega t)}\\ &=A_c B_g e^{k h}\left(e^{k(h+z)}+e^{-k(h+z)}\right)A_h e^{i(k x-\omega t)}\\ &=2\,A_c B_g A_h e^{k h}\cosh(k(h+z))e^{i(k x-\omega t)}\end{aligned} \tag{33}$$

The remaining boundary conditions require linearisation to simplify the mathematics. From this point on, it is assumed that the waves are infinitesimally small and the velocities and pressures are also small. Thus, any products of these variables are negligible. Using the Taylor series expansion of the Bernoulli equation, and ignoring any terms involving the products of variables, the dynamic free surface boundary condition reduces to the following:

$$\left(-\frac{\partial \phi}{\partial t}+g\eta\right)\Bigg|_{z=0}=C(t) \tag{34}$$

Or:

$$\eta=\frac{1}{g}\frac{\partial \phi}{\partial t}\Bigg|_{z=0}+\frac{C(t)}{g} \tag{35}$$

The displacement function, η, is defined as the displacement of the fluid from the original still water level which will have a temporal and spatial mean of zero. This means that $C(t)=0$. Substituting Equation 33 into Equation 35:

$$\eta=-i\frac{2\omega A_c B_g A_h e^{kh}}{g}\cosh(kh)e^{i(kx-\omega t)} \tag{36}$$

The constants may be either real or complex. It is possible to combine all the constants in Equation 36 into a single constant $Ae^{i\alpha}$. In this form A is a real value constant representing the amplitude of the surface displacement and α represents the phase of the wave. Define:

$$Ae^{i\alpha}=\frac{2\omega A_c B_g A_h e^{kh}\cosh(kh)}{g} \tag{37}$$

The surface displacement becomes:

$$\eta=-iAe^{i\alpha}e^{i(kx-\omega t)} \tag{38}$$

And the constrained rectangular general solution for a periodic surface wave, also known as the plane wave solution ϕ_p, is:

$$\phi_p=\frac{g}{\omega\cosh(kh)}Ae^{i\alpha}\cosh(k(h+z))e^{i(kx-\omega t)} \tag{39}$$

Note: defining the term D as:

$$D=\frac{g}{\omega\cosh(kh)} \tag{40}$$

Equation 39 becomes:

$$\phi_p=DAe^{i\alpha}\cosh(k(h+z))e^{i(kx-\omega t)} \tag{41}$$

The remaining boundary condition is the kinematic free surface boundary condition and can also be linearised using the same technique used for the dynamic free surface boundary condition. Equation 27 reduces to:

$$-\left.\frac{\partial \phi}{\partial z}\right|_{z=0} = \frac{\partial \eta}{\partial t} \tag{42}$$

Substituting in Equation 38 and 41 results in the following relationship.

$$\omega^2 = g\,k\tanh(k\,h) \tag{43}$$

Equation 43 is known as the dispersion relationship. It states that the frequency of the wave is determined by both the wavelength and the depth of the fluid. i.e. a 100 meter long wave will have a different frequency if the fluid depth is shallower compared to that of a deeper fluid. This characteristic differentiates surface waves from acoustic and light waves.

4.1.3.2 Summary of the Plane Wave Solution

A constrained solution to the Laplace equation in rectangular coordinates has been determined. The constraints applied are that the solution should be periodic in both time and the x direction, that there is a solid boundary where $z=-h$ and that there is a deformable free surface at $z=\eta$ which has a temporal and spatial mean of $z=0$. During this analysis the dynamic and kinematic free surface boundary conditions were linearised and it was assumed that the surface displacement, pressure and velocities were small so that the product of these terms tends to zero. The wave number, k, was defined as $k=\frac{2\pi}{\lambda_\infty}$ and the dispersion relationship, $\omega^2 = g\,k\tanh(k\,h)$, was determined by the kinematic free boundary.

The solution is:

$$\begin{aligned} &\phi_p = D\,A\,e^{i\alpha}\cosh(k(h+z))\,e^{i(k\,x-\omega t)} \\ &where \quad D=\frac{g}{\omega\cosh(k\,h)} \end{aligned} \tag{44}$$

4.1.3.3 Variations of the rectangular solutions

It is possible to describe a wider range of plane waves by rotating the axis along which the plane wave propagates. This necessitates the introduction of the angle of incidence, γ, measured anti-clockwise from the positive x axis. The velocity potential for a plane wave from any given direction is:

$$\phi_p = D\,A\,e^{i\alpha}\,e^{ik(x\cos(\gamma)+y\sin(\gamma))}\cosh(k(h+z))\,e^{-i\omega t} \tag{45}$$

As further calculations are focused on results from the circular cylindrical coordinates it is useful to note that the above equation can be expressed in terms of r and θ:

$$\phi_p = D\,A\,e^{i\alpha}\,e^{ikr\cos(\theta-\gamma)}\cosh(k(h+z))\,e^{-i\omega t} \tag{46}$$

4.1.4 The Circular Cylindrical Solutions

The solution for the Laplace equation in circular cylindrical coordinates is not widely documented. Different forms of the general solution are listed in several texts although this is usually as a theoretical exercise or simply for interest [17]. The complete derivation is included here as these solutions form a core part of this thesis. Note that the final result recorded in this section will be further refined. The method is almost identical as that followed in Section 4.1.3.

The Laplace Equation in circular cylindrical coordinates is:

$$\nabla^2\phi = \frac{1}{r}\frac{\partial}{\partial r}\left(r\frac{\partial\phi}{\partial r}\right)+\frac{1}{r^2}\frac{\partial^2\phi}{\partial\theta^2}+\frac{\partial^2\phi}{\partial z^2} \tag{47}$$

The process of separation of variables can be applied again by defining the velocity potential as:

$$\phi = E(r)F(\theta)G(z)H(t) \tag{48}$$

It is assumed that the velocity potential is periodic in time and so $H(t)=A_h e^{-i\omega t}$ where A_h is a constant, ω is the phase velocity and t is time. Substituting Equation 48 into Equation 47 and dividing by ϕ yields:

$$\nabla^2\phi=\frac{1}{E(r)}\frac{\partial^2 E(r)}{\partial r^2}+\frac{1}{rE(r)}\frac{\partial E(r)}{\partial r}+\frac{1}{r^2F(\theta)}\frac{\partial^2 F(\theta)}{\partial \theta^2}+\frac{1}{G(z)}\frac{\partial^2 G(z)}{\partial z^2}=0 \qquad (49)$$

As the last term on the left hand side is only a function of z and the first three terms are independent of z we can make the following statements which mean that the Laplace equation is always satisfied.

$$\frac{1}{G(z)}\frac{\partial^2 G(z)}{\partial z^2}=k^2 \qquad (50)$$

$$\frac{1}{E(r)}\frac{\partial^2 E(r)}{\partial r^2}+\frac{1}{rE(r)}\frac{\partial E(r)}{\partial r}+\frac{1}{r^2F(\theta)}\frac{\partial^2 F(\theta)}{\partial \theta^2}=-k^2 \qquad (51)$$

The same process can be applied again to the θ term in equation 51.

$$\frac{1}{F(\theta)}\frac{\partial^2 F(\theta)}{\partial \theta^2}=-m^2 \qquad (52)$$

$$\frac{r^2}{E(r)}\frac{\partial^2 E(r)}{\partial r^2}+\frac{r}{E(r)}\frac{\partial E(r)}{\partial r}+k^2r^2=m^2 \qquad (53)$$

Dividing Equation 53 through by k^2r^2 and making the substitution $s=kr$ results in:

$$\frac{\partial^2 E(s)}{\partial s^2}+\frac{1}{s}\frac{\partial E(s)}{\partial s}+\left(1-\frac{m^2}{s^2}\right)E(s)=0 \qquad (54)$$

As seen from Section 4.1.3, Equations 50 and 52 are second order ordinary differential equations with solutions that are dependant on either m or k.

Equation 54 is known as Bessel's equation and has known solutions in the form of Bessel, Neumann and Hankel functions. The two periodic components of the general solution are Bessel functions of the first kind, $J_m(kr)$, and Bessel functions of the second kind, $Y_m(kr)$. Hankel functions are defined using these two functions. Table 4 summarises the relationships between Bessel functions, Hankel functions and physical interpretation of the waves.

Kind of Hankel Function	Notation	Expression in Bessel Functions	Physical Interpretation when $H(t)=e^{-i\omega t}$
First Kind	$H_m^{(1)}(kr)$	$J_m(kr)+iY_m(kr)$	Waves radiated from the origin
Second kind	$H_m^{(2)}(kr)$	$J_m(kr)-iY_m(kr)$	Waves gravitating to the origin

Table 4: The Relationship Between Bessel Functions and Hankel Functions

As this study is looking at the interactions of waves emitted from a point, it will look exclusively at the first kind Hankel solutions. Note for clarity of the notation the superscript denoting the order of the Hankel function will be dropped for the remainder of these calculations.

Selecting the appropriate solutions to the various differential equations leads to the unconstrained circular-cylindrical general solution to the Laplace equation:

$$\phi=H_m(kr)\left(A_f\cos(m\theta)+B_f\sin(m\theta)\right)\left(A_g e^{kz}+B_g e^{-kz}\right)A_h e^{-i\omega t} \tag{55}$$

4.1.4.1 Periodicity along the surface

It is important to note that the Hankel function is not strictly periodic along the radial axis. However, as kr tends to infinity the Hankel function does converge to a periodic value:

$$H_m(kr)\rightarrow\sqrt{\frac{2}{\pi kr}}e^{i\left(kr-\frac{m\pi}{2}-\frac{\pi}{4}\right)} \quad as \quad kr\rightarrow\infty \tag{56}$$

The wave can be considered to be periodic at large values of kr if $H_m(kr)=H_m(k(r+\lambda_\infty))$. Examining Equation 56:

$$\begin{aligned} H_m(k(r+\lambda_\infty)) &\rightarrow\sqrt{\frac{2}{\pi k(r+\lambda_\infty)}}e^{i\left(k(r+\lambda_\infty)-\frac{m\pi}{2}-\frac{\pi}{4}\right)} \quad as \quad kr\rightarrow\infty \\ &\rightarrow\sqrt{\frac{2}{\pi k(r+\lambda_\infty)}}\left(\cos\left(k(r+\lambda_\infty)-\frac{m\pi}{2}-\frac{\pi}{4}\right)\right. \\ &\quad \left.+i\left(\sin\left(k(r+\lambda_\infty)-\frac{m\pi}{2}-\frac{\pi}{4}\right)\right)\right) \end{aligned} \tag{57}$$

1 of 2

$$H_m(k(r+\lambda_\infty)) \to \sqrt{\frac{2}{\pi k(r+\lambda_\infty)}}\left(\cos\left(k r-\frac{m\pi}{2}-\frac{\pi}{4}\right)\cos(k\lambda_\infty)\right.$$
$$-\sin\left(k r-\frac{m\pi}{2}-\frac{\pi}{4}\right)\sin(k\lambda_\infty)$$
$$+i\left(\sin\left(k(r+\lambda_\infty)-\frac{m\pi}{2}-\frac{\pi}{4}\right)\cos(k\lambda_\infty)\right.$$
$$\left.\left.+\cos\left(k r-\frac{m\pi}{2}-\frac{\pi}{4}\right)\sin(k\lambda_\infty)\right)\right) \quad (57)$$

2 of 2

Note that, for a large value or r :

$$\sqrt{\frac{2}{\pi k(r+\lambda_\infty)}} \approx \sqrt{\frac{2}{\pi k r}} \; as \; r \to \infty \quad (58)$$

As in the case for the rectangular coordinate solutions, the resulting definition of wave number, k, is $k=\frac{2\pi}{\lambda_\infty}$. It is important to note that the wavelength of the wave does change as $r \to 0$ but the wave number does not.

4.1.4.2 Boundary Conditions

The same boundary conditions applied for the rectangular solution can be applied to the circular cylindrical solutions once they are re-written in circular cylindrical coordinates.

The bottom boundary condition of a flat boundary at $z=-h$ (Equation 26) can be applied to the unconstrained circular cylindrical solution. Noting that the boundary conditions are linear, the second trigonometric θ term can be removed without the loss of generality and Equation 26 applied to Equation 55 gives:

$$-\left.\frac{\partial \phi}{\partial z}\right|_{z=-h} = H_m(kr) A_f \cos(m\theta)\left(k A_g e^{-kh} - k B_g e^{kh}\right) A_h e^{-i\omega t} = 0 \quad (59)$$

Hence:

$$\begin{aligned}\left(k A_g e^{-k h}-k B_g e^{k h}\right)&=0\\ \Rightarrow A_g&=B_g e^{2 k h}\end{aligned} \tag{60}$$

Substituting Equation 60 into Equation 55 yields:

$$\begin{aligned}\phi&=H_m(kr) A_f \cos(m\theta)\left(B_g e^{2kh} e^{k z}+B_g e^{-k z}\right) A_h e^{-i\omega t}\\ &=A_f B_g e^{k h} A_h H_m(kr)\cos(m\theta)\left(e^{k(h+z)}+e^{-k(h+z)}\right) e^{-i\omega t}\\ &=2 A_f B_g e^{k h} A_h H_m(kr)\cos(m\theta)\cosh(k(h+z)) e^{-i\omega t}\end{aligned} \tag{61}$$

The next step is to assume infinitesimally small wave amplitudes, linearise the boundary conditions and define η as the surface displacement function with a temporal and spatial mean of zero. This results in Equations 35 and 42 as the dynamic and kinematic free surface boundary conditions respectively.

Substituting Equation 61 into Equation 35 with $C(t)=0$:

$$\eta=-i\frac{2\omega A_f B_g e^{k h} A_h}{g} H_m(kr)\cos(m\theta)\cosh(k h) e^{-i\omega t} \tag{62}$$

The group of constants can be combined into a single constant $B e^{i\beta}$. B is a real value constant representing the mathematical amplitude of the surface displacement and has units of metres. It is important to distinguish this from the wave amplitude A as the height of a radiated wave changes as it propagates further into the r domain. β represents the phase of the wave. Define:

$$B e^{i\beta}=\frac{2\omega A_f B_g e^{k h} A_h}{g} \tag{63}$$

Hence the surface displacement becomes:

$$\eta=-i B e^{i\beta} H_m(kr)\cos(m\theta)\cosh(k h) e^{-i\omega t} \tag{64}$$

And the constrained circular-cylindrical general solution for a periodic surface wave, referred to as the circular wave solution, ϕ_c, is:

$$\phi=\frac{g}{\omega\cosh(k h)} B e^{i\beta} H_m(kr)\cos(m\theta)\cosh(k(h+z)) e^{-i\omega t} \tag{65}$$

Noting the definition of D from Equation 41:

$$\phi = D\,B\,e^{i\beta} H_m(kr)\cos(m\theta)\cosh(k(h+z))e^{-i\omega t} \tag{66}$$

The final boundary condition is the kinematic free surface boundary condition. Substituting Equation 66 into Equation 42 results in the dispersion relationship derived for the plane wave i.e. $\omega^2 = g\,k\tanh(k\,h)$. This result is important as it indicates that circular waves have the same characteristics as plane waves. It would be expected that if r tended toward infinity, the properties of the circular wave would tend toward those of the plane wave.

Note that Wehausen and Laitone list the circular cylindrical solutions in the form used here [25 pg 475]:

$$\phi = \cosh(k(h+z))\left(A\,J_m(kr) + B\,Y_m(kr)\right)\cos(m\theta - \zeta)\cos(\omega t - \beta) \tag{67}$$

4.1.4.3 Summary of the Circular Wave Solution

A constrained solution to the Laplace equation in circular cylindrical coordinates has been derived. The constraints applied are that the solution should be periodic in both time and the r direction, there is a solid boundary where $z = -h$, there is a deformable free surface at $z = \eta$ which has a temporal and spatial mean of $z = 0$. During this analysis the dynamic and kinematic free surface boundary conditions were linearised and it was assumed that the surface displacement, pressure and velocities were small so that the product of these terms tends to zero. The wave number, k, was defined as $k = \frac{2\pi}{\lambda_\infty}$ and the dispersion relationship, $\omega^2 = g\,k\tanh(k\,h)$, was determined by the kinematic free boundary.

The solution is:

$$\begin{aligned} &\phi = D\,B\,e^{i\beta} H_m(kr)\cos(m\theta)\cosh(k(h+z))e^{-i\omega t} \\ &\textit{where}\quad D = \frac{g}{\omega\cosh(k\,h)} \end{aligned} \tag{68}$$

4.1.5 Linear Theory and Wave Spectra

The derivations thus far have been concerned with the description of single plane (or regular) waves. Real ocean waves are considered to be irregular and have a spectral and spatial distribution. The stochastic nature of waves and the linearity of the developed wave theory allows the superposition of regular waves to approximate an ocean spectrum [19]. This thesis examines waves of a single frequency and these are known as regular waves. While the implications of a wave field's frequency distribution are not examined in depth, the implications of having the other waves present is noted where appropriate.

4.2 Factors to Consider for Scaled Prototypes

The relevance and accuracy of scale model depends on how well the model represents the full scale effects. This section is a summary of the relevant information from Hughes. [11]

By using the governing physics of the wave mechanics, namely continuity and the Navier-Stokes equation, it is possible to determine scaling criterion so that the model is as relevant as possible. For complete similitude the model must have the same Froude, Strouhal, Reynolds and Euler numbers as the full scale situation. The practicality of realising these criteria varies from criterion to criterion.

For short-wave hydrodynamic models, where $\frac{h}{\lambda} > \frac{1}{20}$, it is possible to satisfy Froude scaling with careful experimental design. The length scaling factor, $N_l = \frac{\text{size of prototype}}{\text{size of full scale device}}$, can be applied to the dimensions of the body, wave amplitudes and wavelengths alike. The satisfaction of the Froude criterion means that there is a similitude of gravitational and inertial forces between full scale and the model.

The Strouhal criterion preserves the relationship between temporal inertial forces and convective inertial forces within a fluid. Assuming the Froude criterion is satisfied and given the difficulty in changing the force of gravity in an experiment, the Strouhal number can be kept constant by equating the time scaling factor equal to the square root of the length scaling factor, i.e. $N_t = \sqrt{N_l}$. Note that for wave models, if the wavelength is scaled by the length scaling factor, the dispersion relationship determines the wave frequency and applies the correct time scaling to satisfy the Strouhal criterion.

The Reynolds criterion relates the inertial forces to the viscous forces within the fluid and is particularly relevant when viscous effects dominate the flow. Assuming gravity is constant in both full scale and the experiment, simulating the same Reynolds number in the model requires using a fluid that is significantly less viscous than water. While these fluids do exist for moderate scaling factors, they are usually volatile chemicals and pools of significant size would pose a serious safety hazard. In short, it is not practically possible to hold the Reynolds criterion and hence, the viscous stresses, and therefore viscous losses, will not be representative in the model. For the ease of experimentation water is used as the working fluid for model testing. The result of using water as the working fluid and Froude scaling is that the viscous forces are likely to be over represented in the scaled down experiment unless the Reynolds number in the model is sufficiently high so that the skin friction is a negligibly small component of the overall drag.

The final condition for model similitude is that of the Euler criterion. This is automatically satisfied as it is considered the dependant force in scaled models.

In summary, by applying a physical scaling length of N_l to the model, wave height and wave length, and a time scaling factor of $N_t = \sqrt{N_l}$, the model is representative in all relevant forces except those of due viscosity. This assumes that the acceleration due to gravity and the fluid used is the same for both full-scale and model.

5 Literature Review

This review aims to explore the state-of-the-art of modern ocean wave energy conversion theory. It will focus on linear wave theory, the methods used to calculate the properties of ocean waves and the factors affecting the performance of a single point absorbing WEC. The goal is to discover if there are any key factors that must be considered in the design of PAWECs and how the interactions of waves in three dimensions affects these key factors.

5.1 What is a WEC?

A WEC or wave energy converter is any device that can extract energy from an incident wave field and convert that energy into another form.

The actual components of a WEC vary depending on the underlying mechanism of energy absorption. Some devices have no moving parts in contact with the water (e.g. the Limpet Oscillating water column (OWC) barrage [26]) while others consist of a number of moving floats (e.g. the Pelamis wave snake [26]). The common conversion methods include conversion to electricity, storage as hydraulic head, or storage as a salinity gradient. The great diversity of WECs has provided a need for a classification system.

5.1.1 Classifications of WECs

The classification of WECs has become increasingly difficult due to the diversity of devices available. The European Marine Energy Centre lists more than 100 devices in varying stages of development [27]. Existing literature uses a wide range of categories to differentiate WEC depending on the context. Three such categories are outlined in this section: the required water depth, the physical extent of the device and the method of power take-off. While the three categories presented do not make up a comprehensive system by which WECs can be classified, they do identify some of the

major characteristics that should be considered when examining WECs. Figures 6 to 11 show some of the leading WEC designs.

Figure 6: The Limpet OWC from Voith Hydro Wavegen Ltd

Figure 7: The Oyster WEC from Aquamarine Power

Figure 8: The Pelamis WEC from Pelamis Wave Power

Figure 9: The Wave Dragon WEC from Wave Dragon ApS

Figure 10: The Ocean Energy Buoy WEC from Ocean Energy Technology

Figure 11: The WET-NZ Device Developed by Industrial Research Ltd and Power Projects Ltd

The design of the WEC may determine the water depth required by the device for effective operation. This characteristic has been broken up into three groups: shoreline, near shore and offshore. An example of each device would be the Limpet ([26] and Fig 6), Oyster ([28] and Fig 7) and Pelamis ([26] and 8) respectively. The Limpet is an

OWC device constructed from a concrete chamber mounted on the shore. Many of the OWC devices are shore mounted as this provides a stable reference against which the water can compress the air. In comparison, the Oyster (a bottom hinged surging plate device) requires a minimum depth of water so that the fluid can flow around the device. However, if the device is too deep then the extent of the device becomes too large and construction costs become prohibitive. This limits the Oyster's operation to those areas of shallow water depth which are mostly found in near-shore areas. The Pelamis does not have the same constraint, although it theoretically performs better in deep water. As a deep water wave transitions into shallow water the crest steepens and trough widens, thereby increasing the impact loading of the wave on a heaving WEC. As the device is cable moored, the deep offshore waters are more suitable.

WECs can also be categorised into one of three classes by the size of the device with respect to the wave. A long (relative to the wavelength of the waves) device that is orientated parallel with the oncoming wave front is described as a terminator, while a long device that is perpendicular to the wave front is described as an attenuator. The final classification is that of a point-absorber, which is defined as having a small horizontal extent when compared to the wavelength. Examples of a terminator, attenuator and point-absorber are Wave Dragon ([26] and Fig 9), Pelamis and the WET-NZ ([29] and Fig 11) device respectively. Note that the point-absorber WEC is referred to as PAWEC throughout this text.

The last method of classification is based on the technology of power take-off. The sub-classes in this area are still growing as different techniques are applied to wave energy. Some of the common categories are bi-directional turbines, hydraulic pressure, hydraulic head, rotational direct drive and linear direct drive. Some of the more exotic methods are electro-active polymer and salinity gradient.

An example can be made by examining the Ocean Energy Buoy (described by Cashman [30]) and illustrated in Fig 10). This device is classified as an offshore point absorber with a bi-directional turbine power take-off.

Two more developed systems for classifying WECs have been presented, one by Wolfram [31] and another by Hagerman [32]. Wolfram divides wave energy converters into three categories depending on the method of operation (namely over-topping, oscillating water column or wave actuated buoy) and then sub-divides these into categories depending on the mooring location relative to the shore line. Hagerman's approach divides the devices by the mooring method and then subdivides based on the primary power take off motion. As the mooring method often reflects water depth there are similarities between the two systems. Even so, neither system is robust enough to classify all the WECs listed on the EMEC website, with devices like the Anaconda [33] not fitting into either system.

5.2 Further Properties of Surface Waves

Section 4 in the previous chapter provided a basic introduction to surface waves and surface wave theory. The material in this section (Section 5.2) aims to supplement the background information by reviewing further properties of surface waves from the available literature to develop foundations for work completed in this thesis.

5.2.1 Property Variation with Depth

It is interesting to note that the properties of linear plane waves vary with depth. For instance, the vertical particle displacement can be calculated and tends to zero at the bottom boundary. This variation of depth means that, in deep water, there is little interaction with the bottom boundary. In fact, below $\frac{\lambda}{2}$ from the SWL, the particle motion is almost zero and waves can travel significant distances (up to tens of thousands of kilometres) without requiring further energy input [2].

Indeed, for a regular plane wave in deep water, 96% of wave power is within the first $\frac{\lambda}{4}$ of the SWL [14]. This is significant to wave energy conversion because it determines the zone within which a WEC must operate. If a device is situated too far

below the free surface it will not be able to interact with the wave and therefore not be able to capture energy.

5.2.2 Group Velocity

Group velocity is a physical phenomenon and is described as the appearance of shorter frequency waves to move forward along a space defined by two nodal points in the wave field. Alternatively, consider two points (nodes) which have zero vertical displacements and are a fixed distance apart in the wave field. If these points are tracked as they progress across the surface, it will appear that the waves within the bounds of the nodes (or group) will progress forward between the nodes, disappearing at the leading nodal point only to reappear at the trailing nodal point . The velocity at which these nodal points travel is known as the group velocity [22].

The group velocity is important to the field of wave energy conversion because it also represents the rate at which energy is transmitted [17] [34]. There are various methods for calculating the group velocity and these are noted in Section 5.6.7.

5.2.3 Circular-Cylindrical Interpretations of a Plane Wave

The complex potential that represents a linear plane wave can also be expressed as an infinite sum of Bessel functions. This means that a linear plane wave progressing from $-\infty$ to $+\infty$ can be represented by an infinite sum of circular waves radiated and gravitated from the origin of the wave field. The mathematics behind this interesting representation are noted by Rahman [22]:

$$c^{i\,k\,r\cos(\theta)} = \sum_{m=0}^{\infty} \varepsilon_m i^m J_m(k\,r)\cos(m\theta) \tag{69}$$

where
$\varepsilon_0 = 1$ *and* $\varepsilon_m = 2$ *for* $m \geq 1$

This can be adapted to express the plane wave velocity potential given by Equation 46:

$$\phi_p = D A e^{i\alpha} \cosh(k(h+z)) e^{-i\omega t} \sum_{m=0}^{\infty} \varepsilon_m i^m J_m(kr) \cos(m(\theta-\gamma)) \tag{70}$$

Davis [35] notes that this equation can also be expressed as the sum of Hankel functions of the first and second kind as:

$$\begin{aligned} H_m^{(1)}(kr) + H_m^{(2)}(kr) &= J_m(kr) + iY_m(kr) + J_m(kr) - iY_m(kr) \\ &= 2J_m(kr) \end{aligned} \tag{71}$$

A Hankel function of the first kind ($H_m^{(1)}(kr)$) represent waves that are radiated from the origin to infinity and Hankel function of the second kind ($H_m^{(2)}(kr)$) represent waves gravitated from infinity to the origin. In this way, a plane wave can be viewed as the infinite sum of incoming and outgoing circular waves.

While this mathematical representation is not used further in this thesis, it is worth noting as it provides an underlying connection between the plane waves and circular waves. This goes some way to explaining how a circular wave can destructively interfere with a component of the plane wave to remove power from the wave field.

5.2.4 Modified Circular-Cylindrical Solutions – Evanescent Waves

The modified Bessel functions ($K_m(kr)$ and $I_m(kr)$) may also be used to solve the modified Bessel equations. These functions are included in various texts and are used to represent evanescent modes[1] as they are not periodic in $\hat{r}$. $I_m(kr)$ is often neglected as it is a non-propagating wave with a maximum at infinity and does not represent a useful phenomenon in ocean waves. For further information see Mei et al. [17].

[1]Evanescent modes are a surface displacement that oscillates with time and decays exponentially with distance from the point of radiation. Evanescent waves do not propagate and are considered a near field effect.

5.2.5 Wave Interactions

Wave interactions can be divided into two major categories: conservative and dissipative [2]. Conservative processes are those interactions in which energy within the wave field remains constant. For example, shoaling (the variation in height due to changes in water depth), refraction (the bending of wave fronts due to variations in water depth and by sea currents), diffraction (the scattering of waves impacting on a boundary) and some types of reflection (the change in direction of a wave front, usually due to a large uniform boundary) are conservative.

Dissipative processes are those interactions that decrease the amount of energy in the wave field. Such processes include wave breaking, bottom friction, percolation[2] and some types of reflection (like those involved with sloping or rough boundaries). The end point for the dissipated energy is usually heat generated by some form of friction.

It is useful to keep the division of processes in mind when considering wave energy conversion. Linear wave theory and a significant amount of work surrounding the analysis of WEC are dependent on wave interactions being conservative (see Section 5.4 for further details). However, as will be seen in later sections (particularly Chapter 9) it is dissipative processes which limit wave radiation and therefore wave energy absorption.

5.2.6 Wave Breaking

Wave breaking occurs when a wave becomes too steep and the crest topples over in a turbulent process that dissipates energy. The most common example is that of the wave that crashes onto a beach. Here the changes in water depth have forced the wave to increase in height and become unstable.

Wave breaking is a non-linear process that arises in finite amplitude waves. Small amplitude wave theory assumes infinitesimally small wave amplitudes and hence cannot make predictions about wave breaking directly. This is one of the limits of

[2]Percolation is flow through porous soil or rocks.

small amplitude wave theory and alternative theories must be utilised to predict the boundaries and effects of wave breaking.

Wave breaking is of particular interest in wave power generation as it affects the maximum amount of energy that can be transmitted in a monochromatic wave. It will also have implications for the interaction of waves as localised effects may induce wave breaking at certain points in the wave field, causing a departure from the linear models.

Oh Sang-Ho [36] provides a good summary of the various types of wave breaking criteria and notes that they can be divided into three main groups: geometric, kinematic and dynamic. It is also noted here that the mechanism for governing the inception for wave breaking is not well understood.

The geometric criteria are those involved with the wave's physical dimensions. For example, MIT offers a set of open course notes [37] that defines the breaking criteria as a ratio between the wave amplitude and the wave length $\frac{A}{\lambda} \leq 0.07$.

Another geometric criteria was generated theoretically by Stokes. Stokes examined the wave solution using a second order non-linear perturbation method, and noted that the crest became sharper and the troughs shallower than in linear theory [23]. Stokes determined that a wave would break if the angle of the wave crest became 120°. It was noted by Taylor [38] that experimental data from standing waves agreed with this criteria.

Pontes [2] provides another example of a geometric breaking criteria, in this case for random seas. The criterion is that a wave will break when the water depth becomes less than twice the significant wave height[3]. Oh Sang-Ho [36] notes that geometric criterion are “quite sensitive” to wave modulation, fetch length and directionality.

[3]Significant height is a measure of wave height used for stochastic sea states.

Kinematic criteria are those based on the fluid particle velocity. An example of such is that if the horizontal particle speed at the crest of the wave is greater than that of the wave celerity then the wave will spill forward. This particular criterion has been analysed extensively with varying results. Stansell and MacFarlane [39] provide a robust study that indicates that the kinematic criterion does not correlate well to experimental data. In this situation they reported results where waves broke when the crest horizontal particle velocity reached between 0.97 and 0.98 times the wave celerity. Stansell and MacFarlane also quote Banner and Peregrine [40], who state that studies of waves have shown examples where the horizontal particle velocity was measured to be greater than the wave celerity with no wave breaking.

The remaining category is that of the dynamic criteria. This group of criteria is based on the definition that downward acceleration of a particle must not exceed a certain value, most often expressed as a factor, f_b, of gravity, g. Taylor [38] noted that a standing wave will break if the downward crest acceleration is greater than g. Longuett-Higgins [41] showed theoretically that for a progressive wave the downward crest acceleration was $0.5g$ when the stokes criteria 120° was fulfilled. Further studies noted different values depending on the conditions being examined. Values of f_b between 0.52 [42] and 0.33 [43] have been suggested depending on whether the waves are regular or irregular, or whether there is a wind present.

5.3 WEC and Wave Interactions

The performance and survivability of a WEC is determined by the way in which it interacts with the ocean waves. The capture and storage of energy requires the movement of mass relative to some form of reference; i.e. the movement of air past a turbine in the case of an OWC device. The dynamics of the situation determine how much energy is transferred from the medium of the ocean to the device. This section aims to provide a summary of common approaches used to analyse these complex dynamic situations.

The study of the coupling between the ocean and the device is the subject of numerous papers. More often than not, the study is specific to a given WEC design, although the underlying tools used to analyse each situation tend to be similar. This section provides a description of common approaches to the analysis of WEC and wave interactions.

5.3.1 Two Dimensional Studies of WEC

Falnes and Budal [12] put forth the concept that, in two dimensions, all of the energy of a wave could be absorbed. They illustrated this using the superposition of three two-dimensional waves: an incident plane wave, a symmetric (heave) wave and an anti-symmetric (surge) wave. Fig 12 summarises this concept.

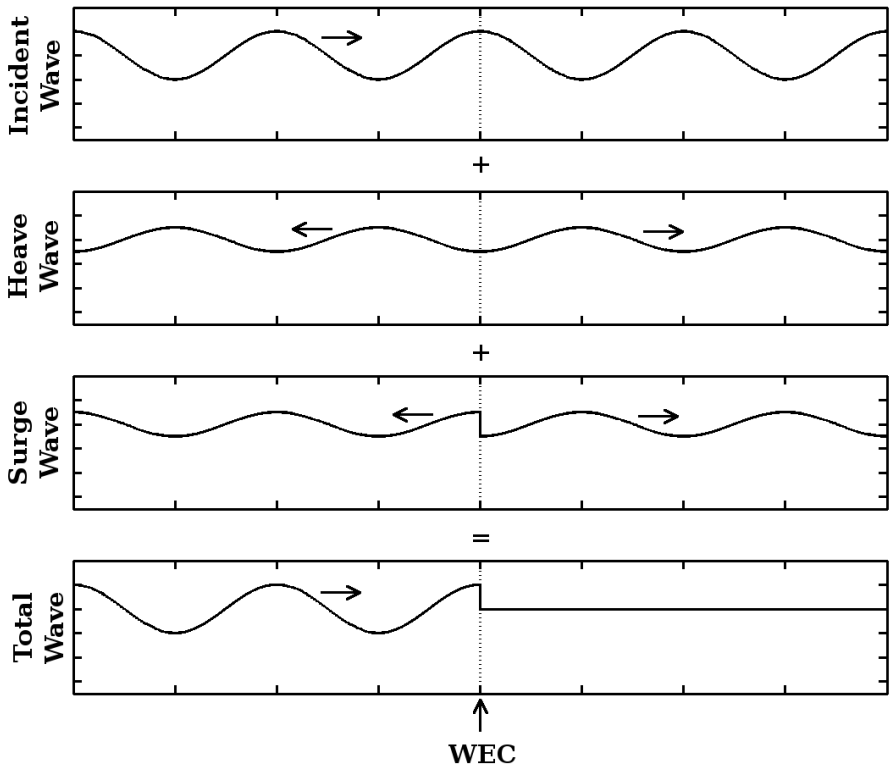

Figure 12: Wave Power Absorption in 2D Based on the Destructive Interference of Incident and Radiated Plane Waves

This two-dimensional cancellation of waves has bought forth the concept summarised by Budal and Falnes:

> In order for an oscillating system to be a good wave absorber it should be a good wave generator [44]

That is, wave energy absorption is based on the superposition of the incident wave with the radiated and diffracted waves and that the energy that can be extracted depends on the destructive interference of these waves. This basic principal is expressed in terms of velocity potential functions describing the total wave field potential, ϕ_T, the incident wave potential, ϕ_i, the diffraction potential, ϕ_d, and the radiated potential, ϕ_r where:

$$\phi_T = \phi_i + \phi_d + \phi_r \tag{72}$$

This approach was presented in an article by Falnes in 1980 [45]. The diffraction potential is defined as the potential resulting from the incident wave impinging on a stationary body of the WEC and is expressed mathematically as:

$$\frac{\partial \phi_d}{\partial n} = \frac{-\partial \phi_i}{\partial n} \quad \text{on the submerged surface(s) of the WEC body [22]} \tag{73}$$

Note that n is the normal vector pointing outwards from the submerged surface(s) of the body. The radiation potential is defined as the potential that the WEC body would generate if it underwent the same motion in a still body of water. McIver notes that, as a plane wave can be represented as the sum of an infinite number of Bessel functions (see Section 5.2.3), a plane wave will excite a large number of modes as it scatters [46]. The same is noted by Davis [35]. For PAWECs it is often assumed that the diffraction potential is small, $\phi_d = 0$, as the physical extent of the body is small. Mei et al. [17] note that this is true if the characteristic body length l_c fulfils the criteria that:

$$k l_c \ll 1 \tag{74}$$

Evans' article [13] on wave power absorption expanded on this principal and used two-dimensional complex potentials and body dynamics to prove that the absorption of a

two dimensional wave could be achieved using a horizontal cylinder. The idea was based on a cylinder that rotated about an off-centre axis, parallel to the cylinder's axis of symmetry. This would create a wave on only one side of the cylinder while leaving the other side of the fluid's surface undisturbed. With the correct motion and phasing compared to the incident wave, the downstream wave could theoretically be completely cancelled without interfering with the incident wave. This is an extension of the work done by Ogilvie on the forces on submerged cylinders [47].

Despite the points raised in the last paragraph, there are differences between the two-dimensional case, as represented by laboratory test flumes, and what would occur in the open ocean [19]. The walls of a flume create interferences that change the way in which the WEC interacts with the wave [48]. This limits the understanding that can be gained about a device's performance in the open ocean. Hence the examination of the three-dimensional case becomes important.

5.3.2 Analytical Three Dimensional Studies

Analytical solutions in three dimensions are rare as the solutions quickly become very complex. The source of this complexity is solving the water to body coupling, which is dynamic and depends on a large range of factors. Due to this complexity, analytical methods are usually supplemented with simplifications using experimental data or solved numerically.

In the analysis of wave energy conversion there are three main components to be modelled: the mechanics of the device, the dynamics of the power take-off and the mechanics of wave interactions. The approach followed in many examples, in particular Falnes [45], is summarised here. The study begins with the simple proposition that the total force in direction j (F_{Tj}) on the PAWEC body is equal to the sum of the forces due to the incident wave (F_{ij}) and forces due to the waves radiated by the body's motion (F_{rj}):

$$F_{Tj} = F_{ij} + F_{rj} \tag{75}$$

The forces are assumed to have complex amplitudes as they are derived from oscillating systems with complex amplitudes. This allows the time-averaged absorbed power from the motion of the body in direction j ($\overline{P}_{aj}$) to be calculated from the total force in that direction and the velocity of the body (v_j):

$$\overline{P}_{aj} = \frac{1}{2}\Re\left(F_{Tj}v_j^*\right) \tag{76}$$

where v_j^* is the conjugate of v_j.

At this point in the analysis there is a theoretical fork. Some groups solve for the forces due to radiation by determining an impedance matrix and solving for the elements of the matrix. This can be achieved through various methods including numerical calculations, theoretical analysis or experimentation. Other groups resolve the forces by examining the velocity potentials of radiated waves and applying the Haskind relationship. The Haskind relationship relates the forces upon an oscillating body to the velocity potentials of the radiated waves at infinity. Each approach will be covered in the following two sections.

5.3.2.1 Radiation Impedance Theory

The study of body dynamics derives a quantity called the radiation impedance, $Z_r(\omega)$ [19]. The radiation impedance is made up of two components, the radiation resistance ($R_r(\omega)$) and the radiation reactance ($X_r(\omega)$), such that $Z_r(\omega)=R_r(\omega)+i\,X_r(\omega)$.

The radiation resistance, also known as the damping coefficient, is the coefficient that relates the amplitude of motion of the body to the the amount of power radiated:

$$P_r=\frac{1}{2}R_r(\omega)\left|\hat{u}^2\right| \tag{77}$$

The radiation resistance must be real and non-negative. It has also been noted, that in the case for a submerged sphere, the radiation resistance in heave is roughly twice that in surge [49]. The reason for this is that, given the same magnitude of body velocity and planar cross-section, the heave wave must radiate energy in all directions while the

surge wave only radiates energy for ward and backward of the device (no energy is radiated sideways as there is no surface displacement in these directions).

The radiation reactance is related to the amount of energy that is stored in the fluid and returned to the oscillating body during each cycle of oscillation. The physical effect of the radiation reactance is seen in the phenomenon known as added mass (m_a). Note that $X_r(\omega)=m_a\omega$. Practically the added mass can be explained as the mass water that must be accelerated or decelerated as the body changes speed.

McIver and Evans [50] note that, in particular situations, the added mass can be negative. This occurs where a submerged body oscillates close to the surface or the body encircles an area e.g. a floating torus. The added mass may also be directional for non-symmetric bodies.

The outcome of this is that the relationship between the velocity of the body and the force experienced by the body, when expressed in the frequency domain, has a complex component. This also means that if the radiation impedance is matched to that of the incident wave, a resonant condition can be created where the absorbed power is a maximum real value. This process has been termed impedance matching and is summarised by Lockett:

> The physical system impedance should be set equal to the complex conjugate of the hydrodynamic impedance. [51]

Both components of the radiation impedance can be determined numerically using either a CFD program or WAMMIT. This, in turn, allows the calculation of the potential absorbed power.

5.3.2.2 Velocity Potential Theory and the Haskind Relationship

An in-depth treatment of this analysis can be found in the article by Mei and Newman [52].

The velocity potential approach to defining the radiation wave forces starts by assuming that the radiation potential (Equation 72) can be subdivided into six potentials based on the six degrees of freedom (heave, surge, sway, pitch, roll and yaw). Hence:

$$\phi_r = \sum_{j=1}^{6} v_j \phi_j \tag{78}$$

Where v_j is the velocity of the body in degree of freedom j and ϕ_j is the velocity potential resulting from a unit velocity measurement in degree of freedom j. Hence Equation 72 becomes:

$$\phi_T = \phi_i + \phi_d + \sum_{j=1}^{6} v_j \phi_j \tag{79}$$

The Haskind relationship is then used to determine the forces on the body. Note that it is often, but not always, assumed that the radiated potentials have the same frequency of oscillation as the incident wave frequency.

The Haskind relationship builds a connection between the forces and moments on a body and the velocity potential for forced oscillations of the body in calm water. The main reference in English comes from a summary of the relationship by Newman [53] and a later summary authored by jointly between Haskind and Newman [54].

Mathematically the Haskind relationship is summarised by:

$$F_j = i\omega\rho e^{i\omega t} \iint_S \left(\phi_i \frac{\partial \phi_j}{\partial r} - \phi_j \frac{\partial \phi_i}{\partial r} \right) dS \tag{80}$$

Where F_j is the force in direction j, ϕ_i is the incident potential, ϕ_j is the radiated potential function caused by the oscillation of body in direction j, and S is the surface of the body. The derivation of this formula requires the use of the Sommerfeld radiation condition noted in Section 5.6.2.

The approach to determining the radiation potentials varies from study to study. Numerical methods are covered in Section 5.3.3. Another common approach is the modelling of wave profiles using Green's functions.

5.3.2.3 The Green's Function Solutions

Two analytical functions referred to within various texts are the Green's function and the Kochin function. These represent the more mathematically advanced solutions in the field of wave energy.

The Green's function refers to a potential function that describes the effects of a periodic point source at a given point. Newman [55] describes the Green's function as using the solutions to the Laplace equation solved in spherical coordinates and consisting of three components: a source located at the given point, an image source located above the free surface and a function to satisfy the free surface boundary condition. Thorne presents a variety of point source wave solutions and comments that they can be reduced to this three term format [56].

The various boundary conditions used to derive linear wave theory are applied to Green's functions. This includes: incompressibility and continuity, the free surface boundary, a spatial harmonic criterion, a bottom boundary condition and the Sommerfeld radiation condition.

The Green's function, G_r, can be written in a variety of ways. A form that easily represents the description above comes from Mei [17]:

$$G_r = -\frac{1}{4\pi}\left(\frac{1}{r_s}+\frac{1}{r_s'}\right)+\frac{1}{4\pi}\int_0^\infty dK\, J_0(K r_p)\frac{2(\sigma+K)e^{-Kh}}{\sigma\cosh(Kh)-K\sinh(K h)} \times\cosh(K(z+h))\cosh(K(z_0+h)) \tag{81}$$

where

$r_s=\sqrt{(x-x_0)^2+(y-y_0)^2+(z-z_0)^2}$

$r_s'=\sqrt{(x-x_0)^2+(y-y_0)^2+(z-z_0+2h)^2}$

K *is the fourier transform variable*

$r_p=\sqrt{(x-x_0)^2+(y-y_0)^2}$

$\sigma=\frac{\omega^2}{g}$

(x_0, y_0, z_0) *is the origin of the point source*

The Green's theorem, given by Mei as Equation 82, can then be used to determine the scattering or radiated potential by setting $f_1 = \phi_d$ or ϕ_r, and $f_2 = G_r$.

$$\int\int\int_{\Omega} (f_1 \nabla^2 f_2 - f_2 \nabla^2 f_1)\, d\Omega = \int\int_{\partial\Omega} \left(f_1 \frac{\partial f_2}{\partial n} - f_2 \frac{\partial f_1}{\partial n} \right) dS \tag{82}$$

This means that, providing the positions of the source and the boundary conditions are known, it is possible to solve for the entire wave field.

The usefulness of this approach is in its ability to deal with irregularly shaped bodies. By breaking the surfaces of the bodies up into smaller elements and applying a panel method, it is possible to solve the interactions of complex shapes. An example of this technique is provided by Ursell, who solves the velocity potential for a two-dimensional submerged cylinder [57]. The major limitation is the complexity in solving all of the boundary conditions for all of the sources at each panel, hence numerical methods are involved to solve any but the simplest of cases.

The Kochin function is derived from Green's theorem and the interaction of a plane wave on the surface of the body. Mei and Newman [52] provide a good reference for further information. By assuming that the radiation condition holds at large radii, the components of Equation 79 can be written as:

$$\phi_j = \frac{i e^{\frac{-i\pi}{4}}}{\sqrt{2\pi k r}} H_j(\theta)\, e^{ikr} \qquad \text{as } r \to \infty \tag{83}$$

Where the Kochin function is:

$$H_j(\theta) = -k \iint_S \left(\frac{\partial \phi_j}{\partial n} - \phi_j \frac{\partial}{\partial n} \right) \left(e^{kz - ik(x\cos(\theta) + y\sin(\theta))} \right) dS \tag{84}$$

Maeda and Kinoshita [58] notes that the Kochin function is proportional to a radiation wave amplitude at infinity.

Mei and Newman go on to solve the Kochin function using slender body theory. This theory is outside the scope of this thesis, although the researches provide one comment worth noting. On completion of the analysis Mei and Newman note that the solutions

are spherical Bessel functions and that the modes 0 and 1 are heave and pitch. They also note that higher order modes relate to flexural motions of polynomial form.

The linearised Bernoulli equation is used to come full circle and relate the solutions of ϕ_j to the radiation reactance:

$$i\omega\rho\iint_S (\phi_j)\frac{\partial \phi_j}{\partial n}dS \equiv R_{rj} - i m_{aj}\omega \tag{85}$$

Further information about the application of this theory can be found in Kuznetsov et al. [59].

5.3.2.4 Alternative Methods

There are other methods of calculating the forces on partially submerged bodies. These techniques include the calculation of Morison forces, the Froude-Krylov theory and the perturbation method. Each method has limitations of applicability and suitability. Most notably for the Morison forces and Froude-Krylov calculations no consideration is given to the changes in wave heights caused by the presence of the body. For a summary of force calculations see Rahman [22].

5.3.2.5 The Antenna Effect

Using the tools described in Section 5.3 it is possible to examine the maximum theoretical performance for a point-absorber WEC. The analysis is outlined by Evans for two different modes of oscillation [13]. Evans uses the relationships between exciting forces and damping presented by Newman [53] to calculate the optimum energy absorption. This optimum absorption occurs at the point described by the impedance matching criteria and is expressed as an absorption length, as defined by Falnes and Budal [60].

The absorption length (also known as capture width) is a ratio between the total power absorbed by the WEC and the amount of power in one meter of wave front of the

incident wave. Two expressions for the maximum absorption length were derived depending on the mode of oscillation of the body.

Given an incident plane wave of wavelength λ and a symmetric radiated wave (or wave generated from a heaving axisymmetric buoy) the maximum absorption length, L_{a0}^{max}, is:

$$L_{a0}^{max} = \frac{\lambda}{2\pi} \tag{86}$$

For a non-symmetric wave with a single order of rotational symmetry (or wave generated from a surging buoy) Evans found that the maximum absorption length was:

$$L_{a1}^{max} = \frac{\lambda}{\pi} \tag{87}$$

This is an interesting result as it describes the possibility that a WEC could potentially absorb more energy than is incident on its physical extent. For instance, if a 10 meter wide device radiates a surge wave that interferes with a 100 meter long wave in an optimal manor, the absorption length for the device would be approximately 32 meters. If this were possible the absorption length would be more than 3 times the device's extent.

The effect is analogous to the antenna effect for a radio aerial. A radio aerial can absorb more energy than is incident on the frontal area of the aerial and hence can be made from thin structural members rather than solid panels.

Falnes [19] predicts that the maximum absorption length occurs when the absorbed power is equal to the power that would be radiated by the body's motion in still water. This result connects the power radiated by a body to its maximum performance as a wave energy converter. Careful note should be made that the absorbed power can be larger than the radiated power (though the size of the device will be suboptimal in this condition).

5.3.3 Numerical Three Dimensional Studies of WEC

Many three-dimensional numerical studies have been used to analyse the characteristics and performance of different WECs. The majority of these fall into three categories: computational fluid dynamics, dynamic system analysis and numerically computed potential flow.

Computational fluid dynamics (CFD) models have been used for modelling a number of WEC devices e.g. the CETO wave device [61]. This method tends to be favoured for devices that are subsurface, as the dynamics of the device tend to be dominated by the flow effects around the device rather than the radiation of waves.

Dynamic system analysis has also been used extensively to model and couple various components of a WEC from simplified water interactions through to grid connections and dynamics. An example of such a model built in simulink is provided by Amilibia [62] while another solved numerically is provided by Le-ngoc [29]. Due to the complexity in modelling the interactions of so many components, simplifying assumptions are usually made with regards to the hydrodynamics. For example Amilibia assumes that there is no effect on the hydrodynamics due to radiated waves and similarly Le-ngoc assumes that the wave height of the incident wave is unaffected by the device's interaction. The strength of this method lies in the ability to model complete systems of WECs and its weakness is that careful attention must be made to the assumptions applied in each step.

A common approach used to analyse the hydrodynamics of floating bodies is to combine the Green's function point sources (see Section 5.3.2.3) and a panel method to calculate the wave field. WAMIT [63] automates the application of these point sources to a panel method and represents numerically computed potential flow. WAMIT has been used to determine hydrodynamic (added mass and damping) characteristics of bodies.

Studies have been completed comparing the outputs from different approaches with experimental results. These comparisons depend on the accuracy of the experimental

measurement and, as noted by Payne et al. [64], the ideal constraints in numeric packages can be distorted by experimental constraints.

5.4 The Study of Point-Absorbers

There are two key reasons why PAWECs have been the focus of a significant amount of study. The first is that, by definition, a PAWEC is physically smaller than either a terminator or attenuator design. A smaller physical size implies a lower construction cost and therefore a more profitable installation. The other key feature is described above in Section 5.3.2.5. If the antenna effect can be utilised it would suggest that a point absorber WEC can capture a significant amount of the energy in the wave-field without having to span the entire wave front. This has lead some observers to believe that the PAWEC has an excellent potential to become a commercially viable opportunity e.g. [65].

The design of a PAWEC has been discussed in great detail in the literature after much theoretical and experimental work. This section summarises some of the relevant findings scattered throughout the literature.

5.4.1 Design Criteria for a PAWEC

The body of a PAWEC makes waves as it moves through the water. These waves interfere with the incident wave to extract energy. Theoretically if a smaller WEC body is moved through a greater amplitude than a larger body, it should be able to produce the same radiated wave [66]. This brings up the concept that if the motion of a WEC were to resonate at the incident wave frequency, the excitation force and velocity would be in phase and this would allow the maximum absorption of power. There is also a potential at this point that the resulting amplitude of motion could be greater than the incident wave height.

Theory has been developed in both two and three dimensions. The principals developed in each area do not necessarily apply to the other but it is worth noting the limitations and attributes discovered in each.

5.4.1.1 Two-Dimensional Limits of Energy Absorption

For a two-dimensional symmetric body moving in only one direction, the maximum amount of energy that can be absorbed is 50% of the incident wave energy [66]. It is further noted that it is possible to absorb 100% of the incident wave energy if the symmetric body is allowed to move in more than one direction or the body is non-symmetric. It is important to keep this in mind for the three-dimensional case as it will impact the performance of wave farms. Although, in theory, a point absorber can absorb more energy than is incident upon the device, a row or array of point absorbers will approximate the two-dimensional case.

5.4.1.2 Dynamic Reflectors

A related concept developed for the point absorbers is that of a dynamic reflector. Budal and Falnes point out that although a line of axisymmetric PAWECs moving in only one direction can absorb 50% of an incident plane wave, if another row of non-absorbing buoys are added behind the absorbing row it is possible to use these as dynamic reflectors and thereby improve the efficiency of power absorption [66]. The second row of non-absorbing buoys acts like a reflecting wall. This concept applies equally well to two- and three-dimensional WEC.

5.4.1.3 A Relationship Between Displaced Volume and Power

Other design criteria have been derived for specific WEC configurations. Budal derived a relationship that ties the displaced volume for a heaving WEC to its maximum power output [67]. This relationship is outlined by the following equation:

$$\frac{P}{V} < \frac{\pi \rho g H}{4T} \quad \text{where} \quad V = \text{Volume} \tag{88}$$

Note that this relationship is constrained by 5 conditions. The key constraints are that the oscillation is small (so that the displaced volume tends to zero) and the motion is limited to heave. The other assumptions are based around it being physically possible for the body to oscillate in the manner described.

5.4.1.4 Criteria for Wave Radiation

Various authors (Evans [49], Mei and Newman [52]) have mentioned the fact that an ideal wave energy absorber should, when moved in still water, radiate a wave in a direction opposite to the wave incidence. Srokosz [48] notes the same principal after studying the two-dimensional case and adds that the energy absorber will only radiate waves of the same wavelength as the incoming wave.

Mei and Newman [52] note that:

> In all cases the optimum combination of an even and odd mode shape is related in precisely the manner to cancel the radiated waves downstream, ($\theta = 0$) and reinforce the separation components upstream ($\theta = \pi$).

This condition assumes that the WEC reflects the incident wave completely so that the downstream wave field consists of only the the radiated waves. Combining this criteria with the directionality criteria suggests that an efficient WEC should cancel out the incoming wave by reflecting the wave and radiating a wave toward the source of the incident wave.

5.4.1.5 Load Shedding

The principal that an efficient WEC only radiates a wave upstream can also be utilised in reverse by radiating waves to lower efficiency when required. Salter used an interesting design feature where he added a “hump back” to one of the Ducks. This meant that high displacements produced waves astern which then limited the power absorption and the mooring loads in high seas [68]. The technique of reducing the

loads on a WEC by radiating waves in suboptimal directions is known as load shedding. This principal was at the heart of the design of the Pelamis (Fig 8).

5.4.1.6 Optimum Amplitude and Phase Criteria

Mei and Newman also comment that for a wave to have an optimum absorption it must have a motion at the optimum amplitude and phase. This relates to the device having the correct radiation reactance for the incident wave. Hence, a device that can have optimum absorption at various frequencies will need to tune its inertia and damping.

Falnes [66] expresses the same concept by saying that, at optimum absorption, the velocity of the body should be in phase with the forces from the waves. Falnes also notes that the optimal radiated wave has an amplitude that is proportional to the wave amplitude.

5.4.1.7 Energy Storage for Multispectral Waves

The ability to match the device's impedance to the incoming waves becomes significantly more challenging in spectral seas. Falnes [19] notes that it may be necessary to use stored energy to meet the reactive needs of the match. Falnes [14] quantifies the size of the reservoir required by ensuring that the device has 100 seconds of stored wave energy. This will allow the device to provide sufficient reactive energy to maintain optimum conditions.

5.4.1.8 Location of the Water Displacing Surface

Alves [69] introduces the concept that, as waves are surface phenomena, the distance of the active (water displacing) surface of the body to the still water level will affect performance. It is noted that the depth of the submerged device must be similar to the vertical movement of the device to be able to radiate waves. Further submergence will reduce the body's ability to radiate waves. Alves states this results in a simple design principal:

> To improve the radiation condition of a WEC its active surface might be located as close as possible to the free surface.

Alves also notes that flat bottomed devices have viscous effects and that by changing the bottom to be round or pointed, these effects can be reduced. In another paper [70] Alves notes that the reduction in radiation ability comes from the inability of the submerged base to interfere with the free surface and that:

> As the submerged base of the cylinder is more and more submerged, its ability to generate waves is smaller and smaller.

5.4.1.9 Convex Surfaces Criterion

Salter [26] notes that sharp edges dissipated more energy than expected in vortex shedding. He also goes on to suggest that low free boards allow waves to break over the top of the device and that concave shapes can amplify peak stresses by focusing wave energy. Hence, all parts of the device should be convex.

5.4.1.10 Overload Design

Salter [26] also notes that it is impossible to apply a restraining force for the largest waves and that end-stops will inevitably be broken. He suggests that if rotary methods can't be used then there needs to be a method of load shedding.

5.4.1.11 Dynamic Magnification

The dynamic magnification is defined as the amplitude of the motion of the body divided by the amplitude of the incident wave. French [65] states that the power absorption is roughly proportional to the dynamic magnifier and that a dynamic magnifier of more than two should be easily achievable at resonance. A similar point is made by Evans [71] when he notes that if the dynamic magnifier of a sphere is limited to one, then the maximum capture width is limited to 0.7. Evans extends this statement to say that capture widths in excess of 1 can only be achieved through dynamic

magnification greater than 1. Salter [26] extends the range of dynamic magnification by stating that it is possible to have the motion of the body an order of magnitude more than the wave amplitude. Falnes and Budal [12] also come to a similar conclusion.

5.4.2 Scale Testing

As there is considerable expense involved with building full size devices, laboratory testing of scale prototypes is a common avenue to increasing investor confidence. Jefferey et al. [68] note that testing between scales of 1/150 and 1/15 give representative results. One of the difficulties of scaling is that not all scales are linear. For instance, where N_l is the model length over the full size length, power scales by a factor of $(N_l)^{3.5}$, and forces scale by $(N_l)^2$ [11].

5.4.3 Wave Measurement

Wave measurement is an integral part of the laboratory study of PAWEC. Common methods for measuring wave heights include capacitance-based wave gauges, ultrasonic sensors and pressure measurements. In this thesis, the economics of using a large number of sensors lead to the use of low cost pressure sensors.

There is some discussion around the transfer function appropriate for using pressure sensors to measure wave height. In 1994 Kuo [72] presented an empirical transfer function to estimate wave height rather than simply calculating the wave height from the pressure based on wave height.

$$TF = e^{-0.905\frac{\omega^2 z}{g}-0.027} \quad for \quad 0.1 \le \frac{\omega^2 z}{g} \le 5.0 \quad ; \quad \frac{h}{\lambda} \ge 0.07 \tag{89}$$

However, a 2005 article by Tsai et al. [73], showed that this transfer function over-estimated wave heights by as much as 30% in certain situations and was derived from deep to intermediate water waves with small wave steepness and negligible transducer depth effect. They go on to state that the pressure to wave height transfer function

based on linear wave theory was accurate within 3.6% providing robust experimental procedure was followed and a suitable sensor was used.

Experimentally, it is good procedure to place the sensors more than one wavelength from wave generators to allow the waves to become plane, noted by Falnes [12].

Hughes [11] notes that one of the key concerns when completing wave measurements in the laboratory is the interference of reflections from wave generator and the surrounding walls. Attenuation methods include short burst testing to avoid the interference of reflections or energy dissipating beaches with rough elements such as horse hair mats. Drag from the side of the tanks and higher harmonics in wave or current generation are also mentioned.

5.5 Waves and Spectra

Wind does not generate waves of a single frequency, instead ocean waves have a spectrum of frequencies. While this study remains focussed mainly upon monochromatic waves it is important to keep in mind the context of multispectral ocean waves.

The variability of ocean waves was summed up by Trujillo and Thurman [18] who note:

> In the open ocean one wave in 23 will be over twice the height of the average wave, one in 1175 will be three times as high, and one in 300,000 will be four times as high.

They also note that waves twenty times the average wave height are reported regularly and that 10 ships a year are lost to freak waves. Hence, spectral effects should always be kept in mind when considering wave energy.

A range of different spectra exist for describing the distribution of ocean wave frequencies. As spectral wave scenarios do not play a significant role in this thesis, this section will be limited to examining a single spectrum: the P-M Spectrum

5.5.1 The Significant Wave Height

The significant wave height, H_s, is defined as the average height of the highest third of the waves [74]. The definition dates back to the time of manual measurement and calculation of wave statistics. The more modern approach has defined the significant wave height as four times the square root of the zeroth order spectral moment m_0:

$$H_s = 4\sqrt{m_0} \tag{90}$$

Spectral moments are defined based on the spectrum $S(f)$ where f is wave frequency [75]:

$$m_n = \int_0^\infty f^n S(f) \partial f \tag{91}$$

The zeroth order spectral moment is calculated by setting $n=0$ in Eqn 91.

5.5.2 The Energy Period and Power

Jeffrey et al. [68] summarised various calculation methods associated with spectral sea states. The method of calculating wave energy period and power depends on whether discrete or continuous data is available. For simplicity, the following equations are presented based on a continuous spectrum data.

The energy period, T_e, is used as a useful comparator for sea states and is defined as the period of a regular wave that has the same power density and significant height as the spectral sea state. It can be calculated using spectral moments defined in Eqn 91.

$$T_e = \frac{m_{-1}}{m_0} \tag{92}$$

Hence, the time averaged power per meter wave front of a spectral sea can be calculated:

$$\overline{P}_{/m} = \frac{\rho g^2}{64\pi} H_s^2 T_e \tag{93}$$

5.5.3 The Pierson-Moskowitz Spectrum

The Pierson-Moskowitz spectrum (also known as the P-M spectrum) was developed by Pierson and Moskowitz, and a study made by weather ships based in the North Sea. The P-M spectrum describes a fully developed, wind created sea. This excludes effects of swell from far away storms. For such a sea state to develop there needs to be a relatively consistent wind, with velocity U_O, for 6-18 hours over a fetch between 200km and 600km. Mathematically the spectrum is described based on wind speed as:

$$S(\omega)=\frac{\alpha_{pm} g^2}{\omega^5} e^{\left(-\beta_{pm}\left(\frac{\omega_O}{\omega}\right)^4\right)}$$

where

$$\alpha_{pm}=0.0081 \qquad \beta_{pm}=0.74 \qquad \omega_O=\frac{g}{U_O} \tag{94}$$

Note that the wind speed is measured at 19.5 meters above the still water level. If it is not, further correction factors can be applied [68].

The P-M spectrum can also be calculated based on a significant wave height by adjusting two of the three variables [76]:

$$\alpha_{pm}=0.0081 \qquad \beta_{pm}=1.25 \qquad \omega_O=\sqrt{\frac{0.161\, g}{H_s}} \tag{95}$$

Subsequent work by Hasselmann et. al. also studies data collected in the north sea and notes that the wave spectrum never fully develops [77]. Hasselmann et al. propose another spectrum known as the JONSWAP spectrum which has a more pronounced peak than the P-M spectrum. For further reference Rahman [22] provides a good introduction to a range of spectra.

5.6 Methods of Calculation

This section summarises the approaches to calculating various properties of surface waves. For some properties there are various methods of calculation and only those

relevant to this thesis, in particular those relevant to linear wave theory, have been included here.

5.6.1 Particle Displacement and Acceleration

The particle velocities during the derivation of the velocity potential and are given by Equation 15. To calculate the displacements and accelerations of a particle all that is needed to be done is integrate or differentiate with time.

Particle displacement for the plane wave potential presented by Equation 45 are:

$$x_x = \frac{\cos(\gamma) A e^{i\alpha}}{\sinh(k h)} e^{ik(x\cos(\gamma)+y\sin(\gamma))} \cosh(k(h+z)) e^{-i\omega t} \tag{96}$$

$$x_y = \frac{\sin(\gamma) A e^{i\alpha}}{\sinh(k h)} e^{ik(x\cos(\gamma)+y\sin(\gamma))} \cosh(k(h+z)) e^{-i\omega t} \tag{97}$$

$$x_z = \frac{i A e^{i\alpha}}{\sinh(k h)} e^{ik(x\cos(\gamma)+y\sin(\gamma))} \sinh(k(h+z)) e^{-i\omega t} \tag{98}$$

Rahman [22] notes that the particle displacement should never be greater than the wave amplitude.

The particle velocity for the plane wave potential presented by Equation 45 are:

$$v_x = -\frac{i k g \cos(\gamma) A e^{i\alpha}}{\omega \cosh(k h)} e^{ik(x\cos(\gamma)+y\sin(\gamma))} \cosh(k(h+z)) e^{-i\omega t} \tag{99}$$

$$v_y = -\frac{i k g \sin(\gamma) A e^{i\alpha}}{\omega \cosh(k h)} e^{ik(x\cos(\gamma)+y\sin(\gamma))} \cosh(k(h+z)) e^{-i\omega t} \tag{100}$$

$$v_z = -\frac{k g A e^{i\alpha}}{\omega \cosh(k h)} e^{ik(x\cos(\gamma)+y\sin(\gamma))} \sinh(k(h+z)) e^{-i\omega t} \tag{101}$$

The particle acceleration for the plane wave potential presented by Equation 45 are:

$$a_x = -\frac{k g \cos(\gamma) A e^{i\alpha}}{\cosh(k h)} e^{ik(x\cos(\gamma)+y\sin(\gamma))} \cosh(k(h+z)) e^{-i\omega t} \tag{102}$$

$$a_y = -\frac{k g \sin(\gamma) A e^{i\alpha}}{\cosh(k h)} e^{ik(x\cos(\gamma)+y\sin(\gamma))} \cosh(k(h+z)) e^{-i\omega t} \tag{103}$$

$$a_z = -\frac{i\,k\,g\,A\,e^{i\alpha}}{\cosh(k\,h)} e^{ik(x\cos(\gamma)+y\sin(\gamma))} \sinh(k\,(h+z))\, e^{-i\omega t} \tag{104}$$

Various forms of these Equations 96 to 104 can be found in most of the linear wave theory references e.g. [20] [22] [23] etc.

5.6.2 Sommerfeld Radiation Condition

The Sommerfeld radiation condition states that scattered and radiated waves must have only outward flowing energy at infinity [22] [78]. The radiation condition is often used as a mathematical constraint when solving Green's functions (see Section 5.3.2.3) and is important to note when examining the waves radiated from a body. In potential flow theory where the time harmonic is $e^{-i\omega t}$ the radiation condition is represented mathematically as:

$$\sqrt{r}\left(\frac{\partial}{\partial r} - i\lambda\right)(\phi_r) = 0 \quad as \quad r \to \infty \tag{105}$$

Note that ϕ_r is the diffracted or radiated potential and that λ is an eigenvalue greater than 0. In first order wave theory the eigenvalue is simply the wave number k.

5.6.3 Energy

The amount of energy stored within and transmitted by a surface wave is important to the study of wave power absorption as it indicates the forms of energy storage and relative quantities. The approach taken by a significant number of the books on ocean waves is to simply add the potential energy per wavelength and the kinetic energy per wavelength components as calculated from the particle displacement and velocities.

5.6.3.1 Potential Energy

The change in potential energy for a control volume bounded by the free surface, the bottom boundary and with surface dimensions dx and dy is given by:

$$d(PE) = d(mass)\, g\, \bar{z} \tag{106}$$

Where $\bar{z}$ is equal to the mean height of the element and can be calculated using the fluid depth, h, and the surface displacement, η:

$$\bar{z} = \frac{h+\eta}{2} \tag{107}$$

As the fluid is incompressible, $d(mass)$ is given by:

$$d(mass) = \rho(h+\eta)\,dx\,dy \tag{108}$$

Substituting Equations 107 and 108 into Equation 106 and then integrating gives an equation for the total potential energy of the fluid:

$$PE_{fluid} = \frac{\rho g}{2}\int\int (h^2 + 2h\eta + \eta^2)\,dx\,dy \tag{109}$$

Note that the term independent of η inside the integral represents the potential energy of the static fluid and can therefore be neglected. Hence the potential energy associated with the wave is:

$$PE_{wave} = \frac{\rho g}{2}\int\int (2h\eta + \eta^2)\,dx\,dy \tag{110}$$

The time averaged potential energy, per unit surface area, for a regular plane wave is:

$$PE_{/m^2} = \frac{\rho g A^2}{4} \tag{111}$$

5.6.3.2 Kinetic Energy

The change in kinetic energy of an infinitesimally small element is:

$$d(KE) = \frac{1}{2}d(mass)|\vec{V}|^2 \tag{112}$$

Noting that, in rectangular coordinates:

$$|\vec{V}|^2 = \left(\frac{\partial \phi}{\partial x}\right)^2 + \left(\frac{\partial \phi}{\partial y}\right)^2 + \left(\frac{\partial \phi}{\partial z}\right)^2 \tag{113}$$

And:

$$d(mass) = \rho\,dx\,dy\,dz \tag{114}$$

This gives the following formula for the kinetic energy:

$$KE_{wave} = \frac{\rho}{2} \int\int\int \left(\left(\frac{\partial \phi}{\partial x}\right)^2 + \left(\frac{\partial \phi}{\partial y}\right)^2 + \left(\frac{\partial \phi}{\partial z}\right)^2 \right) dx\, dy\, dz \tag{115}$$

The time averaged kinetic energy, per unit surface area, for a regular plane wave is:

$$KE_{/m^2} = \frac{\rho g A^2}{4} \tag{116}$$

It has been noted that the time averaged energy per unit surface area in both the kinetic and potential forms is equal. This is referred to as the equipartition of energy [17].

5.6.4 Pressure

In the derivation of linear wave theory the pressure field is defined through the Bernoulli equation and features in the dynamic free surface condition. The ability to calculate the pressure at a given point in the wave field is particularly important to this thesis, as the experimental section relies upon pressure measurement to determine the wave height (see Section 7.2).

The pressure beneath a wave is comprised of the hydrostatic pressure and the dynamic pressure. The hydrostatic pressure is caused by the changes in water depth and the dynamic pressure is caused by the motion of the fluid. The total pressure, p, can be calculated from the following equation outlined by Dean and Dalrymple [20]:

$$p = \rho \frac{\partial \phi}{\partial t} - \rho g z - \rho \frac{|\vec{V}|^2}{2} \tag{117}$$

Noting that the velocity can also be calculated from the velocity potential by Equation 15.

Hence the pressure can be derived for the regular plane wave potential in Equation 45:

$$p = -\frac{\rho g A e^{i\alpha}}{\cosh(kh)} e^{ik(x\cos(\gamma) + y\sin(\gamma))} \cosh(k(h+z)) e^{-i\omega t} - \rho g z - \frac{\rho k g A^2 e^{2i\alpha}}{\sinh(2kh)} e^{2ik(x\cos(\gamma) + y\sin(\gamma))} e^{-2i\omega t} \tag{118}$$

As linear theory assumes that the velocities are small, it is possible to drop the last term and reduce the pressure to:

$$p=\frac{\rho g A e^{i\alpha}}{\cosh(kh)} e^{ik(x\cos(\gamma)+y\sin(\gamma))}\cosh(k(h+z))e^{-i\omega t}-\rho g z \tag{119}$$

5.6.5 Time-Averaged Power

The time-averaged power is the power in a wave averaged out over one wave period. This represents the transmitted power within a wave and is of crucial importance to estimating the size of the energy resource in a given wave climate. This section examines the calculation of time-averaged power for monochromatic waves and excludes calculations for spectral seas as they are beyond the scope of this thesis.

5.6.5.1 Regular Plane Waves

The section follows the method in Mei [17]. The time-averaged value of a harmonic function $\overline{f}$ is defined as:

$$\overline{f} = \frac{1}{T}\int_0^T f\,dt \tag{120}$$

Where T is the period of function f. It is interesting to note that the time-averaged value for a perfectly harmonic function (say $f=\sin(\omega t)$) is equal to zero. The concept becomes useful in the potential theory context when the time-averaged value of the product of two complex functions is calculated. For two time harmonic functions with complex amplitudes i.e. $f_1=\Re\left(F_1 e^{-i\omega t}\right)$ and $f_2=\Re\left(F_2 e^{-i\omega t}\right)$:

$$\overline{f_1 f_2} = \frac{1}{T}\int_0^T f_1 f_2\,dt = \frac{1}{2}\Re\left(F_1^* F_2\right) \tag{121}$$

Where F_1^* is the complex conjugate of F_1.

Power, P, is defined as:

$$Power = \frac{Force \cdot Distance}{Time} = Pressure \cdot Area \cdot Velocity \quad (122)$$

For a regular plane wave the power is calculated per meter of wave front. This defines the area as a vertical plane extending from the free surface to the bottom boundary and having a unit width. It is also noted that this area is perpendicular to the wave incidence.

The pressure, as calculated in Equation 117 and remembering to ignore the velocity component, consists of a static head component and a dynamic head component. As the time-averaged value of sinusoidal functions is zero, the product of the velocity and the static head component of pressure can be ignored. This means that the power per meter of wave front, $P_{/m}$, is:

$$\overline{P}_{/m} = -\int_{-h}^{0} \frac{\partial \phi}{\partial t} \nabla \phi \, dz \quad (123)$$

For a regular plane wave, as derived in Section 4.1.3, the time averaged power is:

$$\overline{P}_{/m} = \frac{\rho g \omega A^2}{4k}\left(1+\frac{2kh}{\sinh(2kh)}\right) \quad (124)$$

This form of the time averaged power equation is a simple re-organisation of that recorded by Falnes and Budal [79]. The same equation is presented by Payne et al. [64] with the slight modification that it is in terms of the wave period rather than the wave phase velocity:

$$\overline{P}_{/m} = \frac{\rho g^2 T A^2 \tanh(kh)}{8\pi}\left(1+\frac{2kh}{\sinh(2kh)}\right) \quad (125)$$

Salter [80] also presents the wave power in terms of the significant wave height, H_s, derived from examination of the gravitational potential energy:

$$\overline{P}_{/m}\big|_{gravity} = \frac{\rho g^2 T H_s^2}{64\pi} \quad (126)$$

By the law of equipartition of energy (see Section 5.6.3.2) the total time-averaged power is twice the value given in Eqn 126.

Various other formulae have been presented for calculating the time-averaged power for a wave field consisting of plane waves with a distribution of frequencies. These are not included here, as spectral seas are beyond the scope of this thesis.

5.6.5.2 Regular Circular Waves

Falnes ([19 pg 90]) also calculates the radiated power associated with an out-going circularly symmetric circular wave. The complex potential for the wave is defined as:

$$\phi = a_m H_m(kr)\left|\cos(\vartheta_m)\cos(m\theta)-\sin(\vartheta_m)\sin(m\theta)\right| e(kz) \tag{127}$$

Where ϑ_m is an undefined integration constant and the term $e(kz)$ is defined as:

$$e(kz)=\frac{\cosh(k(z+h))}{\cosh(kh)} \tag{128}$$

The velocity potential defined by Equation 127 is then evaluated in the far field conditions (where $kr \gg 1$) and divided into a far field coefficient $A(\theta)$ and a near field potential ϕ_l. It is then noted that, in the far field, the curvature of the wave can be neglected and the far-field coefficient can be combined with the power per metre wave front for a plane wave (Eqn 124). This provides a total radiated power for a circular symmetric radiated wave:

$$P_r = \frac{\pi\omega\rho D(kh)}{2k}|A|^2 \tag{129}$$

Where $D(kh)$ is defined as:

$$D(kh) = 2k\int_{-h}^{0} e^2(kz)dz = \left(1+\frac{2kh}{\sinh(2kh)}\right)\tanh(kh) \tag{130}$$

Note that, in the case of a symmetric heave wave, $A(\theta)$ is expressed in terms of a_0 from Equation 127:

$$A(\theta)=\sqrt{\frac{2}{\pi}}a_0 e^{i\frac{\pi}{4}} \tag{131}$$

And A is defined as the θ independent far field coefficient found by calculating $\int_0^{2\pi} A(\theta) d\theta$.

5.6.6 Energy Flux

While time-averaged power is useful in calculating the net power flows over a complete wavelength, it does not provide an instantaneous result that can be examined moment to moment. Energy flux, on the other hand, represents the rate of energy flow through a given, mathematically-defined surface and can be used to study both active and reactive power fluctuations at any point of the wave. It is also utilised when calculating the group velocity (see Section 5.6.7). To calculate the change in energy within a control volume over time, or energy flux, of a volume:

$$\frac{dE}{dt} = \iint_S \rho \frac{\partial \phi}{\partial \vec{n}} \frac{\partial \phi}{\partial t} dS \tag{132}$$

Note that S is the bounding surface of the volume and $\vec{n}$ is the normal vector pointing out of the volume. See Wehausen and Laitone for further details [25]. Note that the normal vector definition means that energy leaving the volume is positive.

5.6.7 Group Velocity

For an explanation of group velocity and its importance to wave power absorption, see Section 5.2.2. Based on an examination of two plane waves, McCormick [23] defines the group velocity, c_g, as:

$$c_g = \frac{\partial \omega}{\partial k} \tag{133}$$

And notes that for a plane wave:

$$c_g = \frac{\omega}{2k}\left(1 + \frac{2kh}{\sinh(2kh)}\right) \tag{134}$$

This approach works well for plane waves but is limited in more complex situations where simplifications of the combined waves may not be possible. A more robust definition is provided by Newman [24 pg 264] when he states:

> The mean rate of energy flux across a fixed surface is the product of the energy density and the group velocity.

This can be rearranged to give a mathematical definition of group velocity in its most general form:

$$c_g = \frac{\rho \frac{d}{dt} \iiint_V \left(\frac{1}{2} |\vec{V}|^2 + gz \right) dV}{\rho \iiint_V \left(\frac{1}{2} |\vec{V}|^2 + gz \right) dV} \tag{135}$$

By examining the energy flux per unit area and the energy density per unit area, it is possible to calculate the group velocity at any point in the wave field. Noting the definition for energy flux, Equation 132, Equation 135 becomes:

$$c_g = \frac{-\int_{-h}^{0} \overline{\rho \frac{\partial \phi}{\partial t} \nabla \phi} dz}{\frac{\rho g}{2} \overline{\eta^2} + \frac{\rho}{2} \int_{-h}^{0} \overline{|\vec{V}^2|} dz} \tag{136}$$

5.6.8 Wave Celerity

Wave celerity is part of the three different velocities used when describing waves. i.e. phase velocity, group velocity and wave celerity. It is described as the speed with which a regular plane wave front advances and is defined by Chakrabati [76] as the wavelength divided by the wave period:

$$c = \frac{\lambda}{T} \tag{137}$$

Mathematically, McCormick [23] derives wave celerity by examining the plane wave solution for displacement, $A\cos(kx - \omega t)$, setting the term inside the bracket equal to

zero and then determining the differential angle. Hence $k\,dx-\omega\,dt=0$ and the wave celerity, c, is:

$$c=\frac{d\,x}{d\,t}=\frac{\omega}{k} \tag{138}$$

5.6.9 Properties of Bessel Functions

The mathematical properties of Bessel functions will be used extensively throughout this thesis. They are included here as a reference. Unless otherwise stated the properties are from Abramowtiz and Stegan [81]. All references are for Bessel functions of integer order. See Section 4.1.4 for a description of Bessel functions and how they arise as solutions of the Laplace equation in circular-cylindrical coordinates.

5.6.9.1 Negative Integer Order Identities

These identities show the relationship between a Bessel function of order $-m$ and a Bessel function of the same kind and of order m.

$$J_{-m}(k\,r) = (-1)^m J_m(k\,r) \tag{139}$$

$$Y_{-m}(k\,r) = (-1)^m Y_m(k\,r) \tag{140}$$

$$H^{(1)}_{-m}(k\,r) = e^{i m\pi} H^{(1)}_m(k\,r) \tag{141}$$

$$H^{(2)}_{-m}(k\,r) = e^{-i m\pi} H^{(2)}_m(k\,r) \tag{142}$$

5.6.9.2 Recurrence Relationships

These two relationships illustrate the connection between Bessel functions of order m and Bessel functions of order $m-1$ and $m+1$. Note: $\wp$ is any linear combination of J, Y, $H^{(1)}$ or $H^{(2)}$ where the coefficients of the combination are independent of m or r.

$$\wp_{m-1}(k\,r)+\wp_{m+1}(k\,r) = \frac{2\,m}{k\,r}\wp_m(k\,r) \tag{143}$$

$$\wp'_m(k\,r) = \frac{k}{2}(\wp_{m-1}(k\,r)-\wp_{m+1}(k\,r)) \tag{144}$$

$$\wp'_m(kr) = k\wp_{m-1}(kr) - \frac{m}{r}\wp_m(kr) \tag{145}$$

$$\wp'_m(kr) = -k\wp_{m+1}(kr) + \frac{m}{r}\wp_m(kr) \tag{146}$$

5.6.9.3 Wronskians

A Wronskian is a determinant that is used in the study of differential equations and can be used to show that a set of solutions in linearly independent.

$$\begin{aligned} W\left\{J_m(kr), J_{-m}(kr)\right\} &= J_{m+1}(kr)J_{-m}(kr) + J_m(kr)J_{-(m+1)}(kr) \\ &= \frac{-2\sin(m\pi)}{\pi kr} \end{aligned} \tag{147}$$

$$\begin{aligned} W\left\{J_m(kr), Y_m(kr)\right\} &= J_{m+1}(kr)Y_m(kr) - J_m(kr)Y_{m+1}(kr) \\ &= \frac{2}{\pi kr} \end{aligned} \tag{148}$$

$$\begin{aligned} W\left\{H_m^{(1)}(kr), H_m^{(2)}(kr)\right\} &= H_{m+1}^{(1)}(kr)H_m^{(2)}(kr) - H_m^{(1)}(kr)H_{m+1}^{(2)}(kr) \\ &= \frac{-4i}{\pi kr} \end{aligned} \tag{149}$$

5.6.9.4 Values for a Large Argument

As $kr \to \infty$ the values of Bessel functions of the first and second kind tend toward sinusoidal functions. This is interesting to note, as it suggests that the properties of radiated waves based on Bessel functions should also take the form of the properties of plane waves when the radiated wave is examined at a great distance from the origin of radiation.

$$J_m(kr) \to \sqrt{\frac{2}{\pi kr}}\cos\left(kr - \frac{m\pi}{2} - \frac{\pi}{4}\right) \quad as \quad kr \to \infty \tag{150}$$

$$Y_m(kr) \to \sqrt{\frac{2}{\pi kr}}\sin\left(kr - \frac{m\pi}{2} - \frac{\pi}{4}\right) \quad as \quad kr \to \infty \tag{151}$$

5.7 Limitations of Small Amplitude Linear Wave Theory

The linearisation of various properties and the assumption that the waves are infinitely small may well bring into question how well the mathematics model real life waves. The general consensus is, within limitations, real waves are modelled well. This section outlines a range of limitations that are relevant to small amplitude linear wave theory (SALWT) and notes their implications.

5.7.1 Wave Height and Wavelength Limitations

McCormick states that the theory has excellent accuracy providing the wavelength is at least fifty times longer than the wave amplitude [4]. Kuznetsov et. al. [59] agree that the wave height must be much smaller than the wavelength and adds that Ursell's number must be much less than 1 i.e.

$$\frac{2A}{h}\left(\frac{\lambda}{h}\right)^2 \ll 1 \tag{152}$$

The inclusion of a depth factor in Ursell's number suggests that SALWT will model deep waves better than shallow water waves of similar amplitudes. Tsai et al. [73] note that the linear approximation matches real waves in deep water, however, in shallow water non-linear terms become significant.

5.7.2 Stokes Drift

Linear theory predicts that particles move in circular paths and so that there is no mass transport within a linear wave. Real waves, however, have a shallower trough than crest which causes the particle paths not to close. This means that particles progress forward in the direction of wave propagation. This is known as Stokes drift. Stokes presented a non-linear theory that incorporated both the difference in crest and trough heights as well as the mass transfer [82].

5.7.3 Small Amplitude Approximation

Another limitation is that, when integrating properties over the depth, it is often assumed that the integral $\int_{-h}^{\eta} f(z)\,dz \approx \int_{-h}^{0} f(z)\,dz$. As an example, Mei et. al. [17] note that when the kinetic energy is integrated across the interval $z \in [0, -h]$ the result has an accuracy of $O((kA)^2)$. Hence, the accuracy of linear wave theory increases as the amplitude reduces or the wavelength increases.

5.7.4 Wave Breaking

Linear wave theory also does not provide an insight into when a wave will break. Non-linear theories show the difference between the crest and trough shapes and can thereby show that the crest may attain a peak beyond which it must break. Further criteria must be applied to limit the wave size in linear theory (see Section 5.2.6).

5.7.5 Flow Separation

Flow separation is when the streamlines of a fluid detach from a body interacting with the fluid. This usually creates downstream vortices and viscous mixing. Complex potential theory does not model flow separation although it can be used to predict the onset of separation. Mei et al. [17] note that if the amplitude of the incident wave is greater than the characteristic leading dimension of the body i.e.

$$\frac{A}{l_c} \geq O(1) \tag{153}$$

then flow separation occurs and “form drag” must be taken into account. A good rule of thumb is that there is no separation when the orbit of the water particles is much less than, say, the diameter of a cylinder.

5.8 Review of the Literature

Modern PAWEC theory has developed a range of excellent technical tools to analyse the interaction of bodies and incident waves. For example, using a distribution of Green's function point sources along the surface of a body to numerically solve for body dynamics. These tools have facilitated detailed studies on a small range of body shapes.

Perhaps the biggest challenge that these complex analysis methods have is their complexity. The mathematics involved is difficult to visualise and the numerical solutions often only provide results for the specific case being studied. It is a challenge to look at these problems and see what a radiated wave looks like or which attributes of the body shape affect wave radiation. The complexity also makes it difficult to extract rules of thumb or widely applicable generalisations about device performance.

Another area within the existing literature that could be improved is the number of practical experiments carried out in three-dimensional wave basins. A considerable number of tests are preformed in wave flumes as these test facilities are more accessible than larger wave basins. Wave flume studies are useful for comparing results with two dimensional wave theory, however, they are not consistent with the practical application of absorbing wave energy in an open wave field.

When theoretically and experimentally examining WEC interactions in three dimensional oceans the limitations of wave theory must be understood. For example, there is a significant body of work that has examined wave breaking in planar ocean waves but there is little to now information on how wave breaking will occur in radiated waves. This is a particularly important gap in modern understanding as the various results derived using linear theory may be limited by this three dimensional effect.

The scope of this thesis aims to address these points by focusing on a mathematical solution that is simpler than the previous solutions. The aim is to investigate a simpler

solution that is easily visualised and develop a method that can apply these solutions to a range of different bodies. See Section 2.3 for further details.

6 Circular Waves and Wave Energy Conversion

One of the main questions this thesis looks to answer is: Can circular wave theory be used to determine design constraints for wave energy converters? This chapter covers a new theoretical study that aims to answer this question. The first step is understanding the characteristics of circular waves. The second is to determine if the circular wave theory can be used to make predications about wave power absorption and compare any predictions to existing theory. The third step is to examine the interaction of plane and circular waves for constraints that may affect the performance of a WEC.

To the knowledge of the author all of the proofs and theoretical constructs contained within this chapter and the associated appendices are original unless otherwise stated. The results from Sections 6.1, 6.2 and 6.3 have been published in the Ocean Engineering [83].

This study begins with the assumption that the horizontal extent of a PAWEC body is small. This allows the assumption that the wave created by the diffraction of the incident wave upon the body is small. With these two assumptions, the wave field can be described as the sum of two waves: the incident wave and the radiated wave.

Another way to reach the same position is to group the diffracted wave and the radiated wave into one potential function. This is logical as both are radiated waves and share similar properties. It also incorporates the idea that the diffracted waves will have an impact on the power absorption properties of the WEC.

In complex potential terms the total velocity potential for the wave field is:

$$\phi_T = \phi_i + \phi_r \tag{154}$$

Given that destructive interference between the waves must occur in order to be able to remove power, understanding the interaction between the incident wave and the radiated wave may indicate what is required from a wave energy converter.

The incident wave should represent the waves observed in the ocean. Ocean waves are variable in spectra and spatial distribution. That noted, ocean wave fields can be re-constructed from the mathematical frame work of the regular plane wave. Providing the waves remain linear (i.e. there is no breaking) the regular plane waves provide accurate models, particularly in deep water (See Section 5.7.3).

The radiated wave is not as easily represented. The common approach of the use of Green's functions is complex and seldom yields a concise analytical solution. Numerical solutions can be calculated, although they are often only valid for a very specific set of conditions and do not yield general rules.

6.1 The Circular Wave Velocity Potential

Each of the equations for the circular wave velocity potential referenced in Section 4.1.4 express the same solution in different forms. For this study the form that will be used is a combination of several from the literature.

The derivation begins with the unconstrained circular-cylindrical general solution to the Laplace equation given by Eqn 55:

$$\phi = H_m(kr)\left(A_f \cos(m\theta) + B_f \sin(m\theta)\right)\left(A_g e^{kz} + B_g e^{-kz}\right)A_h e^{-i\omega t} \qquad (155)$$

As in the previous derivation (Section 4.1.4) the bottom boundary condition can be applied and the $A_g e^{kz} + B_g e^{-kz}$ expression is reduced to $2B_g \cosh(k(h+z))$. The following trigonometric identity can be used to reduce the angular component of Eqn 155.

$$A_f \cos(m\theta) + B_f \sin(m\theta) = C_f \cos(m\theta - \zeta)$$

Where

$$C_f = \sqrt{A_f^2 + B_f^2} \quad \text{and} \quad \zeta = atan\left(\frac{B_f}{A_f}\right) \qquad (156)$$

The result is the velocity potential:

$$\phi = 2\, A_h B_g C_f H_m(kr)\cos(m\theta - \zeta)\cosh(k(h+z))e^{-i\omega t} \quad (157)$$

Applying the kinematic free boundary condition allows the replacement of the various constants of integration with the amplitude of the surface displacement and Eqn 158 gives the constrained circular-cylindrical solution to the Laplace equation, ϕ_c :

$$\phi = \frac{g B e^{i\beta}}{\omega \cosh(k h)} H_m(kr)\cos(m\theta - \zeta)\cosh(k(h+z))e^{-i\omega t} \quad (158)$$

This definition takes the constrained solution found in Eqn 68 as base and utilises components of the Wehausen and Laitone form (Eqn 67). The benefit of this will be seen when examining the components of circular waves.

6.1.1 Components of the Circular Wave Velocity Potential

A systematic study of the components of the circular wave velocity potential provides an initial understanding into the function of each component.

The $Be^{i\beta}$ component was defined in Section 4.1.4.2 as consisting of B, the mathematical wave amplitude, and β, the surface displacement phasing component. The reason B is referred to as a mathematical wave amplitude is because the actual surface displacement is also modified with distance from the origin (r), the angle relative to the positive x-axis (θ) and the order of the Hankel function (m) i.e. $|\eta| = f(B, r, \theta, m)$. B does however allow for the linear scaling of wave heights given the spatial modifications.

The radial component of Eqn 158 ($H_m(kr)$) affects the wave height based on the radial distance of the point from the origin. The Hankel function provides the periodicity of the surface displacement in the radial direction and it is coupled to the angular component ($\cos(m\theta - \zeta)$) through the order m .

The angular component of Eqn 158 contributes several properties to the surface displacement of the circular wave. The first aspect to note is that continuity of the surface displacement is required to construct physically relevant waves. Surface

continuity requires two constraints: zeroth order functional continuity and first order functional continuity.

Zeroth order functional continuity is achieved when the function has equal values on either side of the angular domain boundaries. Given that $\theta \in [-\pi, \pi]$, the following criteria must be fulfilled to meet zeroth order functional continuity:

$$\cos(m\theta - \zeta)|_{\theta=-\pi} = \cos(m\theta - \zeta)|_{\theta=\pi} \tag{159}$$

Similarly, first order functional continuity assumes the gradient of the function on either side of the angular domain boundaries is equal. Hence the criteria for first order functional continuity is:

$$-m\sin(m\theta - \zeta)|_{\theta=-\pi} = -m\sin(m\theta - \zeta)|_{\theta=\pi} \tag{160}$$

The constraint that satisfies the two functional continuity criteria is that m must be an integer i.e. $m \in \mathbb{Z}$.

The second aspect to note about the angular component of Eqn. 158 is that the new variable, ζ, can be used to rotate the angular modification to the wave height. Hence it is called the angle of radiation. The actual angle by which the angular spatial modification is rotated is $\frac{\zeta}{m}$. Note that when the order m is equal to zero the radiated wave is axisymmetric and the concept of an angle of rotation becomes redundant. To preserve B as the mathematical amplitude for a zeroth order circular wave, the angle of radiation must always be zero i.e. if $m = 0$ then $\zeta = 0$.

The remaining components of Eqn. 158 are familiar from linear wave theory. $\frac{\cosh(k(h+z))}{\cosh(kh)}$ characterises the variation in properties with fluid depth and $e^{-i\omega t}$ provides the temporal oscillation for the wave.

6.1.2 Circular Waves and Body Motions

The complex potentials of circular waves provide a considerable amount of information about the radiated surface waves including particle velocity, pressure distributions and surface heights. One of the key areas of interest is what these waves actually look like and how they relate to the motions of a PAWEC body. This section provides visualisations of the circular waves.

The simplest wave to examine is the zeroth order circular wave where $m=0$. In this case $\zeta=0$. This reduces the surface displacement to:

$$\eta=-i\,B\,e^{i\beta}H_0(kr)\,e^{-i\omega t} \tag{161}$$

The surface displacement can be plotted by assuming various values for the non-spatial variables.

Figs. 13 and 14 present a phasing study for the zeroth order circular wave. The figures illustrate the form of the wave and how the component β adjusts the phasing of the circular wave. Note that a similar series of graphs could be generated by setting β to $-\pi$ and incrementing t in steps of $\frac{\pi}{2\omega}$.

Intuitively the zeroth order circular wave represents a wave that would be generated by a smooth, axisymmetric body moving vertically (i.e. heaving) in the fluid. Henceforth, the zeroth order circular wave will be referred to as a theoretical heave wave.

The first order circular wave is not axisymmetric and has a rotational order of 1. This suggests that an axisymmetric body moving horizontally in the fluid could generate such a wave. The first order circular wave can also be rotated relative to the x-axis with the use of the ζ variable and hence, the direction the body would need to oscillate would also be rotated.

As the motions of the body in the horizontal direction have been defined relative to the incident wave (see Fig. 4) the same procedure must be followed for circular waves. Hence, a theoretical surge wave is defined as a first order circular wave with an angle

of radiation equal to the angle of incidence i.e. $\gamma - \zeta = 0$. A theoretical sway wave is defined as a first order circular wave with an angle of radiation equal to the angle of incidence plus or minus half of pi i.e. $\gamma - \zeta = \pm\frac{\pi}{2}$.

Another way of expressing these two criteria is that a theoretical surge wave is a first order circular wave that has its nodal line (line of no surface displacement) parallel to the incoming wave front. The theoretical sway wave is a first order circular wave that has its nodal line perpendicular to the incoming wave front.

Figs 15 and 16 present a rotation study for the first order circular wave. The figures illustrate how the component ζ adjusts the angle of radiation for a non-symmetric circular wave. Note that the surface displacement in Fig. 15c would represent a surge wave if the incident wave was travelling along the x -axis and a sway wave if the incident wave was travelling along the y -axis.

The higher order circular waves do not intuitively match the waves generated by the motions of a solid body. As the magnitude of the order is increased the order of symmetry also increases. The surface displacements have a rotational order equal to the circular wave order. Fig. 17 depicts a second order circular wave and is included for reference. The validity of this intuitive step will be reviewed when examining the experimental results. See Chapter 8.

Note that Figs 15 to 17 represent a surface displacement of the circular waves at a single point in time. The waves can also be plotted with time and captured as videos. Videos of zeroth and first order circular waves are included in Digital Appendix 6.

6.1.3 Limitations of the Body Motion Approximation

The relationships between the body motions and the circular waves suggested in the previous section are limited by the point source approximation. Circular waves model a wave source at the origin. A body heaving at the origin does not move in either the r

or θ directions. This allows the circular wave to model the radiated heave waves regardless of the amplitude of the motion.

A surging or swaying body, on the other hand, moves in the direction of wave propagation. This means that if the amplitude of motion is large compared to the radiated wavelength, the body may no longer appear as a point source. For this reason it must be assumed that the amplitude of motion, a, remains much smaller than the wavelength of the radiated wave i.e. $a \ll \lambda$ for surging or swaying bodies.

6.1.4 Rotational Degrees of Freedom

Section 6.1.2 relates circular waves to the three body translations. This leaves the three rotations of pitch, roll and yaw still to be described. In the same way that the surge and sway of an axis symmetrical body are related by the fact that they are both translations in the horizontal plane, pitch and roll can be considered rotations of each other in the $\hat{\theta}$ direction.

The waves radiated from pitch and roll will depend on the form and shape of the body. If limitations were applied to the form of the body and the radiated waves analysed it may be possible to use combinations of circular waves to model pitch and roll waves, however, there is no direct intuitive relationship. For this reason, these modes of oscillation are not included within the scope of this study.

Yaw cannot be modelled using the circular wave theory as the separation of variables isolates the oscillations of time from variation in the theta direction.

(a)

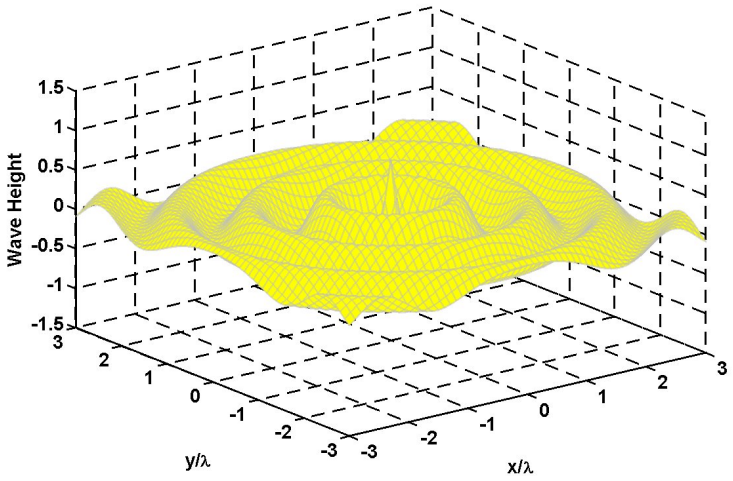

(b)

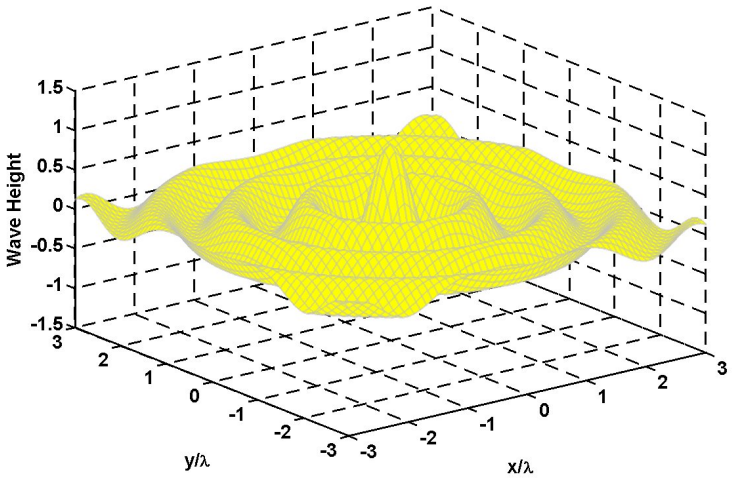

(c)

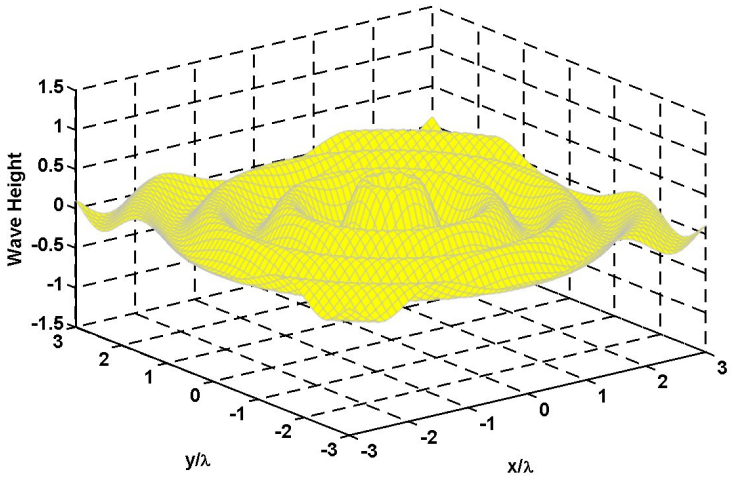

Figure 13: Phasing Study for a Deep Water Zeroth Order Circular Wave - 1 of 2

(a) $B=1 \quad \beta=\pi \quad m=0 \quad \zeta=0 \quad t=0$ (b) $B=1 \quad \beta=\frac{\pi}{2} \quad m=0 \quad \zeta=0 \quad t=0$

(c) $B=1 \quad \beta=0 \quad m=0 \quad \zeta=0 \quad t=0$

(a)

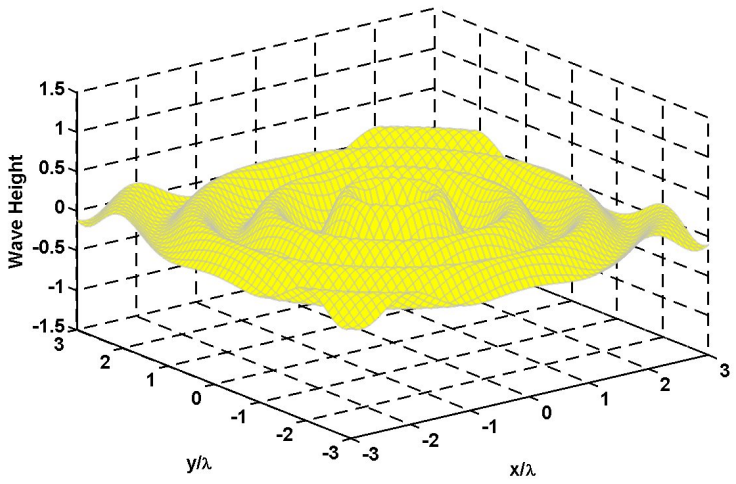

(b)

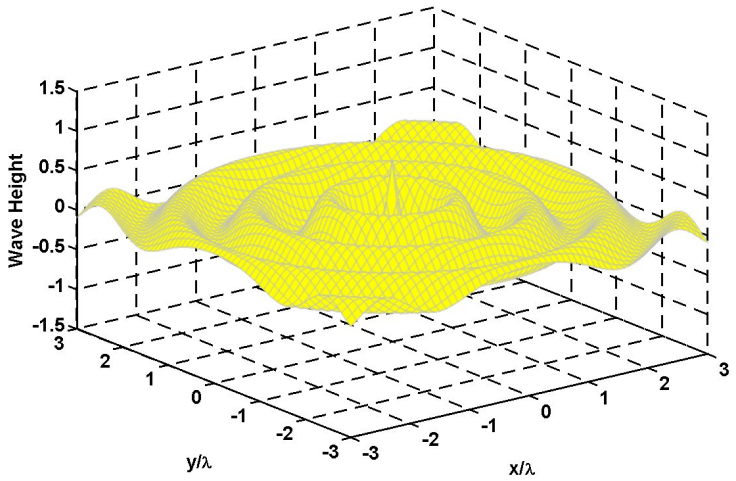

Figure 14: Phasing Study for a Deep Water Zeroth Order Circular Wave - 2 of 2

(a) $B=1 \quad \beta=-\frac{\pi}{2} \quad m=0 \quad \zeta=0 \quad t=0$ (b) $B=1 \quad \beta=-\pi \quad m=0 \quad \zeta=0 \quad t=0$

(a)

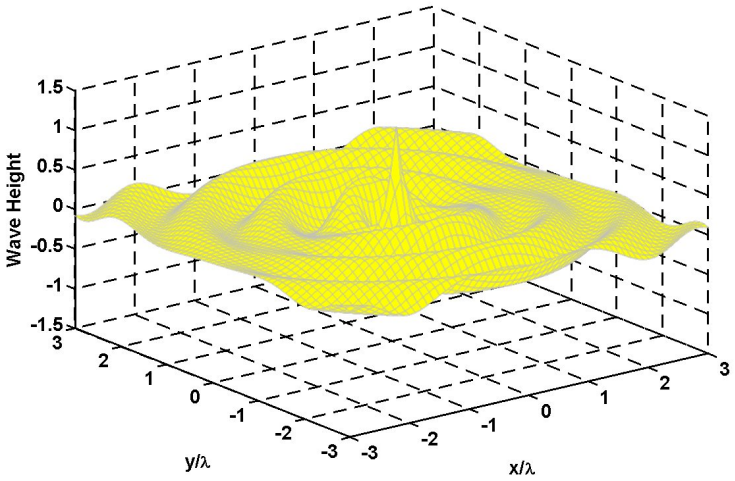

(b)

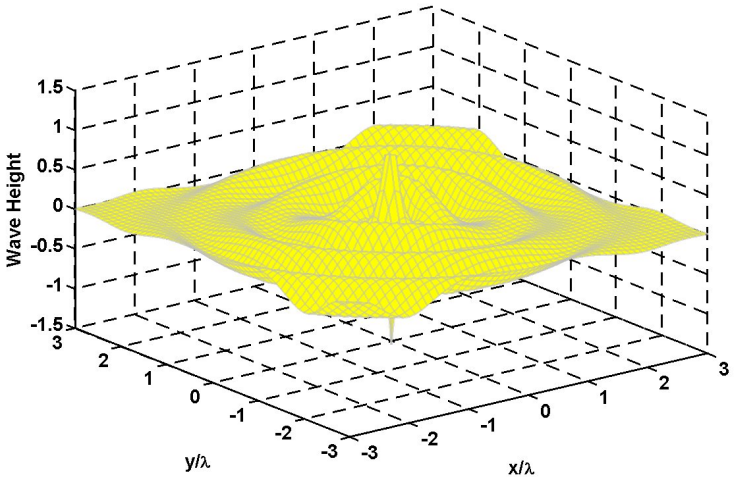

(c)

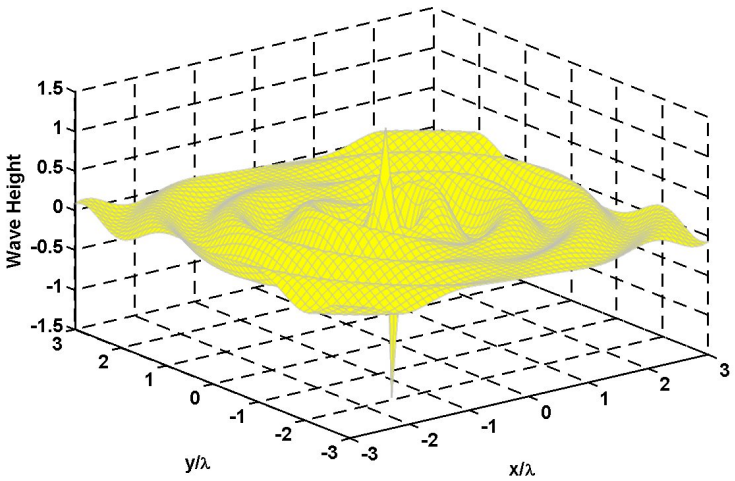

Figure 15: Rotation Study for a Deep Water First Order Circular Wave - 1 of 2

(a) $B=1 \quad \beta= \quad m=0 \quad \zeta=\frac{\pi}{2} \quad t=0$ (b) $B=1 \quad \beta=0 \quad m=0 \quad \zeta=\frac{\pi}{4} \quad t=0$

(c) $B=1 \quad \beta=0 \quad m=0 \quad \zeta=0 \quad t=0$

(a)

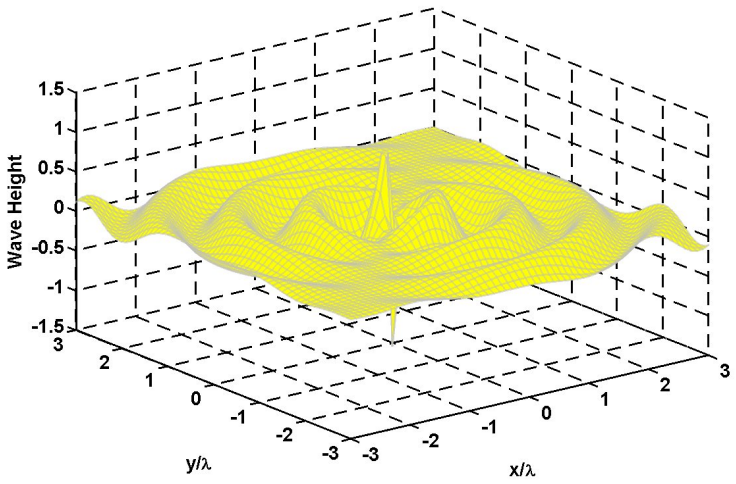

(b)

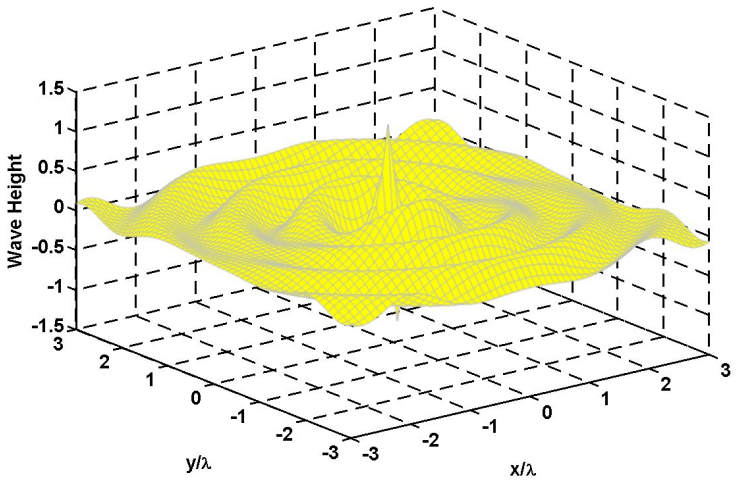

Figure 16: Rotation Study for a Deep Water First Order Circular Wave - 2 of 2

(a) $B=1 \;\; \beta=0 \;\; m=0 \;\; \zeta=-\frac{\pi}{4} \;\; t=0$ (b) $B=1 \;\; \beta=0 \;\; m=0 \;\; \zeta=-\frac{\pi}{2} \;\; t=0$

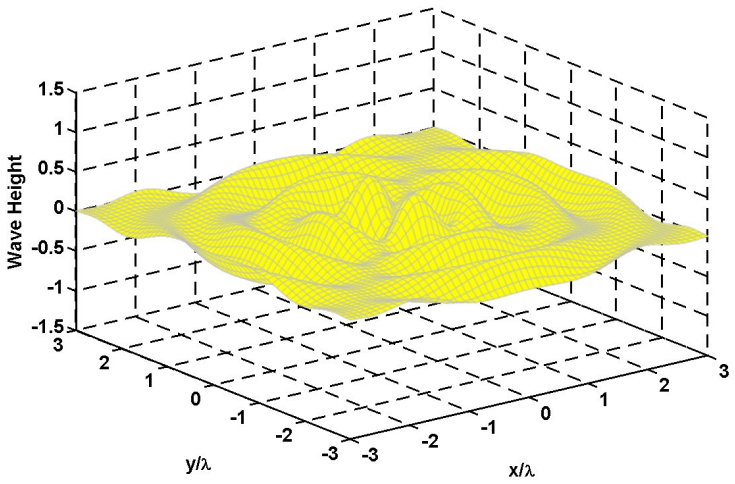

Figure 17: An Example of a Deep Water Second Order Circular Wave

$B=1 \quad \beta=-\pi \quad m=0 \quad \zeta=0 \quad t=0$

6.2 Properties of Circular Waves

The understanding of circular waves gained by examining the surface plots can be further supplemented by mathematically determining various properties of the circular waves. This section establishes and comments on the derivation and assumptions of various wave properties.

Note that the derivations of the time averaged power radiated from a circular source, the power absorbed from the interaction of plane waves and circular waves and the group velocity of circular waves were completed as part of the unique work for this PhD. The derivations were first recorded in two reports written by the author for IRL [84], [85].

6.2.1 Time-Averaged Power for Circular Waves

The time-averaged power for circular waves can be calculated in a similar fashion to the regular plane wave in Section 5.6.5.1. One of the significant differences is that a total time-averaged power radiated must be calculated instead of calculating a time-averaged power per meter of an infinitely long wave crest. The fundamental equation for power (Eqn 122) requires the particle velocity, the pressure and the definition for

an area through which the power flows. The definition of particle velocity is an integral component of velocity potential theory and can be calculated from the Eqn 15.

The small amplitude assumption made in Section 4 requires that the displacements and velocities in the wave field are small. This means that products of these quantities can be neglected and hence the expression used for pressure given by Eqn 117 can be reduced to:

$$p = \rho \frac{\partial \phi}{\partial t} - \rho g z \tag{162}$$

As the variation in circular waves is based on the distance from the origin (r), a cylindrical area centred on the origin is appropriate. The area must extend from the bottom boundary to the free surface. Noting that no energy crosses the bottom boundary or free surface, all of the power transmitted by the point source must be transmitted through the cylindrical area. Mathematically an element of area can be expressed as:

$$dA_r = r\, d\theta\, dz\, \hat{r} \tag{163}$$

Noting, from the properties of the time average value in Section 5.6.5.1, that the time-averaged value of a single sinusoidal function is zero and hence, when calculating time-averaged power, the gravity term in the pressure can be neglected. The expression for time-averaged radiated power, $\overline{P}_r$, is:

$$\overline{P}_r = -\rho r \int_{-h}^{\eta} \int_{-\pi}^{\pi} \overline{\frac{\partial \phi}{\partial t} \frac{\partial \phi}{\partial r}}\, d\theta\, dz \tag{164}$$

The velocity potential for the circular wave (Eqn 158) can be substituted into Eqn 164. Appendix 2 records the full derivation and the result is:

$$\overline{P}_r = \frac{\rho \omega g B^2}{2k^2} \left(1 + \frac{\sin(2m\pi)\cos(2\zeta)}{2m\pi}\right) \left(1 + \frac{2kh}{\sinh(2kh)}\right) \tag{165}$$

The mathematical derivation of the above formula is one of the unique achievements performed in this doctoral project and forms a corner stone for the remaining work.

It is worth noting that the formula can be reduced to one of two forms depending on the selection of m. Selecting $m=0$ leads to the first bracketed term of Eqn 165 being undefined. However, in the limit as m tends toward 0, the term $\sin(2m\pi)$ tends toward $2m\pi$ and the first bracketed term tends toward the value of 2. Hence:

$$\overline{P}_{r0} \rightarrow \frac{\rho \omega g B^2}{k^2}\left(1+\frac{2kh}{\sinh(2kh)}\right) \quad as \quad m \rightarrow 0 \tag{166}$$

This method can be compared directly to the derivation of the radiated power provided by Falnes and reviewed in Section 5.6.5.2. The velocity potential used by Falnes in Eqn 127 can be compared to Eqn 158 and the value of a_0 determined:

$$a_0 = \frac{g B e^{i\beta}}{\omega} \tag{167}$$

If value of a_0 is substituted into Eqn 131, and time-averaged power is calculated by substituting the result into Eqn 129, the power calculated is the same as Eqn 166. This means that both the method presented by Falnes and the method followed for this thesis yield the same results. The key difference is that the derivation performed as part of this thesis makes no assumptions about the far-field condition and the time-averaged radiated power is valid throughout the r domain.

The conditions for continuity allow m to take any integer value. When m is any integer other than 0 (for example a surge wave), the first bracketed term of Eqn 165 is equal to 1 and so:

$$\overline{P}_{rn} = \frac{\rho \omega g B^2}{2k^2}\left(1+\frac{2kh}{\sinh(2kh)}\right) \quad when \quad m \in \mathbb{Z} \;\; m \neq 0 \tag{168}$$

This result is unique to this study and has no previous results to compare with.

The determination of the time-averaged radiated power leads to the question what other properties of circular waves can be determined. The next section determines the group velocity of circular waves.

6.2.2 Group Velocity of Circular Waves

The group velocity determines the rate at which energy is transmitted by a wave. The group velocity for a plane wave is given by Eqn 134. The same calculation can be completed for circular waves.

Appendix 3 provides the complete derivation of the general solution for the group velocity for circular waves (Eqn 312). Two special cases of the general solution are examined further and the results are the solution for a theoretical heave wave at a large distance from the origin (Eqn 169), and the solution for a theoretical surge wave at a large distance from the origin and away from the nodal lines (Eqn 170).

The general solution remains too complex to intuitively derive any further information. However, the solution can be evaluated numerically at any given point in the wave field. Fig 18 shows the group velocity of a theoretical heave wave divided by the group velocity of a plane wave of the same wave number.

The key properties to note are that, close to the origin of the wave, the group velocity tends to zero. As the point being observed moves away from the origin the group

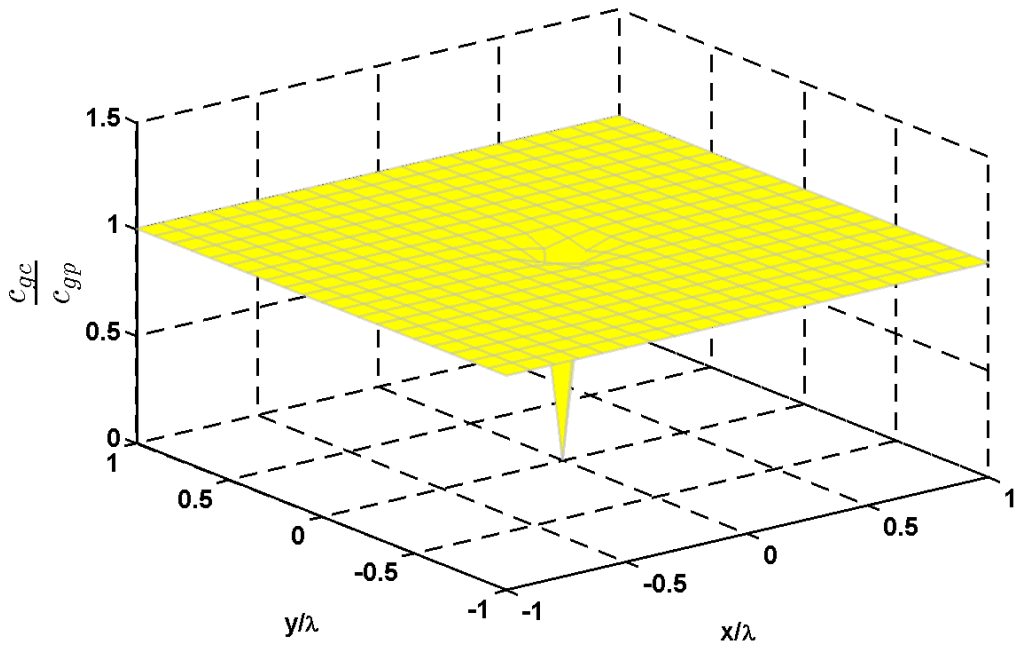

Figure 18: Group Velocity for a Theoretical Heave Wave

velocity quickly tends to the value of the group velocity of a plane wave of the same wave number. This is important for two reasons. Firstly, at large distances from the origin, intuitively, circular waves should have properties that tend to the properties of plane waves. And secondly, circular waves of a given wave number transmit energy at the same speed as a plane wave of the same wave number.

That the group velocity should tend to the plane wave value is confirmed analytically with the result calculated for a theoretical heave wave at a large distance from the origin (see Appendix 3):

$$c_{g\infty}\big|_{m=0} \rightarrow \frac{\omega}{2k}\left(1+\frac{2kh}{\sinh(2kh)}\right)\hat{r} \quad \text{as} \quad kr\rightarrow\infty \tag{169}$$

A group velocity plot can also be generated for a theoretical surge wave and is included as Figure 19. The plot shows a similar trend for the group velocity at a large distance from the origin. The discerning feature is that the plot also tends to zero along the nodal line. As the surface displacement is zero at the nodal line there can be no energy transmission. Hence the group velocity must tend to zero.

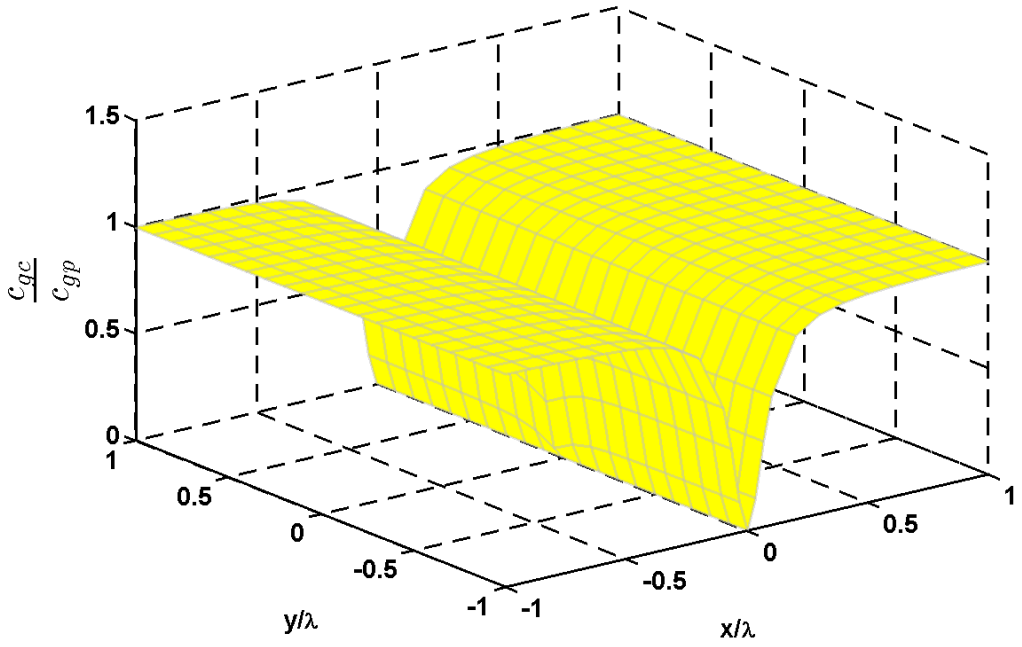

Figure 19: Group Velocity for a Theoretical Surge Wave

This result of the convergence of the circular wave group velocity to that of the plane wave group velocity is confirmed by the analytical calculation at large distances from the origin. The calculation of the group velocity as $kr \to \infty$ requires an additional clause. The point of observation must also be away from any nodal lines. In this case the group velocity becomes:

$$c_{g\infty}\Big|_{m\neq 0 \;\; (m\theta-\zeta)\neq\left(\frac{\pi}{2}+a\pi\right)} \to \frac{\omega}{2k}\left(1+\frac{2kh}{\sinh(2kh)}\right)\hat{r} \quad \text{as} \quad kr\to\infty, \quad a\in\mathbb{Z} \tag{170}$$

Which is the same as the result in Eqn 169.

6.2.3 Circular Waves and The Sommerfeld Radiation Condition

The Sommerfeld radiation condition determines if the energy of a wave is outgoing at infinity (see Section 5.6.2). The circular waves defined by Eqn 158 can be examined using the Sommerfeld radiation condition. This study is recorded in Appendix 4.

The result is that all of the circular waves defined by Hankel functions of the first kind are radiated waves and circular waves defined by Hankel functions of the second kind cannot be radiated waves. It is also important to note (as mentioned in Section 4.1.4) that the relationship between the kind of Hankel function and wave radiation is reliant on the definition of $H(t)$ as $e^{-i\omega t}$ and that the relationship is reversed for $H(t)=e^{i\omega t}$.

6.3 Time-Averaged Power for Plane and Circular Waves

Having examined circular waves and determined various properties, the next logical extension to the theory is to examine the interactions of circular waves with plane waves. An understanding of the form, amplitude and phasing of the radiated waves required to extract power from plane waves will aid in the definition of what makes a good PAWEC.

The Appendices 5 to 8 contain various derivations of radiated power for wave fields containing plane and circular waves. These derivations have been completed as part of this thesis.

6.3.1 The General Solution for Time-Averaged Power

Appendix 5 contains the derivation of the general solution for radiated power. This derivation makes no assumptions about the area that the energy flux will be examined through and simplifies the equation for radiated power based solely on the mathematics of the wave field. The result is a general solution (see Eqn 369) that can be used to calculate the radiated power given a specific wave field and area through which to examine the energy flux (power).

There are several properties worth noting that result from the derivation of time-averaged power. The first is that the properties of time averaging require that all functions of dissimilar frequencies result in a time-averaged effect of zero. This means that if the wave field consists of two waves of different frequencies there is no time-averaged interaction between them.

This observation provides the first rule for the extracting wave power: To extract power from incident waves, the waves radiated by the body must be the same frequency as the incident waves. Radiated waves of frequencies different to the incident waves do not interact in a time-averaged sense and can be considered losses. This extends the conclusion drawn by Srokosz (see Section 5.4.1.4) to the three-dimensional case.

The second property to note is that all of the $\hat{z}$ terms in the general solution reduce to zero. Hence, regardless of the area selected or waves present, there is no net vertical power flow. This suggests that the time-averaged power is vertically stratified. The vertical stratification of time-averaged power means that if a PAWEC launches energy vertically it must either be reactive energy, be dissipated through friction or be redirected horizontally. This suggests that an efficient radiator will launch energy horizontally rather than vertically.

6.3.2 Time-Averaged Power for a Plane Wave

Appendix 6 utilises the general solution derived in Appendix 5 to calculate the time-averaged power for a plane wave in two different situations. The first situation is for a planar area, parallel to the wave front, of unit width and extending from the free surface to the bottom boundary. The result is:

$$\overline{P}_{y/m} = \frac{1}{4}\frac{\rho g \omega A^2}{k}\left(1+\frac{2kh}{\sinh(2kh)}\right) \tag{171}$$

This result is the same as that derived by other authors from the rectangular coordinate geometry in Section 5.6.5.1. This supports the method used in the derivation completed in Appendices 5 and 6, as the method provides documented solutions.

The second situation is for a cylindrical area of radius r centred on the origin and extending from the free surface to the bottom boundary. The area is the same used for deriving the radiated power for a circular wave and is described by Equation 163. The result is:

$$\overline{P}_{r\ p} = 0 \tag{172}$$

This result is sensible for a plane wave and a closed surface as the total power entering the closed surface is equal to the power leaving when averaged out over the whole wavelength. This is true regardless of the size or shape of the closed surface.

6.3.3 Time-Averaged Power for a Plane Wave and a Circular Wave

Appendix 7 utilises the general solution derived in Appendix 5 to calculate the time-averaged power for the combination of a plane wave and a circular wave. The resulting equation is:

$$\begin{aligned}\overline{P}_{r\ p+m}\big|_{m\in\mathbb{Z}} = \frac{\rho\omega g}{k^2}\left(1+\frac{2kh}{\sinh(2kh)}\right)\left(\frac{B^2}{2}\left(1+\frac{\sin(2m\pi)\cos(2\zeta)}{2m\pi}\right)\right.\\ \left.+AB\cos(\alpha-\beta+m\frac{\pi}{2})\cos(m\gamma-\zeta)\right)\end{aligned} \tag{173}$$

The key aspect to note about the solution is that even though the solution was derived based on a cylindrical area of radius r (see Eqn 163) the solution is independent of r. This means that the time-averaged radiated power for a plane wave combined with a circular wave is constant in the $\hat{r}$ direction.

The time-averaged absorbed power ($\overline{P}_a$) is simply the negative of the time-averaged radiated power and from Eqn 173:

$$\overline{P}_{a\ p+m}\Big|_{m\in\mathbb{Z}} = -\frac{\rho\omega g}{k^2}\left(1+\frac{2kh}{\sinh(2kh)}\right)\left(\frac{B^2}{2}\left(1+\frac{\sin(2m\pi)\cos(2\zeta)}{2m\pi}\right)+AB\cos(\alpha-\beta+m\frac{\pi}{2})\cos(m\gamma-\zeta)\right) \tag{174}$$

The circular wave could have been generated by a axisymmetric PAWEC excited by the incident wave. In order for the PAWEC to extract energy from the wave field the time-averaged absorbed power must be positive. The first two groups of terms in Eqn 174 are greater than zero by definition. Hence the criteria for a PAWEC to absorb power from an incident wave is that it must radiate a circular wave that satisfies the inequality:

$$\left(\frac{B^2}{2}\left(1+\frac{\sin(2m\pi)\cos(2\zeta)}{2m\pi}\right)+AB\cos(\alpha-\beta+m\frac{\pi}{2})\cos(m\gamma-\zeta)\right) < 0 \tag{175}$$

This inequality sets constraints on the amplitude and phase of a circular wave, beyond which power cannot be absorbed.

It is interesting to note that a circular wave can be of any order, and providing it has the correct phasing and amplitude, it may absorb wave power. This is logical from the perspective of the circular wave representation of a plane wave (see Section 5.2.3) which is the sum of an infinite series of ever increasing Bessel functions. There is a practical limit on how useful these higher order waves are in wave power absorption. This limit is defined by the complexity of the body required to generate the waves. The higher orders of symmetry present in higher order circular waves would require a multifaceted oscillating body which would be difficult to construct,

6.3.3.1 Amplitude-Phase Envelope for Theoretical Heave

If it is assumed that the circular wave is a theoretical heave wave ($m \to 0$ and $\zeta = 0$) then Eqn 175 reduces to:

$$\left(B^2 + A\,B\cos(\alpha - \beta)\right) < 0 \tag{176}$$

Which leads to the criteria for time-averaged power absorption for a plane wave combined with a theoretical heave wave:

$$B < -A\cos(\alpha - \beta) \tag{177}$$

Noting that the circular wave amplitude B must be positive, the phasing differential must be within the following range for energy absorption:

$$-\frac{\pi}{2} + 2a\pi < \alpha - \beta < \frac{\pi}{2} + 2a\pi \qquad a \in \mathbb{Z} \tag{178}$$

The envelope within which the phase and the amplitude of the circular wave absorbs power can be shown graphically by plotting an absorption gain factor for theoretical heave, G_{a0}. G_{a0} is defined by Eqn 179:

$$G_{a0} = \frac{\overline{P}_{a\ p+m}\Big|_{m=0}}{\frac{\rho\,\omega\,g}{k^2}\left(1 + \frac{2\,k\,h}{\sinh(2\,k\,h)}\right)A^2} \tag{179}$$

Graphically this can be represented by Fig 20 and note that positive values of the gain factor represent absorbed power. The transition between absorbed and radiated power is signified by the blue plane.

6.3.3.2 Amplitude-Phase Envelope for Theoretical Surge

It is also possible to assume that the circular wave is a first order circular wave ($m = 1$) which means Eqn 175 reduces to:

$$\left(\frac{B^2}{2} - A\,B\sin(\alpha - \beta)\cos(\gamma - \zeta)\right) < 0 \tag{180}$$

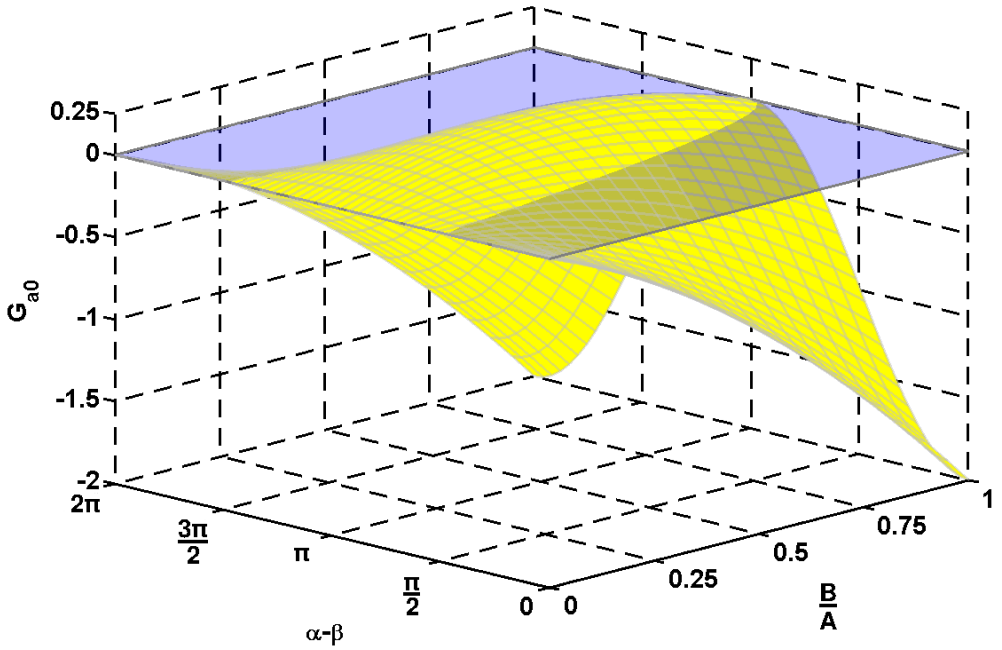

Figure 20: Gain Factor for Theoretical Heave Power Absorption

Which leads to the criteria for time-averaged power absorption for a plane wave combined with a first order circular wave:

$$B < 2A\sin(\alpha-\beta)\cos(\gamma-\zeta) \tag{181}$$

Noting that the circular wave amplitude B must be positive, the product of the sine of the phasing differential and the cos of the difference between the angle of incidence and angle of radiation must be greater than 1.

In the special case of a theoretical surge wave ($m=1$ and $\gamma-\zeta=0$) Eqn 181 reduces to:

$$B < 2A\sin(\alpha-\beta) \tag{182}$$

Again the envelope within which the phase and the amplitude of the circular wave absorbs power can be shown graphically by plotting an absorption gain factor for theoretical surge G_{al}. G_{al} is defined by Eqn 183:

$$G_{a1} = \frac{\overline{P}_{a\ p+m}\big|_{m=1}}{\frac{\rho\,\omega\,g}{k^2}\left(1+\frac{2\,k\,h}{\sinh(2\,k\,h)}\right)A^2} \tag{183}$$

Graphically this can be represented by Fig 21 and note that positive values of the gain factor represent absorbed power. The transition between absorbed and radiated power is signified by the blue plane.

6.3.3.3 Amplitude-Phase Envelope for Theoretical Sway

In the special case of a theoretical sway wave ($m=1$ and $\gamma-\zeta=\pm\frac{\pi}{2}$) the cosine of $\gamma-\zeta$ is zero and the inequality in Eqn 180 cannot be fulfilled. Hence, a theoretical sway wave cannot absorb energy. This result is an important result from the study of time-averaged power as it proves that theoretical sway waves are a source of power loss in the wave field and the design of a PAWEC should look to minimise the radiation of theoretical sway type waves.

It is noted that the power loss caused by emitting sway waves may actually be used to the advantage of a PAWEC. The Pelamis device, mentioned in Section 5.1, improves

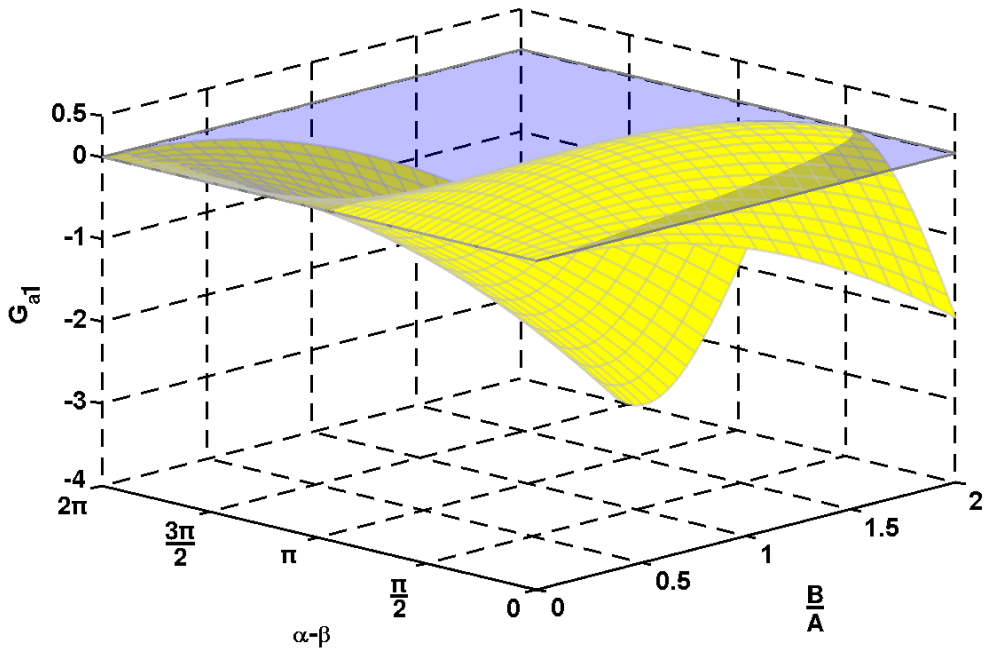

Figure 21: Gain Factor for Theoretical Surge Power Absorption

the survivability of the device by using the the sideways motions of the various segments to shed bending moments in rough seas [65].

6.3.3.4 *Time-Averaged Power for a Plane Wave and Multiple Co-located Circular Waves*

Appendix 8 contains the derivation of the power for the interaction of a theoretical heave, a theoretical surge and a theoretical sway wave with a plane wave. All four waves are assumed to have the same wavelength. It is shown that the three circular waves do not interact with each other with respect to time-averaged power. The total absorbed power is simply the sum of the components of each circular wave interacting with the plane wave in isolation. Eqn 436 is reproduced as Eqn 184 where B_1, B_2 and B_3 are the amplitudes of the heave, surge and sway waves respectively. Also note that β_1 represents the phasing of the heave wave while β_2 represents the phasing for the surge wave.

$$\overline{P}_{r\ p+h+sg+sw} = \frac{\rho \omega g}{k^2}\left(1+\frac{2kh}{\sinh(2kh)}\right)\left(B_1^2+AB_1\cos(\alpha-\beta_1)+\frac{B_2^2}{2} - AB_2\sin(\alpha-\beta_2)+\frac{B_3^2}{2}\right) \tag{184}$$

6.3.4 Optimum absorption

Figs 20 and 21 show that the absorption gain factors have a peak value. This point represents the optimum absorption of the incident wave power.

6.3.4.1 *Optimum Absorption for Theoretical Heave*

For a theoretical heave wave the optimum power absorption occurs when:

$$B = \frac{A}{2} \quad \text{and} \quad \alpha-\beta = \pm\pi \tag{185}$$

At this point the power absorbed is:

$$\overline{P}_{a\ p+m}\Big|_{m=0}^{max} = \frac{\rho\omega g A^2}{4k^2}\left(1+\frac{2kh}{\sinh(2kh)}\right) \tag{186}$$

6.3.4.2 Optimum Absorption for Theoretical Surge

For a theoretical surge wave the optimum power absorption occurs when:

$$B = A, \quad \gamma-\zeta = a\pi \quad \text{and} \quad \alpha-\beta = (-1)^a\frac{\pi}{2} \qquad a\in\mathbb{Z} \tag{187}$$

At this point the power absorbed is:

$$\overline{P}_{r\ p+m}\Big|_{m=1}^{max} = \frac{\rho\omega g A^2}{2k^2}\left(1+\frac{2kh}{\sinh(2kh)}\right) \tag{188}$$

Note that the maximum time-averaged power absorbed for a theoretical surge wave is twice the maximum absorbed for a theoretical heave wave.

6.4 Absorption Length for Circular Waves

With the derivation of the time-averaged power absorbed by the interaction of a circular wave and a plane wave it is possible calculate the absorption length as described in Section 5.3.2.5. The absorption length, L_a, is found by dividing the total absorbed power (Eqn 174) by the power per unit wave front of a plane wave (Eqn 171). Hence:

$$\begin{aligned} L_{am} &= \frac{-\frac{\rho\omega g}{k^2}\left(1+\frac{2kh}{\sinh(2kh)}\right)\times\left(\frac{B^2}{2}\left(1+\frac{\sin(2m\pi)\cos(2\zeta)}{2m\pi}\right)+AB\cos(\alpha-\beta+m\frac{\pi}{2})\cos(m\gamma-\zeta)\right)}{\frac{1}{4}\frac{\rho g\omega A^2}{k}\left(1+\frac{2kh}{\sinh(2kh)}\right)} \\ &= -4\frac{\left(\frac{B^2}{2}\left(1+\frac{\sin(2m\pi)\cos(2\zeta)}{2m\pi}\right)+AB\cos(\alpha-\beta+m\frac{\pi}{2})\cos(m\gamma-\zeta)\right)}{A^2k} \end{aligned} \tag{189}$$

This general solution can be examined for both heave and surge and may also be inspected at the point of optimum absorption.

6.4.1 Absorption Length for Theoretical Heave

For a theoretical heave wave the general solution for absorption length reduces to:

$$L_{a0} = -4\frac{\left(B^2 + A\,B\cos(\alpha-\beta)\right)}{A^2 k} \tag{190}$$

The absorption length at the optimal absorption point (as described by Eqn 185) is:

$$\begin{aligned} L_{a0}^{opt} &= -4\frac{\left(\frac{A^2}{4}-\frac{A^2}{2}\right)}{A^2 k} \\ &= \frac{1}{k} \\ &= \frac{\lambda}{2\pi} \end{aligned} \tag{191}$$

This result confirms the result derived by Evans ([13] and Section 5.3.2.5) although the approach taken differs significantly. While Evans examined the body dynamics and defined the optimum point in terms of impedance matching, the approach documented here considers only the interaction of a circular heave wave with an incident plane wave and defines the optimum in terms of the amplitude and phase of the radiated wave.

6.4.2 Absorption Length for Theoretical Surge

For a first order circular wave the general solution for absorption length reduces to:

$$L_{a1} = -4\frac{\left(\frac{B^2}{2} - A\,B\sin(\alpha-\beta)\cos(\gamma-\zeta)\right)}{A^2 k} \tag{192}$$

The absorption length at the optimal absorption point (as described by Eqn 187) is:

$$
\begin{aligned}
L_{a1}^{opt} &= -4\frac{\left(\frac{A^2}{2}-A^2\right)}{A^2 k} \\
&= \frac{2}{k} \\
&= \frac{\lambda}{\pi}
\end{aligned}
\tag{193}
$$

This result also confirms the result derived by Evans ([13] and Section 5.3.2.5) although the approach taken differs significantly as outlined in the previous section.

6.4.3 Absorption Length for Combined Heave and Surge

As noted in Section 6.3.3.4 and Appendix 8, the time-averaged absorbed power for the combination of a theoretical heave, a theoretical surge and a plane wave is simply the sum of the absorbed powers for each of the circular waves' interactions with the plane wave. Hence, the absorption length for the combined case is simply the sum of the absorption lengths in each isolated case. Therefore the total absorption length at optimal absorption conditions for the combined scenario is:

$$
L_{a\ 0+1}^{opt} = \frac{3\lambda}{2\pi} \tag{194}
$$

6.5 Three-Dimensional Plots of the Optimum Absorption

With the definition of the circular wave forms and the identification of the optimum conditions for energy absorption it is possible to examine the the optimum energy absorption condition. Figs. 22 and 23 represent the optimum three-dimensional destructive interference for a plane wave travelling from $x=-\infty$ to $x=\infty$. This can be contrasted to the two-dimensional case depicted in Fig. 12.

The most significant difference when comparing Figs 22 and 23 with Fig 12 is that in the three-dimensional case the down stream the wave begins to re-form as it progresses away from the origin of the circular waves. This is a three dimensional artefact as the

total effect of the energy removed by the PAWEC is spread across a larger area of the wave front the further downstream the wave is observed.

The optimal absorption heave and surge waves can be examined in the absence of the plane wave. The result is Fig 24. This figure shows that the combination of heave and surge waves required for optimal power absorption radiate a wave downstream of the WEC and minimise the wave radiated upstream. This contrasts the results advocated in

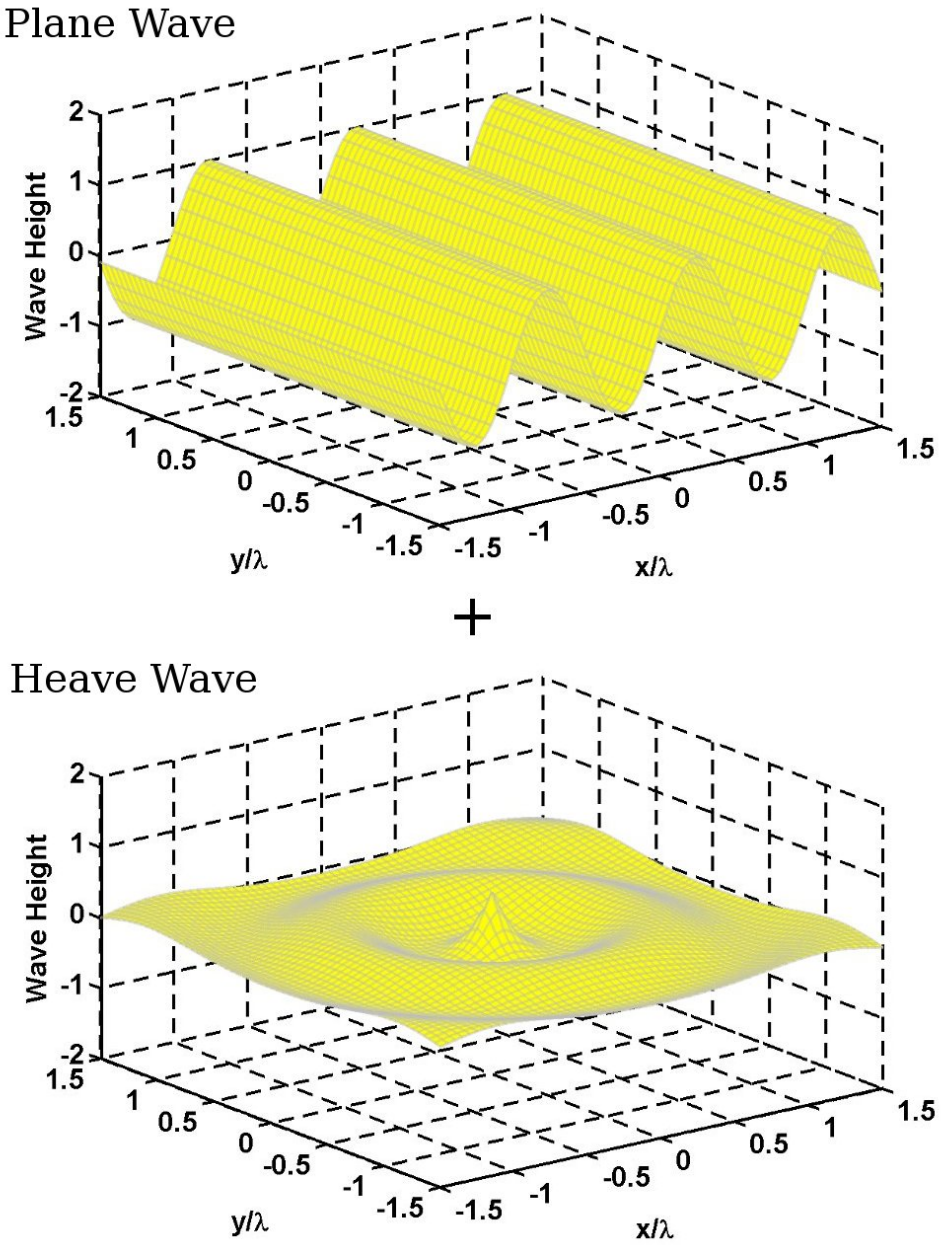

Figure 22: Optimum Absorption of Wave Energy for a Deep Water 3-D Point Absorber 1 of 2

Section 5.4.1.4 which state that an effective WEC must be radiated waves upstream. The key difference between the two-dimensional case and the three-dimensional case is that there is no assumption of reflection of the incident wave.

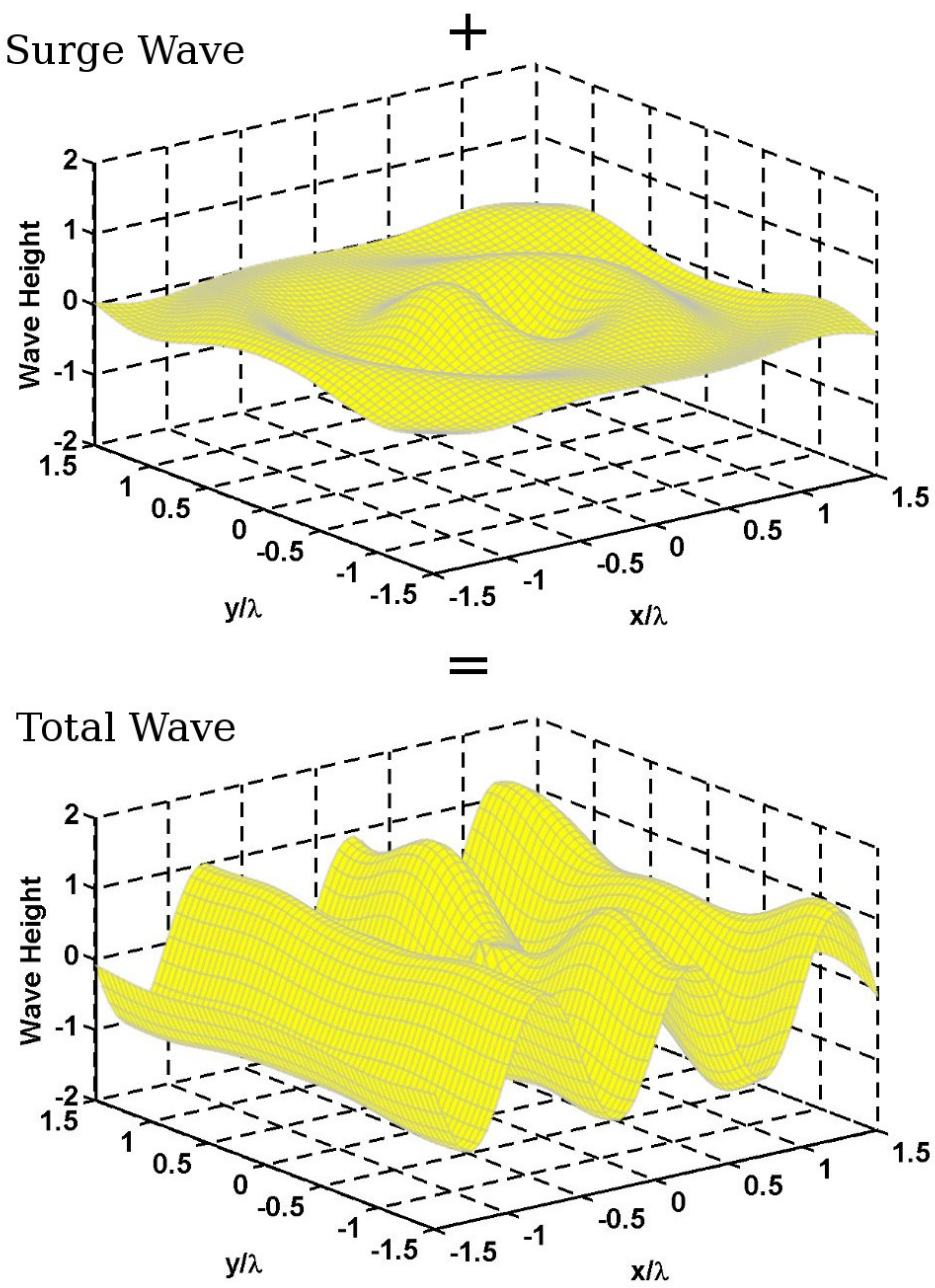

Figure 23: Optimum Absorption of Wave Energy for a Deep Water 3-D Point Absorber 2 of 2

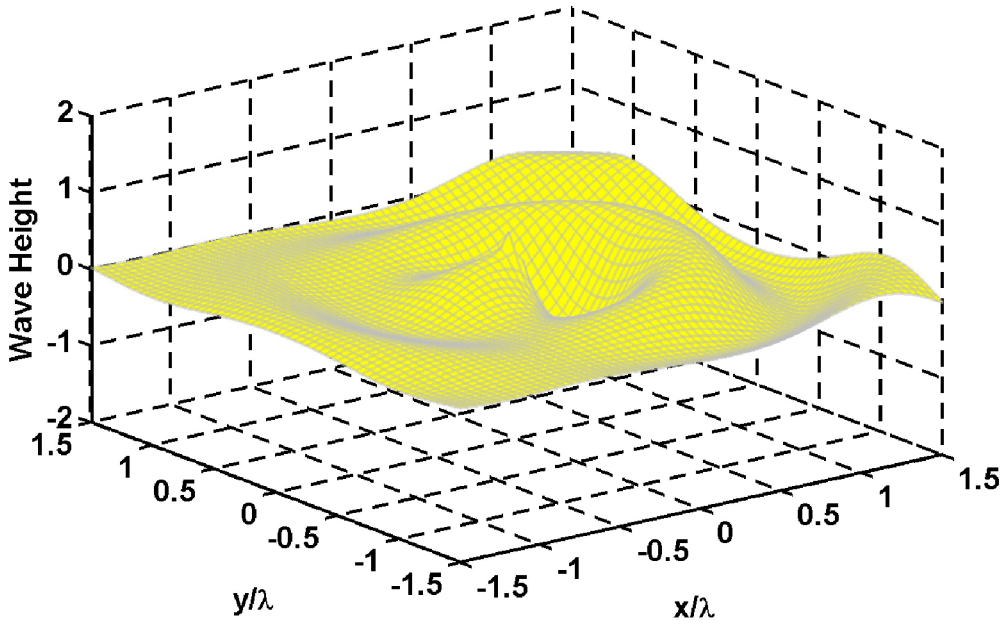

Figure 24: The Combined Heave and Surge Wave Required for Optimal Absorption of a Plane Wave

6.6 Generating Non-symmetric Waves

An example of a two-dimensional non-symmetric wave is shown as Fig 25. One of the key features of a non-symmetric wave is that a discontinuity exists at the origin of the wave for most of the time domain. In order to be able to radiate the non-symmetric wave, a wave radiator must provide some sort of physical structure to support the discontinuity. Without such support the wave form would collapse radiating little or no power. This concept determines a guideline for the design of WECs: If a PAWEC is designed to radiate a non-symmetric wave then part of the PAWEC must pierce the surface and support the wave's discontinuity.

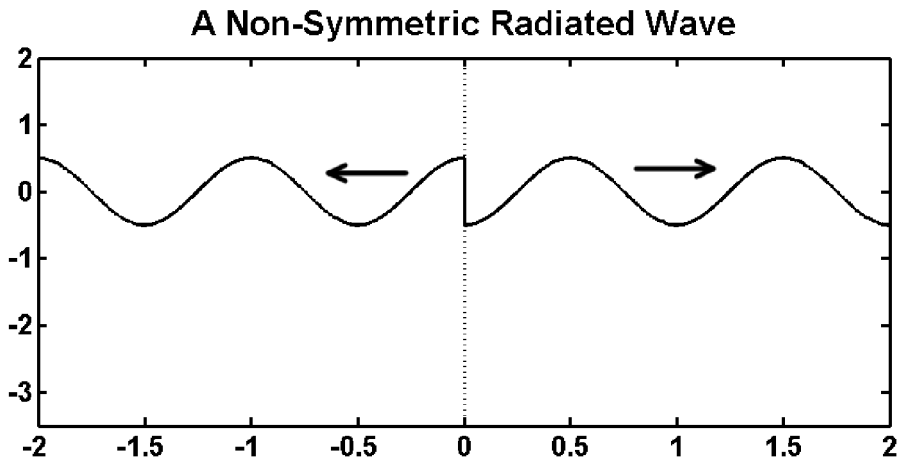

Figure 25: Two-Dimensional Radiation of a Non-Symmetric Wave

6.7 Summary of Circular Wave Theory

The original question stated at the beginning of this chapter is: Can circular wave theory be used to determine design constraints for wave energy converters? To answer this question a form of the circular-cylindrical solutions to the Laplace equation was derived and examined. The zeroth and first order solutions were intuitively equated to heave and surge/sway respectively.

Examination of the circular waves derived new expressions for the time-averaged radiated power. In the case of a theoretical heave wave, the derived expression for time-averaged power was shown to be equivalent to the existing solution provided by Falnes. The note of differentiation is that the value derived here is valid for the entire wave field while the one derived by Falnes is only valid in the far-field. No alternative solution has been found to compare the theoretical surge wave expression.

Calculation of the group velocity for circular waves showed that the group velocity for a circular wave tended toward the value for a plane wave with a similar wave number, provided the point examined was away from the origin, or in the case of a first order circular wave, away from a nodal line. In these two situations the value of the group velocity tended to zero.

The time-averaged power was calculated for different combinations of plane, heave, surge and sway waves. The results for the plane wave confirmed that the method yielded currently existing results. The results for combinations of plane waves and circular waves were used to determine inequalities describing the envelope of circular wave amplitudes and phases that absorb power from a given plane wave. For each combination of plane wave and circular wave, the optimum point of absorption was identified.

Existing theory assumes the form of the radiated wave at infinity and describes the optimum absorption point in terms of added mass and added damping properties. The unique aspect of the theory developed in this chapter is that it describes the optimum absorption point in terms of circular wave amplitudes and phases and that this describes the entire wave field. Both theories yield the same result when the absorption length is calculated.

Hence an inspection of circular waves shows a strong correlation with existing theoretical solutions and provides four key criteria for the design of WEC.

1. The wave radiated from the body of the PAWEC must be of the same frequency as the incident waves for the PAWEC to be able to absorb power.

2. Time-averaged power in linear waves is vertically stratified. Hence a PAWEC that launches energy horizontally is likely to be more efficient than a PAWEC that launches energy vertically.

3. PAWECs should minimise the radiated sway waves as sway waves do not interact with the incident plane wave and can be considered a loss to the system. That noted, there may be times when such a loss is advantageous particularly in reference to survivability.

4. There exists an envelope of amplitude and phase within which a circular wave of a given order can absorb power. A PAWEC should radiate circular waves of the correct amplitude and phase to maximise power absorption.

5. If a PAWEC is designed to radiate a non-symmetric wave then the PAWEC must provide a surface piercing structure to support the discontinuity at the wave's origin.

This prompts a second question which will be the focus of the next two chapters: Do the theoretical circular waves match the waves radiated by physical bodies?

7 Circular Waves and Experimental Measurement

The key question the next two chapters aim to answer is “Do the theoretical circular waves match the waves radiated by physical bodies?” To be able to answer this question, data on the frequency and form of waves radiated from a body was required. A significant amount of information is available for ocean waves (e.g. Pontes [86]) however no such data was found for waves radiated from various bodies.

This chapter focuses on the methodology used to generate and measure radial waves while Chapter 8 will examine the process for matching the recorded data to circular waves and the results collected for this thesis. Part of the unique work undertaken for this thesis was to develop a process by which radiated waves could be consistently generated and measured.

7.1 Wave Basin Selection

There are a significant number of wave tanks that are designed to generate waves from the exterior boundaries into the wave basin [74]. However, finding a wave tank that has a centralised wave generator with the ability to examine waves over several wavelengths proved challenging. Given the limitations of local (within New Zealand) facilities it was determined that a new wave radiator would need to be created and a wave basin selected. The selection of a wave basin came down to four key factors: mechanical cycle times, a 6 wavelength diameter criterion, a deep water criterion and local availability.

Mechanical cycle times play a role in determining the size of wave basin required. As the wave generator has to move a body back and forth within a wave field there are mechanical and operator safety consideration that must be taken into account in the design. It was estimated that a one second period was considered to be on the short end of what would be achievable for a wave generator. Using the dispersion relationship it is possible to determine that a one second period wave has a wavelength of 1.6 meters.

Note that solving the dispersion relationship for a wavelength required a numerical calculation. Dean and Dalrymple [20] show that the dispersion relationship has only one solution for a given phase velocity (ω) and water depth (h). Hence simple solvers like Goal Seek in Open Office Calc [87] can provide accurate solutions.

The minimum wavelength identified by the mechanical cycle times allows the determination of the overall size of the wave basin required. The mathematical solution of circular waves suggest that the decay in wave amplitude occurs at a rate proportional to $\frac{1}{\sqrt{kr}}$. Hence, the amplitude of the wave will be significantly reduced within several wavelengths of the point of radiation. This means, for example, that if the wave were measured at the one wavelength from the body and again at 3 wavelengths, the decay in wave amplitude should be approximately 40%. Such a change in amplitude should be readily measurable. Hence, a wave basin six wavelengths in diameter would allow the decay in wave amplitude to be measured in any direction from the point of radiation.

The criterion for determining the depth of the basin comes from the deep water condition ($h \geq \frac{\lambda}{2}$ from Section 5.2.1). Maintaining the deep water condition reduces the effects on the waves from the bottom surface of the basin.

Combining the width, depth and minimum wave period criteria a suitable wave tank would be at least 0.8 meters deep, and 9.6 meters in diameter. The only local (within Christchurch) body of water that matched this scale of dimensions, and that was readily available for use, was a model boat pond at a local council park known as the Groynes. This man-made lake is approximately 260 meters long, at least 60 meters wide and has a depth ranging from 0.8 meters to 1.1 meters. Fig 26 gives an aerial view of the pond used for the testing basin.

Figure 26: Aerial View of the Testing Basin at the Groynes
Image courtesy of DigitalGlobe and Google Maps

7.1.1 Review of the Testing Site

The chosen testing site provided excellent testing conditions. There were also a number of other considerations that had bearing upon the testing.

The overall size of the Groynes pond, coupled with its natural beaches, provided minimal reflections of the radiated waves. No reflection from the banks or the jetty was detectable above the noise limit of the sensors. This allowed continuous testing and a significant number of tests were completed in rapid succession.

One of the major sources of noise was from the irregular surface displacement caused by wind during testing. A number of the test days were perfectly calm while on others a slight breeze was noted to cause the formation of small waves approximately 3-5mm in height. The zero reading tests performed as part of the testing procedure show that background noise is the limiting factor in identifying the wave forms for the slowest

body oscillation speed. No procedural limitation was set for the level of this noise although testing was postponed on occasion due to wet weather and stormy conditions.

A mildly toxic algae was present in the Groynes testing pond. This seasonal bloom grew largely on the banks and weeds present in the pond. It was only once recorded as interfering with testing. In this case a clump of algae surfaced and collected on one of the sensor posts. The timing of this interference was noted and the data from that sensor examined and eventually excluded from calculations. After several minutes the clump broke up and drifted out of the testing area.

One of the key improvements to reduce variability in the testing configuration would have been to secure the test equipment in-situ overnight. As it was, the agreement with the park wardens required the removal of all equipment after each day of testing. This meant that each day the configuration of the test equipment was open to change. A much larger range of data could have been collected if installation of the test equipment and wave measuring apparatus was not required each day.

7.2 Measuring Radial Wave Height

To be able to correlate radiated waves to the circular wave solutions, the waves radiated from a body had to be measured experimentally. Hence a method for measuring the wave height was required. The goal of determining the form of an entire wave field required the measuring of the radiated wave at a number of points.

The two key aspects that characterise circular wave theory are the decay in wave height with increasing radius (r) and the distribution in wave height in the $\hat{\theta}$ direction. To measure an exponential decay in the radial direction a minimum of three points along a radial line are required.

In measuring the distribution in the $\hat{\theta}$ direction it is important to be able to distinguish between the axisymmetric heave mode and the non-axisymmetric surge mode. By

placing measurement points where $\theta=0$, $\theta=\frac{\pi}{2}$ and $\theta=\pi$ it is possible identify the opposing phase generated on either side of a surging body and the nodal line (if one occurs). The addition of an intermediate measurement point at $\theta=\frac{\pi}{3}$ or $\theta=\frac{\pi}{6}$ gives further information of the variation of the wave field with θ. Therefore, at least four radial measurement lines distributed around the body are required. Hence, measuring the two spatial distributions requires a minimum of twelve sensors.

Due to the minimum number of sensors required, the cost for wire gauge and acoustic sensing options became prohibitive. For example a set of 15 capacitive wave gauges has been quoted at $14,000 Canadian dollars. This led to the development of a low-cost pressure sensor.

Once the design of a specialised sensor removed the budget restrictions, the final decision on the number of sensors was actually made based on the number of inputs into the data acquisition (DAQ) hardware. The chosen DAQ had 32 inputs, only two of which were required for measuring accelerations. Hence testing was conducted with up to 30 pressure sensors.

7.2.1 Design of a Wave Height Sensor

The overall goal of the sensor was to be able to measure a wave height of 1mm out at the extents of the observed wave field. The smallest pressure change is then determined by the extent of the field and the wavelength. The shortest wavelength the radial wave generator is designed to radiate is 1.6 meters waves. As the observable wave field extends three wavelengths (see Section 7.1), the required resolution of the pressure sensor is 13 pascal (or 1.3mm of static water height).

To gain such a fine resolution the pressure sensor needed to be very sensitive. The chosen sensor was an MPXV7002DP differential pressure sensor from Freescale Semiconductor. This sensor is a piezoresistive transducer with a sensing range of

±2kPa. The data sheet for the sensor can be found on the Freescale website [88] or in Digital Appendix 5.

To be able to continually sense the pressure at a given point the opening to the pressure port must be below the free surface. The largest predicted amplitude wave is calculated by assuming a 1.6 meter wavelength wave is radiated with 140 Watts of power (the maximum recorded power output of the controller and motor combinations during dry runs) and is sensed by a sensor at a half wave length from the device. The result is that the largest predicted wave possible would be approximately 84mm in amplitude. Hence, the sensing point must be approximately 100mm below the surface.

The 100mm submergence criterion has two impacts on the design of the sensor. Firstly, if the sensor was designed to remain above the wave field it would require a connection approximately 200mm long. This connection could be filled with either air or water, which would add either damping or added mass effects respectively. These effects can be significantly reduced if the sensor is submerged and the length of the connection between the sensor and the point of measurement is minimised. The second effect caused by submergence is the reduction in sensing range due to approximately 1kPa of static head. This can be eliminated by using a differential sensor and locking off one of the ports after submergence. This removes the static offset allowing the sensor to utilise its full range. A Festo QH-4 ball valve for pneumatic applications was used to lock off the reference pressure. The data sheet for the valve can be found on the Festo website [89] or in Digital Appendix 5.

The requirement that the sensor be submerged means that the sensor must also be water proof. To achieve this the sensor was potted using a two part epoxy. Fig 27 shows the sensor before potting. Fig 28 is a sketch of the sensor installed in the wave field.

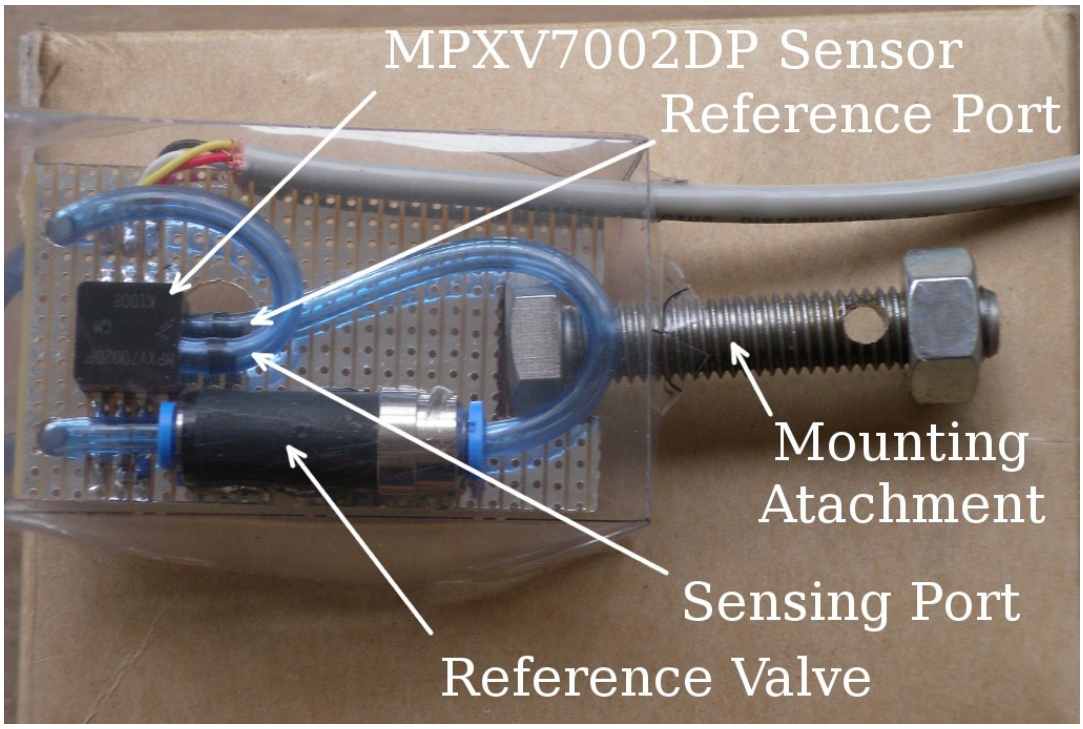

Figure 27: Prototype of Pressure Sensor Used to Measure Wave Amplitudes Before Potting

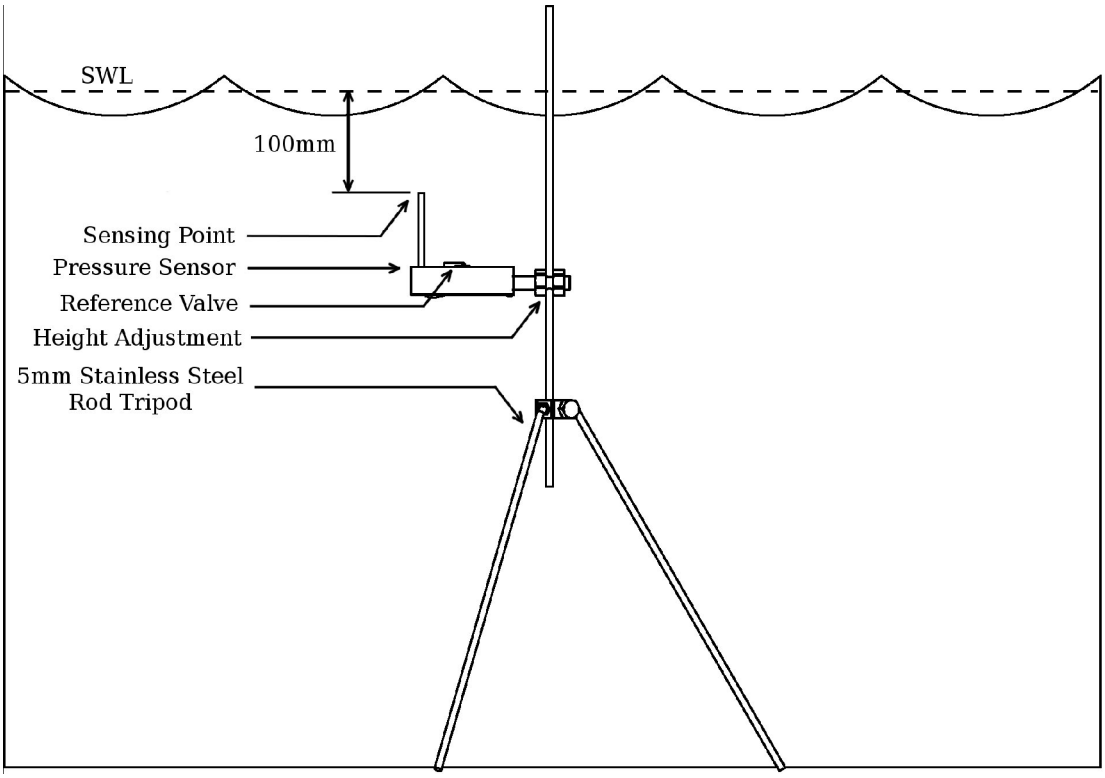

Figure 28: A Sketch of the Installed Pressure Sensor Used to Measure Wave Amplitudes

Fig 29 shows the sensor potted and mounted on a tripod stand. The stand was created using 5mm stainless steel rod with an M16 nut as a hub. The design allowed for height adjustment of the sensor while presenting a very small area to interfere with the wave.

The tubes attached to the reference and sensing ports were left at a length of 55mm above the potted surface. This was done to ensure that the pressure measurement was taken away from any localised flow effects caused by the presence of the potted body in the wave field.

To install the sensor for testing, the reference valve must be open as the sensor is submerged. After a period of time that allows for thermal stabilisation the reference switch can be closed. This creates a reference pressure that eliminates the static head.

The result is a pressure sensor that has a resolution smaller than 0.3mm of static head. This resolution equates to being able to detect a 1.6m wavelength wave with an amplitude smaller than 0.25mm at three wavelengths distance from the point of origin. The total cost, not including labour, for all 30 sensors and stands was $2,250 New Zealand dollars.

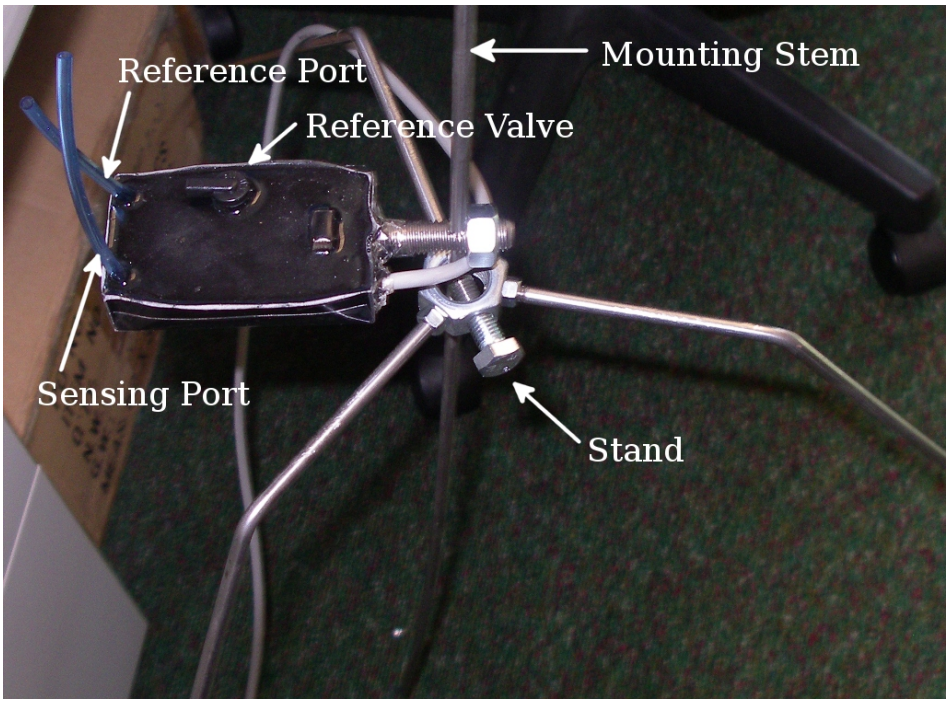

Figure 29: Complete and Potted Pressure Sensor With Mounting Stand

7.2.2 Calibration of the Wave Height Sensor

Literature reviewed in Section 5.4.3 suggests that pressure sensors may or may not be a reliable method of measuring wave height. As the wave height sensor was created for this thesis, the calibration of the sensor needed to be confirmed.

The method of calibration involved comparing data recorded from the pressure sensors to that of resistance wave gauges deployed in the same wave flume. The wave flume testing was carried out alongside the testing of the WET-NZ device at the O. H. Hinsdale Wave Research Laboratory at Oregon State University.

The verification tests required by IRL were of similar frequency and size to the tests conducted at the Groynes testing basin. The tests included wavelengths of 1.9m to 8.2m and wave amplitudes from 33.5mm to 166.5mm (This particular range of waves was chosen to cover the 1/30th scale of the wave tests described in the IEA testing plan for wave energy devices [74]).

Three of the custom-made pressure sensors were used in the experiments. They were situated approximately 1.5m from the wave basin side wall on the stands used for testing at the Groynes. The three sensors were aligned perpendicular to the wave generator with a separation of 1.6m between the first and second sensor and 1m between the second and third sensor. The sensors were mounted 1.21m off the flume floor. It was noted that the second sensor had an issue with the mounting that caused the stand to be unstable. The data from the second sensor was noted as unstable and was neglected from the calculations.

The resistance wave gauges used in the tests were statically calibrated against a reference pressure gauge and an ultrasonic level gauge as the testing basin filled. The linearity of the gauges on the static fill had a correlation coefficient of 0.999 or better. This noted, there was no reference available as to the overall accuracy of the wave gauges.

The sensor gain was calculated from the collected data and the error in the gain estimated. Two major factors contribute to the error: sensing error and fit error.

7.2.2.1 Estimating the Sensing Error

The sensing error is the error involved in detecting and recording the data and consists of error from the sensor itself and error from the DAQ system. As a note, other forms of error affecting the measured pressure (e.g. the variation in the sensing position caused by the curve of the sensing tubes) are documented in Section 8.6.

The data sheet for the pressure sensor states that the accuracy of the sensor is typically 2.5% across the full range of temperature and scale.

Information on the accuracy of the resistance wire gauges at the O. H. Hinsdale laboratory was not available. The static linearity tests comparing the resistance wave gauges with a static pressure sensor were the only form of calibration performed. Fortunately, Hughes notes that the linearity test is all that is required to obtain accurate results from resistive wave gauges [11] and Sharp [90] notes that the resolution is about ±0.1mm. A short survey of the wave gauges available for purchase suggests that the accuracy is in the range of ±0.15% to ±0.4%. The error of the resistance wave gauges was assumed to be ±0.4%.

The National Instruments DAQ used to record data had a noise level of 116uV and a resolution of 46.4uV. The noise level is equivalent to 0.166Pascal and is negligible compared to the 138Pascal amplitude of the smallest calibration reading. The resolution of the DAQ is more than 60 times that of the pressure sensor. Hence it is assumed that any error introduced by the DAQ is negligible.

7.2.2.2 Estimating the Fit Error

Each of the signals recorded during the wave tank experiments was matched to a sinusoidal function to determine the amplitude of the signal. A sample of the signal, approximately ten periods long, was extracted from the middle of the experimental

data and the function $a\sin(b\,x+c)+d$ was fitted to the sample. The resulting match had a level of error associated to the fit depending on the coefficient of determination R^2.

A numerical experiment was performed to determine the relationship between the coefficient of determination (R^2) and the error in the fit of a sinusoidal function. A sine function of the form $a_f\sin(\omega_f t+\alpha_f)$ was calculated and matched to the same function with an introduced error in the amplitude and phase of the function. The new function took the form $G_f a_f\sin(\omega_f t+\alpha_f+\xi_f)$ where G_f is the error gain and ξ_f is the phase error. The resulting relationship was that for a pure sinusoid:

$$G_f^2-2\,G_f\cos(\xi)-R^2 \;=\; 0 \tag{195}$$

The relationship described by Eqn 195 can be solved for the error gain:

$$G_f \;=\; \cos(\xi)\pm\sqrt{\cos^2(\xi_f)-R^2} \tag{196}$$

To maintain real solutions it is noted that:

$$\xi_f \;\le\; acos(\sqrt{R^2}) \tag{197}$$

Eqn 197 provides limits for the value of phase error which then applies limits to the error gain. By allowing the phase error to vary between its theoretical limits and calculating the corresponding error gain, it is possible to generate an error envelope around the fitted sinusoid. Fig 30 shows an example of a fit with the original data and the error envelop. For this example the coefficient of determination was 0.992.

When an experimentally measured signal is fitted to a sinusoid, it is possible to calculate the error envelope based upon the value of R^2. The error envelope includes all of the data points except a few extreme outliers. The error envelope gives the maximum and minimum values of a_f and α_f. For better fits, or values of R^2 closer to 1, the error envelope is relatively small. As value of R^2 reduces, the error envelope becomes larger.

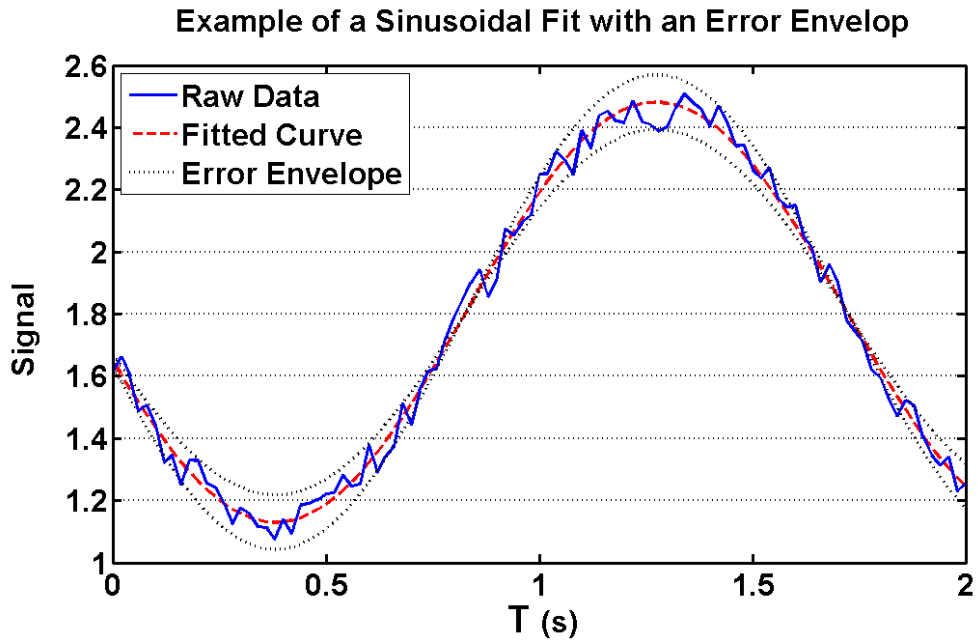

Figure 30: An Example of Fitting a Sinusoidal Curve to Data Recorded from a Plane Wave with an Error Envelope

Using this approach it is possible to calculate the errors caused by the fitting process and apply percentage bands to the fitted amplitudes. For instance, if the fit of a signal to a sinusoidal function has an amplitude of a_f and a coefficient of determination of R^2 then the range of values the true amplitude could possibly take is:

$$a_f \pm a_f \sqrt{1-R^2} \tag{198}$$

Similar statements can be made for the error in phasing estimation although this is not relevant in estimating the sensor gain error.

7.2.2.3 Estimating the Sensor Gain

The sensor gain was calculated by dividing the predicted amplitude of pressure oscillation by the amplitudes of the best sinusoidal fit to the pressure sensor data. The predicted amplitude of pressure oscillation was calculated by fitting sinusoidal functions to the resistance wave gauge data and applying linear wave theory to calculate the change in pressure at the sensing point.

Data from the first trial is used to illustrate the calculation of the sensor gain and associated error:

1. Record data from an experiment with the wave maker generating monochromatic waves of a known amplitude and period. Extract a 10 period sample of data for each sensor.

2. Fit the sinusoidal function $a_{rwg}\sin(b_{rwg}t+c_{rwg})+d_{rwg}$ to the resistance wire gauge data and calculate the error:

$$\begin{aligned} A_{rwg} &= a_{rwg}\pm\left(\sqrt{1-R^2}\times 100\,\%+\text{sensor accuracy}\right) \\ &= 29\text{mm}\pm(8.2\,\%+0.4\,\%) \\ &= 29\text{mm}\pm 8.6\,\% \\ &= 29\text{mm}\pm 2.5\text{mm} \end{aligned} \tag{199}$$

3. Linear theory can be used to predict the amplitude of the pressure fluctuations at the sensing point of the pressure sensors. To complete the calculation the wave number (k_{rwg}) is calculated numerically from b_{rwg} using the dispersion relationship (Eqn 43). The wave number is assumed to be accurate. From Eqn 119:

$$\begin{aligned} |p_{rwg}| &= \frac{\rho g A_{rwg}\cosh(k_{rwg}(h+z_{sens}))}{\cosh(kh)} \\ &= \frac{1000\times 9.81\times(0.029\pm 0.0025)\cosh(3.33\times(1.210\pm 0.001))}{\cosh(3.33\times(1.352\pm 0.001))} \\ &= 176\text{Pa}\pm 16\text{Pa} \\ &= 176\text{Pa}\pm 8.9\,\% \end{aligned} \tag{200}$$

4. A sinusoidal function was also fitted to each set of data from the pressure sensors. The amplitudes of the two valid pressure sensors was then averaged and the associated error calculated:

$$\begin{aligned} p_{ps1} &= a_{ps1}\pm\left(\sqrt{1-R^2}\times 100\,\%+\text{sensor accuracy}\right) \\ &= 145\text{Pa}\pm(3.3\%+2.5\,\%) \\ &= 145\text{Pa}\pm 5.8\,\% \\ &= 145\text{Pa}\pm 8.4\text{Pa} \end{aligned} \tag{201}$$

$$\begin{aligned} p_{ps2} &= a_{ps2} \pm \left(\sqrt{1-R^2} \times 100\% + \text{sensor accuracy} \right) \\ &= 131\text{Pa} \pm (3.4\% + 2.5\%) \\ &= 131\text{Pa} \pm 5.9\% \\ &= 131\text{Pa} \pm 7.8\text{Pa} \end{aligned} \tag{202}$$

$$\begin{aligned} p_{psa} &= \frac{p_{ps1} + p_{ps2}}{2} \\ &= 138\text{Pa} \pm 5.9\% \\ &= 138\text{Pa} \pm 8.1\text{Pa} \end{aligned} \tag{203}$$

5. The sensor gain can then be calculated:

$$\begin{aligned} \frac{p_{psa}}{p_{rwg}} &= 0.78 \, {}^{+0.91}_{-0.68} \\ &= 0.78 \, {}^{+16.2\%}_{-13.62\%} \end{aligned} \tag{204}$$

6. The process was repeated for all twenty trials. The resulting sensor gains and errors were averaged and the final value of the sensor gain is:

$$\begin{aligned} \textit{sensor gain} &= 0.83 \, {}^{+15\%}_{-13\%} \\ &= 0.83 \, {}^{+0.13}_{-0.11} \end{aligned} \tag{205}$$

Note that the sensor gain is lower than unity. In one respect this agrees with Kuo (see Section 5.4.3) in that the pressure sensor measures less pressure variation than would be expected given linear theory. For the example used to illustrate the sensor gain calculation, Kuo's theory predicts a sensor gain of 0.72. This value falls at the lower extreme of the error tolerance.

Noting that early experiments with the 200mm long tube displayed a considerable damping effect, it is safe to assume that the current design will still have a damping component. Considering this factor, it is likely that Tsai et al. are also correct in saying that a well configured sensor should measure the pressure variation accurately. Hence, if the sensor were to be re-designed effort should be made to minimise the length of the sensing tubes and thereby reduce the effects which require the use of a sensor gain factor.

7.2.3 Review of the Pressure Sensor Design

The pressure sensor design provided a very sensitive method for estimating the wave heights of small radial waves.

The flexible tubes used as sensing points (those extending from the epoxy potting) had a tendency to remain curved. This meant that the exact location and orientation of the port relative to the origin of the radial wave was not known for each individual sensor. The error introduced by this design attribute is discussed further in Section 8.6.

A more consistent design would be to use metal tubes at the sensing points and connect these to the pressure sensor and reference valve using the flexible tubing. If the transitions between the metal tubes and the flexible pipe were within the potting it would ensure that the joint was sealed. If a jig was used during the casting of the sensors, the metal tubes could be systematically located with reference to the sensor mounting point. The end result would be that the location of the sensing point would be known with greater accuracy, reducing the overall error. Note that the greatest error in locating the sensors is actual caused by the method of triangulation (See Section 8.6.1).

There would also be some advantage in reducing the length of the sensing port tube. This would reduce the amount of damping in the sensing system. Note also that there will be a limit to how short the reference port to reference valve connection can be before the change in volume due to the flexing of the internal membrane in the pressure sensor affects the reference pressure.

The accuracy of the calibration was affected significantly by the fitting of the signals to sinusoidal functions. The error associated with the fitting process accounted for $\frac{4}{5}$ of the 15.5% error.

One possible source of error is that the individual fitting scenarios may have determined a local maximum rather than a global maximum. Further examination of

the fits with the greatest error may yield better fits when starting values appropriate to that particular scenario are used.

Another possible source of error is the assumption the waves are sinusoidal. A more sophisticated non-linear model of the plane waves may yield better fits and therefore more accurate results. Another approach may be to forego matching the signals to an intermediate function and simply match the pressure signal to the resistance wave gauge readings. This would eliminate the need to estimate wave height. The only challenge with this method is that the signal attenuation dependant on the depth of the pressure sensor must be accounted for in some manner.

A more robust approach would have been to use a combination of capacitive wave gauges and pressure sensors. Utilising just a few capacitive wave gauges at key measuring points would have offered a direct calibration between the wave height and pressure readings. This would also explore the accuracy of the pressure predictions of linear wave theory.

7.3 Selection and Construction of Wave Generating Bodies

The three most common body shapes in existing literature are the cylinder, the sphere and the flat plate. The cylinder is perhaps the simplest axisymmetric shape a wave radiator can take, and can operate in both heave and surge. The sphere offers another axis symmetric shape that can be compared and contrasted with the cylinder. A vertical flat plate does not make waves while moving in heave, however, it does offer the ability to compare the surging properties of the cylinder and sphere with a non-axisymmetric body.

Of the three bodies the flat plate was the easiest to construct. The plate was 300mm wide, 600mm tall and constructed from 8mm-thick aluminium. A mounting bracket constructed from a 75mm x 50mm x 3mm aluminium rectangular hollow section (RHS) was bolted to the top of the plate.

The 300m diameter, 600mm tall, vertical axis cylinder was fabricated from a single piece of wire-cut polystyrene. A 75mm x 50mm RHS mounting bracket was secured in the top of the cylinder by simply carving out an undersize hole, applying PVA glue to the RHS and then pressing the RHS into the polystyrene. The cylinder was then coated with three layers of papier-mache to provide a base for a sealant layer. Three coats of two-part epoxy marine paint were then used to seal the body. This reduced the amount of water absorbed by the polystyrene and also met the environmental code of practice at the Groynes.

A 500mm sphere was constructed in a similar manner to the cylinder. Starting from a 500mm cylinder the outer edges of the cylinder were wire-cut until the body resembled a sphere. Again, a mounting bracket was secured into the sphere and the papier-mache / epoxy sealant process was followed as for the cylinder.

The RHS mounting brackets provided an attachment point to fix the bodies to the compound slide. The mounting brackets were sized so that when the compound slide was at the midpoint of the heave motion the body was half submerged. This minimised the torque required of the motor. Fig 31 shows the cylinder and sphere bodies used for testing.

The minimum wavelength prescribed during the wave basin selection (Section7.1) also determines the smallest scaling factor between the model and full sized bodies. If it is assumed that the full sized wave has a period of 8 seconds (a value commonly used for ocean waves) then, utilising Froude scaling (Section 4.2), the dispersion relationship (Eqn 43) and the minimum wave length, the smallest physical scale between the experimental model and the real ocean waves is approximately $\frac{1}{64}$. This means that the largest full sized bodies to which the experiments could be related are a 32m sphere, a 19m cylinder and a 19m plate.Review of the Body Selection

Figure 31: Two Bodies Constructed for the Radial Wave Generator

The three chosen bodies provided sufficient contrast to allow robust examination of circular wave theory. A greater range of information could have been extracted from the study if the body selection was altered in the following two ways. Firstly, the original design of the bodies occurred before various advancements in the mathematical theory were made. After the study in Chapter 9 was completed, it was noted that the cylinder and sphere would have been more comparable if the displaced volumes in heave or swept volumes in surge had been the same. Secondly, if the range of selected bodies had been expanded to include two additional spheres of different diameters, then it would have been possible to explore how physical scaling affected wave radiation.

7.3.1 Review of the Body Construction

Overall the various bodies performed well. The design and construction were suitable for the relatively small amount of testing completed.

It was noted that the sphere and cylinder bodies sustained minor damage from general handling. This indicates that the papier-mache construction of the bodies was just sufficient for the testing regime. If more robust bodies were required, the use of fibre glass would be recommended.

The flat bottom surface of the cylinder was subject to significant negative pressure fluctuations during actuation and the papier-mache delaminated from the polystyrene core. There are three ways to avoid this failure mechanism: change the shape of the face to minimise the negative pressure fluctuations, embed anchors into the composite layers that provide better connection with the substrate material or avoid composite skins all together e.g. construct the body from wood.

A method of height adjustment somehow incorporated into the body mounting system may remove the requirement for height adjustment of the radial wave generator. Adjusting the body height would be significantly easier than adjusting the whole test jig and would allow experiments to see how the depth of submergence affected the radiated waves.

7.4 Mechanical Design of the Radial Wave Generator

This is a summary of the design brief written for the radial wave generator.

The first major design goal was that the radial wave generator must be able to accommodate a range of different body shapes and sizes. The details of the bodies are outlined in Section 7.3.

The second major design goal is that the radial wave generator must be able to move the body in different combinations of heave and surge. The ideal flexibility was for there to be a range of heave and surge amplitudes with the ability to operate in both modes simultaneously. A mechanism to allow the adjustment of the phasing and amplitudes of each motion was also desired. This would allow the body to be moved in a range of motions from vertical, horizontal or diagonal straight lines to full circular

motion in a single plane. One of the key complexities of this goal is that the two motions must be driven at exactly the same speed or else the phasing relationship between the two may potentially drift.

The third major design goal was that the radial wave generator must be portable. As the chosen wave basin was an outdoor pond in a community park it was not possible to permanently install the radial wave generator. This meant that all of the apparatus and power equipment had to be able to be moved from location to location.

The design for the radial wave generator that meets these three design criteria is detailed in the following sections.

7.4.1 Construction of the Compound Motion Generator

The radial wave generator is a unique piece of equipment that actuates the motion of a body in two degrees of freedom. Fig 32 shows a basic schematic of the mechanical drive chain for the radial wave generator. Fig 33 shows the exploded view of the compound motion generator, the core of the radial wave generator. Fig 34 shows the compound slide on the jetty at the Groynes awaiting assembly of the supporting frame. Each slide and carriage is based on the DualVee rail and roller bearing arrangement manufactured by Hepco. Adjustment of the slide fit is achieved through the use of bearings with eccentric bushings. See Fig 35 for further details. The product data sheet is available in Digital Appendix 5 or from the Hepco website [91].

The two degrees of freedom, heave and surge, one driven from each side of the radial wave generator, are run off a single drive shaft connected to an electric motor. This ensures that each is driven at exactly the same speed. Each degree of freedom is connected to the drive shaft by a toothed drive belt run through a set of speed reduction pulleys. Changing the angular alignment of the pulleys, relative to the drive shaft, allows the phasing relationship between heave and surge to be altered.

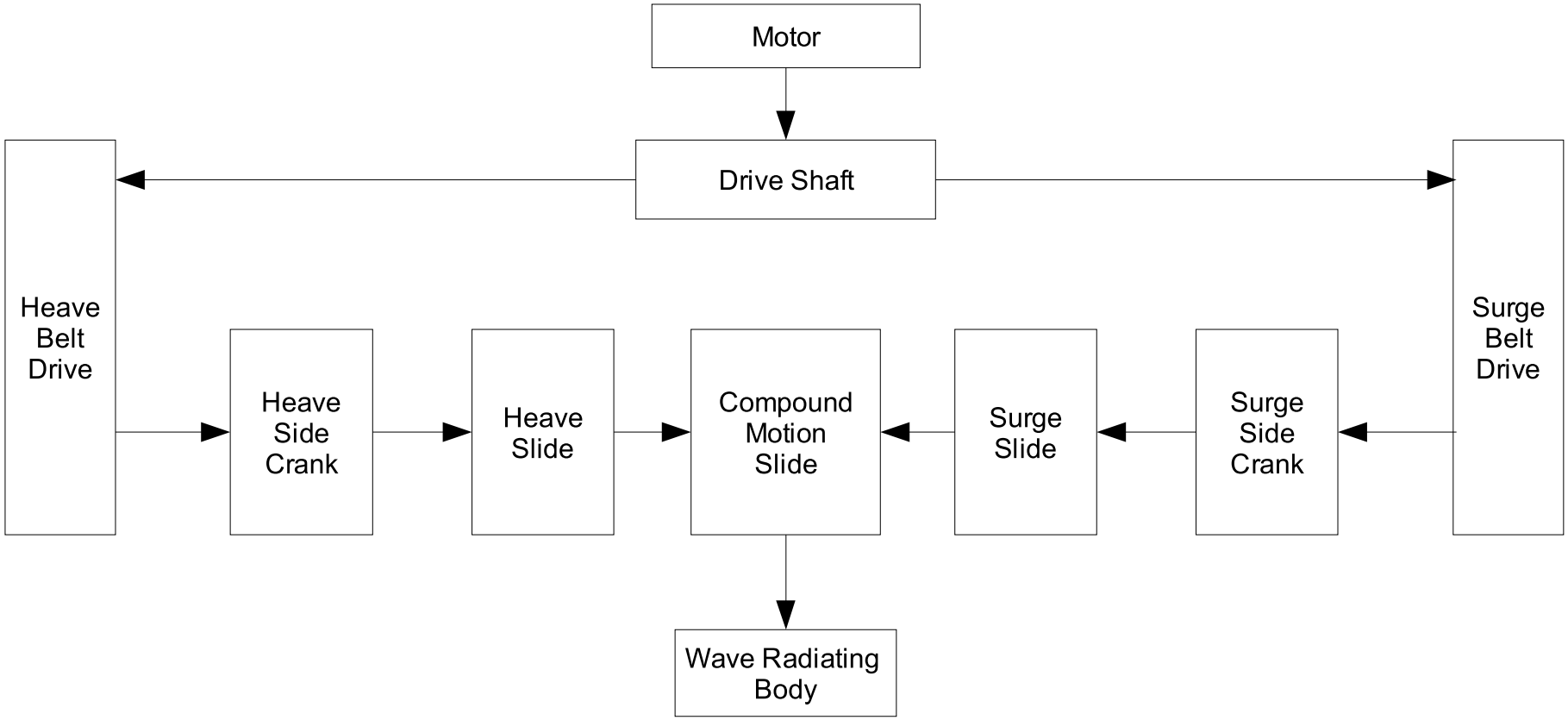

Figure 32: Basic Schematic of the Radial Wave Generator

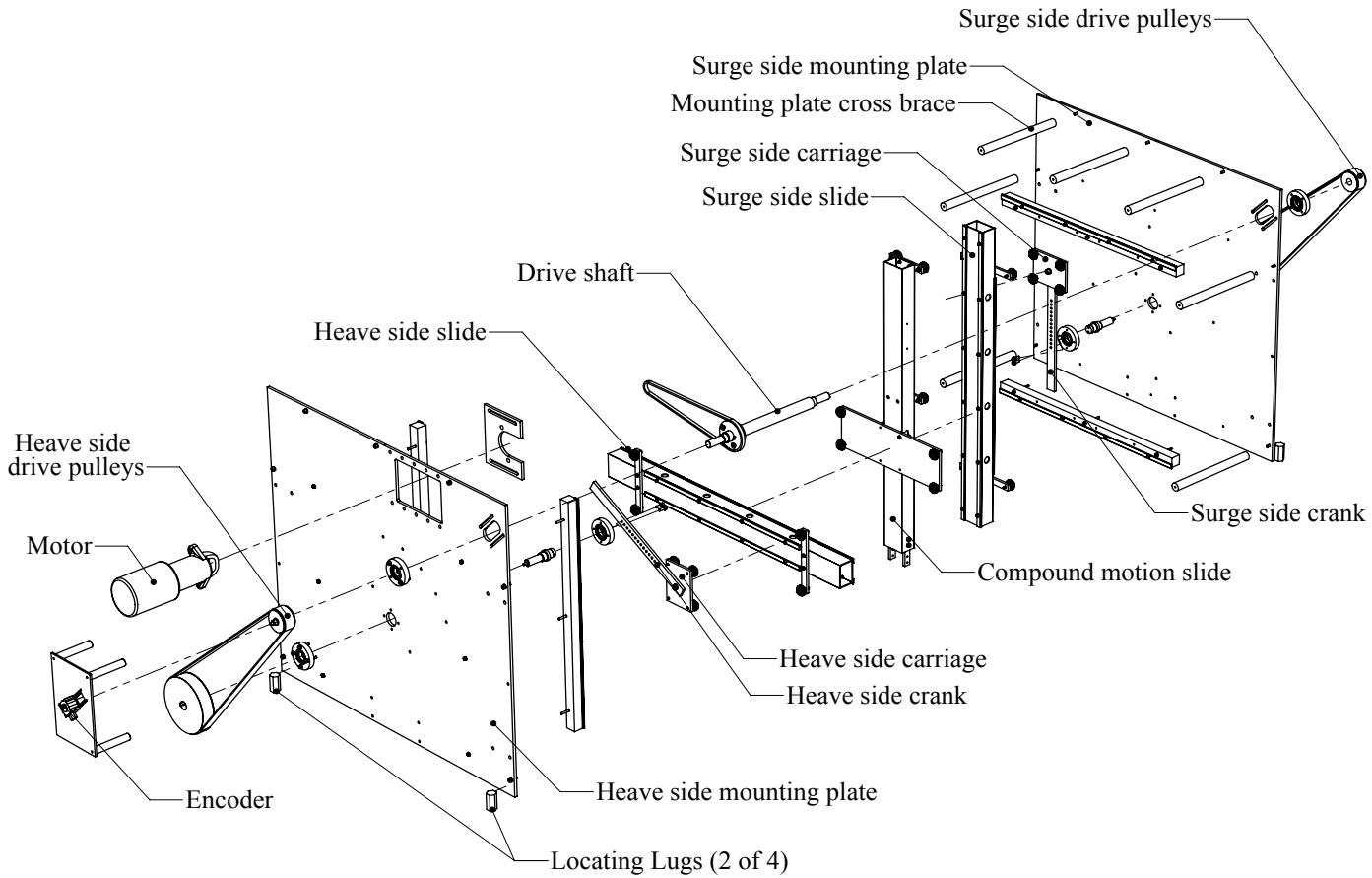

Figure 33: Exploded View of the Compound Motion Generator

Figure 34: Radial Wave Radiator During Assembly at the Groynes Testing Site

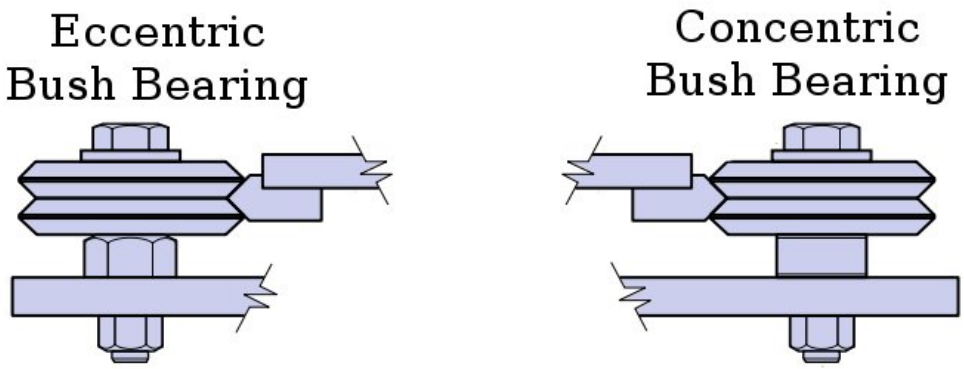

Figure 35: Bearing arrangement for the Compound Motion Slides on the Compound Motion Generator
This image was adapted from the DualVee product data sheet from Hepco

Each set of pulleys drives a crank that moves a slide through the sinusoidal motion. The crank has a range of mounting positions machined along its length and can vary the amplitude of motion between 107mm and 211mm in heave and between 107mm and 250mm in surge. The slightly reduced heaving amplitude was due to interference from the mounting plate cross braces.

The heave and surge slides are connected by carriages to the compound motion slide which, through the nature of its orientation, is driven independently in each degree of freedom. At the bottom of the compound motion slide is a point to which different bodies can be attached. The compound slide also has mounting points to which dead weights can be added. This allows the up-thrust from the bodies' buoyancy to be counteracted when necessary.

7.4.1.1 Review of the Compound Slide Mechanism

The design of the compound slide system was robust given the loads to which it was subjected to. The only change made to the slide system during testing was to enlarge the brackets mounting the eccentric bushings on heaving and surging slides. This was done to provide stiffer location for the eccentric bush bearing. This change contributed to the identification of the issue with the transit stops described in Section 7.6.5.

The heaving transit stops should be redesigned so that there is the ability to adjust the level of each stop independently. The method of adjustment must also have a locking mechanism so that it is not prone to moving under vibration. This would reduce the post-testing maintenance required on the radial wave generator.

One of the base assumptions in linear wave theory is that the wave amplitude is relatively small. Similarly, those analysing body motion also assume that the bodies undergo small amplitude motion. This leads to another potential improvement. If the design of the connection between the crank and the carriage connecting the crank to the heave/surge slide was modified to allow for a smaller minimum amplitude of motion, it may be possible to compare experimental results to those derived based on linear theory. The current minimum of 107mm was determined by the size of the carriage and the interference of the carriage with the crank mounting bolts. If this connection was redesigned to a low profile connection, for instance a spline and a retaining circlip, it may be possible to drop the minimum amplitude of motion to significantly smaller values. This would allow a greater range of testing. If this design change were implemented, further thought would have to be given as to how to

disconnect the crank during testing where only one of the degrees of freedom is required.

Another limitation of the compound slide mechanism is that it can only provide a linear surge motion. Linear wave theory shows that the maximum horizontal velocity decays with depth. In contrast, the compound slide moves the body horizontally, which means that the horizontal velocity profile for a water particle on the surface of the body is constant with depth. This is likely to affect the efficiency with which large draft surging bodies radiate wave power. The compound slide could be altered to allow the body to pitch at a hinge point well below the still water level which should provide large draft surging bodies with a motion that would approximate the decay with depth.

7.4.1.2 Review of the Phasing Adjustment

The process of adjusting the phasing between heave and surge could be improved. Currently the system requires re-adjusting the taper-lock pulleys used to drive each crank. If the joint between the crank and driving axle was turned into a spline joint, then once the heave and surge crank were aligned, it would be a simple matter of detaching the crank and indexing around a number of steps on the spline to change the phasing relationship. This would be more accurate, discrete adjustment to the phasing of the two motions.

There are two other points of note about the recommended change to the crank. The first is that the crank would need to be made out of steel instead of aluminium to reduce the risk of flogging out the spline joint. The second is that it would keep the un-keyed design of the taper-lock connection to the drive pulleys. This has turned out to be an important soft connection in the case where the slides have been driven into end stops or transit locks, greatly reducing the damage to the compound slides in these situations.

7.4.2 The Supporting Frame of the Radial Wave Generator

Portability of the generator was achieved through the modular construction of the radial wave generator and the choice of a low voltage DC power source.

The compound motion generator was designed as a single unit. The total weight of the compound motion generator was just below 100kg, which meant with the aid of an engine hoist and trolley, the unit could be handled by two people.

The supporting frame provided the structure to suspend the compound generator above the surface of the pond. Slots in the supporting legs allows the height of the test-jig to be adapted to suit the water depth. Fig 36 shows the assembled radial wave generator and Fig 37 shows the supporting frame construction.

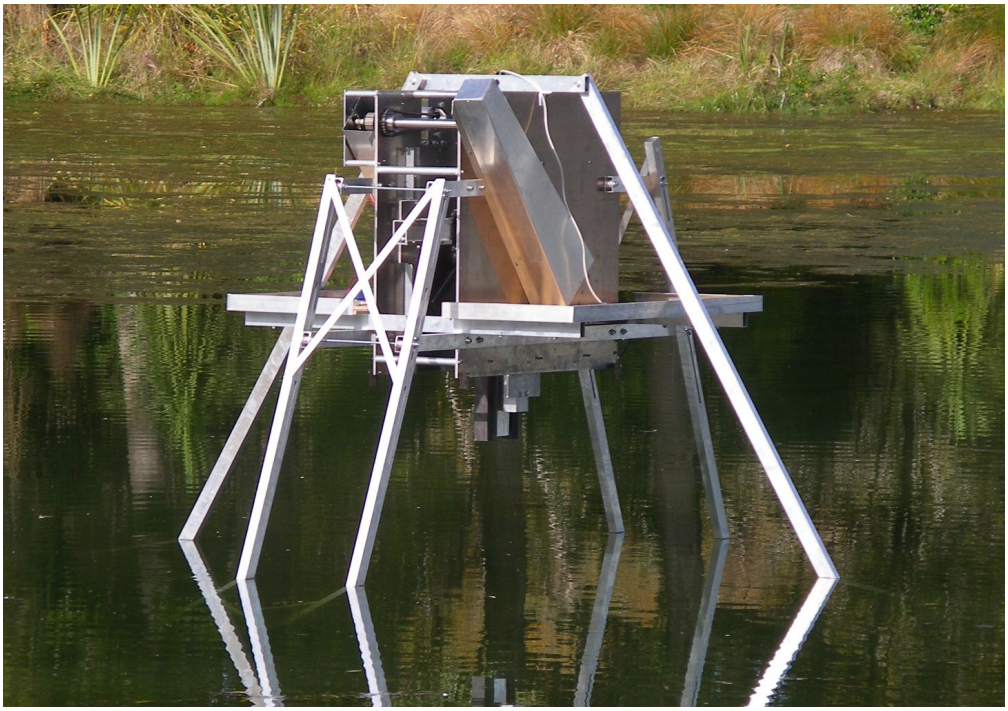

Figure 36: The Radial Wave Generator Installed in the Groynes Testing Basin

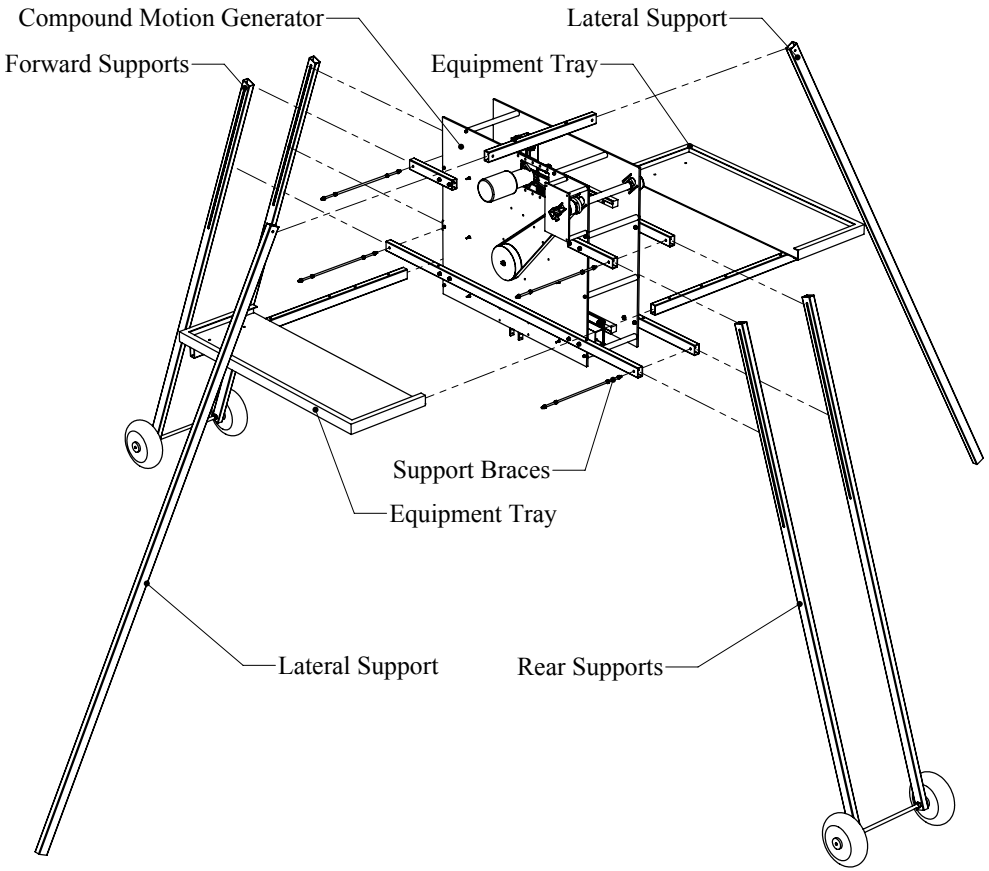

Figure 37: Exploded View of the Radial Wave Generator

The forward, lateral and rear supports were aligned so that the longer dimension of the extrusion was as close to radial as possible. This helped to minimise the interference between the supporting frame and the radiated wave. The desire not to interfere with the radiated wave also drove the design of the supporting frame to have minimal cross bracing. The addition of wheels at either end allowed the radial wave generator to be moved once assembled. Concrete block chocks were used to prevent movement during testing.

As the testing was being conducted at a remote location a portable power source was required. A DC electric motor and DC electronics meant that deep cycle lead acid batteries could be used as the power source. See Section 7.5 for further information on the radial wave generator's electrical system.

7.4.2.1 Review of the Supporting Frame

The supporting frame structure was the weakest element of the design. The drive to minimise the interference with the radiated waves caused the design to be unstable under high loads. The structure stability would have benefited from the addition of cross bracing and the use of heavier sections to reduce flexing. In addition, the radial wave generator would have been less prone movement if the wheels that had been used to manoeuvre the radial wave generator into place could have been locked or removed.

Another approach that may have been suitable to the testing site used would have been to use the jetty as a supporting structure and brace the radial wave generator against this structure. Ideally the test-jig would be supported by a rigid structure from above, however, this was not possible.

7.5 Electrical Design of the Radial Wave Generator

The design of the electronics for the radial wave generator consists of three major blocks: the power source, the data acquisition components and the motor control

components. Fig 38 is a basic schematic of the radial wave generator and Table 5 is a list of the components used.

The data acquisition block consists of the pressure sensors, the accelerometers the input/output (I/O) box, the analogue to digital converter (DAQ) and the laptop. The construction of the pressure sensors has been described in Section 7.2.1.

A dual-axis accelerometer was secured to the compound motion slide to record the accelerations of the slide. The alignment of the accelerometer was fine tuned by rotating the accelerometer until the signal on the vertical axis was a maximum. The vertical alignment of the radial wave generator was confirmed in both the lab and the testing basin using a spirit level.

The I/O box provided an interface between the sensors and the DAQ. It also provided a regulated 5V source for the sensors and accelerometers and is powered off either a 12V

Component	Manufacturer	Part Number	Description
Accelerometer	Analog Devices	ADXL 321	3 axis, 18g accelerometer
DAQ	National Instruments	NI cDAQ-9172 with NI 9205 module	A 32 Channel A2D converter with a 250kS/s sample rate
Encoder	Hengstler	RI38-500-EQ-11-K-B	512 pulse incremental optical encoder
Motor	Unite Motors	MY1020	500W, 48VDC motor with custom 3:1 gear box
Motor Controller	RoboteQ	AX2850	Dual-channel speed controller
Laptop	Lenovo	2055-RK6	Windows platform to run Roborun and LabVIEW software
Pressure Sensors	Freescale	MPXV7002DP	2kPa, ±5V output differential pressure sensor
12V Battery	Long Batteries	U1-36NE	12V, 36Ah sealed lead acid battery

Table 5: Electronic components used in the radial wave generator

or a 24V DC source. It also acts as a junction box, combining the 32 individual signals into a single plug connector for the DAQ.

The DAQ is a National Instruments compact DAQ (part number NI cDAQ-9172) with a 32 channel analogue to digital component (part number NI 9205). A laptop using the LabVIEW software provided the control over the data acquisition and motor controller settings as well as a sink for the collected data.

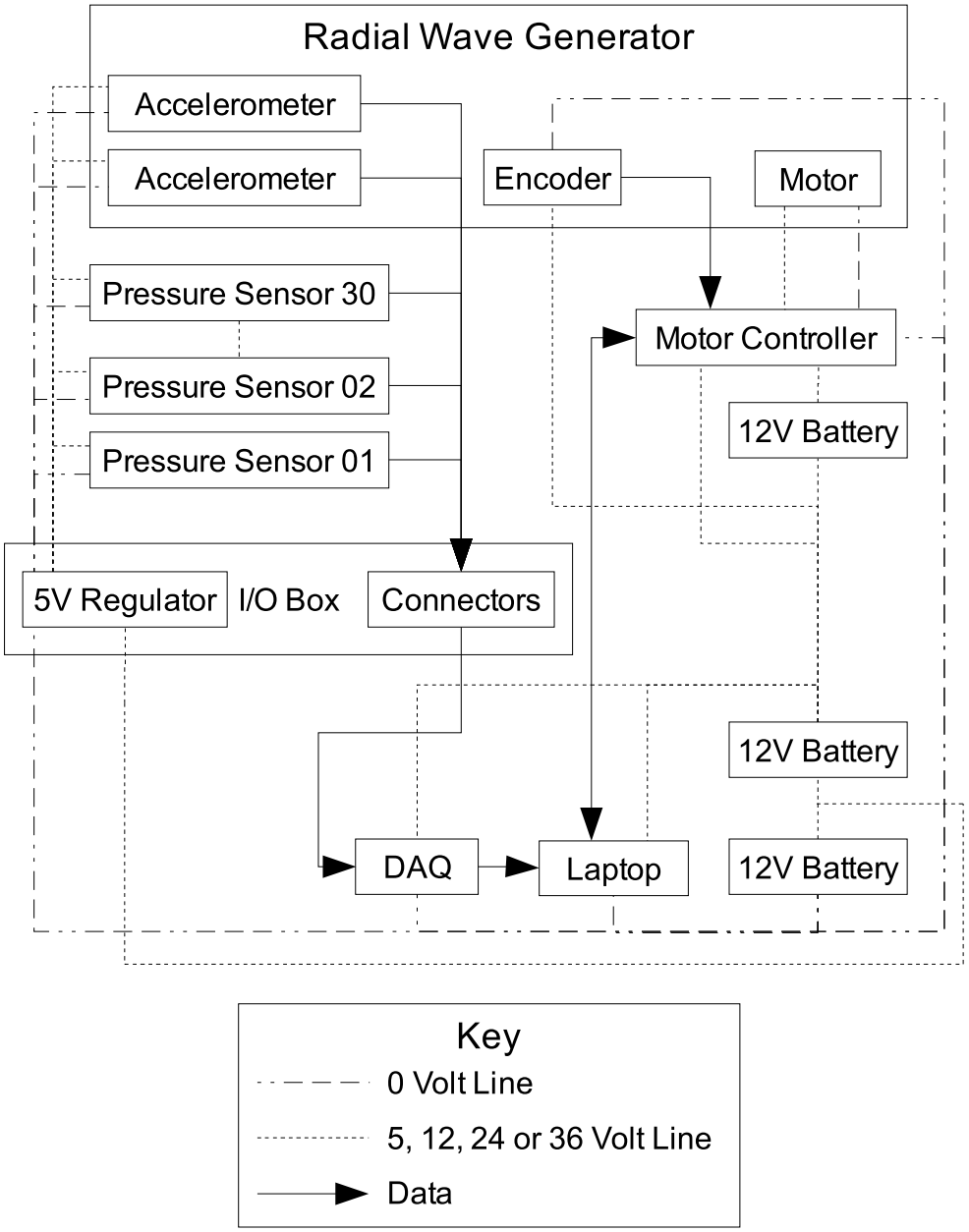

Figure 38: Electrical Schematic of the Radial Wave Generator

The motor control components consist of the motor, the motor controller and the encoder. The motor available motor was a 500 Watt, 48 Volt DC motor.

The RoboteQ motor controller was configured to run in speed control mode. Using the Roborun software, the motor speed could be accurately and repeatably set. The feedback from the encoder ensured that the motor speed was as consistent as possible.

The power source was required to be portable and to run low voltage electronics. This suggested that a DC battery pack would be suitable. Five 36Ah deep cycle lead acid batteries were available and a bank of three were used at any one time.

7.5.1 Software Design for Data Acquisition

An original LabVIEW program was written by the author with the assistance of the electrical technicians from the University of Canterbury. This program collected the data from the National Instruments data acquisition (DAQ) unit. It was designed to log the data from 32 Channels to a text file for post-testing analysis. The interface was configured to be simple and instructive for any user. Fig 39 shows the user interface with labels for the relevant features. Fig 40 provides a block diagram showing the major components of the program including input and output information. The source code and compiled executable are available in Digital Appendix 2.

One particular issue worth noting is the effect of computation cycle time on the data acquisition. As the program loops acquiring the data and writing to the file have a finite processing time, it is possible to configure the DAQ Assistant in a way that results in irregular sampling times. The data can be transferred to the DAQ in chunks of samples, for example 100 samples of data taken at 200Hz. If the LabVIEW program takes a longer amount of time to return to the sampling part of the code than the chunk size (in this case 0.5s) data may be lost.

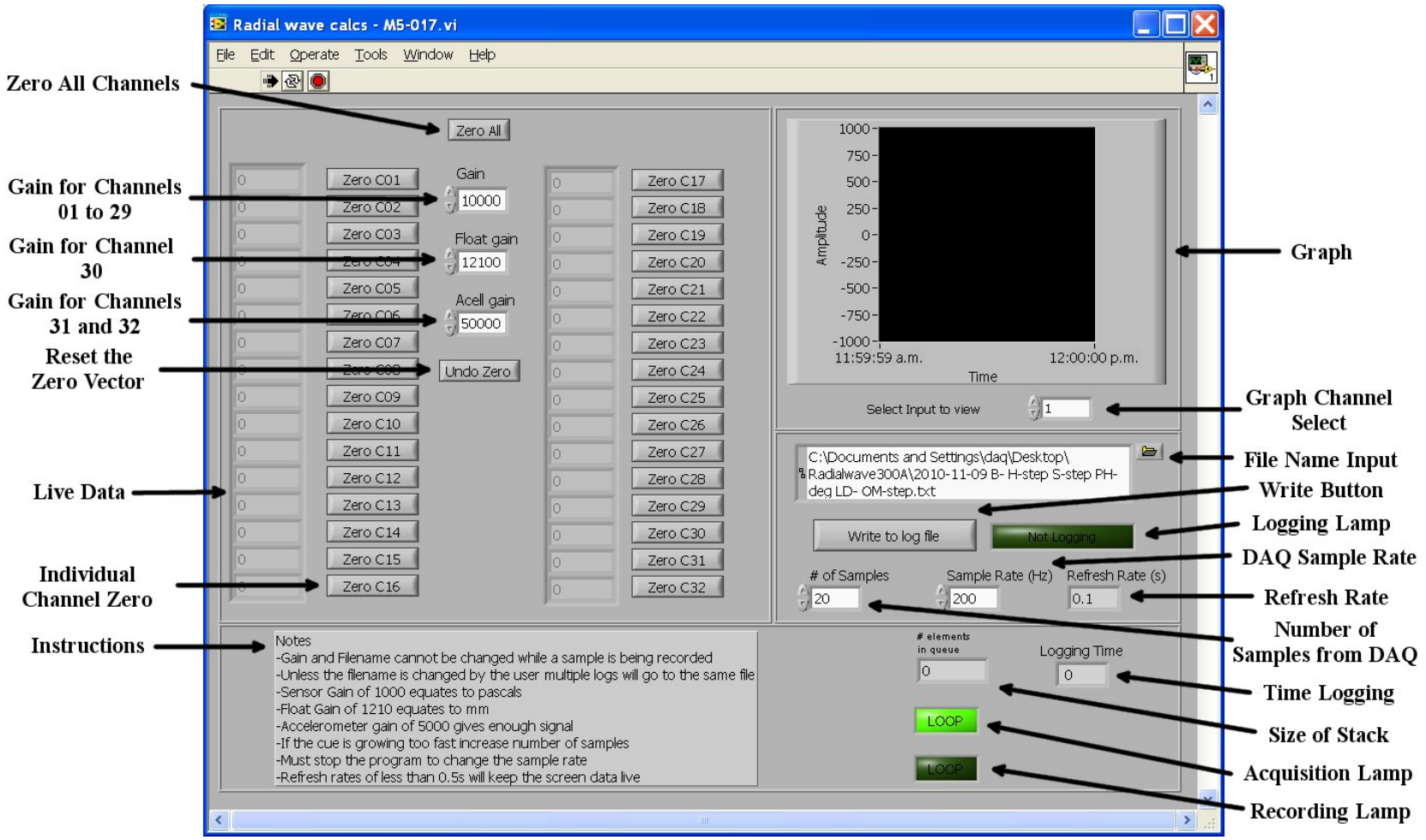

Figure 39: LabVIEW Program User Interface for the Data Acquisition System

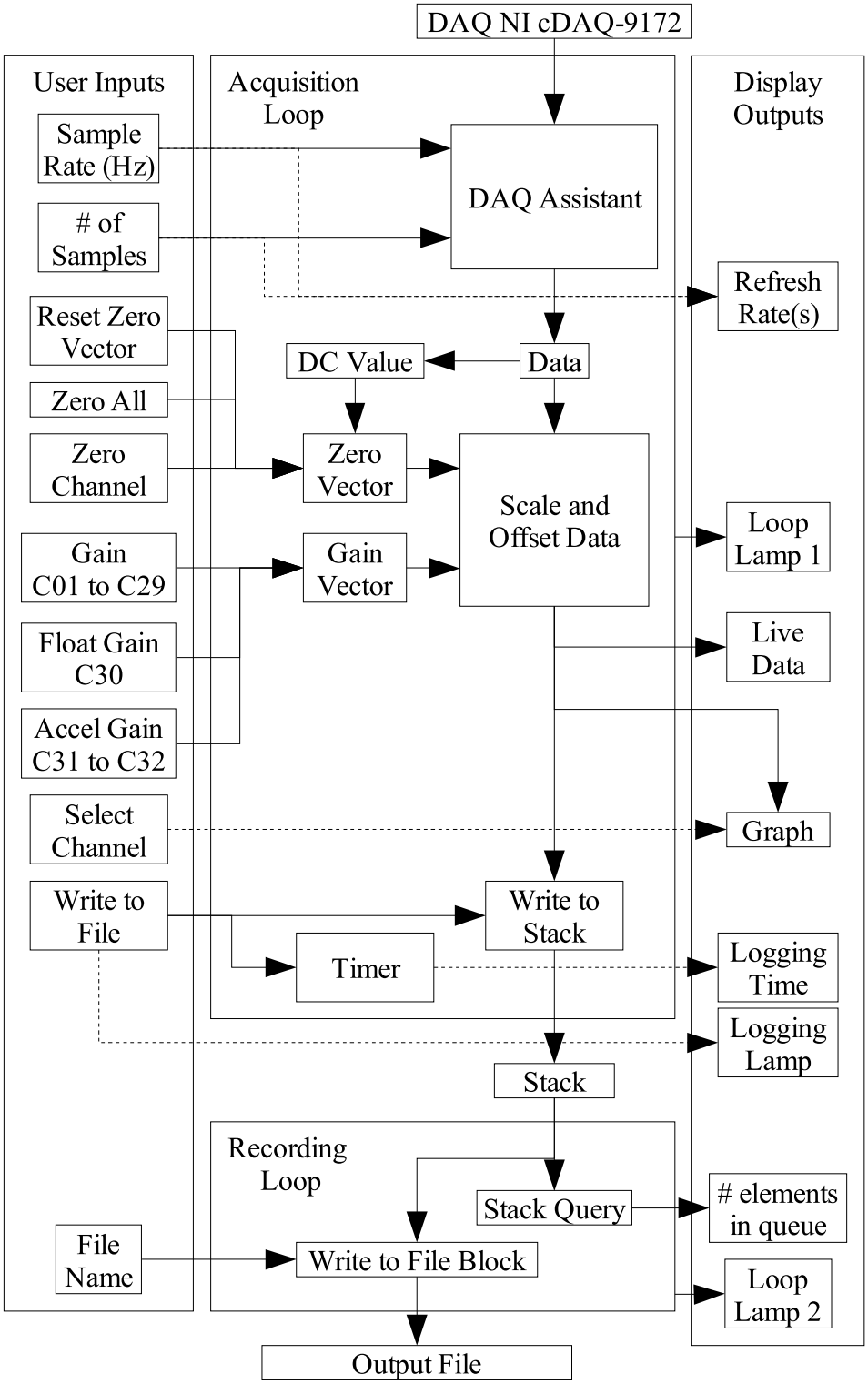

Figure 40: Block Diagram of the LabVIEW Data Acquisition Program

The speed at which the program runs is affected by the hardware on which the program is run. Two user configurable variables were created to control data acquisition and tailor the chunk size to suit the hardware. The user can set both the sample rate of the data (DAQ sample rate) and the size of the chunk (number of samples from DAQ). These two numbers are then used to calculate the refresh rate. A monitoring system is provided in the form of a stack counter (Size of Stack). This shows the number of chunks in the stack and therefore whether the program is keeping up with the data logging. If the stack continually grows then the user should consider increasing the chunk size or decreasing the sample rate.

Note that Figs 39 and 40 indicate a user input called “float gain”. The original intention was to use a magnetic wave gauge with a float to calibrate the wave height. This feature was not utilised and the DAQ channel reserved for the float was used for another pressure sensor.

7.5.2 Review of the Electrical Design

Overall the electrical design of the test rig performed in a robust and satisfactory manner. The only significant change from the original design was to move the encoder from its mounting point on the crank axle to a mounting point on the end of the drive shaft. This was done because the limitations in the motor controller settings required greater resolution from the encoder to be able to provide a greater range of speed increments. The balance for the greater resolution of speed was slightly less accurate control over the velocity of the body. Moving the encoder up the gear chain meant that the feedback loop no longer included the effects of the belt drive. If the design was to be revisited the original encoder position would be reinstated using an encoder with a greater number of counts.

A potential improvement for future projects would be to implement position control on the motor feedback loop. The main benefit of this would be the ability to move a body so that the displaced volume matched a specific profile. For instance, the displaced volume of a sphere has an intrinsic third harmonic due to the curve of the sphere. The

variation in displaced volume may be able to be minimised by adjusting the motion of the sphere.

Another minor improvement would have been to use an accelerometer with a more appropriate scale. The fastest oscillation undertaken during testing had an acceleration of 0.98 g . The ADXL321 had a full scale rating of ±18 g . A similar accelerometer with a full scale range below 5g would provide greater resolution of the accelerations.

7.6 Experimental Procedure

The experimental procedure described in this section is an outline of the process followed and notes how key data was obtained.

7.6.1 Configuration and Setup of the Test Jig

Before each day's testing the radial wave generator was configured. This consisted of adjusting the phasing relationship between the heave and surge components so that any compound motion experiments were pre-set. For instance, if the day's testing contained a compound in-phase heave and surge test, the angular alignment of the two cranks relative to the drive shaft would be adjusted so that the maximum heave displacement occurred at the same moment as the maximum surge. In this instance, this would correlate to the heave crank being vertical when the surge crank was horizontal and the resulting compound motion would move the body on a diagonal line. This procedure could have been carried out at the testing basin if required, although for ease and the maximising of testing time it was carried out before hand.

The radial wave generator was then loaded onto a sport utility vehicle (SUV). This was achieved by placing an engine hoist on the deck of the SUV and using it to lift the radial wave generator off the ground. Then the equipment trays and forward, rear and lateral supports could be removed allowing the generator to fit onto the SUV.

On arrival at the testing site the engine hoist was used to manoeuvre the compound slide unit to the end of the jetty (as seen in Fig 34). At this point the support frame work and equipment trays were reassembled and the radial wave generator was moved out into the testing position (Fig 36). The wheels were then chocked with cement bricks to limit any movement of the rig.

7.6.2 Locating the Sensor Positions

Once the radial wave generator was installed, it was important to accurately reference the position of the sensors to the radial wave generator. Variations in the pressure field with radius, r, and angle, θ, are only relevant in a context where the sensor positions relative to the wave origin are known. The procedure for setting up the sensors was as follows.

Four locating lugs were attached to the compound slide of the radial wave generator (see Fig 33). The four lugs provided at least two visible lugs from any given point in the test basin. A laser measuring device was then used to accurately triangulate the position of any given sensor location. This was accomplished by measuring the distance between the sensor post and two different lugs, and recording which quadrant the sensor was in.

The placement of sensors was determined by the conditions laid out in Section 7.2. Sensors were placed so that there were at least three sensors radially aligned in each of the $\theta=0$, $\frac{\pi}{6}$, $\frac{\pi}{3}$, $\frac{\pi}{2}$ and π directions. As the DAQ had a large number of available ports, additional angles were also used to provide further spatial data.

Laying out radially aligned sensors involved a piece of lightweight rope marked with the distances of 0.75m and attached to the centreline of the compound slide using a mounting bracket. The compound slide was set to the mid-surge, low heave position with travel stops used to prohibit the slide from moving during transit. The rope provided a reference to the origin of the wave field so that the mounting posts of the sensors could be placed along a radial line. Each set of sensors was positioned by

attaching the rope to a sensor post at the 4.5m mark, measuring the distances between this post and two of the locating lugs with a laser measuring guide, and then positioning the remaining sensors along the rope at the appropriate marks.

The distance data collected as part of the above process was used to triangulate the position of the outermost sensor from the centre of the compound slide in radial coordinates. The location of the remaining sensors was calculated by assuming that the sensors were located along the same radial line at the distances given by the markings on the rope.

As each sensor was being placed, it was ensured that the reference valve was open so that the sensor could thermally stabilise before the reference pressure was locked off. It was found that if the sensors were locked off before thermal equilibrium had been reached, the air locked in the tubing between the valve and the sensor would continue to contract as the sensor cooled and the reference pressure would drop significantly.

7.6.2.1 Sensor Location Calculation

This section provides an example of the sensor location calculation, including an estimation of the position errors. Fig 41 illustrates the geometry and location terms associated with determining the sensor position. The data recorded during the experiments consists of two distances to location lugs mounted on the compound slide mechanism of the radial wave generator. These values correspond to $M1$ and $M2$.

The calculation is as follows:

1. Pythagoras' theorem can be used to adjust the measurements for the height of the locating lugs above the free surface ($H1$). The location lugs are 50mm long pieces of hex bar with an effective diameter of 27mm ($2R1$) and hence the actual height of the measurement from the free surface has an accuracy of ±25mm. The horizontal distances to the centre of the locating lugs are given by $L2$ and $L3$.

$$
\begin{aligned}
L2 &= \sqrt{M1^2 - H1^2} + R1 \\
&= \sqrt{(3900\text{mm} \pm 2\text{mm})^2 - (572\text{mm} \pm 25\text{mm})^2} + \frac{26.9\text{mm} \pm 2\text{mm}}{2} \\
&= 3871\text{mm}\,{}^{+10\text{mm}}_{-10\text{mm}}
\end{aligned}
\tag{206}
$$

$$
\begin{aligned}
L3 &= \sqrt{M2^2 - H1^2} + R1 \\
&= \sqrt{(4713\text{mm} \pm 2\text{mm})^2 - (572\text{mm} \pm 25\text{mm})^2} + \frac{26.9\text{mm} \pm 2\text{mm}}{2} \\
&= 4692\text{mm}\,{}^{+9\text{mm}}_{-9\text{mm}}
\end{aligned}
\tag{207}
$$

2. The Cosine rule allows the calculation of Y noting that $Y = Y1 - \frac{L1}{2}$:

$$
\begin{aligned}
Y &= \frac{L3^2 - L2^2}{2\,L1} \\
&= \frac{\left(4692\text{mm}\,{}^{+9\text{mm}}_{-9\text{mm}}\right)^2 - \left(3871\text{mm}\,{}^{+10\text{mm}}_{-10\text{mm}}\right)^2}{2\,(950\text{mm} \pm 2\text{mm})} \\
&= 3697\text{mm}\,{}^{+93\text{mm}}_{-92\text{mm}}
\end{aligned}
\tag{208}
$$

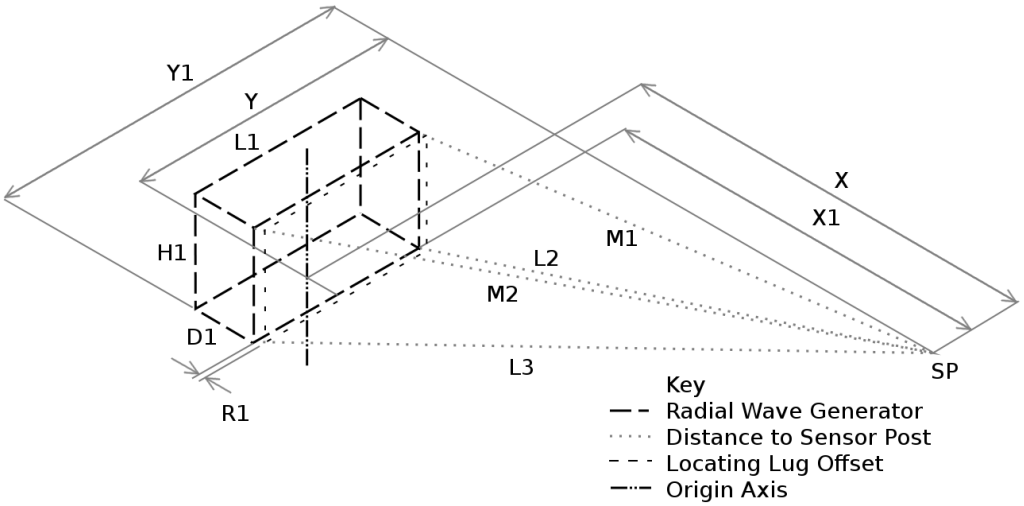

Figure 41: Pressure Sensor Location Calculation Geometry

3. The value of $X1$ can be calculated from another application of Pythagoras' theorem.

$$\begin{aligned} X1 &= \sqrt{L3^2 - \left(Y + \frac{L1}{2}\right)^2} \\ &= \sqrt{\left(4692\text{mm}\,^{+9\text{mm}}_{-9\text{mm}}\right)^2 - \left(3697\text{mm}\,^{+93\text{mm}}_{-92\text{mm}} + \frac{(950\text{mm} \pm 2\text{mm})}{2}\right)^2} \\ &= 2146\text{mm}\,^{+151\text{mm}}_{-166\text{mm}} \end{aligned} \tag{209}$$

4. The horizontal position of the sensor post can be calculated by adding the offset between the origin and the mounting point of the locating lugs.

$$\begin{aligned} X &= X1 + \frac{D1}{2} \\ &= 2146\text{mm}\,^{+151\text{mm}}_{-166\text{mm}} + \frac{(340\text{mm} \pm 2\text{mm})}{2} \\ &= 2316\text{mm}\,^{+152\text{mm}}_{-167\text{mm}} \end{aligned} \tag{210}$$

5. The r and θ coordinates of the sensor post can then be calculated.

$$\begin{aligned} r_{sensor\ post} &= \sqrt{X^2 + Y^2} \\ &= \sqrt{\left(2316\text{mm}\,^{+152\text{mm}}_{-167\text{mm}}\right)^2 + \left(3697\text{mm}\,^{+93\text{mm}}_{-92\text{mm}}\right)^2} \\ &= 4363\text{mm}\,^{+160\text{mm}}_{-166\text{mm}} \end{aligned} \tag{211}$$

$$\begin{aligned} \theta_{sensor\ post} &= atan\left(\frac{Y}{X}\right) \\ &= atan\left(\frac{3697\text{mm}\,^{+93\text{mm}}_{-92\text{mm}}}{2316\text{mm}\,^{+152\text{mm}}_{-167\text{mm}}}\right) \\ &= 0.560\text{rad}\,^{+0.041\text{rad}}_{-0.044\text{rad}} \end{aligned} \tag{212}$$

6. The point at which the sensor senses the pressure is offset from the sensor mounting post. The flexibility of the sensing tubes means that the precise location of the sensing point from the sensor post is not well defined. However, this adds a relatively small amount of error. The position of the sensing point is given by:

$$\begin{aligned} r_{sensor\ point} &= r_{sensing\ post} - 95\text{mm} \pm 10\text{mm} \\ &= 4268\text{mm} \begin{matrix} +170\text{mm} \\ -176\text{mm} \end{matrix} \end{aligned} \tag{213}$$

$$\begin{aligned} \theta_{sensor\ point} &= \theta_{sensor\ post} - \frac{13\text{mm} \pm 10\text{mm}}{2\pi r_{sensing\ point}} \\ &= 0.560\text{rad} \begin{matrix} +0.044\text{rad} \\ -0.040\text{rad} \end{matrix} \end{aligned} \tag{214}$$

The significance of this error is highlighted in Section 8.6.1.

7.6.3 Completing the Testing Setup

Once the radial wave generator had been installed and the sensors distributed around the origin, the body could be attached.

For the sphere and cylinder, the buoyancy of the body construction meant that there was a significant up-thrust when submerged. The buoyancy force of the sphere was sufficient that it could stall the motor before reaching the bottom dead centre position. Steel weights were added to the compound slide to balance the buoyancy. Enough weight was added so that the equilibrium point of body with the weight of the compound slide and steel weights occurred when the body was half submerged.

Assembling the body also allowed any further adjustments to the amplitudes of the heave and surge motion to be completed. In the cases where only a single degree of freedom was required, the crank for the idle motion was disconnected and the transit stops were used to set the position of the slide.

The unsecured electronics were then transferred to the equipment trays. The batteries, laptop and DAQ were all mounted at this point and the wiring was completed.

The last step was to close all of the reference valves on the pressure sensors. The time taken to perform the mounting of the body and electronics allowed for thermal stabilisation of the pressure sensors. The radial wave generator and data capture system was then ready for testing.

7.6.4 The Testing Procedure

The testing was grouped into series of tests. Each series consisted of tests of increasing oscillation speed given a set body, amplitude of motion and phasing combination. The first test in each series was a zero reading test. The radial wave generator was left still and the data from the pressure sensors was recorded for approximately 10 seconds. This test provided an indication of the level of noise for each test run.

The series of tests continued with the incremental increase of the body oscillation speed. For each speed increment the motor control setting would be adjusted and a 30 second period allowed for the wave field to stabilise. The DAQ would then be set to record for approximately 30 seconds at 200Hz. This sample period covered between 4.5 and 37 complete wave cycles depending on the frequency of motion.

The speed of body motion was limited by one of two factors: motor controller power output or structure stability. Although a 48V, 500W motor was used, the motor controller was run limited to run at 36V and a peak power of 140W was recorded during testing. In all tests moving in purely heave, it was this power output that limited the highest test speed. For the tests involving purely surging motions the rigidity of the testing structure proved the limiting factor. As the speed of body oscillation increased the reaction forces experienced by the radial wave generator also increased. This resulted in flexing of the forward and rear supports, and the repeated motion tended to push out the wheel chocks keeping the radial wave generator in place. This limited the surging motion of the constructed bodies to periods longer than 1.27 seconds.

7.6.5 Post-Testing Procedures

At the end of a day's testing the procedure for setting up the radial wave generator was reversed to remove all the equipment from the testing basin and return it to the laboratory. After returning to the laboratory the sensors required cleaning and recoiling. The cleaning was particularly important for the health of the operators as the algae bloom in the pond was mildly toxic.

After several days testing it was noted that adjustment of the eccentric bushings on the heave slide would loosen, creating a judder in the slide motion. The movement of the eccentric bushings was traced to vibrational loading during transit. It was found that if the heave slide was not in direct contact with both transit stops before driving to and from the test site, the vibration loading during the trip forced the eccentric bushings to move to allow the heave slide to rest on both stops. Simply re-adjusting the eccentric bushings returned the slides to smooth operation with a minimum of play.

7.6.6 Collected Data

Table 6 summarises the range of experiments completed using the radial wave generator and data capture systems. The raw, unprocessed data has been included as Digital Appendix 4. Note that not all of the data had been analysed at the time of writing due to project time constraints.

7.6.7 Review of the Testing procedure

Overall the testing procedure was successful and provided a significant amount of useful data. That noted several improvements to the testing procedure and gathered data could be made.

ID	Body	Amplitude of Heave Motion (mm)	Amplitude of Surge Motion (mm)	Surge Phase Lead (°)	Body Oscillation Speeds (rad/s)
1	Sphere	159	0	N/A	1.4 – 7.8
2	Sphere	159	107	0	1.4 - 5
4	Sphere	159	120	0	1.4 - 5
5	Sphere	159	133	0	1.4 - 5
6	Sphere	159	146	0	1.4 - 5
7	Sphere	159	159	0	1.4 - 5
8	Sphere	146	159	0	1.4 - 5
9	Sphere	133	159	0	1.4 - 5
10	Sphere	120	159	0	1.4 - 5
11	Sphere	107	159	0	1.4 - 5
12	Sphere	0	159	N/A	1.4 - 5
13	Plate	0	107	N/A	1.4 - 5
14	Plate	0	133	N/A	1.4 - 5
15	Plate	0	159	N/A	1.4 – 4.25
16	Plate	0	185	N/A	1.4 – 4.25
17	Sphere	107	0	N/A	0.9 – 6.6
18	Sphere	133	0	N/A	0.9 – 6.6
19	Sphere	159	0	N/A	0.9 – 6.6
20	Sphere	185	0	N/A	0.9 – 6.6
21	Sphere	133	133	90	0.9 – 4.7
22	Sphere	159	159	90	0.9 – 3.9
23	Cylinder	133	0	N/A	0.9 – 7.5
24	Cylinder	159	0	N/A	0.9 – 6.6
25	Cylinder	185	0	N/A	0.9 – 6.6
26	Plate	0	107	N/A	0.9 – 5.7
27	Plate	0	133	N/A	0.9 – 5.7
28	Sphere	107	0	N/A	0.9 – 6.6
29	Sphere	133	0	N/A	0.9 – 8.4
30	Sphere	159	0	N/A	0.9 – 7.5
31	Sphere	0	107	N/A	0.9 – 4.7
32	Sphere	0	159	N/A	0.9 – 4.7

Table 6: Experiments completed with the Radial Wave Generator

Further data could be collected to monitor the effects from further variables. Three individual sources have been identified: water depth, water temperature and accelerations from the radial wave generator.

One of the issues noted in the post processing of data is that there was no independent measurement of water depth. Measuring changes in the water depth outside the wave field would have identified any sledging effects (changes in still water level) caused by uneven water flow into or out of the testing basin.

The pressure sensors have a minimum operating temperature 10°C. It is possible that the water temperature could drop below this level decreasing, the accuracy of the sensor. The measurement of water temperature was not included in the original testing schedule. Post experimental measurement has shown that the water temperature is not likely to have dropped below 10°C on the testing days. To limit the exposure of the tests to further error, the water temperature should be measured before commencement of testing and after testing is completed.

One of the conclusions made during the data analysis (See Section 8.7) is that the stability of the radial wave generator limited the oscillating speed for surging objects. If an accelerometer were attached to the radial wave generator and monitored, it would be possible to identify any relationship between movement of the radial wave generator and any additional error in the the match of theoretical circular waves to measured radiated waves.

7.6.7.2 Depth of Sensors

It was also noted that the pressure sensors at the outer edges of the test area were placed at the same depth as the sensors closer to the body, despite a significantly smaller surface displacement. If the outer most sensors were placed closer to the free surface there would be less depth attenuation which would allow smaller wave heights to be detected with greater accuracy.

7.7 Summary of the Radial Wave Generator

The mobile radial wave generator described in this chapter is a unique piece of equipment developed as part of this study. The ability to move a body at different amplitudes in two degrees of freedom, with the same oscillation speeds, allows the waves radiated by different bodies to be studied in a controlled and repeatable manner. Along side the radial wave generator, a low cost pressure sensor was designed for the application of wave height measurement.

Overall, the performance of the radial wave generator and data capture system was remarkably good and it generated a significant amount of data. The collected data is unique in that it explores a range of oscillating body motions and captures the various wave forms radiated by the body. The processing and analysis of the data is documented in the following chapter.

8 Matching Experimental Data

To answer the question "Do the theoretical circular waves match the waves radiated by physical bodies?" experimental test data must be matched to the theoretical models of the circular waves. In this chapter, the data captured using the equipment and processes outlined in Chapter 7 are post-processed and matched to circular waves. The results for each body are then examined, compared and contrasted.

Various tools were developed for the review and analysis of the recorded data sets. These tools include the creation of a data analysis panel that captures a significant amount of information on a single diagram.

8.1 Post-processing and Data Matching

The post-processing and data matching were accomplished using custom written MATLAB programs. Figure 42 provides a summary of the procedure and identifies the custom files generated for these calculations. These files are available in Digital Appendix 3.

The main data processing file begins by defining the physical constants and variables used throughout the calculations. Gravity is assumed to be $9.81 ms^{-2}$, the density of water to be 1000 Kgm^{-3} and the depth of The Groynes testing basin 1.07m. The scope of the calculation is also set by defining which files are to be loaded, which series of matches are trialled and which visual aids are output.

8.1.1 Importing Data and DC Correction

There are three sets of data required to complete the calculations: sensor position data, zero reading data and wave data. The zero reading data and wave data were acquired by the DAQ which sampled 32 channels at 200Hz. The 32 channels consisted of 2 accelerometers and up to 30 pressure sensors (see Section 7.6.4).

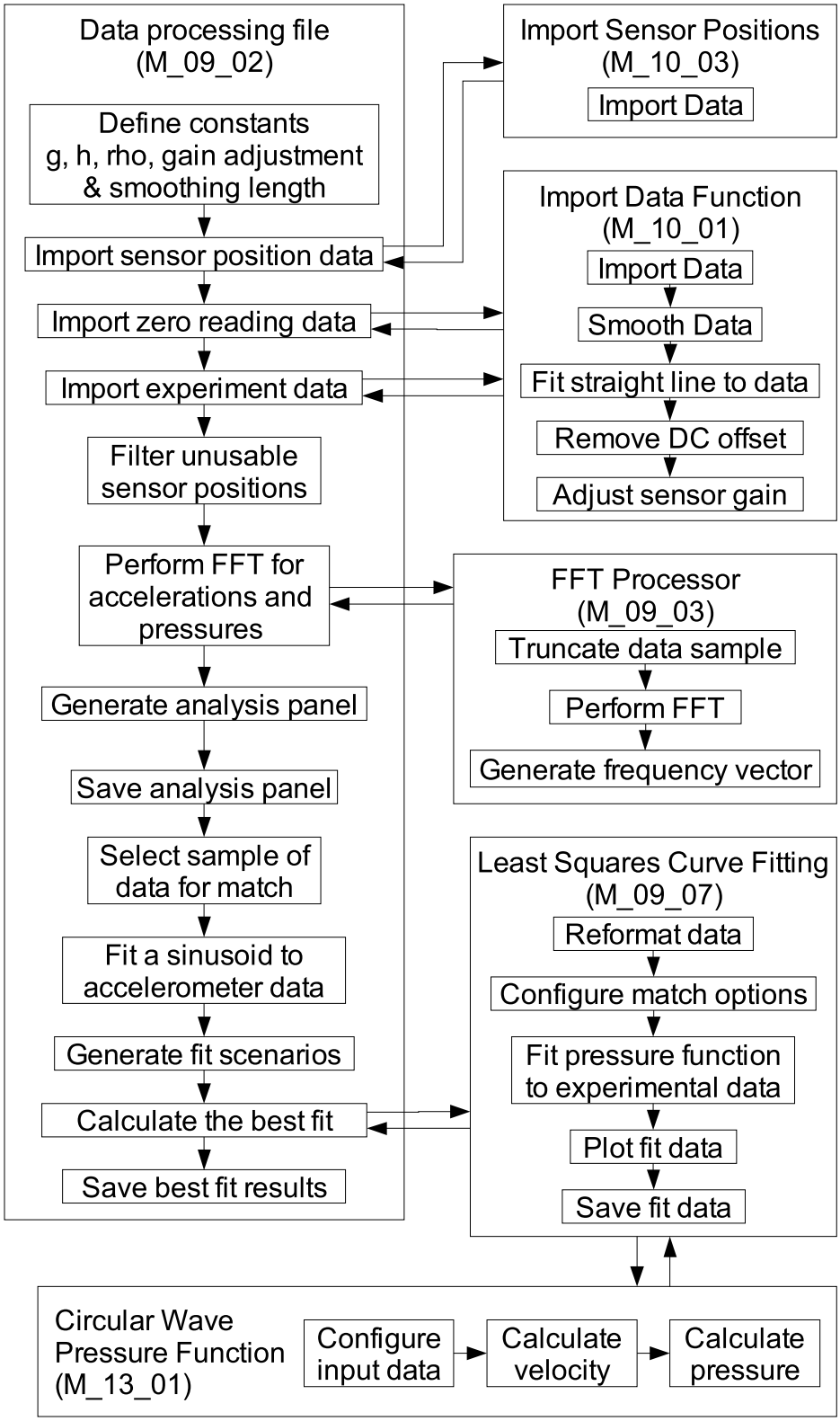

Figure 42: MATLAB Procedure for post-processing Pressure Data and Determining Matches to Circular Waves

(1) See Section 8.1.2

The sensor position data is critically important to the measurement of wave forms. Without the locations of the sensors the collected data is meaningless. The sensor positions were calculated from the position data recorded on each day of testing (see Section 7.6.2). The spreadsheet used to calculate the values was saved to a text file so that it could be imported into MATLAB.

The sensor position data also contained flags for excluding sensors from the calculations. It was found that on certain days there were valid reasons for excluding specific sensors from the matching calculations. A particular sensor stand falling over at some point during testing or nonsensical sensor locating coordinates are examples of grounds for sensor exclusion.

The two sets of pressure readings (i.e. the zero reading data and the wave data) were imported and processed in the same manner. Importing included reading the data from the text file, filtering the data to remove noise and removing linear offset and drift components from the data.

The noise reduction filtering involved applying the MATLAB *smooth* function. The amount of the filtering provided by *smooth* depends on the specified sample length. A sample length was selected that maximised the noise reduction without attenuating the signal significantly. Trial and error determined that a sample length of 51 samples (equivalent to a sample period of 0.25 seconds) was optimal. The *smooth* function was preferred to using standard low pass filters because *smooth* conserved the phasing relationships of different frequency components within the signal.

The linear offset and drift were also removed by the import function. The zero offset applied by the LabVIEW program depended on the DC value of the readings at the moment zero button was pressed. The zero could drift over time if, for instance, the height of the still water level in the basin changes, or the sensors change temperature slightly with the variation in sunlight during a group of tests. For this reason the pressure data was matched to a line with the equation $a\,t+b$ (where t is time) using a least-squares fit and this line was then subtracted from the data. This also had the effect of removing the DC component of the signal.

The importing and post processing was completed by scaling the pressure signals by the appropriate gain factors to turn the voltage reading into a pressure reading. As the gain applied by the LabVIEW program was always 10,000 and the Pascal per Volt conversion factor of the sensor is 1,000, the gain adjustment factor was 0.1.

8.1.2 Data Analysis Panel

Once all of the data had been imported and filtered, the next step was to create an analysis panel. The analysis panel consisted of 7 graphs and summarised a variety of information in a single figure. Figure 43 shows an example of the analysis panel for a surging sphere.

Starting at the top left of the figure, the graph showing the Accelerometer Sensor Output shows the offset corrected and smoothed data for the accelerometers. Each line represents one of the two axes of motion. This plot allows the examination of any anomalies within the signal and can also be used to determine how sinusoidal the wave form is.

The graph below the Accelerometer Sensor Output is the Fast Fourier Transform (FFT) of the accelerometer signals and indicates the position of the peak frequency of motion and any significant sub-harmonics within the motion.

The last graph on the left hand side of the panel is the FFT for all of the pressure sensors. The graph gives a significant amount of information about the radiated wave. In the example used, the graph shows the fundamental frequency peak as well as several sub-harmonics and a low frequency component. The fundamental frequency peak is shown to line up with the peak accelerometer signal. The sub-harmonics then occur at multiples of the fundamental.

Another key element that can be seen from the FFT graph of the pressure signals is which mode may be present in the signals. Fig 43 indicates two areas at the base of the harmonic peaks. The first area is noted as “harmonic with nodal line”. Within the area it can be seen that a number of the signals have a significantly lower maximum value

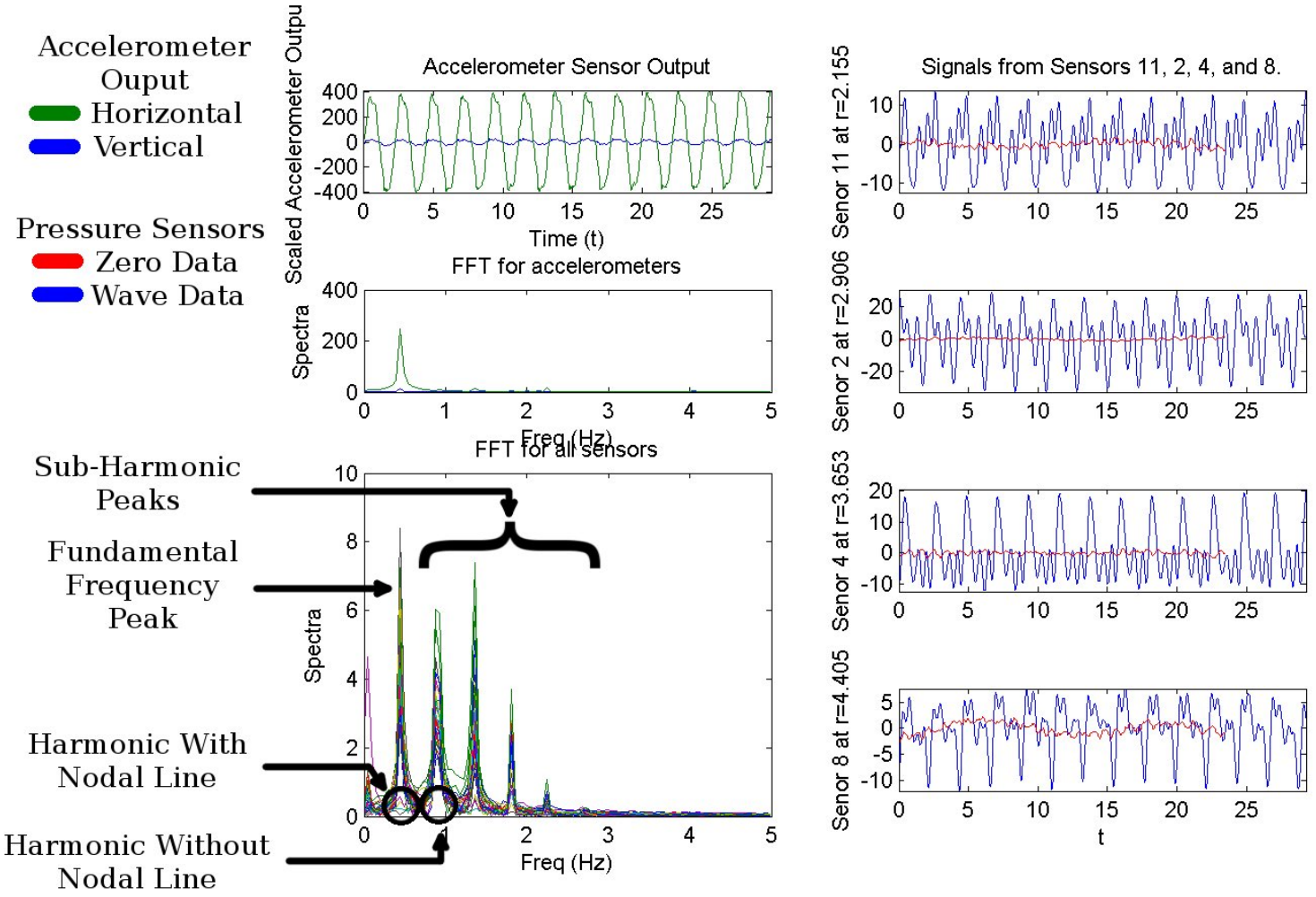

Figure 43: An Example of the Analysis Panel for a Surging Sphere

at that harmonic when compared with the signals at the same harmonic. These low lines represent points of little or no surface displacement. Such points were attributed to the nodal lines identified in circular wave theory and occurred when the order of the Hankel function was greater than zero (see Section 6.1.2).

In contrast, the second area noted in Fig 43 is “harmonic without nodal line”. In this area there are no pressure signals without a significant spectral peak. Hence, all of the sensors see a similar displacement. The lack of sensors with little or no surface displacement suggests that a component of the signal is a zeroth order circular wave or heave wave.

The remaining plots show a sample of the zero reading data and the pressure data from four sensors at different radii. These graphs offer a quick method of checking the signal quality and shape of the detected pressure fluctuations. The signal to noise ratio can be evaluated and considered in the subsequent matching process. These plots are also useful for spotting other data errors such as non-continuous time domains.

8.1.3 The Fitting Process

The fitting process began by selecting a pressure data set to match circular waves to. A sample size of 3,500 samples was used providing the recorded data set was sufficiently long. The sample was taken from the centre of the imported data to minimise any end effects from the testing procedure. The sample size was chosen as it represents a 17.5 seconds of testing time and a minimum of 2.5 periods of the longest wave period.

The matching process used the MATLAB function *LSQCURVEFIT*. This function minimises the least squares error of a model compared to a given set of data. The calculation method is non-linear and can be configured to match any number of input variables. *LSQCURVEFIT* also allows the specification of an initial guess and the upper and lower bounds for each calculation.

The goal of these fits was to determine whether or not the theoretical circular waves could be matched to the recorded pressure data. For this, it was decided that a wide

range of circular waves, including different orders (m) and wave numbers (k), should be used as candidates. The calculation times for the fit depend heavily on the number of circular waves being fitted to the data. The calculation time grows exponentially with the increase in the number of waves. For this reason the circular waves were organised into groups. Each group, or trial, consisted of up to six different circular waves.

Each circular wave in the trial was defined by the order of its Hankel function and harmonic of fundamental oscillation frequency. Tables Error: Reference source not found and 8 show the two starting trials that were used to identify likely candidates for further examinations. The fitting process adjusts the theoretical match by iterating the wave number (k), the amplitude of the circular wave (B) and the phase of the circular wave (β).

Circular Wave ID	Hankel Function Order (m)	Associated Motion	Harmonic
1	0	Heave	1st
2	1	Surge	1st
3	2	N/A	1st
4	0	Heave	2nd
5	1	Surge	2nd
6	2	N/A	2nd

Table 7: First Standard Trial for Data Fitting

Circular Wave ID	Hankel Function Order (m)	Associated Motion	Harmonic
1	0	Heave	3rd
2	1	Surge	3rd
3	2	N/A	3rd
4	3	N/A	1st
5	3	N/A	2nd
6	3	N/A	3rd

Table 8: Second Standard Trial for Data Fitting

The solution space for an accurate fit of theoretical functions to the pressure readings is complicated. If a trial consists of six circular waves, each wave having three variables, there are a total of 18 variables to be optimised. This means that there are multiple local minima that the matching algorithm may focus on. The initial guess values and limit bounds needed to be a realistic starting point for each computation to avoid falling into poorly fitting error minima.

An estimation of the wave number for the fundamental harmonic was obtained by matching a sinusoid to the accelerometer signal and using the resulting phase velocity to compute a wave number. The wave numbers for the higher harmonics were estimated based on multiples of the phase velocity fitted to the acceleration signal.

Trial and error indicated that an initial amplitude guess of 0.05m usually provided repeatable results, while the phasing initial value was always 0. In the case of the largest measured signals, those from a quickly heaving sphere, an initial amplitude guess of 0.1m or 0.2m was required due to the size of the wave being modelled.

The trial and error approach of initial variable selection was not the most robust method for guaranteeing that the matching algorithm returned the most accurate result. However this approach was quick to implement and suited the goal of assessing whether or not circular waves were a good model. A more in-depth study could be performed using Monte Carlo selections, genetic algorithms or solution mapping techniques to identify the best possible fits based upon a range of input variables. This project is likely to require a considerable amount of computing power to map the complicated solution space.

Once the best fit based on the least-squares method had been calculated, the result was saved to a file for inspection and analysis. An iterative process was applied to determine the simplest model for the radiated waves. The first step was to match the two trials indicated by Tables Error: Reference source not found and 8 to the experimental data from a single test. The composition of the third trial was composed of those waves which contributed more than 1% of the total radiated power from the

first two trials. Each successive trial then simply removed any wave contributing less than 1% to the radiated power, providing an acceptable match was made.

It was noted that some of the trials produced invalid results by returning matches with wave numbers that varied significantly from the initial guess. This wave number drift occurred more frequently in the data sets with low signal to noise ratios and, in the noisiest cases, resulted in poor overall matches. In the cases where the signal to noise ratio was acceptable the trials were recalculated with an alternative initial amplitude guess. This set the least-squares algorithm closer to alternative minimum error solutions within the solution space and often resulted in a significantly better fit.

During the development of this process ,low frequency oscillations in water height of the lake and evanescent waves were also assessed as potential factors that may improve the matches between models and experimental data. Neither were found to have a significant effect on the overall result.

Note that the evanescent waves were represented by Bessel functions of the fourth kind ($K_m^n(kr)$) which describe a surface wave that oscillates between $\pm\infty$ when $r=0$ and has a value of 0 at $r=\infty$. This means that the evanescent waves only affect the wave field close to the body. Therefore, the decision to place the pressure sensors at half a wavelength's distance or more from the body means that evanescent waves are unlikely to be a significant component of the recorded signals.

8.2 Data Fitting for a Heaving Sphere

The heaving sphere generated the largest waves out of all of the bodies tested. This has allowed the heaving sphere to be examined closely and offers the most insight into whether or not circular wave theory can be used to model the waves radiated from oscillating bodies.

8.2.1 Analysis of Heaving Sphere Data

This section records various observations about the heaving sphere data and notes the influence of key factors on the correlation between the measured waves and the mathematical models of circular waves.

8.2.1.1 Accelerometer Signals for the Heaving Sphere

There are two factors that provide information on the motion of the sphere. The match of the accelerometer signals to sinusoidal functions describes how effective the radial wave generator was at achieving sinusoidal motion while the fast Fourier transform of the accelerometer signals has the potential to identify any major harmonics introduced into the body's motion.

Figure 44 shows the plot of the coefficient of determination (R^2) for a number of different experiments. Each experiment is denoted by 2 terms: H denotes the amplitude of oscillation in millimetres and En indicates the encoder position. An En value of 1 represents the encoder being attached to the crank of the radial wave generator and a value of 2 represents the encoder being attached to the drive axle of the radial wave generator. The quality of the matches of the acceleration to sinusoidal functions, as indicated by R^2, show two features: An improvement of the fit as the frequency of oscillation increases and a decline of the fit as the amplitude of oscillation increases.

The improvement of fit as oscillation speed increases reflects both the low resolution of the accelerometer and the increased signal to noise ratio at higher speeds. At the slowest oscillation speed the accelerations had an amplitude of approximately 0.058g and the accelerometer had a theoretical output amplitude of just 3.3mV. The low signal makes the measurement prone to noise. One source of noise is vibration caused by the movement of the bearings along the guides. As the guides are not perfect and are contaminated by grit and dust, there are small fluctuations in the acceleration as the bearings interact with these variations. At slower speeds these fluctuations result in a less accurate fit to the sinusoidal curve.

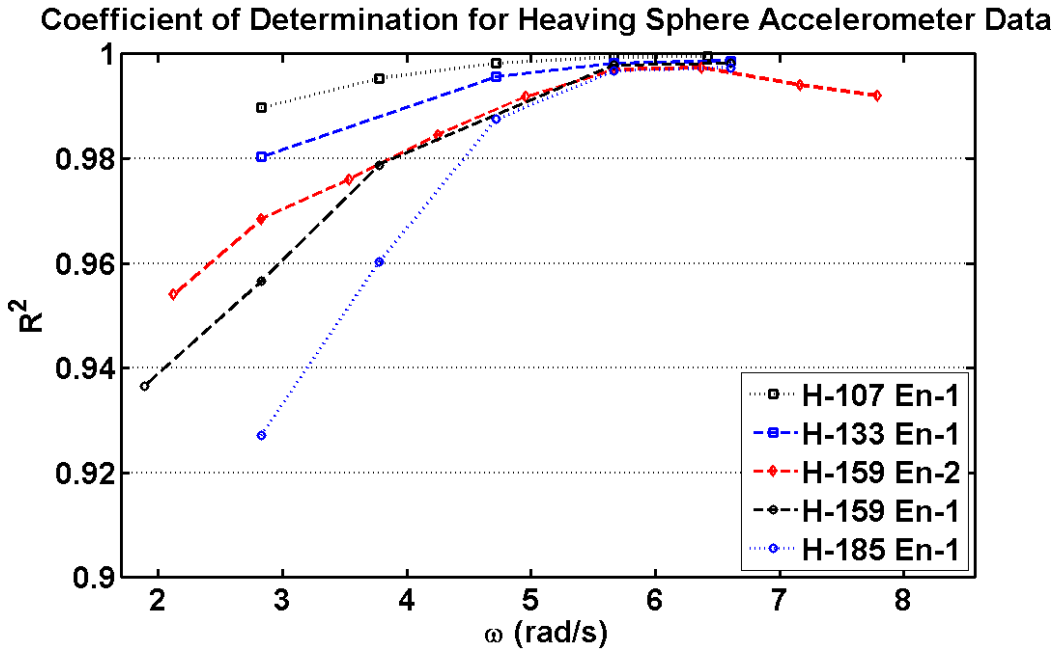

Figure 44: Coefficient of Determination for Sinusoidal Curves Fitted to Accelerometer Data Recorded During a Heaving Sphere Experiment

The decline in the fit seen with increased amplitude of motion is associated with the additional forces required to move the body. The feedback control loop needs a greater error signal to compensate for the larger forces which means that the speed of the crank will deviate from constant to a greater extent than in the low amplitude cases. This deviation from constant crank speed is greater with larger amplitudes of motion and so the fit is less accurate. Overall the accuracy of the fits for the acceleration signal to sinusoidal is acceptable. The average R^2 value of 0.98 shows a strong correlation.

8.2.1.2 Harmonics of the Radiated Waves for a Heaving Sphere

One of the key aspects to note about the waves radiated from a heaving sphere is that the waves are not monochromatic. The Fourier transform plot generated for each test clearly shows harmonic components of the waves. Figure 45 shows the peak values of the FFT for the various harmonic components for a series of tests.

The cause of the harmonic waves is not fully understood. There are small spectral peaks at the third harmonic in the FFT of the acceleration signal. These peaks are likely to be related to the third harmonic change in displaced volume calculated when a

half submerged sphere is moved through a sinusoidal motion (See Appendix 9). However, this does not account for the significance of the second harmonic peaks in Fig 45. Note that the third harmonic peaks in the acceleration become significantly less prominent as the frequency of oscillation increases.

Fig 45 shows a clear variation in the amount of harmonic content depending upon the frequency of oscillation. The spectral peaks of the second harmonics increase until they reach a maximum at 4.2 rad/s. After this point all harmonic components of the radiated wave reduce in spectral amplitude. This suggests that the mechanism for generating the harmonics is limited in some manner. Observation of the video data recorded during the experiments suggest that the maximum harmonic content occurs just before wave breaking effect begins to dominate the wave field. Further study into the onset of wave breaking and any associated effects on harmonic content would be required before further conclusions could be drawn.

The higher harmonics of the radiated waves at higher oscillation speed have wavelength too short to be considered gravity waves. These waves fall into the transition area between gravity waves and capillary waves (See Section 4). The key

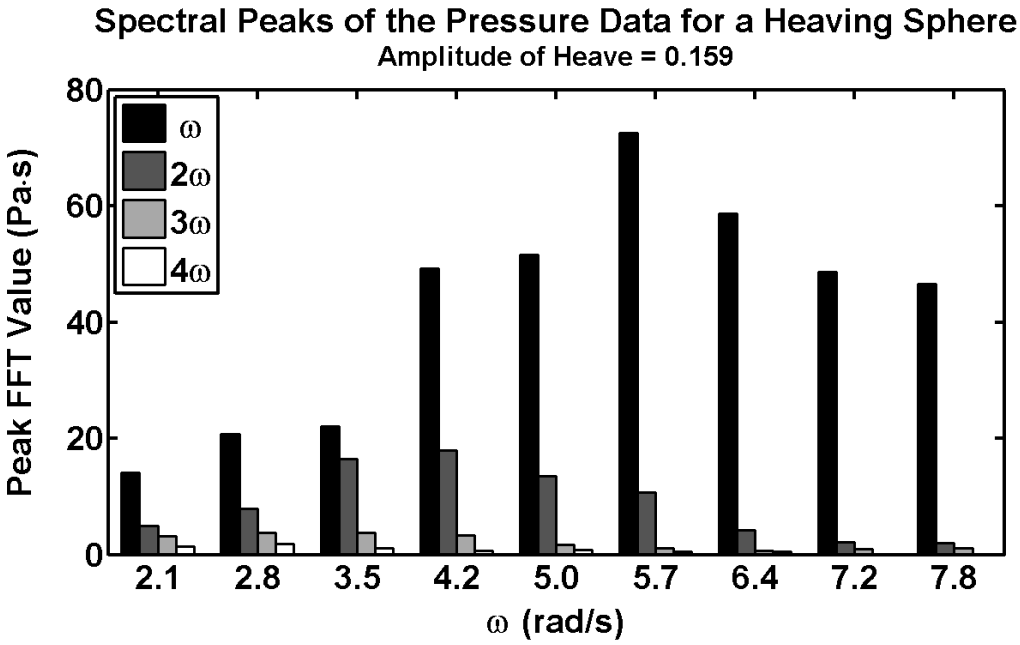

Figure 45: Spectral Peaks of the Subsurface Pressure Data Recorded During the Generation of a Surface Wave by a Heaving Sphere

difference between the two types of waves is in the dominant restoring force: gravity for gravity waves, and surface tension for capillary waves. Table 9 illustrates the transitional zone by highlighting the values that are beyond the testing range recommended by Falnes.

The exact properties of these transition waves was beyond the scope of this study and may or may not account for the attenuation of higher harmonics at higher oscillation speeds. Further investigation would be required to establish the effects of attempting to radiate such short waves.

Using the method described in Section 8.1.2 examination of the area beneath the spectral peaks of the FFT of the pressure signals suggests that all of the sensors are peaking to a similar extent and that there are no nodal lines close to any of the sensors. Hence, it would be expected that the matched waves would be predominately heave type waves.

The harmonic content of the wave is important to understand as waves radiated at harmonics of the body motion do not interact with incident wave. As noted in Section 6.7 the waves radiated by a PAWEC should be of the same frequency as the incident wave to maximise the PAWEC performance. Waves that are not at the fundamental

	Harmonic Phase Velocity (rad/s)			
ω (rad/s)	1st	2nd	3rd	4th
2.13	2.13	4.26	6.39	8.52
2.83	2.83	5.66	8.49	11.32
3.54	3.54	7.08	10.62	15.16
4.25	4.25	8.50	12.75	17.00
4.96	4.96	9.92	14.88	19.84
5.67	5.67	11.34	17.01	22.68
6.37	6.37	12.74	19.11	25.48
7.17	7.17	14.34	21.51	28.68
7.79	7.79	15.58	23.37	31.16

Table 9: Harmonic phase velocities for the heaving sphere experiment highlighting values beyond Falnes' recommended testing range

wave frequency have no effect on the time-averaged power and hence cannot be used for power absorption. This means that any waves radiated at harmonics of the oscillation speed are effectively system losses.

8.2.1.3 Analysis of the Wave Forms

The recorded data shows significant variation in the wave shape depending on the radial position of the sensor.

8.2.1.4 Signal to Noise Ratio

A major source of noise in the experimental data was pressure fluctuations caused by wind generated surface ripples. This was dependent on the amount of wind, and changed from experiment to experiment. The zero readings taken at the start of each set of experiments indicate the amount of signal variation caused by the surface ripples. The ripples can be detected in the signal plots as high frequency variations. A low pass filter could be used to remove these fluctuations although the application of such a filter would risk degrading any higher harmonic information present in the data.

The slowest test speeds produced the smallest waves which were therefore the most vulnerable to noise. The signal to noise ratio can be as low as 1:1 although this was an extreme case with the sphere moving slowly with a small amplitude and with light wind waves across the surface. Noise of this level interfered with the matching process, causing poor fits ($R^2 \ll 0.9$) for the pressure data. These poor fits have been excluded from the presented data.

As the frequency of oscillation increases the amplitudes of the radiated waves also increase and so too does the signal to noise ratio. A signal to noise ratio of at least 8:1 was required to provide good matching results.

8.2.1.5 Other Signal Noise

During the experiments two other forms of noise were noticed: zero offset drift and low frequency ($T \geq 10\text{s}$) oscillation.

Zero offset drift occurred in a number of tests. This drift could have had a range of sources including a variation in the voltage supplied from the battery, change in temperature of the reference pressure due to variations in water temperature, direct solar heating or leakage from the reference pressure volume into the reference tube.

The low frequency oscillation witnessed in some experiments occurred across all of the sensors. This suggests that the still water level of the whole wave field varied. This could have been due to changes in the flow into and out of the testing basin. Another possible explanation is a seiche, possible generated by the wind. Due to the lack of an independent water level sensor this hypothesis cannot be confirmed.

8.2.1.6 Limitations on the Accuracy of the Representation of a Sphere

One source of error that is unique to the sphere is that the sphere may not be completely spherical. As the body was created based on a hand-cut polystyrene shape it is possible that irregularities on the body may add a small amount of bias to the radiated waves. The scale of this error is hard to quantify and would require measuring the spherical body accurately to determine the degree of variation.

8.2.2 Results for a Heaving Sphere

The mathematical models of the circular waves were fitted to the recorded waves of a sphere heaving with an amplitude of 159mm. The resulting wave amplitudes and coefficient of determination are recorded in Table 10. A comparison of the pressure signal data with the signal predicted by circular wave theory is shown in Fig 46. The example examines a typical fit at four pressure sensors at different r and θ coordinates.

The first point of note is that the coefficients of determination show a strong correlation between the recorded data and the matched models. The mathematical models do not match the measured data perfectly. However, given all of the practical variability involved with measuring the waves, the limitations on creating sinusoidal motion and the assumptions inherent in linear theory, it is significant that the matches are as close as they are.

The second point of note is that the predominant wave form radiated by a heaving sphere is the zeroth order circular wave. The significance of the zeroth order circular

		1st Harmonic Amplitude (mm)				2nd Harmonic Amplitude (mm)				3rd Harmonic Amplitude (mm)			
ω (rad/s)	R^2	*m*=0	*m*=1	*m*=2	*m*=3	*m*=0	*m*=1	*m*=2	*m*=3	*m*=0	*m*=1	*m*=2	*m*=3
2.13	0.951	3	-	-	-	2	-	-	-	3	-	-	-
2.83	0.968	6	-	-	-	7	-	-	-	5	-	-	-
3.54	0.956	12	-	-	-	17	-	-	-	-	-	-	-
4.25	0.957	21	-	-	-	26	-	-	-	-	-	-	-
4.96	0.953	33	-	-	-	31	-	-	-	-	-	-	-
5.67	0.957	45	-	-	-	28	-	-	-	8	-	-	-
6.37	0.954	56	9	-	-	29	-	-	-	38	-	-	-
7.17	0.952	58	10	10	10	-	-	-	-	-	-	-	-
7.79	0.924	61	-	-	16	-	-	-	-	77	-	-	-

Table 10: Best Fit Wave Amplitudes for a Sphere Heaving with an Amplitude of 159mm

wave in the matches supports the intuitive assumption made in Section 6.1.2 that the zeroth order circular wave represents a wave radiated by heaving body.

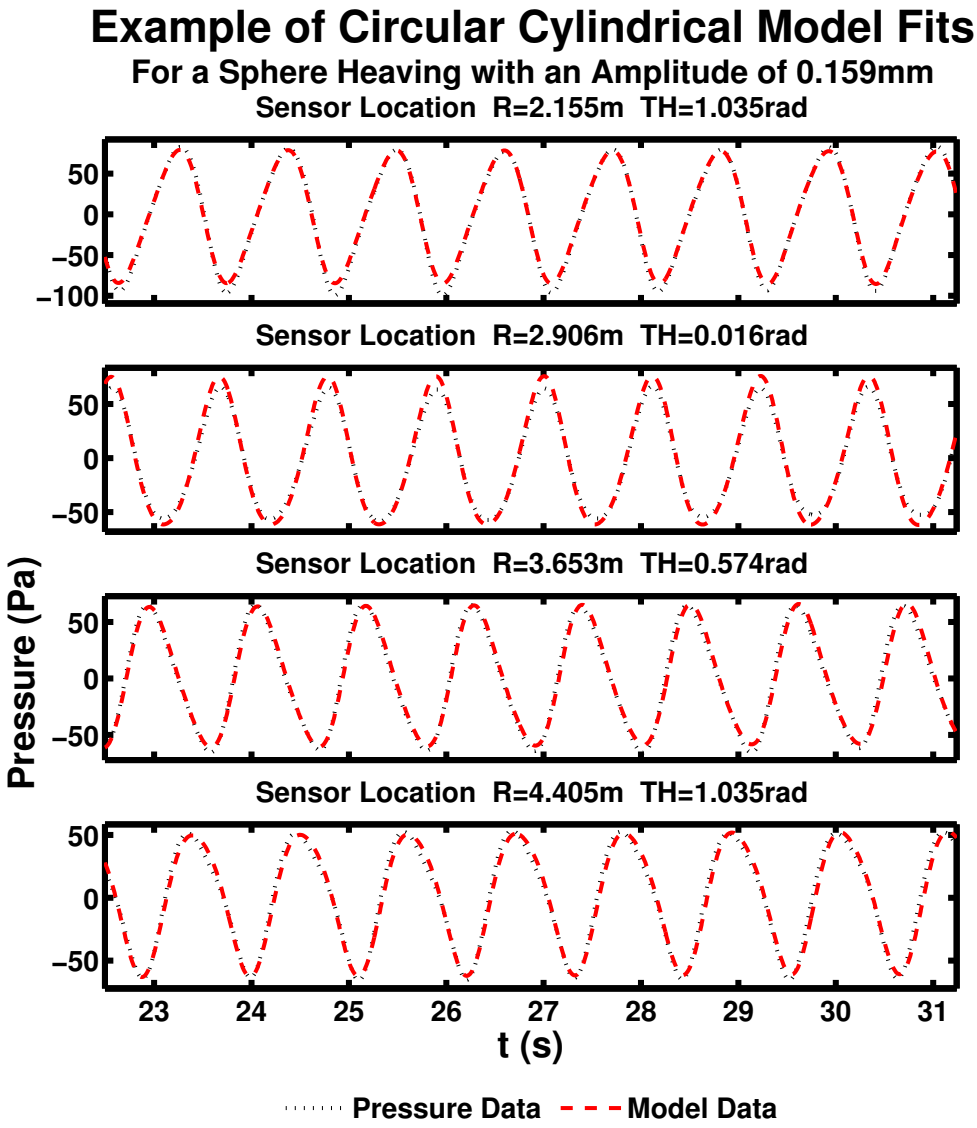

Figure 46: A Comparison of the Recorded Pressure Data with a Best Fit Circular Wave Theory Model for a Heaving Sphere Experiment

Figure 47 displays the total amount of radiated power as well as the amount of power radiated in each harmonic. The figure shows that the first harmonic contains a significant proportion of the radiated power. Combining this with the data in Table 10 allows the conclusion that the zeroth order circular wave is the dominant form in which power is radiated from a heaving sphere.

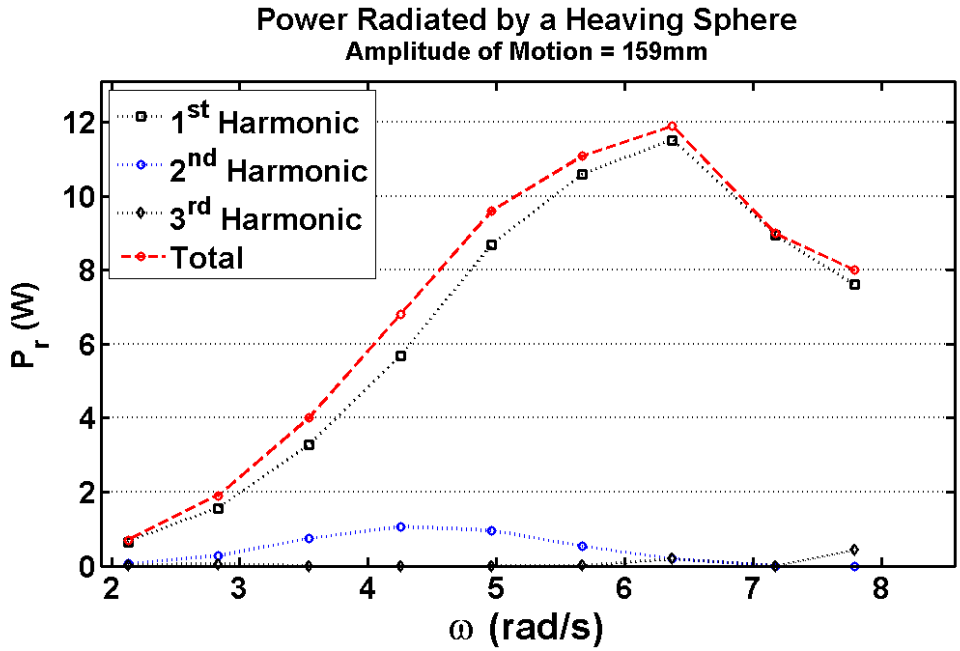

Figure 47: Power Radiated by a Heaving Sphere

The experimental conditions at which the maximum power is radiated can be compared to peak period of a spectral ocean to determine an approximate scaling factor. In the case of the heaving sphere, the peak power was radiated at a frequency of 6.4 rad/s which equates to a wavelength of 1.52m. If it is assumed that the wave at the spectral peak of ocean wave spectrum is an 8 second, 100m long wave then the scaling factor is approximately $\frac{1}{66}$. The scaling factor can be used to estimate the amount of power radiated from a 33 meter diameter sphere heaving with an amplitude of 10.5m. Utilising the scaled power relationship in Section 2.1.2 the predicted maximum radiated power is 26 megawatts. This assumes that frictional and non-linear effects scale linearly, which is often not the case.

The first harmonic, zeroth order circular wave that would, in theory, be radiated from the 33m sphere would have an amplitude of 3.7 meters. Using the Eqns 185 and 186 it is possible to predict that the optimum power absorption occurs when the incident wave has an amplitude of 7.4m and absorbs 26MW. This illustrates two points. First is that, at optimum absorption conditions, a WEC can only absorb as much energy as it can radiate. Hence a good wave absorber must be a good radiator. The second is that

the amplitude of motion of the sphere is greater than the wave amplitude at optimum absorption (see Section 5.4.1.11).

8.2.3 A Note on Repeatability

As there is a considerable amount of variation in the configuration of the radial wave generator and the matching process of the signals, it is important to establish that the results are repeatable. Fig 48 shows the results for the power radiated from a heaving sphere for two distinct experiments. The first set of data (Trial 1) was presented in Section 8.2.2. The second set of data (Trial 2) was recorded on another day, which means that the sensor array configuration is different and that the radial wave generator has been completely re-installed. This shows that the method of gathering data and matching the data to circular waves can produce repeatable results.

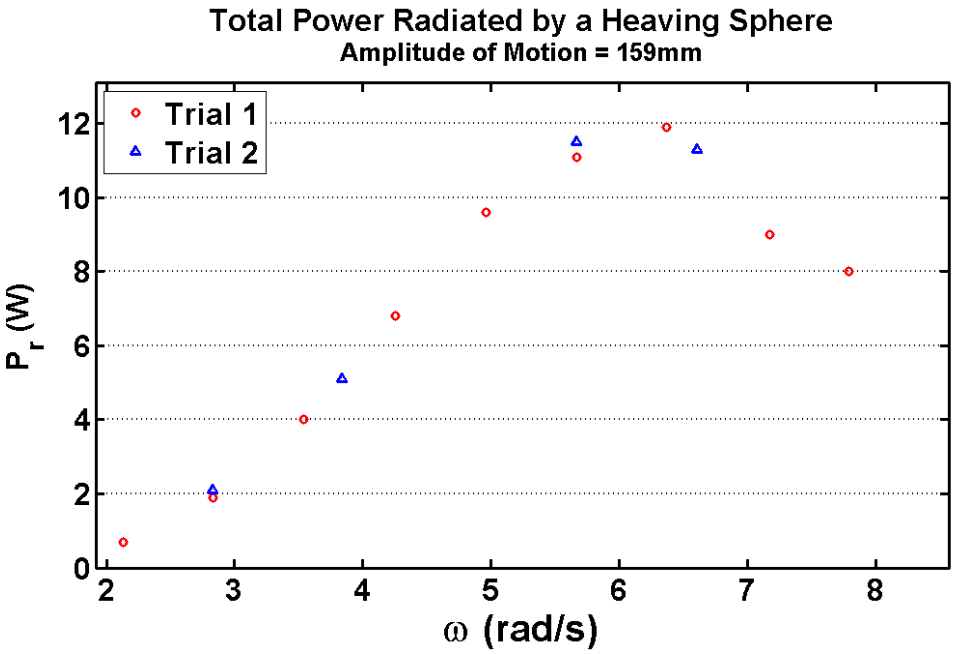

Figure 48: Repeated Measurements of the Power Radiated from a Heaving Sphere

8.2.4 Conclusions for a Heaving Sphere

Several conclusions can be drawn about the experimental testing and matching of circular waves for the case of the heaving sphere.

1. The radial wave generator provided a sinusoidal heave motion. The coefficient of determination for sinusoidal matches to the acceleration signal showed that the acceleration signal was largely sinusoidal.

2. The waves radiated from a heaving sphere have a range of harmonic components.

3. The fundamental harmonic component of the radiated wave accounts for most of the radiated power.

4. The mathematical model of circular waves provides a good model for the recorded pressure data.

5. The dominant wave form radiated from a heaving sphere is a zeroth order circular wave.

8.3 Data Fitting for a Surging Sphere

Experimental data was captured for a half-submerged sphere surging with an amplitude of 159mm. The waves radiated by the sphere were of sufficient size to be distinguished from the background noise. The stability of the radial wave generator provided an upper limit to the frequency of oscillation.

8.3.1 Analysis of Surging Sphere Data

This section records various observations about the surging sphere data and notes the influence of key factors on the correlation between the measured waves and the mathematical models of circular waves.

8.3.1.1 Accelerometer Signals for the Surging Sphere

The accelerometer signals were matched to sinusoidal functions in the same manner as for the heaving sphere's motion (See section 8.2.1.1). The Fast Fourier transform of the accelerometer signal generated in the analysis panel were also examined for harmonics etc. The FFT gave no indication of harmonic components in the acceleration signal.

The fitting of sinusoids to the accelerometer signals is excellent across all speeds of oscillation. The smallest coefficient of determination (R^2) is 0.991 while the peak is 0.995.

8.3.1.2 Harmonics of the Radiated Wave for a Surging Sphere

The peak values of the FFT of the pressure signals collected from waves generated by the surging sphere are recorded in Fig 49. The figure shows that there are substantial harmonic components within the wave and that these harmonic components may dominate the features of the radiated wave.

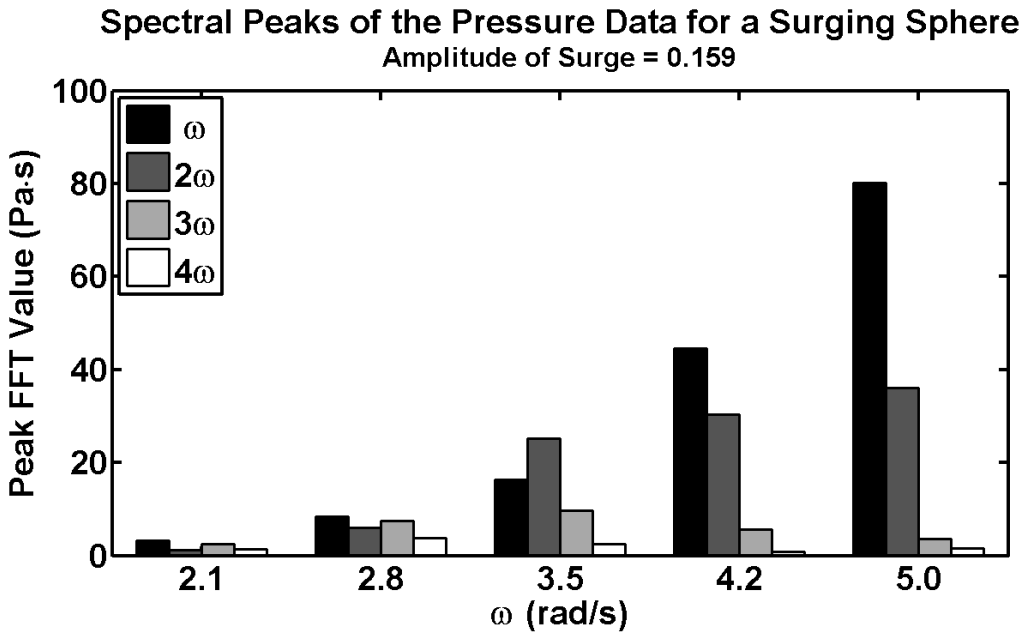

Figure 49: Spectral Peaks of the Subsurface Pressure Data Recorded During the Generation of a Surface Wave by a Surging Sphere

The maximum spectral peak for the surging sphere is of a similar magnitude to the maximum spectral peak for the heaving sphere (see Fig 45). Note also that the maximum peak of the second harmonic for the surging sphere is almost twice the size as that of the heaving sphere, indicating a higher influence of harmonics in the surging case.

Using the method described in Section 8.1.2, examination of the area beneath the spectral peaks of the FFT suggests that the different harmonics will be associated with different orders of circular waves. The first harmonic peaks in all of the tests showed that several of the sensors did not measure any significant waves. This suggests that a nodal line exists in the wave field and that the radiated wave is likely to fit a circular wave with an order greater than 0. This is in contrast to the second harmonic peaks that clearly show an absence of nodal lines and hence a radiated wave that is likely to have a zeroth order circular wave component. The third harmonic also shows the presence of nodal lines while the fourth harmonic is unclear and often lost below the noise limit.

8.3.1.3 Signal to Noise Ratio for a Surging Sphere

The slowest surge speeds produced the smallest waves which were also the most vulnerable to noise. The lowest signal to noise ratio was 2:1. Noise of this level interfered with the matching process, causing poor fits ($R^2 \ll 0.9$) for the pressure data to circular wave models. The peak signal to noise ratio for the surging sphere was 35:1 which is high enough to accurately determine a match.

8.3.2 Results for a Surging Sphere

The mathematical models of the circular waves were fitted to the recorded pressure signals of a half-submerged sphere surging with an amplitude of 159mm. The resulting wave amplitudes and coefficients of determination are recorded in Table 11.

		1st Harmonic Amplitude (mm)				2nd Harmonic Amplitude (mm)				3rd Harmonic Amplitude (mm)			
ω	R^2	*m*=0	*m*=1	*m*=2	*m*=3	*m*=0	*m*=1	*m*=2	*m*=3	*m*=0	*m*=1	*m*=2	*m*=3
2.12	0.741	-	0.9	-	-	0.1	-	0.7	-	-	2.3	-	0.7
2.83	0.850	-	2.9	-	-	2.0	-	6.3	-	-	9.3	-	6.6
3.54	0.913	-	8.5	-	-	12.0	-	23.0	-	-	17.7	-	17.5
4.25	0.922	-	22.5	-	-	33.9	-	55.4	-	-	20.7	-	-
4.96	0.902	-	49.6	-	-	57.0	11.9	71.7	-	-	-	-	-

Table 11: Best Fit Wave Amplitudes for a Half-submerged Sphere Surging with an Amplitude of 159mm

A comparison of the pressure signal data with the signal predicted by circular wave theory is shown in Fig 50. The example examines a typical fit at four pressure sensors at different r and θ coordinates.

The signal to noise ratio limits the lower speed fits as the small pressure signals make matching the waves difficult. Once the signals are significant enough to be read above the noise, the coefficient of correlation (R^2) does become significant. It was noted that matches of significance ($R^2 \geq 0.9$) are more difficult to make for a surging sphere than a heaving sphere, requiring a greater number of iterations and more processing time to compute good fits.

The first harmonic of the radiated wave fit consists entirely of the first order circular wave. This is an important result as it supports the intuitive assumption made in Section 6.1.2 that the first order circular wave represents a wave radiated by a surging body. The second harmonic of the radial wave fit utilises circular waves of the zeroth and second order while the third harmonic consists of first and third order waves. This means that the observations made during the harmonic analysis (Section 8.3.1.2) were correct in regard to the order of circular waves present in each harmonic.

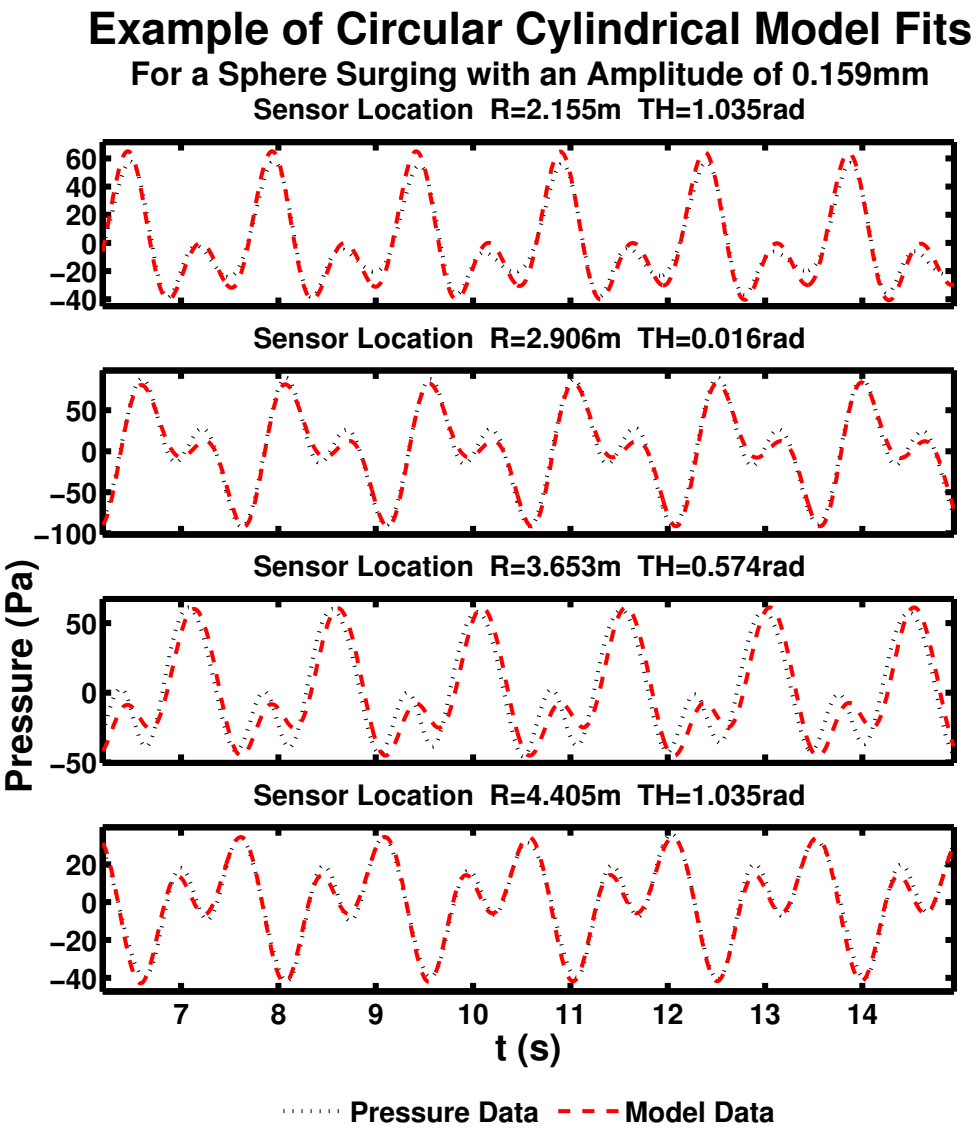

Figure 50: A Comparison of the Recorded Pressure Data with a Best Fit Circular Wave Theory Model for a Surging Sphere

The second harmonic component of the radiated wave may arise from the way in which water accumulates on the face of the sphere as it oscillates back and forth. As the sphere turns around at the end of its motion, the water built up on the leading face of the sphere is no longer supported and can collapse radiating a heave type wave. As this occurs at both ends of the motion, the frequency of the heaving type wave is double the frequency of oscillation.

Figure 51 displays the total amount of power radiated by the surging sphere as well as the amount of power radiated in each harmonic. The Figure shows that the first and second harmonic both contain a significant proportion of the radiated power. Combining this with the data in Table 11 allows the conclusion that the first order circular wave is the dominant form in which power is radiated at the fundamental harmonic. However, at lower speeds the radiated power is concentrated almost equally at the first and second harmonic of the radiated wave.

The experimental data does not contain a peak radiated power as in the case of the heaving sphere. The largest recorded radiated power is used to compare expected performance of the surging sphere at an ocean scale. In the case of the surging sphere, the peak radiated power recorded was at a frequency of 5.0 rad/s which equates to a wavelength of 2.49m. If it is assumed that the wave at the spectral peak of ocean wave spectrum is an 8 second, 100m long wave, then the scaling factor is approximately $\frac{1}{40}$. The scaling factor can be used to estimate the amount of power radiated from a 20 meter diameter sphere heaving with an amplitude of 6.4m. Utilising the scaled power relationship in Section 2.1.2 the predicted maximum radiated power is 6.4MW. Again,

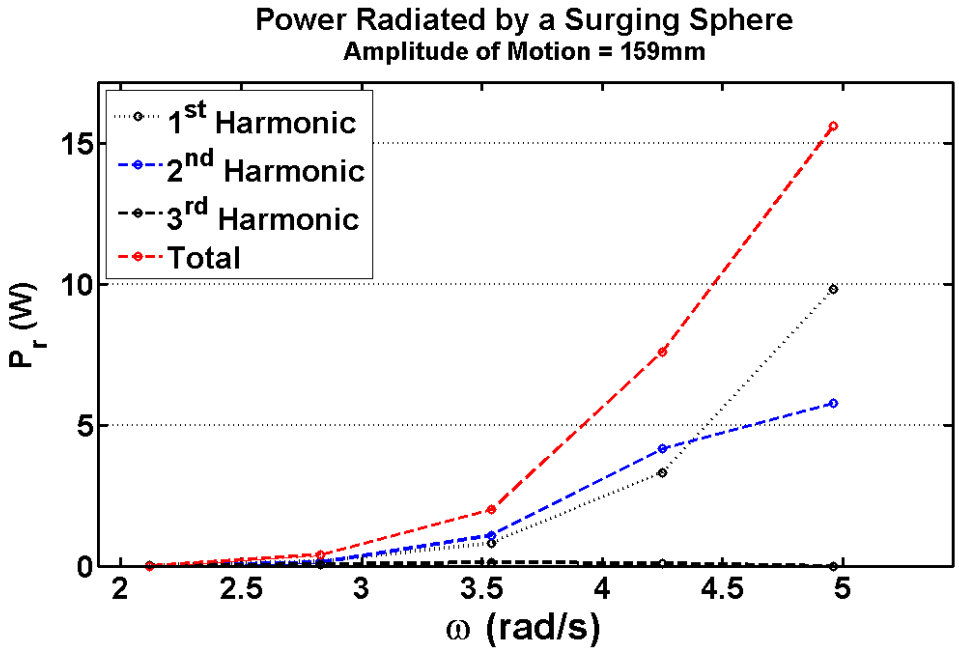

Figure 51: Power Radiated by a Surging Sphere

this has assumed that frictional and non-linear effects scale linearly, which is often not the case.

As the higher harmonic components of the surge wave account for a significant amount of power, they can not be neglected as they were in the case of the heaving sphere. This means that the optimum power absorption conditions have to be applied to several different waves with different phases simultaneously. The solver function in Open Office Calc [87] was used to optimise the incident wave to maximise the absorption length. The result is that the optimum power absorption occurs when the incident wave has an amplitude of 3.2m and absorbs 6.4MW. This illustrates the same two points as for the heaving sphere:namely that at optimum absorption, the amount of energy absorbed is the same as the amount radiated, and that the amplitude of motion of the sphere is greater than the wave amplitude at optimum absorption (see Section 5.4.1.11).

It is interesting to note that the total absorbed power at the optimum absorption conditions is equal to the sum of the radiated power, regardless whether that power is radiated at the fundamental harmonic or not. This may seem to indicate that it therefore does not matter which harmonic the power is radiated at, but this is not the case. The underlying reason is based on the evaluation of the radiated power "at optimum absorption length conditions". If more of the power is radiated at higher harmonics then the optimum absorption length is lower than a scenario where the same amount of power is radiated solely in the fundamental frequency.

8.3.2.1 Band Pass Filter Fits

A further matching experiment was conducted in an attempt to improve the fit of circular waves to the waves radiated by the surging sphere. Band pass filters were applied to the pressure data for one particular test case to isolate each harmonic so that it could be matched separately. The fits obtained for the first and second harmonic had R^2 values greater than 0.97 and involved the same circular wave orders as indicated by Table 11.

The third harmonic proved somewhat more difficult to fit and the coefficient of determination values remained low for any of the point source approximations. One explanation for the reduced accuracy of fit at higher harmonics is that the wave lengths have reduced sufficiently so that the point source approximation is no longer accurate. Table 12 details the wavelengths for the first four harmonics of the surging sphere experiments. These values can be compared to the total movement of the sphere at 0.32m. The second harmonic wavelengths vary from 10 times to 2 times the total surge movement while the third harmonic wavelengths vary from 4.8 times to 0.9 times the total surge movement.

The importance of the relative scales of the harmonic wavelength to the total surge movement can be illustrated using the mechanism of wave generation proposed for the second harmonic. If water building up on the face of the sphere does generate the second harmonic wave, then there are effectively two fundamental harmonic sources: one near the forward end of motion and one near the aft end. If these two point sources are close enough to each other they will appear as a single point source at twice the frequency of fundamental harmonic because of the phasing difference inherent in their creation. However, if the points are separated by a significant distance compared to the wavelength then by the time waves from each source reach the measurement point the phasing relationship has changed, changing the properties of the waves. Hence the wave field is no longer represented by a point source.

The deviation from the point source approximation at higher harmonics will limit the coefficient of determination for the fits of surging axisymmetric bodies. This does not

	Wavelength for Harmonic (m)			
ω (Rad/s)	1st	2nd	3rd	4th
2.12	8.81	3.31	1.52	0.86
2.83	6.14	1.92	0.86	0.48
3.54	4.46	1.23	0.55	0.31
4.25	3.30	0.85	0.38	0.21
4.96	2.48	0.63	0.28	0.16

Table 12: Wavelengths for the Harmonic Components of the Surging Sphere Experiments

occur when examining the wave radiated by a heaving body, as the direction of oscillation of the body is perpendicular to the direction of wave propagation and therefore does not affect affect the point source approximation.

8.3.3 Conclusions for a Surging Sphere

Several conclusions can be drawn about the experimental testing and matching of circular waves for the case of the heaving sphere.

1. The radial wave generator provided a sinusoidal surge motion.

2. At low frequencies the fundamental harmonic and the second harmonic account for similar levels of radiated power.

3. The dominant fundamental frequency wave present in the waves radiated by a sphere is the first order circular wave.

4. The point source approximation is realistic providing the wavelength of the radiated wave is considerably larger than the total displacement undergone by the body.

8.4 Data Fitting for a Cylinder

Four experiments were carried out using the vertical axis cylinder body with the radial wave generator. The first experiment moved the cylinder in surge with an amplitude of 185mm while the remaining three experiments moved the cylinder in heave at amplitudes of 133mm, 159mm and 185mm.

The analysis of the surging experiment did not yield any pressure signals that were distinguishable from the background noise of the testing basin. Review of the video data determined that the wind noise on the day of testing was minimal and that very small waves, if any, were radiated from the surging cylinder. The only conclusion that can be drawn from this is that a thin cylinder is not a good radiator of surge waves.

Of the three heaving experiments, only the largest amplitude of oscillation provided a set of data where the majority of the waves were above the noise level of the sensing system.

8.4.1 Analysis of the Heaving Cylinder Data

This section records various observations about the heaving cylinder experiments and notes the influence of key factors on the correlation between the measured waves and the mathematical models of circular waves.

8.4.1.1 Accelerometer Signals for the Heaving Cylinder

The accelerometer signals recorded during the testing of the heaving cylinder were fitted to a sinusoidal function in the same manner as for the sphere (Section 8.2.1.1). The results followed a similar pattern to those of the sphere in that the higher speeds showed a closer correlation to sinusoidal than the lower speeds.

The noise floor of the accelerometer is noted in the analysis panel for the slowest oscillation. Significant noise interferes with this particular match and results in a relatively poor fit with an R^2 value of 0.83.

The accelerometer signals also show a minor harmonic peak at the third resonance.

8.4.1.2 Harmonics of the Radiated Wave for the Heaving Cylinder

As in the case of the heaving sphere studied in Section 8.2.1.2, the FFT of the pressure signals show some harmonic content. Fig 52 shows the plot of the spectral peak values for each harmonic in the measured pressure data. The lower overall scale of the graph compared to the heaving and surging spheres (Fig 45 and 49 respectively) indicates that there is a significant reduction on the measured pressure and therefore wave height. Note also that the harmonic components of the heaving cylinder never become a significant component of the overall signal.

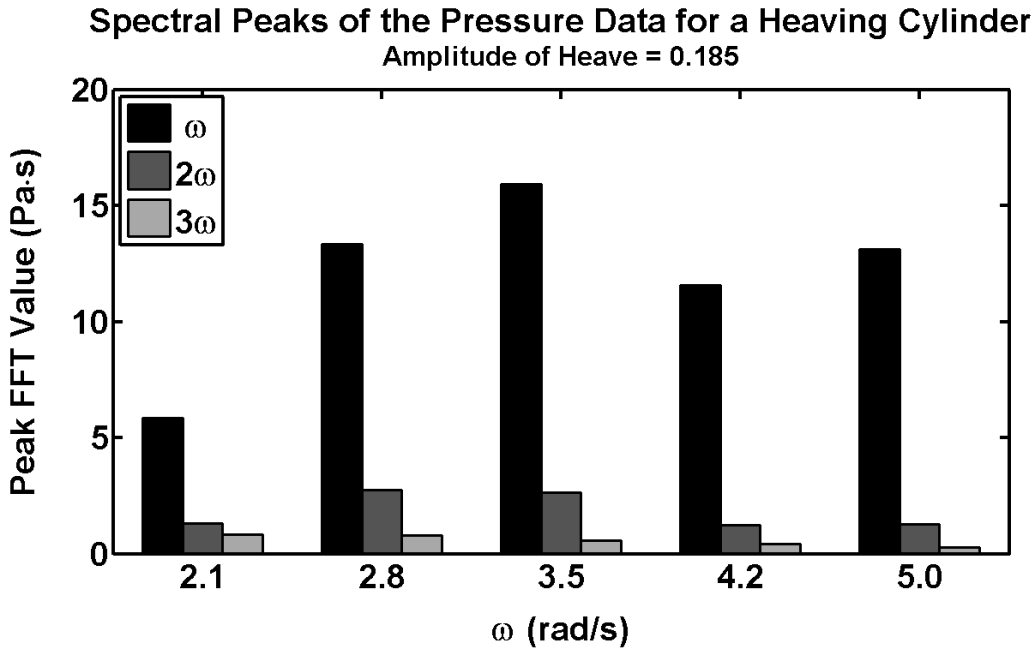

Figure 52: Spectral Peaks of the Subsurface Pressure Data Recorded During the Generation of a Surface Wave by a Heaving Cylinder

The variation in how the volume of water is displaced during the oscillation of the body may contribute to the lower harmonic content of the cylinder radiated wave. If a cylinder is moved in a monochromatic sinusoidal motion then the function describing the displaced volume of water is also monochromatic. This contrasts with the vertically oscillating sphere that adds a third harmonic to the displaced volume function due to the shape of the body.

Using the method described in Section 8.1.2, examination of the area beneath the spectral peaks of the FFT suggests that all of the sensors are peaking to a similar extent and that there are no nodal lines close to any of the sensors. Hence, it would be expected that the matched waves would be predominately heave waves.

8.4.1.3 Signal to Noise Ratio

The signal to noise ratio for the measured waves is critically low, peaking at 5:1. Inspection of the video data collected during testing indicated that the testing basin was

particularly still that day and that the low signal to noise ratio is due to the small amplitude of the radiated wave.

8.4.2 Results for a Cylinder

The mathematical models of the circular waves were fitted to the recorded pressure signals for a cylinder heaving with an amplitude of 185mm. The resulting wave amplitudes and coefficient of determination are recorded in Table 13.

A comparison of the pressure signal data with the signal predicted by circular wave theory is shown in Fig 53. The example examines a typical fit at four pressure sensors at different r and θ coordinates.

The coefficients of determination are not as high as for the case of the heaving sphere. Considering the very low signal to noise ratio and small pressure variations being measured, a lower quality of fit is understandable. However, even with the low signal level seen in the cylinder experiments, the values of R^2 greater than 0.9 show that there is still a relationship between the pressure signals and the mathematical models.

As expected from inspection of the data analysis panels, the fitting favours zeroth order circular waves exclusively. The first harmonic zeroth order circular wave represents at least 97% of the radiated power for a heaving cylinder. This adds further support to the intuitive assumption made in Section 6.1.2 that the zeroth order circular wave represents a wave radiated by a heaving body.

		1st Harmonic Amplitude (mm)				2nd Harmonic Amplitude (mm)				3rd Harmonic Amplitude (mm)			
ω	R^2	*m*=0	*m*=1	*m*=2	*m*=3	*m*=0	*m*=1	*m*=2	*m*=3	*m*=0	*m*=1	*m*=2	*m*=3
1.89	0.742	1.0	-	-	-	0.3	-	-	-	-	-	-	-
2.83	0.902	2.8	-	-	-	1.2	-	-	-	-	-	-	-
3.78	0.935	5.3	-	-	-	1.9	-	-	-	-	-	-	-
4.72	0.879	7.9	-	-	-	-	-	-	-	-	-	-	-
5.66	0.935	8.7	-	-	-	-	-	-	-	-	-	-	-

Table 13: Best Fit Wave Amplitudes for a Cylinder Heaving with an Amplitude of 185mm

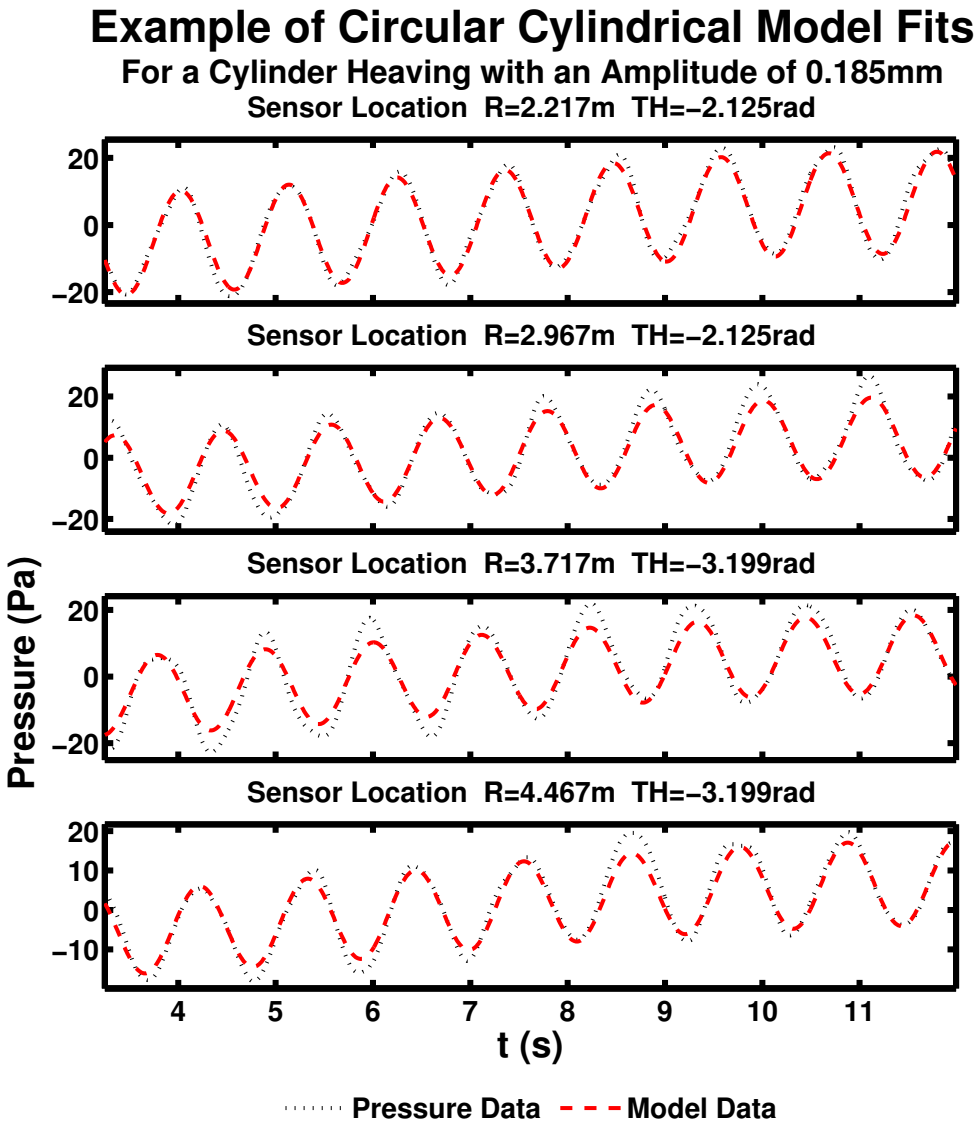

Figure 53: A Comparison of the Recorded Pressure Data with the Best Fit Circular Wave Theory Model for a Heaving Cylinder
Note that the zero drift shown here is discussed in Section 8.2.1.5

The experimental conditions at which the maximum power is radiated can again be compared to the peak period of a spectral ocean to determine an approximate scaling factor. In the case of the heaving cylinder, the peak power was radiated at a frequency of 4.7 rad/s which equates to a wavelength of 2.73 meters. If it is assumed again that the wave at the spectral peak of ocean wave spectrum is an 8 second, 100-meter long wave then the scaling factor is approximately $\frac{1}{37}$. The scaling factor can be used to

estimate the amount of power radiated from an 11 meter diameter cylinder heaving with an amplitude of 6.8 meters. Utilising the scaled power relationship in Section 2.1.2 the predicted maximum radiated power is 172kW. This assumes that frictional and non-linear effects scale linearly, which is often not the case.

The wave that would be theoretically radiated from the 11-meter cylinder would have an amplitude of 0.29 meters. Using the Eqns 185 and 186 it is possible to predict that the optimum power absorption occurs when the incident wave has an amplitude of 0.58 meters and absorbs 172kW. This illustrates the same two points regarding absorber performance and dynamic magnification as the heaving sphere (see Section 8.2.2). It is interesting to note that the required dynamic amplification is significantly larger than that for the sphere (12 vs 1.4).

Other small components may make up the radiated wave, though the signal to noise ratio is so small that any other components may not be detectable. Further experiments with a larger cylinder may provide greater detail.

Fig 54 displays the total amount of radiated power. The peak power radiated by the cylinder is twenty times smaller than that radiated by the heaving sphere.

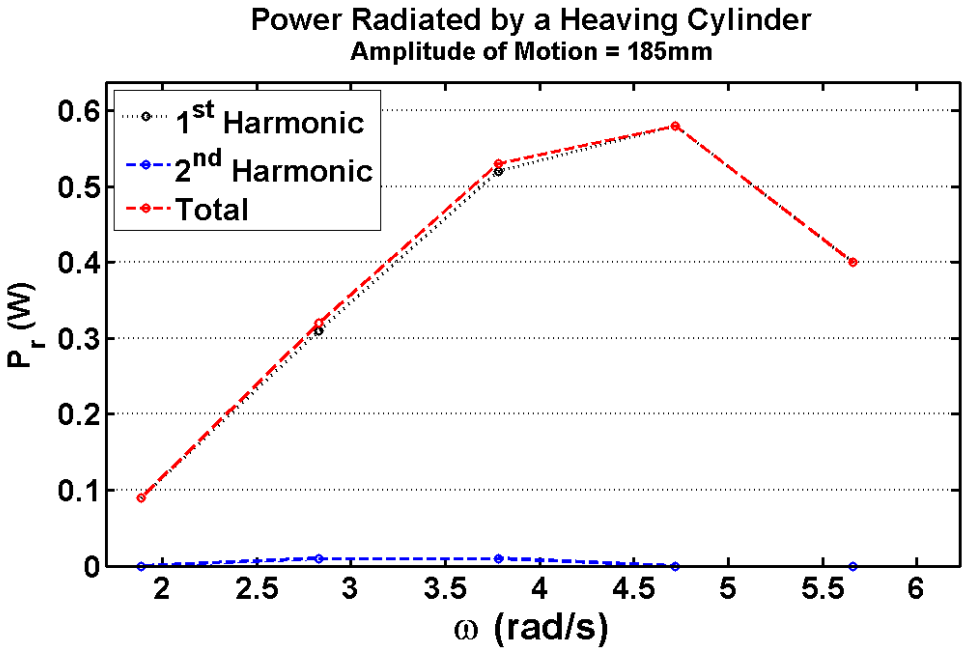

Figure 54: Power Radiated by a Heaving Cylinder

One explanation for the lower power radiated by the heaving cylinder compared to the sphere is the cylinder's smaller diameter and lower displaced volume of water. The cylinder displaces 0.026m^3 while the sphere displaces a total of 0.054m^3. A smaller displaced volume means a smaller wave must be radiated for the same mode of oscillation (see Section 9.4).

Another explanation is the dominance of viscous effects as the heaving cylinder displaces fluid well beneath the free surface. Alves noted that surface waves are a surface phenomenon (See Section 5.4.1.8) and that to radiate waves efficiently fluid must be displaced at the surface. As the cylinder displaces fluid at the bottom of the cylinder, the fluid would need to travel the submerged length of the cylinder (up to 485mm) before reaching the surface. Moving the fluid over such a distance results in a large amount of viscous mixing and power dissipation which equates to poor wave radiation. This concept is supported by a visual observation of a turbulent mixing zone immediately around the heaving cylinder.

8.4.3 Conclusions for a Cylinder

Several conclusions can be drawn about the experimental testing and matching of circular waves for the cases of the heaving and surging cylinder.

1. A tall thin cylinder is a poor radiator of surge waves.

2. The fundamental harmonic component of the radiated wave accounts for almost all of the power radiated by a heaving cylinder.

3. The dominant wave form radiated from a heaving cylinder is a zeroth order circular heave wave.

4. A heaving cylinder is a poor radiator of surface waves as it displaces fluid well below the free surface which results in significant turbulent losses.

5. The fitting of the mathematical models of circular waves to the recorded pressure data was limited by the signal to noise ratio. For the largest waves

circular wave theory did provide a satisfactory model of the measured pressures.

8.5 Data Fitting for a Surging Plate

Six individual series of tests were completed for the surging plate. All of the test results followed similar patterns. Data from a single series of tests will be used to illustrate the trends and results for the surging plate. The selected series involved the plate surging at an amplitude of 185mm. The oscillation speed of the experiments was limited by the stability of the radial wave generator.

8.5.1 Analysis of the Surging Plate Data

This section records various observations about the surging plate experiments and notes the influence of key factors on the correlation between the measured pressure signals and the mathematical models of circular waves.

8.5.1.1 Accelerometer Signals for the Surging Plate

In the case of the surging plate the accelerations of the plate do not correlate to a sinusoidal motion as well as the surging or heaving sphere or cylinder. The coefficient of determination (R^2) has an average of 0.977 with a peak of 0.986 at a frequency of 2.13 rad/s.

Observation of the accelerometer signals shows that the sinusoidal motion has been replaced with a sharp deceleration at the extremes of motion and a long acceleration as the plate changes direction. This may be caused by the available motor torque being below what is required to accelerate the plate and its associated added mass.

Another contributor to non-sinusoidal acceleration may also be the flexing of the radial wave generator support structure. The increased accelerations caused by the added mass of the plate caused visible movement in the testing structure.

8.5.1.2 Harmonics of the Radiated Waves for a Surging Plate

As in the case of the surging sphere studied in Section 8.3.1.2, the FFT of the pressure signals show significant harmonic content. Fig 55 shows the plot of the spectral peak values for each harmonic in the measured pressure data. The overall scale the graph is in the same order as the surging and heaving sphere, indicating that waves of significant size are radiated.

The harmonic components present in the surging plate experiment are considerable. The source of the harmonic components may develop through the mechanisms discussed in Section 8.3.1.2 or it may also be due to the non-sinusoidal accelerations provided by the radial wave generator.

Using the method described in Section 8.1.2, examination of the area beneath the spectral peaks of the FFT suggests that a significant proportion of the wave power will be radiated by circular waves with an order greater than zero. All of the spectral peaks show signs of sensors on nodal lines.

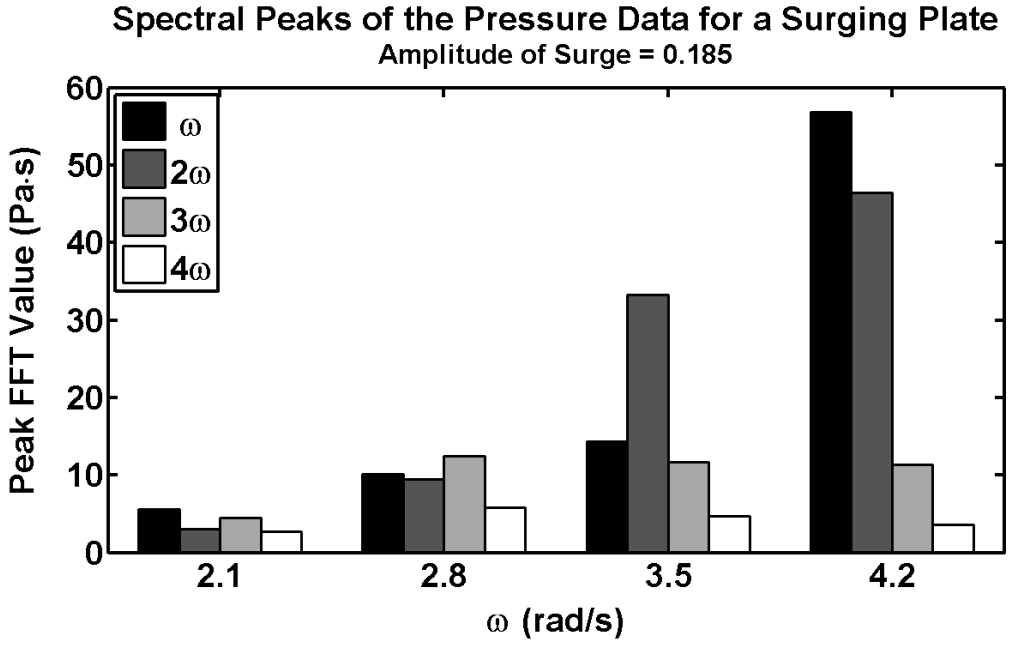

Figure 55: Spectral Peaks of the Subsurface Pressure Data Recorded During the Generation of a Surface Wave by a Surging Plate

One possible factor which may be increasing the harmonic content of the waves radiated by the surging plate is that the plate is being moved in a linear surging motion rather than being pivoted. Pivoting the plate around a low-lying pivot point would mean that the maximum horizontal particle velocity on the surface of the plate would decay with depth in a manner similar to the predictions of linear wave theory. If the radiated wave was launched with a particle velocity profile similar to that produced by linear wave theory, there should be fewer transients and therefore less harmonic content in the wave.

8.5.1.3 Signal to Noise Ratio for a Surging Plate

Signal to noise ratios as low as 1:1 and as high as 33:1 were recorded. These are similar levels to those described in Section 8.2.1.4 for the heaving sphere. This would imply that the signal is large enough to be able to find a good correlation between the measured waves and circular wave theory if one exists for this case.

8.5.2 Results for a Surging Plate

No satisfactory matches between the recorded pressure data and the circular cylindrical models were determined. The best match recorded a coefficient of determination of 0.477 which is well below the level considered significant.

The best matches achieved for each surging plate test demonstrated similar trends in circular wave order selection to the results from the surging sphere (Section 8.3.2). The matches selected first order circular waves for the fundamental harmonic and zeroth and second order circular waves for the second harmonic. This suggests that there are similarities between the two surging wave fields although the circular wave theory did not provide a sufficiently accurate map for the pressure sensor data for the surging plate.

Examination of the sensor positions showed that on that particular day there was an unintentional bias of the sensor layout towards the $\theta=-\frac{\pi}{2}$ line. A study of the various signal plots revealed that the circular wave theory provided a good match to the signals in this area but poor matches to sensors further away from the sensor cluster. This suggests a non-circular aspect to the wave field causes the matching process to bias the result to obtain the best fit for the cluster of sensors and a poor match over larger areas with fewer sensors.

Fig 56 shows a sample of signals from a surging plate test with the associated best match. The sensors selected for this graph were at approximately the same radius and various θ locations. Note that the top graph of Fig 56 represents a sensor closest to the centre of the sensor cluster, and each graph below moves steadily towards less densely populated areas of the wave field.

The additional error may be due to localised distortion caused by the non-axisymmetric aspect of the plate. The coordinate systems examined in Section 3.1 include the elliptical coordinate system which effectively stretches the circular cylindrical solutions along one of the horizontal axes. This causes localised variation in the relationship between r and the phasing of the wave which cannot be accounted for by the circular cylindrical solutions. Experimental observation suggests that the flat plate creates a similarly distorted wave field based on its non-axisymmetric shape. The solutions to the Laplace equation in elliptical cylindrical solutions are Mathieu functions and may provide a more accurate model for the waves radiated from a surging plate. These models are beyond the scope of this thesis.

8.5.3 Conclusions for a Surging Plate

Circular waves do not provide an adequate model for the waves radiated from a surging plate. Although the matched wave fields bear some similarity to the wave fields of the surging sphere, circular wave models are only accurate in the area where sensors are most densely populated. As the surging plate is the only non-axisymmetric

body tested, the results from these experiments show that the circular wave models are not suited to modelling arbitrary body shapes. Experimental observations suggest that elliptical-cylindrical solutions to the Laplace equation may provide a better model.

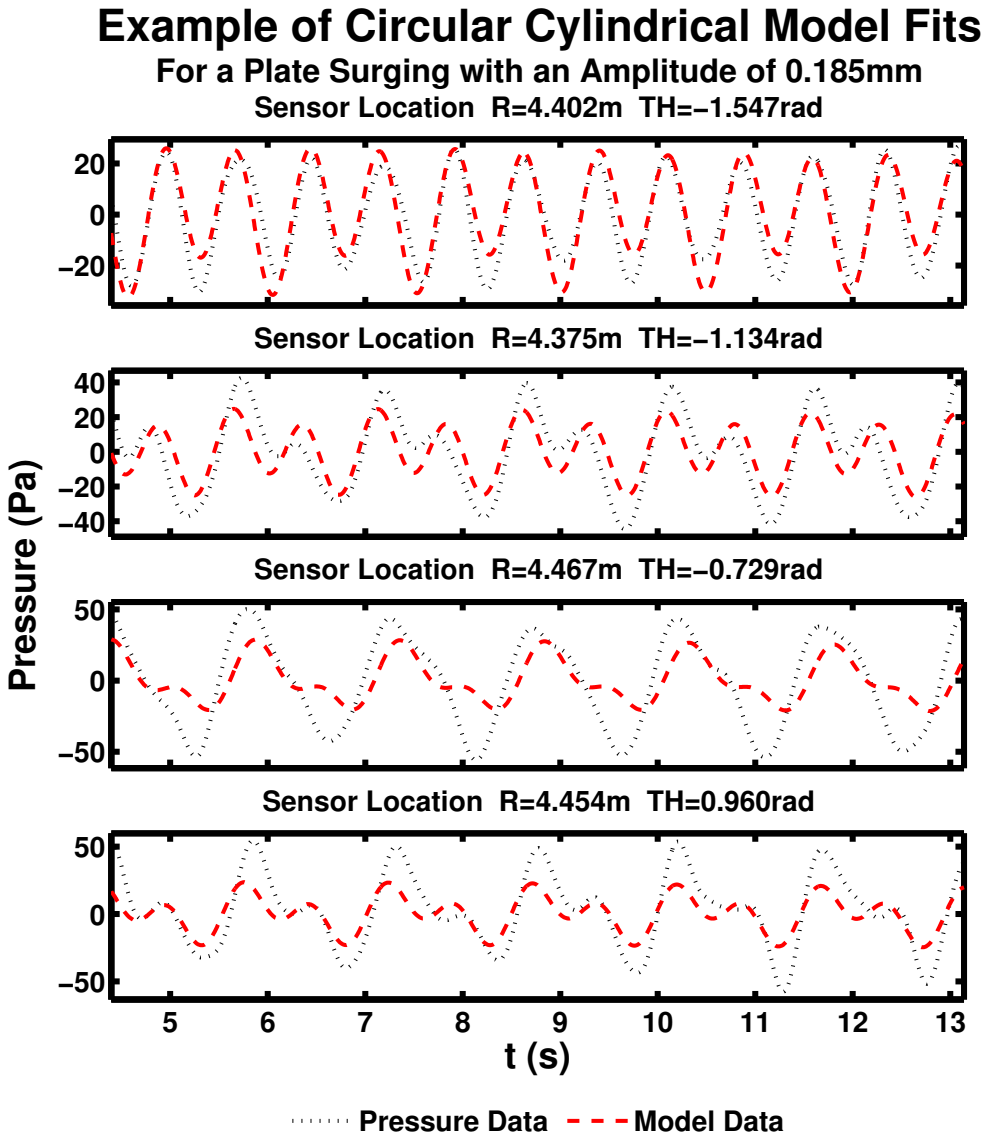

Figure 56: A Comparison of the Recorded Pressure Data with the Best Fit Circular Wave Theory Model for a Surging Plate

8.6 Error Estimation for Power Calculations

The radiated powers calculated for the fitted data have an associated error. This error is made up of four components: sensor error, error of the sensor gain, error in sensing position and fit error. This section examines the various sources of error and estimates their magnitude.

The first two components of the radiated power error have already been identified. The data sheet for the pressure sensor (see Digital Appendix 5) states that the sensor error is typically ±2.5%. The sensor gain and associated error are calculated in Section 7.2.2.3 and are $0.83^{+0.13}_{-0.11}$. The remaining two factors require further exploration.

8.6.1 Sensing Position Error

The sensor position and associated error was calculated from the data recorded as part of the testing procedure (See Section 7.6.2.1). The final error in the sensing point radial location ranged from $^{+30\text{mm}}_{-31\text{mm}}$ to $^{+175\text{mm}}_{-181\text{mm}}$ depending on the geometry of the sensor location. The final error in the sensing point θ location ranged from $^{+0.021\text{rad}}_{-0.019\text{rad}}$ to $^{+0.052\text{rad}}_{-0.051\text{rad}}$.

The importance of the error in the radial direction is dependent on the wave length of the wave. The wavelength of the first order harmonic waves ranges from 1.0m to 8.8m. The shortest wave witnessed in the wave field was the third harmonic during the fastest test which would have had a wavelength of just 0.11m (See Table 9 in Section 8.2.1.2). For the first harmonic waves, the average sensor position error represents a relatively small fraction of the longer wavelengths recorded, however the accuracy of the readings will begin to degrade at the shorter wavelengths. For the higher harmonics

of these shorter waves it is likely that the data will not be representative of the wave, as the sensor position error is in the same order as the wavelength.

The importance of the axial (θ direction) error is dependent on the form of the wave. For instance, an axisymmetric heave wave will have no sensitivity to axial error. The amount of signal distortion caused by the axial sensor position error depends on the order of the wave and the position of the sensor relative to the waves nodal lines. The nodal lines represent the largest axial rate of change of surface height but also have the smallest signals. The lines along the maximum and minimum surface displacements, on the other hand, have the greatest signal but the lowest rate of axial change. The result is that the recorded wave forms are not as sensitive to axial sensor location error as they are to radial sensor location error.

8.6.2 Fit Error Estimation

The amount of error associated with the radiated power depends upon how well the fitted mathematical functions represent the recorded signal. A similar procedure to the one followed for determining the error of the sensor gain fits (See Section 7.2.2.2) can be used to determine the error for the fits for circular waves.

The coefficient of determination (R^2) was calculated for a circular wave and an amplitude gain adjusted, phase shifted circular wave. The results were examined for any underlying relationship between the amplitude gain (G_f), phase shift (ξ_f) and the coefficient of determination. The formula used for single sinusoids (Eqn 195) approximates the connection for circular cylindrical waves. A minor discrepancy is introduced by the non-linear values of pressure calculated from the fluid velocity. Under the assumptions of linear wave theory the contribution of the fluid velocity to pressure is small and is often neglected.

Neglecting the velocity-based component of pressure means that the same relationship between amplitude gain (G_f), phase shift (ξ_f) and the coefficient of determination (R^2) for a single sinusoidal signal also applies to matched circular waves. The same

concepts of an error envelope defined by the coefficient of determination can be utilised and the magnitude of error in amplitude estimated.

8.6.3 Amplitude Error From Sensor Position Error

To estimate the effects of the radial sensor location error, a numerical study was undertaken to identify a relationship between the percentage error in the estimation of wave amplitude based on a systematic shift of the sensors' radial location. The relationship was determined by the following process:

1. Select a typical wave measured during testing e.g. a 4m long, 0.1m amplitude zeroth order circular wave.

2. Select a range of sensor positions typical of the experimental configuration.

3. Generate the pressure values for a theoretical circular wave.

4. Shift all of the sensors radially by x_r and estimate a new amplitude a_f based on the best fit of a similar circular wave with the pressure values from Step 3 and the new sensor positions.

This process was automated and repeated for a range of amplitudes and wave frequencies.

It was determined that there was a strong relationship between amplitude of radial adjustment, x_r, and the percentage error in amplitude estimation, E_a. There was also a weak relationship between E_a and the frequency of the wave. The variation in this relationship was small over the experimental frequency range and was therefore neglected. Hence, for the range of waves examined during testing, the error in amplitude estimation is:

$$E_a \approx -39\,x_r^2 - 19\,x_r \tag{215}$$

Where x_r is in meters and E_a is a percentage error. It was also noted that the maximum and minimum values of E_a for systematic shifts of the radial sensing position were 7.5% and -9.3% respectively.

The measured pressure signals already have a component of position error intrinsically incorporated into the results, as their position will have a degree of random spread.

8.6.4 Final Summary of Power Error

Care must be taken when applying the different sources of error as each is not a completely independent source. For instance, the error calculated for the fit between the pressure data and circular waves will account for the random error in the radial sensor location. The fit error will also have a component that accounts for the discrepancies created by assuming linear wave theory is an accurate model for real waves, which was already incorporated into the gain error. Hence, it is inappropriate to simply sum all of the different sources of error.

The fit error incorporates various components of the position error and gain error. It is also the largest contributor to error and the most conservative error estimate (i.e. largest range of values). It is thereby reasoned that accounting for the sensor error and the fit error gives an acceptable estimation of the total error for radiated power. The error calculation is illustrated using an example from the heaving sphere test results.

The uncalibrated results for the best fit for the sphere heaving at 5.67 rad/s are a heave wave of the first harmonic of 37.4mm amplitude and a heave wave of the second harmonic of 23.5mm. Noting that the sensor error is ±2.5%, that the sensor gain is 0.83 and that the R^2 value for the fit is 0.957, the calibrated amplitudes (A_{1c} and A_{2c}) are:

$$\begin{aligned} A_{1c} &= \frac{37.4\text{mm} \pm 2.5\%}{0.83} \pm \sqrt{1-0.957}\ \% \\ &= 45.1\text{mm} \pm 23.3\% \end{aligned} \tag{216}$$

$$\begin{aligned} A_{2c} &= \frac{23.5\text{mm} \pm 2.5\%}{0.83} \pm \sqrt{1-0.957}\ \% \\ &= 28.3\text{mm} \pm 23.3\% \end{aligned} \tag{217}$$

The total time averaged radiated power, $\overline{P}_R$, can then be calculated using Eqn 165 for each circular wave. Note the increase in error caused by the square of the amplitude.

$$\begin{aligned} \overline{P}_R &= 10.6\text{W}^{+52.0\%}_{-41.2\%} + 0.5\text{W}^{+52.0\%}_{-41.2\%} \\ &= 11.1\text{W}^{+52.0\%}_{-41.2\%} \end{aligned} \tag{218}$$

Overall, this is a relatively large upper bound for the error and is mainly due to the conservativeness of the fit error estimation. Further research into refining the model estimating fit error may significantly reduce the total error. Further analysis and comparison of the measured radiated power in Chapter 9 suggests that the actual calculated power is more accurate than indicated here.

8.7 Discussion of Data Matching

The data matching process described in this chapter is a new process for matching circular waves to the data recorded by a large number of pressure sensors in a radiated wave field. The results provide insight into the accuracy and limitations of circular wave theory and its application to the design of PAWEC.

The two most prominent limitations to the matching procedure were the stability of the radial wave generator and the small size of the waves radiated. The stability of the radial wave generator limited the range of oscillating speeds that could be tested for surging bodies. The noise floor of the sensor system was often encountered when measuring waves for slowly oscillating bodies.

The results from the circular wave models support the intuitive assumptions made with regards to the relationship between the heaving and surging body motions and the zeroth and first order circular waves (see Section 6.1.2). The zeroth and first order

circular waves correspond to the dominant wave form at the fundamental frequency of the measured waves radiated from a heaving and surging body respectively.

The experimental data also showed that the waves radiated from a body tended to have harmonics of the frequency of oscillation present. For a heaving body the higher harmonics of the radiated wave accounted for a small percentage of the total radiated power and could be represented by zeroth order circular waves. For a surging body the higher harmonics of the radiated wave accounted for a large component of the total radiated power and were less regular, requiring a number of circular waves to achieve a good match.

The identification of significant harmonic components in the radiated wave contrasts with one of the assumptions commonly made when using the Haskind relationship. The assumption that the radiated waves consist of only waves of the fundamental frequency (see Section 5.3.2.2) will lead to an over estimation of the performance of an oscillating system as it does not consider the losses due to the harmonic waves.

The higher harmonic content of the waves radiated from surging bodies may have been caused, in part, by the linear surging motion provided by the compound slide mechanism. The linear motion does not replicate a water particle velocity that decreases with depth, as seen in deep water linear wave theory. This suggests that a surging motion which is pivoted well below the free surface may offer more efficient wave radiation.

Overall, the experimental configuration provided repeatable results within the constraints of the project. The choice to use the large shallow pond at the Groynes for a testing environment limited interference from reflected waves, although wind waves increased the noise present in the signals. A deeper, cleaner pond would have limited any dissipative bottom effects that may have been present on the waves with longer wave lengths, as these waves were not technically deep water waves. However, these longer wavelength waves were also low power waves near the bottom end of the signal to noise ratio, making them difficult to measure in any case.

Testing in a closed laboratory would offer some considerable advantages if one of a similar size to the Groynes lake was available. The key improvements would be the reduction of wind noise, greater location accuracy for sensors and reduction of interference from weeds etc. All of these factors could aid in providing more accurate experimental data.

The experimental study has also provided a practical demonstration of the design principal outline by Alves (Sect 5.4.1). The heaving cylinder showed that if the displacement of fluid does not occur near the free surface, the wave radiation will be dominated by frictional losses and the radiated power will be small.

The example of a surging plate demonstrated that the circular wave theory is not necessarily applicable to non-axisymmetric bodies. In the case of a surging plate, the modelling of measured radial waves was poor due to non-circular distortions in the wave field. This shows one of the limitations of the choice of circular waves over other radiated wave models. The fact that the body has one horizontal dimension significantly longer than the other suggests that solutions to the Laplace equation in the elliptical cylindrical coordinates (Mathieu functions) may have been a more accurate model. If the complexity of the Mathieu functions could be overcome, this would allow an interesting comparative study to be completed.

8.8 Conclusions Drawn from Experimental and Data Matching Studies

The main question posed at the beginning of Chapter 7 was “Do the theoretical circular waves match the waves radiated by physical bodies?” The answer to this question is yes, providing the body is axisymmetric and the wavelength of the radiated wave is large compared to the motion of the body in surge. Under these two constraints, circular waves were found to provide a good model of the waves radiated from an oscillating body.

9 Limits on Radiated Wave Power

Theory developed by Falnes states that, at optimum absorption conditions, an oscillating body absorbs as much power from an incident plane wave as the body radiates oscillating in still water (see Section 5.3.2.5 or [19]). A logical question to follow this statement is "what are the limitations on the radiation of wave power from an oscillating body?"

Chapter 8 notes that theoretical circular waves are a good model for the waves radiated from an axisymmetric body oscillating in heave or small amplitude surge. This suggests that an examination of the limitations of circular wave theory may provide some insight into the limitations of wave radiation.

This chapter examines the theoretical flow of fluid within a circular wave and establishes a connection between the volume of fluid displaced from a cylindrical control volume by circular waves and the volume of fluid displaced by an oscillating body. This leads to the identification of two theoretical limits on power radiated by circular waves: the displaced volume limit and the wave breaking limit. These limits are then compared and contrasted to experimental results. Note that the key methods and results from this chapter have been summarised and submitted to a journal for publication.

9.1 Displaced Mass and Volume for Circular Waves

A circular wave, by definition, disturbs the fluids free surface. The change of surface height is associated with a periodic movement of mass from one point in the surface to another. The amount of mass moved must, in turn, be related to the order and amplitude of the circular wave. Calculating the mass moving back and forth across a boundary would provide useful information about the amount of fluid that must be displaced to create the wave.

To begin calculating the displaced mass for a circular wave it is noted that the flow of mass ($\dot{m}$) across a boundary is:

$$\dot{m} = \rho \cdot area \cdot \vec{V} \tag{219}$$

The definition for the particle velocity is defined in complex potential theory and is given by Eqn 15.

The derivation of the time-averaged power in Appendix 2 utilises a cylindrical control volume extending from the bottom boundary to the free surface. The calculation of total mass flow in and out of a cylindrical control volume is simply the total mass flow through the vertical walls of the cylinder, as no fluid is transmitted through the bottom boundary or free surface of the fluid (providing a non-breaking free surface is assumed). The radius of the cylindrical control volume is defined as the radius of radiation, r_r , and has an elemental area, dA_r ,:

$$dA_r = r_r \hat{r}\, d\theta\, r\, dz \tag{220}$$

Hence the total mass flow through the control volume, $\dot{m}_t^{cv}$, for any circular wave is:

$$\dot{m}_t^{cv} = -\rho \int_{-h}^{\eta} \int_{-\pi}^{\pi} \nabla \phi \cdot r_r \hat{r}\, d\theta\, dz \tag{221}$$

Appendix 9 calculates the total mass flow through the cylindrical volume for a monochromatic circular wave. Evaluating Eqn 444 at $r = r_r$ gives:

$$\begin{aligned} \dot{m}_t^{cv} &= -\frac{\rho \omega r_r B}{2k} R_{mr} \cos(\omega t - \beta - \xi_{mr}) \int_{-\pi}^{\pi} \cos(m\theta - \zeta)\, d\theta \\ &\text{where} \\ R_{mr} &= \sqrt{\left(J_{m-1}(k r_r) - J_{m+1}(k r_r)\right)^2 + \left(Y_{m-1}(k r_r) - Y_{m+1}(k r_r)\right)^2} \\ \xi_{mr} &= atan\left(\frac{Y_{m-1}(k r_r) - Y_{m+1}(k r_r)}{J_{m-1}(k r_r) - J_{m+1}(k r_r)}\right) \end{aligned} \tag{222}$$

This result only yields a non-zero value for the symmetric heave wave (where both m and ζ are zero). The total mass flow across a cylindrical boundary at the radius of radiation for a zeroth order circular wave, $\dot{m}_0^{cv}$, is:

$$\dot{m}_0^{cv} = -\frac{\pi \rho \omega r_r B}{k} R_{0r} \cos(\omega t - \beta - \xi_{0r}) \tag{223}$$

For higher order circular waves ($m > 0$) there is no net mass flow through the cylindrical control volume wall. This occurs because the flow across one section of the cylindrical wall is balanced with the flow out across another section. The balancing sections of cylindrical wall are divided by the surface displacement nodal lines. Figs 57 and 58 illustrate the balancing sections with surface contour maps and examples of a control volume boundary.

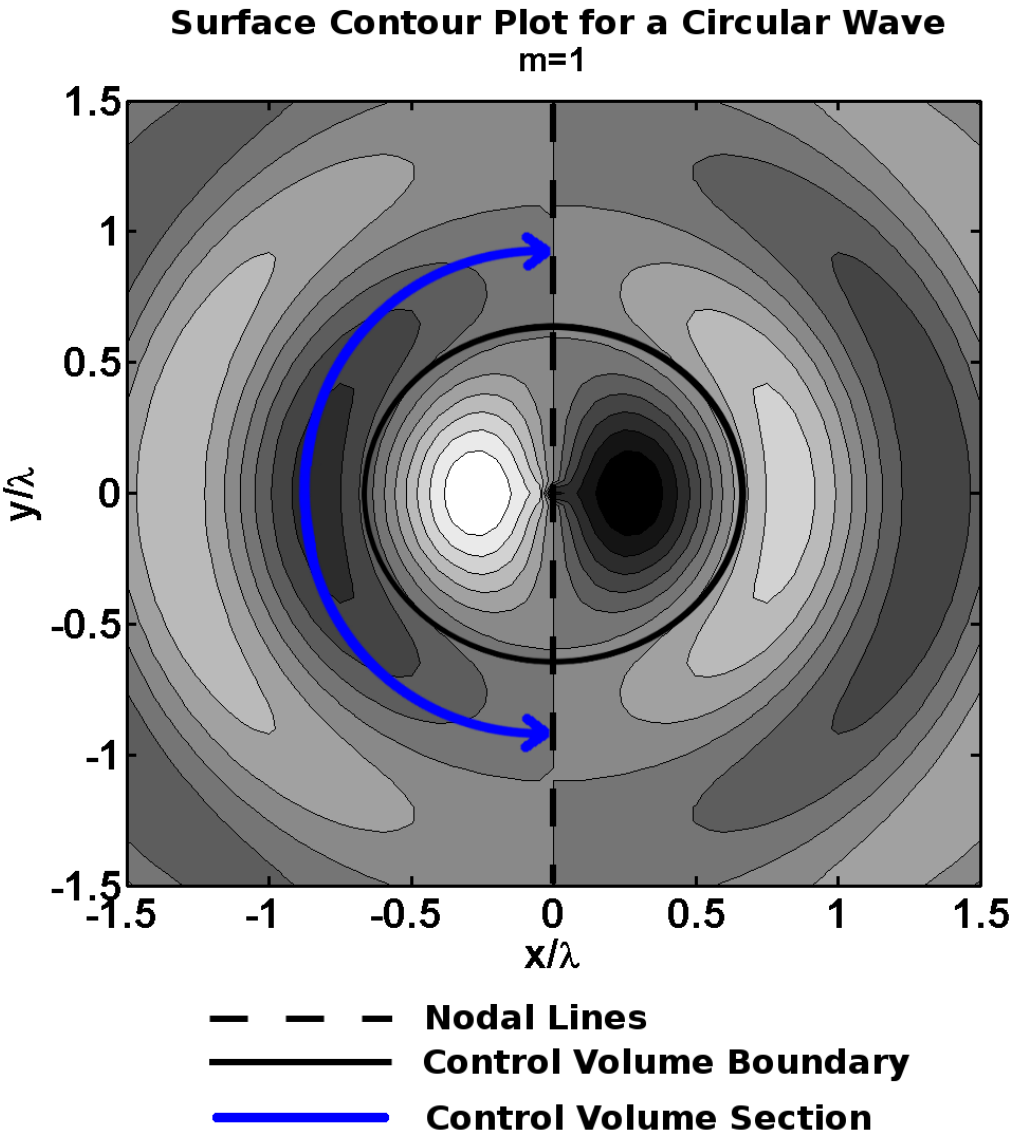

Figure 57: Surface Contour Plot for a First Order Circular Wave Indicating a Section Bounded by Nodal Lines

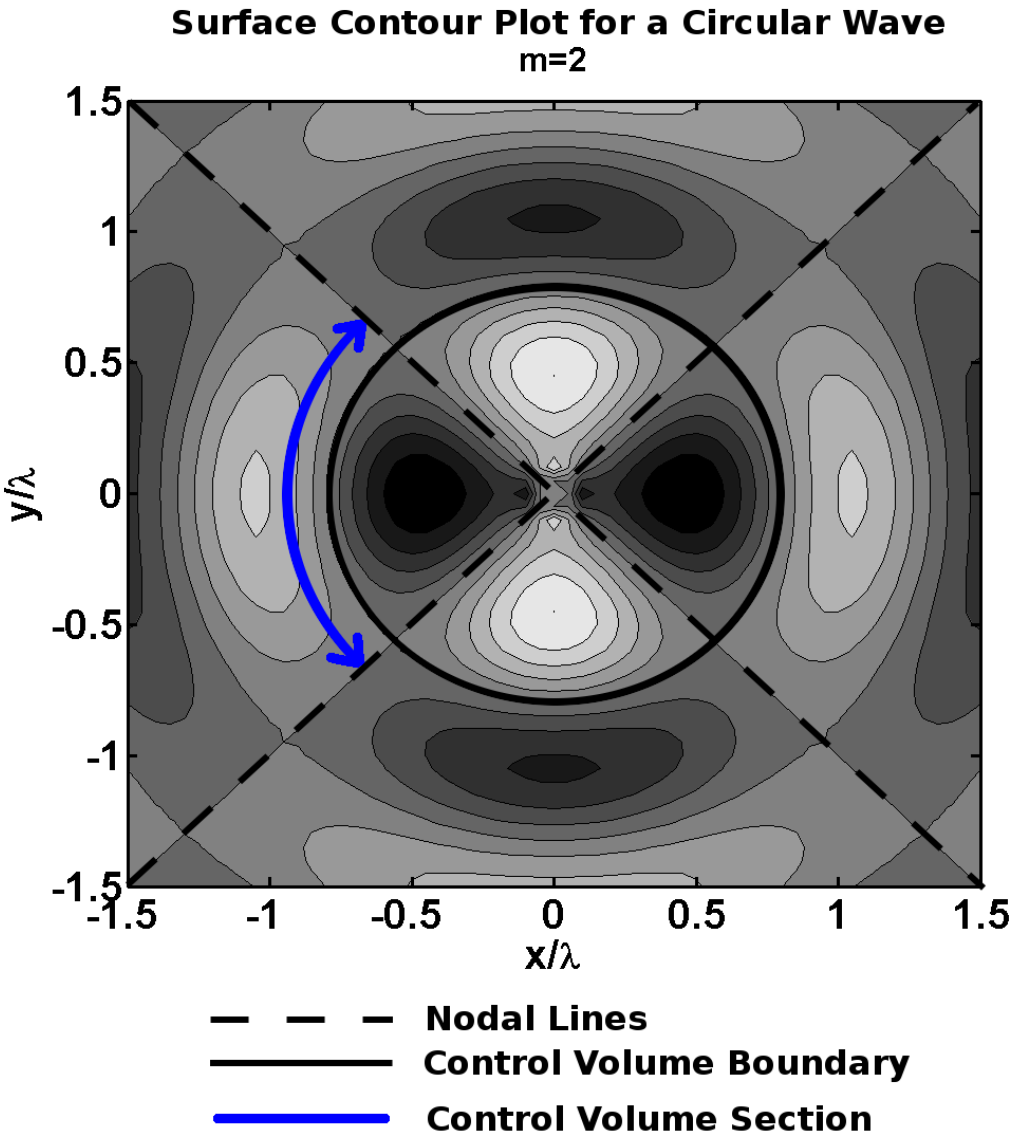

Figure 58: Surface Contour Plot for a Second Order Circular Wave Indicating a Section Bounded by Nodal Lines

For the case of a first order circular wave ($m=1$), the wave field has only one nodal line. This nodal line divides the control volume wall into two sections with equal and opposite flow across each.

It is possible to calculate the resulting flow through any section of cylindrical area between two nodal lines by changing the domain of the θ integral in Eqn 221. The mass flow rate through the cylindrical wall section of radius r_r, bounded by two nodal lines is also calculated in Appendix 9 and is:

$$\dot{m}_n^{cv} = -\frac{\rho \omega r_r B}{nk} R_{nr} \cos(\omega t - \beta - \xi_{nr}) \quad for \quad n \in \mathbb{Z}, n \neq 0 \tag{224}$$

From Eqns 223 and 224 it is also possible to calculate the volume of fluid displaced from the cylindrical control volume in each case. This is achieved by dividing by the fluid density, integrating with respect to t and reversing the sign. Hence the volume displaced from the cylindrical control volume of radius r_r is:

$$V_0^{cv} = \frac{\pi r_r R_{0r} B}{k} \sin(\omega t - \beta - \xi_{0r}) \tag{225}$$

And the volume displaced through a section of cylindrical control volume of radius r_r bounded by two nodal lines is:

$$\Delta V_n^{cv} = \frac{r_r R_{nr} B}{nk} \sin(\omega t - \beta - \xi_{nr}) \quad for \quad n \in \mathbb{Z}, n \neq 0 \tag{226}$$

Both results are sinusoidal with time. The magnitude of each depends upon the wave number, k, the order of the circular wave, m, the radius of radiation, r_r, and the amplitude of the wave, B.

9.2 The Characteristic Cylinder of a PAWEC

With the identification of the displaced volume for radial waves, the next step is to establish a connection between physical bodies and circular waves. Eqns 287 and 288 require the identification of the radius of radiation, r_r.

For a partially submerged cylindrical body heaving in a fluid, the area of the fluid occupied by the cylinder does not have a free surface. For this simple case the wave field exists from the wall of the cylinder out to infinity. The division of the domain into two parts, the wave field and the cylindrical area dominated by the body, is analogous with dividing the wave field by examining the inside and outside of a circular cylindrical control volume. By paralleling these two scenarios it is possible to establish that the radius of radiation for a heaving cylinder is simply the radius of the cylinder.

For more complex shaped bodies like the sphere or the ellipsoid, and alternative modes of oscillation, the radius of radiation is not intrinsically defined. For instance, the geometry of a heaving sphere means that the area of the free surface dominated by the body changes as the sphere moves up and down. This provides a challenge to defining a constant radius of radiation.

To standardise the approach for calculating the radius of radiation, it is proposed that every solid axisymmetric body has an equivalent theoretical vertical cylinder. This cylinder, referred to as the characteristic cylinder, is an ideal wave radiator. An ideal wave radiator displaces fluid with the correct depth profile, frequency and phasing that meets the exact requirements to radiate circular waves efficiently. An ideal wave radiator does not dissipate any energy through friction or generate any near-field effects.

Defining the characteristic cylinder as an ideal radiator differentiates it from a real cylindrical wave radiator. A real cylindrical wave radiator has limitations on the depth at which it must displace fluid, depending on its draft and movement, which may not be optimal. As seen in Section 8.4.2 a real cylindrical radiator may also have near-field effects that dissipate energy and reduce the size of the radiated wave.

The dimensions of the characteristic cylinder are the characteristic radius, r_c, and the characteristic length, l_c. The characteristic length is the submerged vertical length of the characteristic cylinder when the body displacement of the body is zero. This is also known as the draft. These dimensions can be calculated and depend on the motion and shape of the body.

It is assumed that the characteristic cylinder moves in a sinusoidal motion. The displacement of the cylinder is defined by the characteristic amplitude of motion, a_c, the characteristic frequency, ω_c, and the characteristic phase ε_c.

9.2.1 Heaving Bodies and Characteristic Cylinders

This section introduces a proposed method for determining properties of the characteristic cylinder. As there is no pre-existing process, the method outlined here is experimental and the appropriateness of the method can only be judged by comparing the theoretical results with experimental values.

In the case of heave the direction of motion is aligned with the characteristic length of the characteristic cylinder. The assumption that the characteristic cylinder is an ideal radiator means that, regardless of draft, the characteristic cylinder will always radiate a wave as efficiently as possible. Hence, for heave the draft (or characteristic length, l_c) can be ignored. This means that only two relationships are required to define the properties of the characteristic cylinder.

The first relationship proposed is the relationship of common motion. This assumes that the characteristic cylinder moves in a simple harmonic motion with the same displacement as the motion of the body. It is also assumed that the body oscillates with an amplitude a at a frequency of ω with a phase of ε and so the characteristic cylinder must too.

The second relationship proposed is the relationship of common displaced volume. This assumes that the displaced volume of the body must be equal to the displaced volume of the characteristic cylinder. The displaced volumes for a heaving cylinder and a heaving sphere are given by Eqns 227 and 228. Note that each body has a radius R and oscillates with an amplitude a at a frequency of ω and a phase of ε. Appendix 9 provides the proof of the heaving sphere displaced volume.

$$\Delta V_0^c = \pi R^2 a \sin(\omega t - \varepsilon) \tag{227}$$

$$\Delta V_0^s = \pi a \left(R^2 - \frac{a^2}{4} \right) \sin(\omega t - \varepsilon) + \frac{\pi a^3}{12} \sin(3\omega t - 3\varepsilon) \tag{228}$$

The displaced volume for the characteristic cylinder oscillating with an amplitude a_c at a frequency ω_c and a phase ε_c is:

$$\Delta V_0^{cc} = \pi r_c^2 a_c \sin(\omega_c t - \varepsilon_c) \quad (229)$$

Applying the rule that the displaced volumes of the heaving characteristic cylinder and a heaving cylinder is trivial. The relationship of common motion equates the variables defining the motion so that $a_c = a$, $\omega_c = \omega$ and $\varepsilon_c = \varepsilon$. The relationship of common displaced volumes is satisfied by equating Eqns 227 and 229. The result is that the characteristic radius is equal to the radius of the cylinder.

The case of the heaving sphere is complicated by the third harmonic of displaced volume. As each harmonic of the radiated wave does not interact with the others, in a time-averaged sense (see Section 6.3.1), it is possible to treat each harmonic separately. Hence, the sphere could be represented by two characteristic cylinders, one heaving at the fundamental harmonic and another heaving at the third harmonic.

It is proposed that the characteristic radius and the amplitude of motion of a harmonic characteristic cylinder be defined in a different manner to those same properties of the characteristic cylinder oscillating at the fundamental frequency. The rationale behind this is that the radius of radiation must be the same for all harmonic components of a radiated wave. Hence, once the radius of radiation is defined for the fundamental component of the radiated wave it is defined for all components. In the case of a harmonic characteristic cylinder there is only one dimension to be defined: the amplitude of motion. The amplitude of motion of the harmonic cylinder is defined by the applying the comparable displaced volume relationship to the displaced volume of each harmonic.

Using the example of the heaving sphere to illustrate this:

1. The displaced volume of the fundamental characteristic cylinder can be equated to the fundamental component of the displaced volume. Hence from Eqns 228 and 229:

$$\pi r_c^2 a_1 \sin(\omega_c t - \varepsilon_c) = \pi a \left(R^2 - \frac{a^2}{4} \right) \sin(\omega t - \varepsilon) \quad (230)$$

2. The relationship of common motion means that $a_1 = a$ and to ensure the sinusoidal components are equivalent $\omega_c = \omega$ and $\varepsilon_c = \varepsilon$. Hence:

$$r_c = \sqrt{R^2 - \frac{a^2}{4}} \tag{231}$$

3. It is assumed that the third harmonic characteristic cylinder oscillates with a characteristic amplitude a_3 at frequency of 3ω and a phase of 3ε and the displaced volume is:

$$\Delta V_0^{cc3} = \pi r_c^2 a_3 \sin(3\omega t - 3\varepsilon) \tag{232}$$

4. The characteristic amplitude of the third harmonic can be calculated by equating the second term on the right-hand side of Eqn 228 to Eqn 232:

$$\begin{aligned} \pi r_c^2 a_3 \sin(3\omega t - 3\varepsilon) &= \frac{\pi a^3}{12} \sin(3\omega t - 3\varepsilon) \\ \Rightarrow a_3 &= \frac{a^3}{12 r_c^2} \end{aligned} \tag{233}$$

This method for calculating the characteristic cylinder(s) can be applied to a wide range of solid, axisymmetric heaving bodies.

The original goal of developing the characteristic cylinder was to provide a radius of radiation when comparing wave radiating bodies to theoretical circular waves. In the case of the heaving body the radius of radiation is the characteristic radius:

$$r_r = r_c \quad \text{for heave} \tag{234}$$

9.2.2 Surging Bodies and Characteristic Cylinders

This section proposes a method for determining the properties of a surging characteristic cylinder. As in the case for heave there is no pre-existing theory with which to compare this procedure. The method proposed below is similar to the heaving method, with the exception that the characteristic length (or draft) of the characteristic cylinder must also be defined. Hence three relationships are required to calculate all the properties of the characteristic cylinder.

The first two relationships proposed are those utilised for the heaving sphere: Namely relationship of common motion and the relationship of common displaced volume. It is also assumed that the body oscillates with an amplitude a at a frequency of ω with a phase of ε.

For a surging body the displaced volume is defined as the volume the submerged cross sectional area of the body sweeps through when oscillated. Hence, for a vertical cylinder of radius R, submerged to depth l and oscillating with an amplitude a at a frequency of ω and a phase of ε, the displaced volume in surge is:

$$\Delta V_1^c = 2Rla\sin(\omega t-\varepsilon) \tag{235}$$

Similarly, a half submerged sphere of radius R and oscillating with an amplitude a at frequency of ω and a phase of ε, the displaced volume in surge is:

$$\Delta V_1^s = \frac{\pi R^2 a}{2}\sin(\omega t-\varepsilon) \tag{236}$$

The relationship of common motions defines the displaced volume of the vertical surging characteristic cylinder:

$$\Delta V_1^c = 2r_c l_c a_c \sin(\omega_c t-\varepsilon_c) \tag{237}$$

While the relationship of common displaced volumes can be applied to the displaced volume equations, a further relationship is still required to resolve r_c and l_c. This is achieved by equating the second moment of area of the submerged cross section through the axis of symmetry of the characteristic cylinder and the body. This relationship is called the relationship of common second moments of area. The trivial case is when the body is a cylinder, in which case $l_c=l$ and $r_c=R$.

This process is better illustrated using the example of a half submerged sphere:

1. The displaced surging volume for a half submerged sphere is given by Eqn 236 and is equated to the displaced volume of the characteristic cylinder given by Eqn 237.

2. The second moment of area of the submerged cross section for the characteristic cylinder is:

$$I_1^{cc} = \frac{2 r_c l_c^3}{12} \tag{238}$$

3. The second moment of area of the submerged cross section for a half submerged sphere is:

$$I_1^s = \left(\frac{\pi}{8} - \frac{8}{9\pi}\right) R^4 \tag{239}$$

4. Using Eqns 236, 237, 238 and 239, the variables l_c and r_c for a half submerged heaving sphere are calculated. See Appendix 9 for the complete derivation.

$$l_c = \frac{R}{\pi}\sqrt{\frac{9\pi^2 - 64}{3}} \approx 0.86\, R \tag{240}$$

$$r_c = \frac{\pi^2 R}{4}\sqrt{\frac{3}{9\pi^2 - 64}} \approx 0.92\, R \tag{241}$$

The remaining relationship to define is the connection between the radius of radiation and the characteristic radius. The bulk of the displaced fluid is released from the body to interact with the wave field at the end of each stroke. Hence, the fluid is actually displaced at a distance from the origin equal to the characteristic radius plus the amplitude of motion. Hence:

$$r_r = r_c + a_c \quad \text{for surge} \tag{242}$$

It is interesting to note that the concept of the harmonic characteristic cylinders was not required for the case of surge. If a situation does arise that requires surging harmonic cylinders, both the amplitude of motion and the characteristic radius of the harmonic characteristic cylinder would be defined by the fundamental characteristic cylinder, otherwise the radius of radiation would change. This leaves the harmonic characteristic length as the flexible variable with which to match the displaced volumes.

9.3 Theoretical Maximum Radiated Power

In this section two limitations on the radiated power are discussed. The first is the limitation associated with the displaced volume of fluid required to form a given circular wave. The second is the free field wave breaking for circular cylindrical waves.

9.3.1 The Required Displaced Volume Limit

Sections 9.1 and 9.2 establish the displaced volume for circular waves and present a method of standardising axisymmetric bodies to calculate a representative radius of radiation. These two concepts can be utilised to determine the size of the maximum wave that can be radiated by an oscillating body. The logic behind the determined value being a maximum is that, when a body displaces a given amount of fluid, not all of the fluid is necessarily involved in wave radiation. Some of the displaced fluid may account for near-field effects, circulation around the body or evanescent waves. Hence the radiated wave may be smaller than the wave estimated by the displaced volume, but it cannot be larger.

The definitions of the radius of radiation (Eqns 234 and 242), the volume of fluid displaced from a cylindrical control volume by a circular wave (Eqns 225 and 226) and the displaced volume for a characteristic cylinder (Eqns 229 and 237) lead to the definition of the displaced volume limits for the radiation of heave and surge waves, independent of body radiating the wave.

9.3.1.1 The Required Displaced Volume Limit for Heaving Bodies

For a heaving characteristic cylinder, the maximum amplitude of heave wave that can be radiated (B_{m0}^{cc}) is given by equating Eqns 225 and 229 and substituting r_c for r_r.

$$\frac{\pi r_c R_{0c} B_{m0}^{cc}}{k}\sin(\omega t-\beta-\xi_{0c}) = \pi r_c^2 a_c \sin(\omega_c t-\varepsilon_c)$$
$$\Rightarrow B_{m0}^{cc}\sin(\omega t-\beta-\xi_{0c}) = \frac{k r_c a_c}{R_{0c}}\sin(\omega_c t-\varepsilon_c) \quad (243)$$

where

$$R_{0c} = 2\sqrt{\left(J_1(k r_c)\right)^2+\left(Y_1(k r_c)\right)^2}$$
$$\xi_{0c} = atan\left(\frac{Y_1(k r_c)}{J_1(k r_c)}\right)$$

Noting that the sinusoidal components of Eqn 243 must be equivalent and that the amplitudes must also be equivalent, the following two relationships apply to a heaving characteristic cylinder.

$$B_{m0}^{cc} = \frac{k r_c a_c}{R_{0c}} \quad (244)$$

$$\beta+\xi_{0c} = \varepsilon_c \quad (245)$$

Note that the phasing of the motion of the characteristic cylinder (and therefore the body) is related to the phase of the radiated wave and is adjusted for the characteristic radius.

Eqn 244 gives the maximum amplitude of the wave radiated by a heaving characteristic cylinder which, using the expression for radiated power given by Eqn 165, can be used to calculate the maximum power radiated by a heaving characteristic cylinder ($\overline{P}_{r\,m0}^{cc}$):

$$\overline{P}_{r\,m0}^{cc} = \frac{\rho\,\omega\,g\,a_c^2 r_{c0}^2}{\left(R_{0c}\right)^2}\left(1+\frac{2kh}{\sinh(2kh)}\right) \quad (246)$$

From Eqn 246 it is possible to calculate the maximum power radiated by any heaving axisymmetric body by determining the body's characteristic properties using the process outlined in Section 9.2.1 and substituting them for r_c and a_c.

The trivial case is that of the heaving cylinder, which simply replaces r_c with R in Eqn 246 and the identities for R_{0c} and ξ_{0c} in Eqn 243. For the sphere heaving in simple harmonic motion the maximum power radiated by the first harmonic

characteristic cylinder can be calculated by substituting the characteristic radius of a sphere (Eqn 230) for r_c and a for a_c:

$$\overline{P}^{sa}_{rm0} = \frac{\rho \omega g a^2 \left(4R^2 - a^2\right)}{\left(4 R^{sa}_{0c}\right)^2}\left(1 + \frac{2kh}{\sinh(2kh)}\right)$$

where (247)

$$R^{sa}_{0c} = 2\sqrt{\left(J_1\left(k\sqrt{R^2 - \frac{a^2}{4}}\right)\right)^2 + \left(Y_1\left(k\sqrt{R^2 - \frac{a^2}{4}}\right)\right)^2}$$

The total maximum radiated power for the heaving half-submerged sphere can be found by summing the contributions from the first harmonic characteristic cylinder and the third harmonic characteristic cylinder.

Where the amplitude of motion of the sphere tends to the sphere's radius R another maximum is reached. Due to its geometry the half-submerged sphere displaces a maximum amount of fluid when $a = R$, and further increases in amplitude do not increase the total displaced volume. Without any further increases in the displaced volume the heaving half-submerged sphere cannot generate a larger wave.

Hence the maximum power a sphere can radiate is:

$$\overline{P}^{sR}_{rm0} = \frac{3\rho \omega g R^4}{\left(4 R^{sR}_{0c}\right)^2}\left(1 + \frac{2kh}{\sinh(2kh)}\right)$$

where (248)

$$R^{sR}_{0c} = 2\sqrt{\left(J_1\left(\sqrt{\frac{3}{4}}kR\right)\right)^2 + \left(Y_1\left(\sqrt{\frac{3}{4}}kR\right)\right)^2}$$

9.3.1.2 The Required Displaced Volume Limit for Surging Bodies

The same theory applied to the heaving bodies can be repeated for the surging bodies. Here, the volume of fluid displaced by a surging circular wave through a section of a cylindrical control volume bounded by two nodal lines (Eqn 226 evaluated for $n = 1$) is equated to the displaced volume of a surging characteristic cylinder (Eqn 237). The

radius of radiation is equal to the characteristic radius plus the characteristic amplitude of motion (Eqn 242) for a surging body. Hence:

$$\begin{aligned}
&\frac{(r_c+a_c)R_{1c}B^{cc}_{m1}}{k}\sin(\omega t-\beta-\xi_{1c}) \;=\; 2r_c l_c a_c \sin(\omega_c t-\varepsilon_c)\\
&\Rightarrow B^{cc}_{m1}\sin(\omega t-\beta-\xi_{1c}) \;=\; \frac{2kr_c l_c a_c}{(r_c+a_c)R_{1c}}\sin(\omega_c t-\varepsilon_c)
\end{aligned} \tag{249}$$

where

$$\begin{aligned}
R_{1c} &= \sqrt{\left|J_0(k(r_c+a_c))-J_2(k(r_c+a_c))\right|^2+\left|Y_0(k(r_c+a_c))-Y_2(k(r_c+a_c))\right|^2}\\
\xi_{1c} &= atan\left(\frac{Y_0(k(r_c+a_c))-Y_2(k(r_c+a_c))}{J_0(k(r_c+a_c))-J_2(k(r_c+a_c))}\right)
\end{aligned}$$

Noting that the sinusoidal components of Eqn 249 must be equivalent, and that the amplitudes must also be equivalent, the following two relationships apply to a surging characteristic cylinder.

$$B^{cc}_{m1} \;=\; \frac{2kr_c l_c a_c}{(r_c+a)R_{1c}} \tag{250}$$

$$\beta+\xi_{1c} \;=\; \varepsilon_c \tag{251}$$

The corresponding maximum power radiated by a surging characteristic cylinder ($\overline{P}^{cc}_{rm1}$) is:

$$\overline{P}^{cc}_{rm0} \;=\; \frac{2\rho\omega g a_c^2 r_c^2 l_c^2}{(r_c+a_c)^2\left|R_{1c}\right|^2}\left(1+\frac{2kh}{\sinh(2kh)}\right) \tag{252}$$

From Eqn 252 it is possible to calculate the maximum power radiated by any surging axisymmetric body by determining the body's characteristic properties from the process outlined in Section 9.2.2 and substituting it in for r_c, l_c and a_c.

For the trivial case of a surging cylinder of radius R, amplitude of motion a and draft l the result is simply Eqn 252 with R, a and l substituted for r_c, a_c and l_c respectively.

For a surging sphere Eqns 240 and 241 are substituted into Eqn 252:

$$\overline{P}_{rm1}^{sa} = \frac{\pi^2 \rho \omega g a^2 R^4}{8\left(\frac{\pi^2 R}{4}\sqrt{\frac{3}{9\pi^2-64}}+a\right)^2 \left(R_{1c}^{sa}\right)^2}\left(1+\frac{2kh}{\sinh(2kh)}\right) \quad (253)$$

Where R_{1c}^{sa} is found by substituting Eqn 241 for r_c and a for a_c into the appropriate identity in Eqn 249.

9.3.2 The Free Field Wave Breaking Limit

The free field wave breaking limit is defined as the limit at which waves would break if the waves were propagating freely away from the wave source. This definition eliminates the localised effects caused by the wave generator and focuses on the properties of the waves alone. The summary for wave breaking criteria provided in Section 5.2.6 covers a selection of wave breaking theories for plane waves. No reference was found for theory regarding wave breaking of circular waves.

The amplitude and wavelength of circular waves change with distance from the origin making the geometric breaking criteria difficult to calculate. The kinematic conditions involving the particle speed do not seem to provide accurate results and are therefore excluded from this study. It is assumed that the plane wave dynamic breaking condition holds for circular waves. The validity of this assumption will be reviewed in Section 9.4.

The dynamic breaking condition is that the wave will break if the downward particle acceleration at the crest of the wave ($-a_z^{max}$) is larger than a factor (f_b) of gravity i.e.:

$$-a_z^{max} \le f_b g \quad (254)$$

If it is assumed that the wave field consists of a single circular wave then the maximum particle acceleration can be calculated from the velocity potential (see Appendix 9):

$$a_z^{max} = -gkB\tanh(kh)\sqrt{J_m(kr)^2+Y_m(kr)^2} \quad (255)$$

Noting that the $\sqrt{J_m(kr)^2+Y_m(kr)^2}$ term is strictly decreasing with increasing r, the amplitudes of the radiated wave that can exist before the onset of wave breaking occurs at the point of radiation ($r=r_r$) are:

$$B_m^b \leq \frac{f_b}{k\tanh(kh)\sqrt{J_m(kr_r)^2+Y_m(kr_r)^2}} \tag{256}$$

The non-breaking radiated wave amplitude identity can also be used to calculate the radiated power for a non-breaking wave field. Combining Eqns 165 and 256:

$$\overline{P}_{rmb} \leq \frac{\rho\omega g f_b^2}{\varepsilon_m k^4 \tanh^2(kh)\left(J_m(kr_r)^2+Y_m(kr_r)^2\right)}\left(1+\frac{2kh}{\sinh(2kh)}\right) \tag{257}$$

where

$$\varepsilon_m = \begin{matrix} 1 \text{ for } m=0 \\ 2 \text{ for } m=n, n\in\mathbb{Z}, n\neq 0 \end{matrix}$$

The definitions of the radius of radiation (Eqns 234 and 242) can be used to determine the maximum radiated power for a characteristic cylinder before wave breaking occurs. The calculated characteristic radii can then be used to extend the application of this formula to arbitrary solid axisymmetric bodies.

9.4 The Theoretical Limits and the Experimental Results

The theoretical limits of displaced volume and wave breaking can be plotted alongside the experimental results from Chapter 8.

9.4.1 Heaving Sphere

Figs 59 to 62 plot the theoretical limits and experimental results for a 0.5m sphere heaving at four different amplitudes.

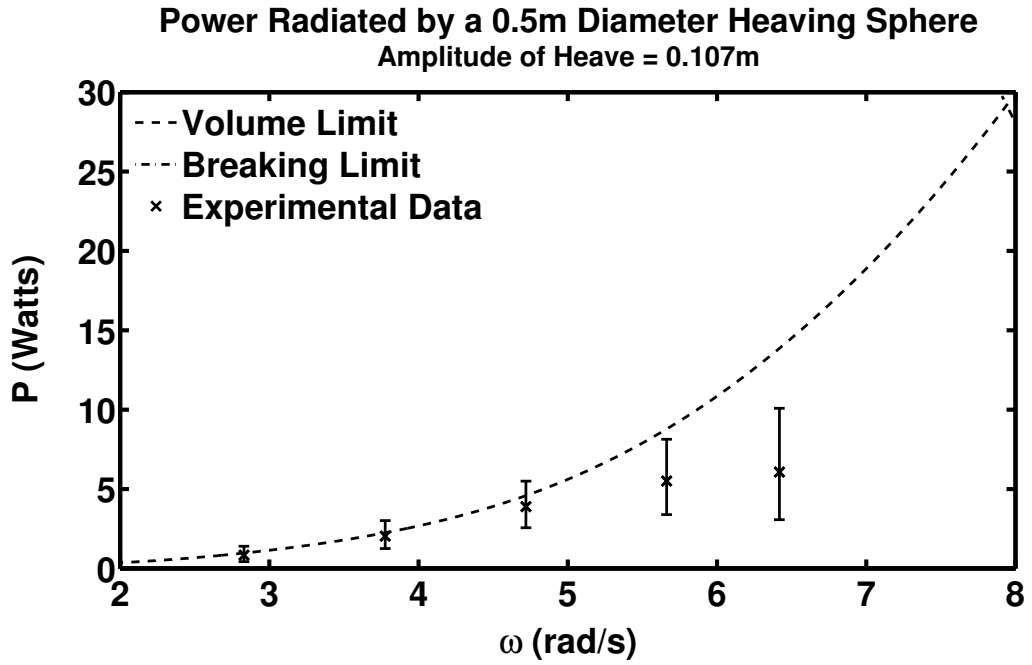

Figure 59: The Power Radiated in the First Harmonic of the Surface Wave Generated by a 0.5m Sphere Heaving with an Amplitude of 0.107m and the Associated Theoretical Radiated Power Limits

Note that the error bars represent the upper bound error limits. See Section 8.6.4 for further details.

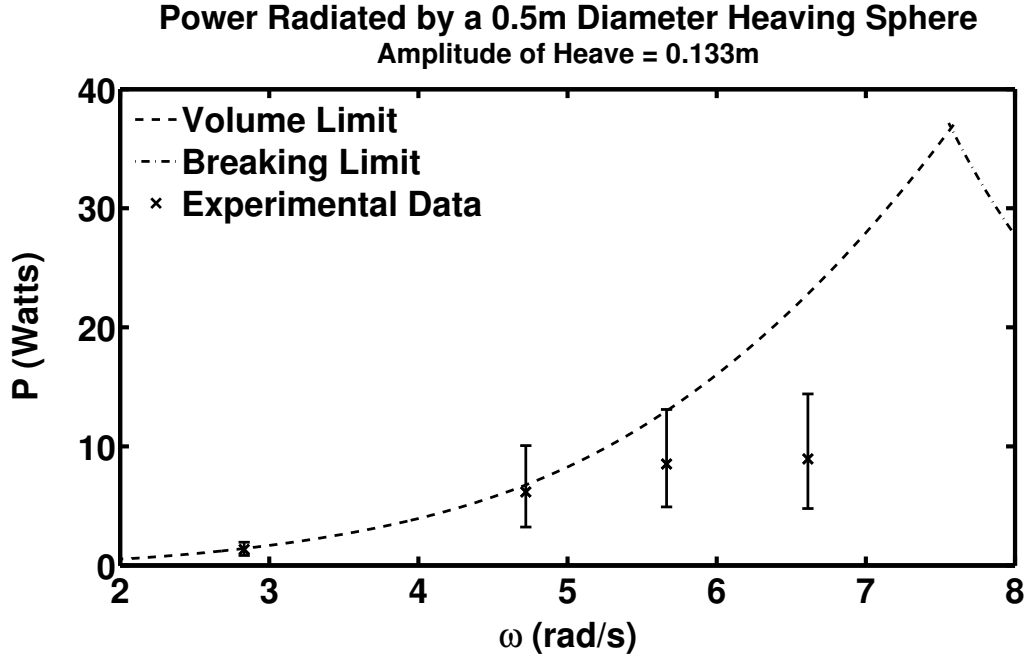

Figure 60: The Power Radiated in the First Harmonic of the Surface Wave Generated by a 0.5m Sphere Heaving with an Amplitude of 0.133m and the Associated Theoretical Radiated Power Limits

Note that the error bars represent the upper bound error limits. See Section 8.6.4 for further details.

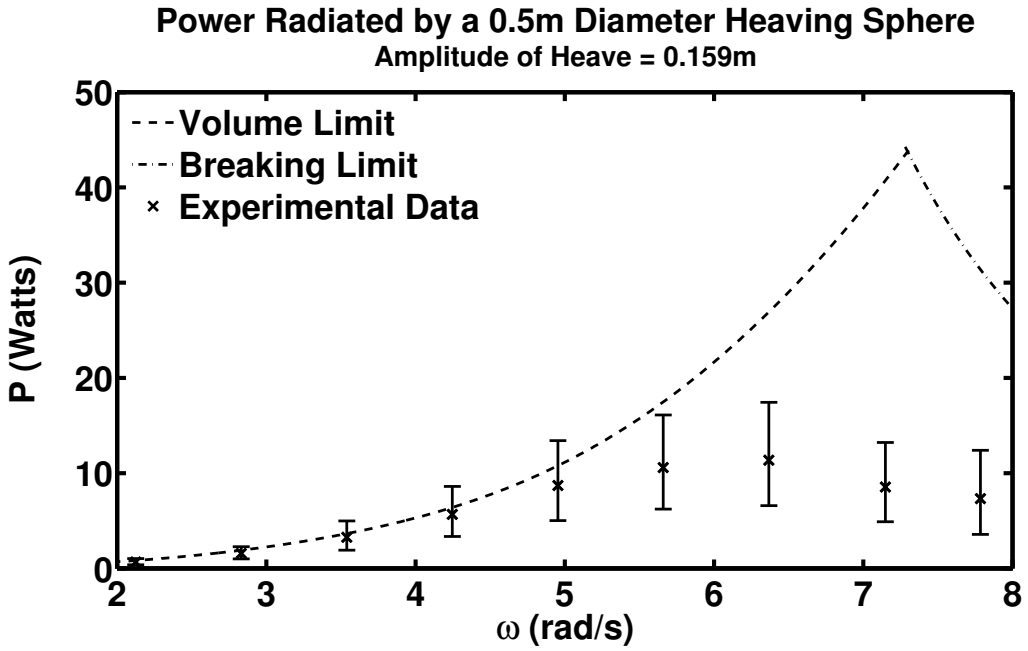

Figure 61: The Power Radiated in the First Harmonic of the Surface Wave Generated by a 0.5m Sphere Heaving with an Amplitude of 0.159m and the Associated Theoretical Radiated Power Limits

Note that the error bars represent the upper bound error limits. See Section 8.6.4 for further details.

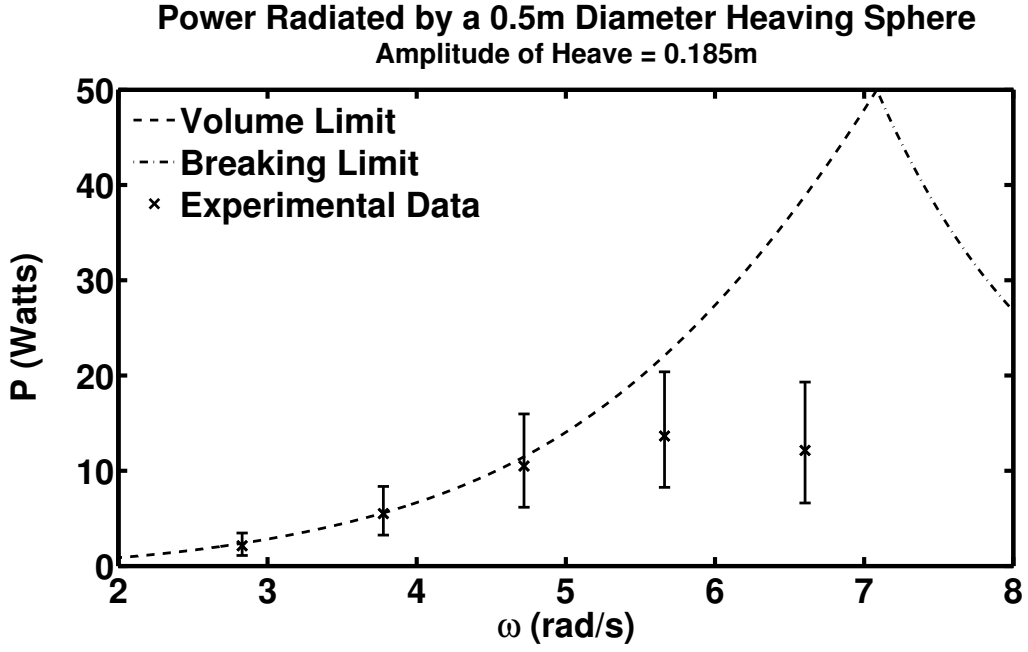

Figure 62: The Power Radiated by the First Harmonic of the Surface Wave Generated by a 0.5m Sphere Heaving with an Amplitude of 0.185m and the Associated Radiated Power Limits

Note that the error bars represent the upper bound error limits. See Section 8.6.4 for further details.

The experimental results for a heaving sphere show that at lower oscillation speeds the radiated power tracks the predicted displaced volume limit. This trend does not hold for higher oscillation speeds, particularly those above 5 rad/s.

The correlation between the displaced volume limit and the experimental results at lower speeds suggest that the predictions made by the utilising the characteristic cylinder theory reflect real-world physics. This result supports the proposed method of calculating the properties of the characteristic cylinder and the associated wave radiation properties.

Video footage of the 0.159m amplitude experiments was reviewed and it was noted that the radiated wave began to break between tests with phase velocities of 4.2rad/s and 5rad/s. Theoretically, wave breaking should not have occurred until the oscillating body reached phase velocities of 7.3rad/s.

As wave breaking is a dissipative effect it limits the amount of power that can be radiated by a body. In Figs 59 to 62 the early onset of wave breaking limited the radiated power well below what was theoretically possible.

There are two possible explanations for the early onset of wave breaking. The first explanation may be that the geometry of the sphere encourages the early onset of wave breaking. It was noted that the wave breaking initiates close to the sphere's surface just as it begins its downward stroke. At this point the wave height is not fully developed, suggesting that a localised effect is causing the wave to break. At the highest point of motion the sphere's surface has a very shallow incline when compared to the free surface. This shallow incline may cause the rate of fluid displacement to initiate wave breaking before the free field wave breaking limit can be reached.

The second possible explanation is that the assumption that the wave breaking condition which applies to plane waves also applies to circular waves may be flawed. Further study into the causes of wave breaking and radiation power limits is required before a conclusion can be drawn.

9.4.2 Heaving Cylinder

Fig 63 plots the theoretical limits and experimental results for a 0.3m cylinder heaving with an amplitude of 0.185m. For the case of the heaving cylinder the contribution to the radiated power of higher harmonic wave is negligible and so the total radiated power has been plotted.

The displaced volume limit of radiated power for the heaving cylinder (dashed line) is approximately ten times smaller than that of the sphere heaving at the same amplitude (compare Figs 62 and 63). This indicates that one of the reasons that the radiated waves from the heaving cylinder were so small is that the cylinder simply did not displace enough fluid to produce larger waves. If the cylinder had had a diameter of 0.46m it would have the same characteristic radius, and hence the same displaced volume limit, as the 0.5m diameter sphere in Fig 62.

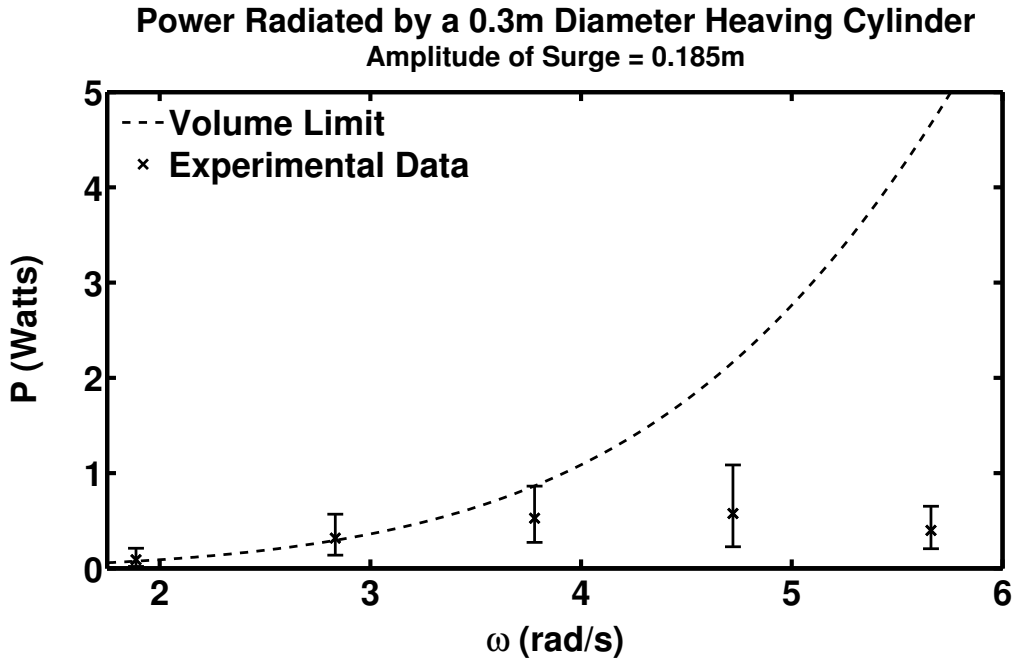

Figure 63: The Total Power Radiated by the Surface Wave Generated By a 0.3m Cylinder Heaving with an Amplitude of 0.185m and the Associated Theoretical Radiated Power Limits Note that the error bars represent the upper bound error limits. See Section 8.6.4 for further details.

The results for the heaving cylinder show similar results to that of the heaving sphere. The powers radiated at lower phase velocities follow the displaced volume limit within error. The powers radiated at higher phase velocity show that losses within the wave field become dominant.

Examination of the video data collected for the heaving cylinder reveals that there is no wave breaking in the wave field. This contrasts with the previous case of the heaving sphere. The video does indicate a zone of viscous mixing around the cylinder at higher oscillation speeds. The zone is characterised by a change in the reflective properties of the free surface caused by the underlying turbulence. The viscous mixing zone will reduce the power available for radiating waves by dissipating power through friction. The turbulence is caused by the cylinder displacing fluid well below the free surface and has been discussed in Section 8.4.2. A cylinder with a larger diameter and smaller amplitude of oscillation may not be as affected by this power radiation limitation.

The correlation between the displaced volume limit and the experimental results at lower speeds adds further support for the proposed method of calculating the properties of the heaving characteristic cylinder and the associated wave radiation properties.

9.4.3 Surging Sphere

Fig 64 plots the theoretical limits and experimental results for a 0.5m sphere surging with an amplitude of 0.159m. For the case of the surging sphere the displaced volume does not have a harmonic component that can contribute to the radiated power and therefore the total radiated power measured in the experiment is used.

It is clear from Fig 64 that the radiated wave power is well below the theoretical value. This can potentially be explained by examining the effects of fluid circulating around the body during oscillation. The displaced volume limit assumes that all of the swept volume is launched through the cylindrical boundary at the radius of radiation. However, as the sphere moves horizontally through the water, a significant amount of water will flow from the high potential area in front of the leading face to the low

potential area behind the trailing face. This means the actual displaced volume of water available for wave generation is significantly smaller than the swept volume.

A similar effect can be seen by examining a completely submerged body heaving below the surface of the fluid. If the body is sufficiently deep then there is nearly no surface effect as the fluid simply moves from one side of the body to the other and back during an oscillation. As there is no displaced volume of fluid, there cannot be a radiated wave. It is only when the body gets close to the free surface that radiated waves can be observed. This occurs when the flow around the body interacts with the free surface, thereby creating a wave.

The dominance of the fluid circulation loss mechanism reduces the performance of the surging sphere sufficiently so that there is no clear correlation between the theoretical maximum and the experimental results. This will be a significant problem for the prediction of power radiation limits for all surging axisymmetric bodies as the rotational form of the body will always allow fluid to flow smoothly around the body. Further insight might be gained by repeating the derivation for elliptical cylindrical

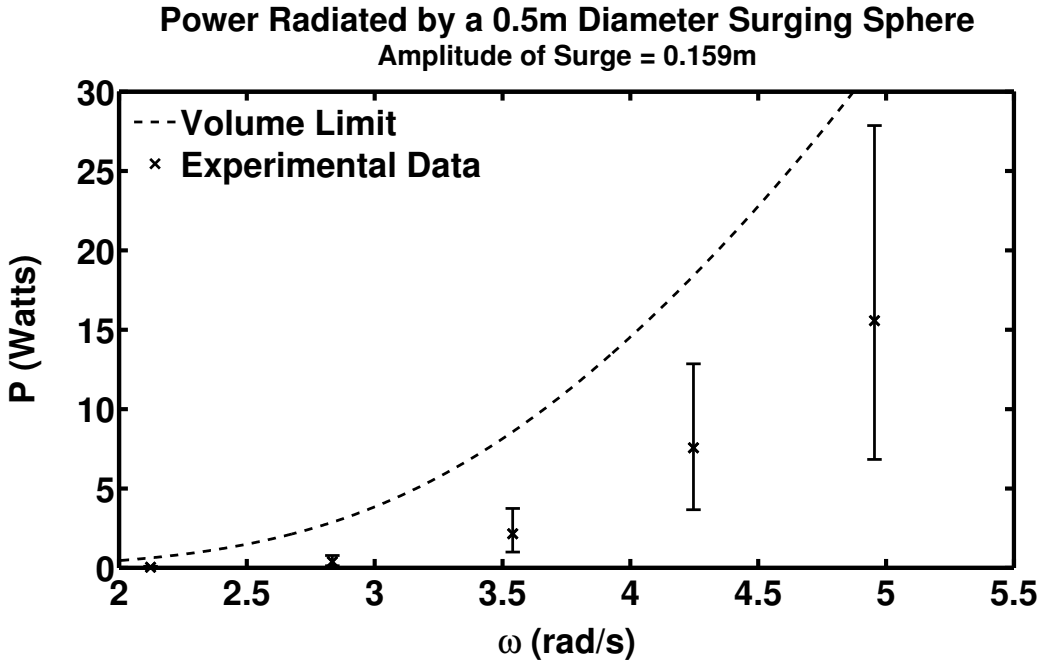

Figure 64: The Total Power Radiated by the Surface Generated by a 0.5m Sphere Surging with an Amplitude of 0.159m and the Associated Theoretical Radiated Power Limits
Note that the error bars represent the upper bound error limits. See Section 8.6.4 for further details.

coordinates and investigating shapes that minimise the circulation losses. The primary conclusion that can be drawn at this stage is that more testing and understanding are required to validate the proposed method for calculating the properties of the surging characteristic cylinder and its associated wave radiation properties.

9.5 Conclusions on the Radiated Wave Power Limits

The aim of this chapter was to determine the limitations that would affect the radiation of wave power. The unique theoretical work of Chapter 6 is extended further with the identification of two theoretical limitations of radiated power. The first is the displaced volume limit and the second is the wave breaking limit. A new method for describing solid axisymmetric bodies as characteristic cylinders has been proposed and investigated.

The following conclusions can be drawn from the analysis conducted in this chapter:

1. The proposed method for calculating the properties of characteristic cylinders can be used to describe the surface wave radiation properties of a heaving axisymmetric body based on displaced volume.

2. There is insufficient proof to substantiate the proposed method for calculating the properties of characteristic cylinders for surging axisymmetric bodies. Further research is required before the theory can be confirmed or disputed.

3. The dynamic wave breaking limit that applies to plane waves may not necessarily apply to circular waves. Further study into the initiation of circular wave breaking or the use of other body shapes may provide greater insight into the free field wave breaking limit.

4. The power radiated by a heaving sphere is limited by wave breaking. The wave breaking occurs earlier than the dynamic wave breaking criteria for plane waves suggests it should.

5. The power radiated by a slender cylinder is limited by viscous mixing caused by displacing fluid too far from the free surface for efficient wave making.

6. The power radiated by a surging sphere may be limited by circulation of fluid around the sphere.

These limitations offer some insight into factors that should be considered when designing a conservative PAWEC. For instance, the shape of any oscillating bodies should be examined for the mechanism by which wave breaking will be initiated, and the any harmonics in the displaced volume. The limitations on radiated power presented above provide a check-list of dynamics to look for during device testing.

10 Conclusions

This thesis has answered three key questions about the waves radiated from bodies oscillating within a fluid. To answer these questions a theoretical and an experimental study was undertaken. The theoretical study derived new formulas for radiated waves and their associated properties. The experimental study confirmed the theoretical constructs, the limits of application of the constructs and illustrated practical considerations of radiating wave power. The completed thesis provides significant new insights into the design considerations for point absorbing wave energy converters (PAWEC).

The original question pursued in this thesis was “Can circular wave theory be used to determine design constraints for wave energy converters?”. It was found that the theoretical circular waves could illuminate the limitations on wave power absorption based upon the underlying physics of the radiated waves and their interaction with plane waves. Expressions for the time-averaged radiated power for a circular wave, circular wave group velocity, absorbed power from a plane wave and absorption length were all derived. These expressions provided power absorption envelopes and optimum absorption conditions defined by the amplitudes and phases of the surface waves. The parameters of the calculations also identified that an effective PAWEC will radiate waves at the same frequency as the incident waves. Radiating waves at other frequencies represents a loss in the energy absorption system. Several of the derived solutions illustrate that pre-existing solutions reliant on far-field assumptions can be extended over the entire wave field using circular wave theory.

Further results from the theoretical study include:

1. Time-averaged power in linear waves is vertically stratified. Hence a PAWEC that launches energy horizontally is likely to be more efficient than a PAWEC that launches energy vertically.

2. PAWECs should minimise the radiated sway waves, as sway waves do not interact with the incident plane wave and can be considered a loss to the

system. That noted, there may be times when such a loss is advantageous, particularly in reference to survivability.

3. If a PAWEC is designed to radiate a non-symmetric wave, then the PAWEC must provide a surface piercing structure to support the discontinuity at the wave's origin.

The follow up question of " Do the theoretical circular waves match the waves radiated by physical bodies?" was investigated with an experimental study. The results of the study indicated that circular waves do match the waves radiated by a body providing the body is axisymmetric and oscillates in either heave, or surge with an amplitude much smaller than the wavelength.

The experimental study required the creation of a unique radial wave generator to oscillate a sphere, cylinder and plate in regular motions. This device performed successfully in most situations and was found to have limitations in the surging motion. A system to capture data from the radiated waves was created, including the development of a pressure-based wave height measurement system. The data capture system measured circular waves with powers as low as 0.5W.

The experimental study produced further results including:

1. The waves radiated from a heaving and surging bodies have a range of harmonic components.

2. The mathematical model of circular waves provides a good model for the recorded pressure data for waves radiated by axisymmetric bodies. The main limitations on measuring the radiated wave pressure data included signal to noise ratio for smaller waves and sensor location accuracy for waves with shorter wavelengths.

3. The dominant wave form radiated from a heaving sphere or cylinder is a zeroth order circular wave at the first harmonic. This wave form accounted for the majority of radiated power. The dominant wave forms radiated from

a surging cylinder were a first order circular wave at the fundamental harmonic and a zeroth order circular wave at the second harmonic. The amount of power radiated in each depended upon the frequency of oscillation.

4. A tall thin cylinder is a poor radiator of both heave and surge waves.

Having noted that circular waves are suitable models for waves radiated from axisymmetric bodies, the next question addressed was “What are the limits of the radiation of wave power?”. The limits of displaced volume and wave breaking are identified based on theoretical considerations of circular waves, while the experimental results point to viscous mixing, fluid circulation and geometry-based wave breaking as practical limitations.

A further theoretical study derives the displaced volume relationship equations and free-field wave breaking limits for heaving and surging circular waves. It also introduces a new theoretical construct called the characteristic cylinder. The characteristic cylinder is an ideal radiator that can be used to reduce complex axisymmetric shapes to simple models that can then be compared to properties of circular waves. The concept of the characteristic cylinder is validated by correctly predicting the low speed radiated powers for all of the heaving bodies.

The radiated powers at higher oscillation speeds did not reach the free-field wave breaking limits predicted by the dynamic plane wave breaking criterion. This suggests that either the dynamic plane wave breaking criterion is not applicable to circular waves or that other practical considerations dominate the wave field before the free field wave breaking limits can be reached.

The dominant practical consideration in PAWEC design depends largely on the body and mode of oscillation. For instance, it is suggested that a geometry-induced wave breaking occurs in the wave field of a heaving sphere before the free-field wave breaking can occur. This may be due to the gradient of the fluid-displacing face. In contrast, the wave field of a heaving cylinder becomes dominated by a viscous mixing

zone caused by fluid being displaced well below the free surface. The last practical consideration identified during testing is the fluid flow around a surging body, which reduces the displaced volume and thereby limits wave power radiation in surge.

This thesis has added to the body of knowledge associated with the design of wave energy converters. A relatively simple model for the waves radiated from a body oscillating in a fluid was proposed and several design guidelines based on the physics of surface waves determined. It was also demonstrated that the models correspond to experimental observations within certain bounds. This thesis examined the limits of wave power radiation which also limit the performance of wave energy converters. The end result is a set of theoretical tools and a practical understanding that can be used to design more effective wave energy converters.

11 Further Research Possibilities

This thesis sets the foundation for a wide range of further research. The developed framework could be used to provide further insight into range of subjects including the form of an efficient wave radiator, the flow of reactive power during power absorption, the criteria for circular wave breaking and the relationship between size and performance for a point absorber. The theory could also be extended from its current monochromatic, linear form into forms that include the spectral waves and non-linear effects seen in real ocean waves. This section provides a brief outline of a range of topics that may be studied and the expected outcomes.

11.1 The Form of an Efficient Wave Radiator

Utilising the approach developed for characteristics cylinders, it is be possible to calculate the volume of water displaced by a circular wave through a surface element of the cylindrical control volume. This result could then be related to the volume of water displaced through the same surface element by an oscillating body, which in turn may be used to determine the profile of the body required to deliver the correct amount of displaced water. For example, if it is assumed that the circular wave is a zeroth order circular wave then the volume of displaced water through the cylindrical control volume is axisymmetric. An examination of the vertical variation in volume of displaced water could be related to the change in submerged cross-sectional area of an axisymmetric heaving body at any given height. This would then determine the profile of the body required to match the radiated wave,

This theoretical study could also be complemented by further experimental work. The power radiated by a range of bodies with identical characteristic radii, including the profile determined above, oscillating through identical conditions could be measured. This could be used to compare efficiencies of different wave radiators and, as noted previously, an efficient wave radiator should make an efficient wave power absorber.

11.2 The Characteristics of Reactive Power

A significant part of this thesis has been focused on the calculation of time averaged power. Now that the mathematical basis for circular waves has been established, it is also possible to calculate the instantaneous power flow through a circular control volume and describe how both active and reactive power change with time. This is an important component of WEC design, as to be able to absorb the maximum amount of active power the WEC system must also provide the correct amount of reactive power to the wave field. Studies in this area could encompass both radiated waves and combinations of radiated waves and circular waves.

11.3 A Criterion for Circular Wave Breaking

As noted in Section 9.5 the dynamic plane wave breaking criterion does not provide an accurate model of what was observed in the case of radiated circular waves. In the case of the heaving sphere, wave breaking limited the maximum amount of radiated power. This limit will also occur in wave power absorption. A study focussed on examining the conditions under which circular waves break and then the conditions under which combinations of plane and circular waves break would provide a greater understanding of the role wave breaking plays in limiting wave power absorption.

11.4 The Size and Performance of a WEC

One of the key areas of interest in the wave energy field is the physical size of a “full sized” WEC. This may seem like a fundamental piece of knowledge but the effects of scaling make it hard to predict what size of device will be most effective. The theory in this thesis may be developed further to help answer his question.

The concept of characteristic cylinders and equating the volume of water displaced by a body to the volume of water displaced through a cylindrical control volume can be extended and applied to combinations of plane and circular waves. It should be

possible to couple the physical motion of the body to that of the size of the radiated wave, based on a given incident wave. The results of the calculation would tie together a range of factors including WEC size, body to incident wave phasing, required dynamic magnification and overall performance. The solution to the calculation should indicate if there was an optimum size of wave energy converter and determine how the size of the WEC affects the amplitude and phasing of the motions required for optimum absorption.

11.5 Spectral Circular Waves and Non-linearity

All of the theory developed in this thesis focusses on the monochromatic case of wave radiation and absorption. However, real-world oceans are not monochromatic and an understanding of the effects of spectral waves will be important in designing an effective WEC. There is a range of work which could be undertaken, including determining how spectral theory applies to circular waves, comparing the monochromatic solutions for time averaged power with those of spectral solutions and developing an understanding of how spectral seas will influence wave power absorption and wave breaking.

It should also be possible to extend this theory into higher degrees of non-linearity. For instance, it would be interesting to see if the same theory used by Stokes to develop Stokes waves could be applied to circular waves. The combination of non-linear effects and spectral seas would provide a detailed theoretical basis for understanding wave power absorption in real oceans.

11.6 Scaling Experiments

Given the difficulty in creating a full sized WEC it is important to understand how a low cost scale model will perform compared to a full size device. An investigation into the effects of scaling based on the radiation of wave power could help bridge the gap between sizes. Repeating the experiments using three or more bodies with the same

shape and different characteristic radii (e.g. a 0.25m diameter sphere, a 0.5m diameter sphere and a 0.75m diameter sphere) would provide information on how the wave radiation changes with scale.

11.7 Pivoting Body Experiments

As mentioned in Section 8.5.1.2 the linear surging motion may be a cause of lower wave radiation efficiency. This hypothesis could be tested by adjusting the test jig configuration to include a pivoting type surge motion. The results from this experiment could be readily applied to existing WECs.

Appendix 1: List of Symbols

Symbol	Definition	SI Unit of Measure
A	Surface displacement amplitude for a linear plane wave	m
A_{1c}	Calibrated wave amplitude	mm
A_{2c}	Calibrated wave amplitude	mm
A_r	A cylindrical area extending from the SWL to the bottom boundary	m^2
A_x	A constant of integration relating to term x	-
$A(\theta)$	A far-field coefficient	$m^2\ s^{-1}$
a	Amplitude of motion for an oscillating body or A constant	m -
a_c	A characteristic amplitude of motion	m
a_e	A constant used in the elliptical cylindrical coordinate system	m
a_f	Amplitude of a fitted function	-
a_m	A velocity potential coefficient for a wave of order m	m^2
a_s	An amplitude of a signal	-
a_x	Particle acceleration in the x direction	$m\ s^{-2}$
a_y	Particle acceleration in the y direction	$m\ s^{-2}$
a_z	Particle acceleration in the z direction	$m\ s^{-2}$
B	Surface displacement amplitude for a circular wave	m
B_{ma}^{b}	Maximum wave amplitude for a wave of order a associated with construct b	m
B_x	A constant of integration relating to term x	-
C_x	A constant of integration relating to term x	-
$C(t)$	A function that varies with t but is independent of x, y and z	-
$C(x)$	A function that varies with x but is independent of y, z and t	-
c	Wave celerity	$m\ s^{-1}$
c_g	Group velocity	$m\ s^{-1}$
D	A constant defined by Eqn 40	m

Symbol	Definition	SI Unit of Measure
$D1$	x distance between locating lugs mounted on the radial wave generator	m
$D(kh)$	A deep water term defined by Eqn 130	-
$D(y)$	A function that varies with y but is independent of x, z and t	-
E	Total energy	J
$\dot{E}$	Energy flux per unit surface area	J s^{-1} m^{-2}
$\vec{\dot{E}}$	Vectorised energy flux per unit surface area	J s^{-1} m^{-2}
E_A	Total energy per unit surface area	J m^{-2}
$\overline{E}_A$	Time-averaged total energy per unit surface area	J m^{-2}
E_a	Percentage error in amplitude estimation	%
$E(r)$	A function that varies with r but is independent of θ, z and t	-
$e(kz)$	Depth attenuation factor defined by Eqn 128	-
F	A function that varies with θ as defined by Eqn 267	-
F_1	A complex constant	-
F_2	A complex constant	-
F_j	Force on a body in direction j	N
$F(\theta)$	A function that varies with θ but is independent of r, z and t	-
$F'(\theta)$	A function that varies with θ as defined by Eqn 293	-
f	A function or Frequency	- Hz
f_b	Dynamic wave breaking factor	-
G	A function that varies with z as defined by Eqn 268	-
G_r	Green's function	m^{-1}
G_{ab}	Absorption gain for a wave of order b	-
G_f	Fit error gain	-
$G(z)$	A function that varies with z but is independent of x, y and t	-
$G'(z)$	A function that varies with z as defined by Eqn 294	-
g	The acceleration due to gravity	m s^{-2}

Symbol	Definition	SI Unit of Measure
H	Wave height	m
H_i	RMS wave height for wave of period T_i	m
H_{rms}	RMS wave height for a spectral sea state	m
H_s	Significant wave height	m
$H1$	Height of the locating lugs on the radial wave generator above the SWL	m
$H(t)$	A function that varies with t but is independent of x, y and z	-
$H_m(kr)$	Hankel function of the first kind of order m	-
$H_m^{(1)}(kr)$	Hankel function of the first kind of order m	-
$H_m^{(2)}(kr)$	Hankel function of the second kind of order m	-
$H_j(\theta)$	Kochin function for body oscillation direction j	-
h	Depth of fluid	m
I_a^b	Second moment of area with reference to wave of order a associated with construct b	m^4
$I_m(kr)$	Modified Bessel function of the first kind	-
i	The square-root of -1	-
$J_m(kr)$	Bessel function of the first kind	-
j	Denotes one of the six degrees of freedom	-
K	The Fourier transform variable	-
$K_m(kr)$	Modified Bessel function of the first kind	-
k	The wave number	m^{-1}
KE	The kinetic energy in a wave	J
$L1$	y distance that between two locating lugs on the radial wave generator	m
$L2$	Horizontal distance from a sensor post to the radial wave generator	m
$L3$	Horizontal distance from a sensor post to the radial wave generator	m
L_{ab}^c	Absorption length under conditions c for a radiated wave of order b	m
l_c	Characteristic length	m

Symbol	Definition	SI Unit of Measure
$M1$	Measurement from a sensor post to the radial wave generator locating lug	m
$M2$	Measurement from a sensor post to the radial wave generator locating lug	m
m	Order of a Bessel or Hankel function	-
$\dot{m}_{ab}^{c}$	Mass flow rate with conditions a for a wave of order b associated with construct c	Kg s^{-1}
m_0	First spectral moment of the wave spectrum	m^2
m_a	Added mass	Kg
n	A subset of the values of m where $m \neq 0$	-
$\vec{n}$	Normal vector pointing out of a control volume	m
N_l	Physical length scaling factor	-
N_t	Time scaling factor	-
P	Power	W
$\overline{P}$	Time-averaged power	W
$\overline{P}_{/m}$	Time-averaged power per meter wave front for a plane wave	W
$\overline{P}_a$	Absorbed time-averaged power	W
$\overline{P}_r$	Radiated time-averaged power	W
$\overline{P}_{ra}$	Radiated time-averaged power for a circular wave of order a	W
$\overline{P}_{rma}^{b}$	Maximum radiated time-averaged power for a circular wave of order a associated with construct b	W
PE	The potential energy in a wave	J
$\wp$	A linear combination of Bessel and Hankel functions	-
p	Pressure	Pa
R	The radius of a body	m
R^2	Coefficient of determination	-
$R1$	Effective radius of the locating lug	m
R_{ab}	A function for a circular wave of order a evaluated at the radius associated with b . See Eqn 222	-
$R_r(\omega)$	Radiation resistance	Kg s^{-1}
r	The circular cylindrical radial coordinate	m
$\hat{r}$	The radial unit vector for the circular cylindrical coordinate system	-

Symbol	Definition	SI Unit of Measure
r_{ca}	The characteristic radius for a mode of oscillation associated with wave order a	m
r_r	The radius of radiation	m
r_p	The polar radial coordinate from a point source	m
r_s	The spherical radial coordinate from a point source	m
r_s'	The spherical radial coordinate from an image of a point source	m
S	An expression describing the wetted surface of the wave radiating body	m^2
$S(f)$	Wave energy spectrum of a wave based on frequency	m^2 s
$S(T)$	Wave energy spectrum of a wave based on period	m^2 s^{-1}
$S(\omega)$	Wave energy spectrum of a wave based on phase velocity	m^2 s
s	A substitution variable used in Eqn 54	-
t	The time coordinate	s
T	The wave period	s
T_a	A group of terms defined locally within the calculations and identified uniquely by number a	-
T_e	The energy period of a spectral sea state	s
$\hat{u}$	Velocity of the body in the direction of wave radiation	m s^{-1}
u_e	The radial coordinate for the elliptical cylindrical coordinate system	-
$\hat{u_e}$	The radial unit vector for the elliptical cylindrical coordinate system	-
U_0	Wind velocity	m s^{-1}
V	Volume	m^3
ΔV_a^b	The change in volume for a wave of order a associated with construct b	m^3
$\vec{V}$	Velocity vector	m s^{-1}
v_e	The angular unit vector for the elliptical cylindrical coordinate system	rad
$\hat{v_e}$	The angular unit vector for the elliptical cylindrical coordinate system	-
v_j	Complex body velocity in direction j	m s^{-1}
v_x	Particle velocity in the x direction	m s^{-1}

Symbol	Definition	SI Unit of Measure
v_y	Particle velocity in the y direction	m s^{-1}
v_z	Particle velocity in the z direction	m s^{-1}
W	The Wronskian operator	-
X	x distance from a sensor post to the origin of the radiated wave	m
$X1$	x distance from a sensor post to the closest radial wave generator mounting plate	m
$X_r(\omega)$	Radiation reactance	Kg s^{-1}
x	A horizontal coordinate for the Cartesian coordinate system	m
$\hat{x}$	A horizontal unit vector for the Cartesian coordinate system	-
$\dot{x}$	Body velocity in direction x	m s^{-1}
x_0	x coordinate of the origin of a point source	m
x_r	Shift in radial sensor location	m
x_x	Particle displacement in the x direction	m
x_y	Particle displacement in the y direction	m
x_z	Particle displacement in the z direction	m
Y	x distance from a sensor post to the origin of the radiated wave	m
$Y1$	x distance from a sensor post to the closest radial wave generator mounting plate	m
y	A horizontal coordinate for the Cartesian coordinate system	m
$\hat{y}$	A horizontal unit vector for the Cartesian coordinate system	-
y_0	y coordinate of the origin of a point source	m
$Z_r(\omega)$	Radiation impedance	Kg s^{-1}
z	The vertical coordinate for the Cartesian coordinate system	m
$\hat{z}$	The vertical unit vector for the Cartesian coordinate system	-
z_0	z coordinate of the origin of a point source	m
α	Surface displacement phase angle for a linear plane wave	rad
α_{pm}	A constant used for the Pierson-Moskowitz spectrum	-
β	Surface displacement phase angle for a linear circular wave	rad
β_{pm}	A constant used for the Pierson-Moskowitz spectrum	-
γ	Angle of incidence for a plane wave	rad

Symbol	Definition	SI Unit of Measure
ε	A phase angle	rad
ε_c	A characteristic phase angle	rad
ε_m	A constant defined by Eqn 69	-
ζ	Angle of radiation for a circular wave	rad
η	Surface displacement	m
η_r	Radial component of surface displacement	m
θ	The angular coordinate for the circular cylindrical coordinate system	rad
$\hat{\theta}$	The angular unit vector for the circular cylindrical coordinate system	-
ϑ_m	An integration constant for a wave of order m	rad
λ	Wavelength	m
λ_∞	Wavelength at a large distance from the origin	m
ξ_f	Fit phase error	rad
ξ_{mr}	A function for a circular wave m evaluated at the radius of radiation (see Eqn 222)	-
ρ	Water density	Kg m^{-3}
σ	A term defined relative to the phase velocity (see Eqn 81)	m^{-1}
ϕ	A complex potential	m^2 s^{-1}
ϕ_d	The complex potential for diffracted waves	m^2 s^{-1}
ϕ_i	The complex potential for incident waves	m^2 s^{-1}
ϕ_j	The radiated complex potential caused by the oscillation of a body in direction j	m^2 s^{-1}
ϕ_l	A near-field complex potential	m^2 s^{-1}
ϕ_p	The plane wave complex potential	m^2 s^{-1}
ϕ_r	The complex potential for radiated waves	m^2 s^{-1}
ϕ_T	The complex potential for the entire wave field	m^2 s^{-1}
ω	A phase velocity	rad s^{-1}
ω_c	A characteristic phase velocity	rad s^{-1}

Appendix 2: Derivation of the Radiated Power for Circular Waves

The expression for power can be written in a number of forms. One of the forms that is useful to fluids is:

$$Power = Pressure \cdot Area \cdot Velocity \tag{258}$$

In the context of circular waves and complex velocity potentials pressure, assuming the particle velocities are small, can be expressed as:

$$Pressure = \rho \frac{\partial \phi}{\partial t} - \rho g z \tag{259}$$

The velocity is given by:

$$Velocity = \vec{V} = -\nabla \phi \tag{260}$$

The area depends on the situation being examined. For instance, if a plane wave was being examined, an area perpendicular to the plane wave extending to the sea floor and infinitely wide would be appropriate. However, if a circular wave was being examined a cylindrical surface of a given radius may give more information. Assume that the area is taken to be a circular cylinder extending from the free surface to the bottom boundary then an element of the area becomes:

$$d\vec{A}_r = r\, d\theta\, dz\, \hat{r} \tag{261}$$

And:

$$\int_A d\,\vec{A}_r = \int_{-h}^{\eta}\int_{-\pi}^{\pi} r\,d\theta\,dz\,\hat{r} \tag{262}$$

Now, because of the cyclic nature of waves examining the time-averaged power, $\overline{P}$, is useful. So:

$$d\,\overline{P} = \overline{-\rho\,g\,z\,d\,\vec{A}_r\nabla\phi} - \overline{\rho\,d\,\vec{A}_r\frac{\partial\phi}{\partial t}\nabla\phi} \tag{263}$$

The time average power of a single sine or cosine function is zero. This means that the $\overline{-\rho\,g\,z\,\nabla\phi}$ term equals zero as the velocities are time harmonic. Therefore in circular cylindrical coordinates:

$$\overline{P}_r = -\rho\,r\int_{-h}^{\eta}\int_{-\pi}^{\pi}\overline{\frac{\partial\phi}{\partial t}\frac{\partial\phi}{\partial r}}\,d\theta\,dz \tag{264}$$

Assume the velocity potential is of form:

$$\phi = \frac{g\,B\,e^{i\beta}}{\omega\cosh(k\,h)}H_m(kr)\cos(m\,\theta-\zeta)\cosh(k\,(h+z))\,e^{-i\omega t} \tag{265}$$

This can be reduced for the sake of reduced notation by making the following substitutions:

$$D = \frac{g}{\omega \cosh(k\,h)} \tag{266}$$

$$F = \cos(m\,\theta - \zeta) \tag{267}$$

$$G = \cosh(k\,(h+z)) \tag{268}$$

So that Equation 265 becomes:

$$\phi = B\,e^{i\,\beta}\,D\,F\,G\,H_m(kr)\,e^{-i\,\omega t} \tag{269}$$

Note the following:

$$\frac{\partial \phi}{\partial t} = -i\,\omega\,B\,e^{i\,\beta}\,D\,F\,G\,H_m(k\,r)\,e^{-i\,\omega t} \tag{270}$$

$$\frac{\partial \phi}{\partial r} = \frac{k}{2}\,B\,e^{i\,\beta}\,D\,F\,G\left(J_{m-1}(k\,r) - J_{m+1}(k\,r) + i\left(Y_{m-1}(k\,r) - Y_{m+1}(k\,r)\right)\right)e^{-i\,\omega t} \tag{271}$$

And:

$$\left(\frac{\partial \phi}{\partial t}\,\frac{1}{e^{-i\,\omega t}}\right)^* = \left(\omega\,D\,F\,G\,B\left(\sin(\beta) - i\cos(\beta)\right)\left(J_m(k\,r) + i\,Y_m(k\,r)\right)\right)^* \tag{272}$$

$$= \left(\omega\,D\,F\,G\,B\left(J_m(k\,r)\sin(\beta) - i\,J_m(k\,r)\cos(\beta) + i\,Y_m(k\,r)\sin(\beta) + Y_m(k\,r)\cos(\beta)\right)\right)^*$$

$$\begin{aligned}\left(\frac{\partial\phi}{\partial t}\frac{1}{e^{-i\omega t}}\right)^{*} &= \left(\omega D F G B\left(J_m(kr)\sin(\beta)+Y_m(kr)\cos(\beta)\right)\right.\\ &\qquad \left.+i\left(\omega D F G B\left(Y_m(kr)\sin(\beta)-J_m(kr)\cos(\beta)\right)\right)\right)^{*}\\ &= \omega D F G B\left(J_m(kr)\sin(\beta)+Y_m(kr)\cos(\beta)\right)\\ &\qquad +i\left(\omega D F G B\left(J_m(kr)\cos(\beta)-Y_m(kr)\sin(\beta)\right)\right)\\ &= T_1+iT_2\end{aligned} \tag{272}$$

$$\begin{aligned}\frac{\partial\phi}{\partial r}\frac{1}{e^{-i\omega t}} &= \frac{k}{2}B e^{i\beta} D F G\left(J_{m-1}(kr)-J_{m+1}(kr)+i\left(Y_{m-1}(kr)-Y_{m+1}(kr)\right)\right)\\ &= \frac{k}{2}B D F G\left(\cos(\beta)+i\sin(\beta)\right)\left(J_{m-1}(kr)-J_{m+1}(kr)+i\left(Y_{m-1}(kr)-Y_{m+1}(kr)\right)\right)\\ &= \frac{k}{2}B D F G\left(i\cos(\beta)\left(Y_{m-1}(kr)-Y_{m+1}(kr)\right)-\sin(\beta)\left(Y_{m-1}(kr)-Y_{m+1}(kr)\right)\right.\\ &\qquad \left.+\cos(\beta)\left(J_{m-1}(kr)-J_{m+1}(kr)\right)+i\sin(\beta)\left(J_{m-1}(kr)-J_{m+1}(kr)\right)\right)\\ &= \frac{k}{2}B D F G\left(\cos(\beta)\left(J_{m-1}(kr)-J_{m+1}(kr)\right)-\sin(\beta)\left(Y_{m-1}(kr)-Y_{m+1}(kr)\right)\right)\\ &\quad +i\left(\frac{k}{2}B D F G\left(\cos(\beta)\left(Y_{m-1}(kr)-Y_{m+1}(kr)\right)+\sin(\beta)\left(J_{m-1}(kr)-J_{m+1}(kr)\right)\right)\right)\\ &= T_3+iT_4\end{aligned} \tag{273}$$

Now, using the definition for time-averaged values from Section 5.6.5.1:

$$\begin{aligned}\overline{\frac{\partial \phi}{\partial t}\frac{\partial \phi}{\partial r}} &= \frac{1}{2}\Re\left(\left(\frac{\partial \phi}{\partial t}\frac{1}{e^{-i\omega t}}\right)^{*}\left(\frac{\partial \phi}{\partial r}\frac{1}{e^{-i\omega t}}\right)\right)\\ &= \frac{1}{2}\Re\left(\left(T_1+iT_2\right)\left(T_3+iT_4\right)\right)\\ &= \frac{1}{2}\left(T_1T_3-T_2T_4\right)\end{aligned} \tag{274}$$

And

$$\begin{aligned}T_1T_3-T_2T_4 &= \left(\omega DFGB\left(J_m(kr)\sin(\beta)+Y_m(kr)\cos(\beta)\right)\right)\\ &\quad\times\left(\frac{k}{2}BDFG\left(\cos(\beta)\left(J_{m-1}(kr)-J_{m+1}(kr)\right)-\sin(\beta)\left(Y_{m-1}(kr)-Y_{m+1}(kr)\right)\right)\right)\\ &\quad-\left(\omega DFGB\left(J_m(kr)\cos(\beta)-Y_m(kr)\sin(\beta)\right)\right)\\ &\quad\times\left(\frac{k}{2}BDFG\left(\cos(\beta)\left(Y_{m-1}(kr)-Y_{m+1}(kr)\right)+\sin(\beta)\left(J_{m-1}(kr)-J_{m+1}(kr)\right)\right)\right)\\ &= \frac{1}{2}k\omega D^2F^2G^2B^2\left(\left(J_m(kr)\sin(\beta)+Y_m(kr)\cos(\beta)\right)\right.\\ &\quad\times\left(\cos(\beta)\left(J_{m-1}(kr)-J_{m+1}(kr)\right)-\sin(\beta)\left(Y_{m-1}(kr)-Y_{m+1}(kr)\right)\right)\\ &\quad-\left(J_m(kr)\cos(\beta)-Y_m(kr)\sin(\beta)\right)\\ &\quad\left.\times\left(\cos(\beta)\left(Y_{m-1}(kr)-Y_{m+1}(kr)\right)+\sin(\beta)\left(J_{m-1}(kr)-J_{m+1}(kr)\right)\right)\right)\end{aligned} \tag{275}$$

$$
\begin{aligned}
T_1 T_3 - T_2 T_4 \;=\; & \frac{1}{2} k \omega D^2 F^2 G^2 B^2 \Big(J_m(kr)\sin(\beta)\cos(\beta)\big(J_{m-1}(kr) - J_{m+1}(kr)\big) + Y_m(kr)\cos(\beta)\cos(\beta)\big(J_{m-1}(kr) - J_{m+1}(kr)\big) \\
& - J_m(kr)\sin(\beta)\sin(\beta)\big(Y_{m-1}(kr) - Y_{m+1}(kr)\big) - Y_m(kr)\cos(\beta)\sin(\beta)\big(Y_{m-1}(kr) - Y_{m+1}(kr)\big) \\
& - J_m(kr)\cos(\beta)\cos(\beta)\big(Y_{m-1}(kr) - Y_{m+1}(kr)\big) + Y_m(kr)\sin(\beta)\cos(\beta)\big(Y_{m-1}(kr) - Y_{m+1}(kr)\big) \\
& - J_m(kr)\cos(\beta)\sin(\beta)\big(J_{m-1}(kr) - J_{m+1}(kr)\big) + Y_m(kr)\sin(\beta)\sin(\beta)\big(J_{m-1}(kr) - J_{m+1}(kr)\big)\Big) \\
=\; & \frac{1}{2} k \omega D^2 F^2 G^2 B^2 \Big(Y_m(kr)\big(J_{m-1}(kr) - J_{m+1}(kr)\big)\big(\cos(\beta)\cos(\beta) + \sin(\beta)\sin(\beta)\big) \\
& - J_m(kr)\big(Y_{m-1}(kr) - Y_{m+1}(kr)\big)\big(\sin(\beta)\sin(\beta) + \cos(\beta)\cos(\beta)\big)\Big) \\
=\; & \frac{1}{2} k \omega D^2 F^2 G^2 B^2 \Big(Y_m(kr)\big(J_{m-1}(kr) - J_{m+1}(kr)\big) - J_m(kr)\big(Y_{m-1}(kr) - Y_{m+1}(kr)\big)\Big)
\end{aligned}
\tag{275}
$$

2 of 2

The Bessel functions at the end of Equation 275 can be further reduced by noting the definition of the Wronskian in Abramowitz and Stegan [81]:

$$
\begin{aligned}
W\big[J_m(kr), Y_m(kr)\big] \;&=\; J_{m+1}(kr) Y_m(kr) - J_m(kr) Y_{m+1}(kr) \\
&=\; \frac{2}{\pi kr}
\end{aligned}
\tag{276}
$$

The Bessel terms in Equation 275 can then be further reduced as follows:

$$
\begin{aligned}
&Y_m(kr)\left(J_{m-1}(kr)-J_{m+1}(kr)\right)-J_m(kr)\left(Y_{m-1}(kr)-Y_{m+1}(kr)\right)\\
&\quad = J_{m-1}(kr)\,Y_m(kr)-J_{m+1}(kr)\,Y_m(kr)-J_m(kr)\,Y_{m-1}(kr)+J_m(kr)\,Y_{m+1}(kr)\\
&\quad = -W\left[J_{m-1}(kr),Y_{m-1}(kr)\right]-W\left[J_m(kr),Y_m(kr)\right]\\
&\quad = -\frac{2}{\pi kr}-\frac{2}{\pi kr}\\
&\quad = -\frac{4}{\pi kr}
\end{aligned}
\tag{277}
$$

Hence:

$$
T_1T_3-T_2T_4 = -\frac{2\omega D^2F^2G^2B^2}{\pi r}
\tag{278}
$$

And:

$$
\begin{aligned}
\overline{\frac{\partial\phi}{\partial t}\frac{\partial\phi}{\partial r}} &= \frac{1}{2}\Re\left(\left(\frac{\partial\phi}{\partial t}\frac{1}{e^{-i\omega t}}\right)^*\left(\frac{\partial\phi}{\partial r}\frac{1}{e^{-i\omega t}}\right)\right)\\
&= \frac{1}{2}\Re\left(\left(T_1+iT_2\right)\left(T_3+iT_4\right)\right)\\
&= -\frac{\omega D^2F^2G^2B^2}{\pi r}
\end{aligned}
\tag{279}
$$

And therefore Equation 264 becomes:

$$\overline{P}_r = \frac{\rho \omega D^2 B^2}{\pi} \int_{-\pi}^{\pi} F^2 d\theta \int_{-h}^{\eta} G^2 dz \tag{280}$$

The integrals can be calculated:

$$\begin{aligned}
\int_{-\pi}^{\pi} F^2 d\theta &= \int_{-\pi}^{\pi} \cos^2(m\theta - \zeta) d\theta \\
&= \int_{-\pi}^{\pi} \frac{1}{2}\cos(2m\theta - 2\zeta) + \frac{1}{2} d\theta \\
&= \left[\frac{1}{4m}\sin(2m\theta - 2\zeta) + \frac{1}{2}\theta\right]_{-\pi}^{\pi} \\
&= \left(\frac{1}{4m}\sin(2m\pi - 2\zeta) + \frac{1}{2}\pi\right) - \left(\frac{1}{4m}\sin(-2m\pi - 2\zeta) - \frac{1}{2}\pi\right) \\
&= \pi + \frac{1}{4m}\left(\sin(2m\pi - 2\zeta) - \sin(-2m\pi - 2\zeta)\right) \\
&= \pi + \frac{1}{4m}\left(\sin(2m\pi)\cos(2\zeta) - \cos(2m\pi)\sin(2\zeta) - \left(\sin(-2m\pi)\cos(2\zeta) - \cos(-2m\pi)\sin(2\zeta)\right)\right) \\
&= \pi + \frac{1}{4m}\left(\sin(2m\pi)\cos(2\zeta) - \cos(2m\pi)\sin(2\zeta) + \sin(2m\pi)\cos(2\zeta) + \cos(2m\pi)\sin(2\zeta)\right) \\
&= \pi + \frac{\sin(2m\pi)\cos(2\zeta)}{2m}
\end{aligned} \tag{281}$$

And:

$$\begin{aligned}
\int_{-h}^{0} G^2\,dz &= \int_{-h}^{0} \cosh^2(k(h+z))\,dz \\
&= \int_{-h}^{0} \frac{1}{2}\cosh(2k(h+z))+\frac{1}{2}\,dz \\
&= \left[\frac{1}{4k}\sinh(2k(h+z))+\frac{1}{2}z\right]_{-h}^{0} \\
&= \left(\frac{1}{4k}\sinh(2k(h+0))+\frac{1}{2}0\right)-\left(\frac{1}{4k}\sinh(2k(h-h))-\frac{1}{2}h\right) \\
&= \frac{1}{2}\left(\frac{\sinh(2kh)}{2k}+h\right)
\end{aligned} \tag{282}$$

Equations 266, 281 and 282 can be substituted into Equation 280 to give the final expression for radiated power:

$$\begin{aligned}
\overline{P}_r &= \frac{\rho\omega g^2 B^2}{\pi\omega^2\cosh^2(kh)}\left(\pi+\frac{\sin(2m\pi)\cos(2\zeta)}{2m}\right)\frac{1}{2}\left(\frac{\sinh(2kh)}{2k}+h\right) \\
&= \frac{\rho\omega g^2 B^2}{2\pi g k\tanh(kh)\cosh^2(kh)}\left(\pi+\frac{\sin(2m\pi)\cos(2\zeta)}{2m}\right)\left(\frac{\sinh(2kh)}{2k}+h\right) \\
&= \frac{\rho\omega g B^2}{2\pi k\sinh(kh)\cosh(kh)}\left(\pi+\frac{\sin(2m\pi)\cos(2\zeta)}{2m}\right)\left(\frac{\sinh(2kh)}{2k}+h\right)
\end{aligned} \tag{283}$$

$$\overline{P}_r = \frac{\rho\,\omega\,g\,B^2}{2\,\pi\,k\,\frac{1}{2}\sinh(2\,k\,h)}\left(\pi+\frac{\sin(2\,m\,\pi)\cos(2\,\zeta)}{2\,m}\right)\left(\frac{\sinh(2\,k\,h)}{2\,k}+h\right)$$

$$= \frac{\rho\,\omega\,g\,B^2}{2\,k^2}\left(1+\frac{\sin(2\,m\,\pi)\cos(2\,\zeta)}{2\,m\,\pi}\right)\left(1+\frac{2\,k\,h}{\sinh(2\,k\,h)}\right) \tag{283}$$

Note that the first bracketed term in the result of Equation 283 is undefined when $m=0$. However, as m tends to zero, $\sin(2\,m\,\pi)$ tends toward $2\,m\,\pi$ and, noting that if m tends to zero ζ must too, the bracketed term tends to the value of 2. Hence:

$$\left(1+\frac{\sin(2\,m\,\pi)\cos(2\,\zeta)}{2\,m\,\pi}\right)\to 2 \quad as \quad m\to 0$$

$$and \tag{284}$$

$$\left(1+\frac{\sin(2\,m\,\pi)\cos(2\,\zeta)}{2\,m\,\pi}\right)=1 \quad for \quad m\in\mathbb{Z}, \quad m\neq 0$$

A2.1 A Bessel Function Identity Based on Wronskians

Certain combinations of Bessel functions have arisen frequently throughout the derivations in Appendices 2 to 8. The reduction of the formula utilises the following identity based on the Wronskians of Bessel functions (see Section 5.6.9.3)

$$\begin{aligned} & Y_m(kr)\left[J_{m-1}(kr)-J_{m+1}(kr)\right]-J_m(kr)\left[Y_{m-1}(kr)-Y_{m+1}(kr)\right] \\ &= J_{m-1}(kr)\,Y_m(kr)-J_{m+1}(kr)\,Y_m(kr) \\ &\qquad -J_m(kr)\,Y_{m-1}(kr)+J_m(kr)\,Y_{m+1}(kr) \\ &= -W\left[J_{m-1}(kr),Y_{m-1}(kr)\right]-W\left[J_m(kr),Y_m(kr)\right] \\ &= -\frac{2}{\pi kr}-\frac{2}{\pi kr} \\ &= -\frac{4}{\pi kr} \end{aligned} \tag{285}$$

Appendix 3: Derivation of Group Velocity for Circular Waves

The derivation requires the calculation of two quantities. These are the rate of energy flux per unit area and the energy density. The method followed here shadows the same method used by McCormick (pg 37-40) [23] and uses properties summarised in Mei [17] pg 19. The properties of Bessel functions used in the mathematics are either directly from or derived from Abramowitz [81].

A3.1 Calculating the rate if energy flux per unit area

The rate of energy flux per unit surface area, $\dot{E}$, can be defined as the time averaged power per unit surface area. Both Mei and McCormick continue as follows with the exception of the negative sign. The negative sign has been added for consistency with the definition of the velocities based on the potential functions.

$$\vec{\dot{E}} = -\int_{-h}^{0} \rho \overline{\frac{\partial \phi}{\partial t} \nabla \phi} \, dz \tag{286}$$

This assumes that the wave heights are infinitesimally small so that $\int_{-h}^{\eta} dz \approx \int_{-h}^{0} dz$.

The gradient in cylindrical coordinates is defined as follows.

$$\nabla \phi = \frac{\partial \phi}{\partial r}\hat{r} + \frac{1}{r}\frac{\partial \phi}{\partial \theta}\hat{\theta} + \frac{\partial \phi}{\partial z}\hat{z} \tag{287}$$

Substituting Equation 287 into Equation 286 and assume a constant density.

$$\begin{aligned} \vec{\dot{E}} &= -\rho \int_{-h}^{0} \overline{\frac{\partial \phi}{\partial t}\frac{\partial \phi}{\partial r}\hat{r} + \frac{1}{r}\frac{\partial \phi}{\partial t}\frac{\partial \phi}{\partial \theta}\hat{\theta} + \frac{\partial \phi}{\partial t}\frac{\partial \phi}{\partial z}\hat{z}}\, dz \\ &= -\rho \int_{-h}^{0} \overline{\frac{\partial \phi}{\partial t}\frac{\partial \phi}{\partial r}}\hat{r} + \overline{\frac{1}{r}\frac{\partial \phi}{\partial t}\frac{\partial \phi}{\partial \theta}}\hat{\theta} + \overline{\frac{\partial \phi}{\partial t}\frac{\partial \phi}{\partial z}}\hat{z}\, dz \end{aligned} \tag{288}$$

For a radial wave the velocity potential is defined as follows.

$$\phi_r = \frac{g B e^{i\beta}}{\omega \cosh(k h)} H_m(kr)\cos(m\theta - \zeta)\cosh(k(h+z))e^{-i\omega t} \tag{289}$$

To simplify the mathematics the following notation will be used.

$$\begin{aligned} D &= \frac{g}{\omega \cosh(k h)} & G(z) &= \cosh(k(h+z)) \\ E(r) &= H_m^n(kr) = J_m(kr) + i Y_m(kr) & H(t) &= e^{-i\omega t} \\ F(\theta) &= \cos(m\theta - \zeta) & so \quad \phi &= e^{i\beta} D E(r) F(\theta) G(z) H(t) \end{aligned} \tag{290}$$

Calculating the required factors for the rate of energy flux per unit surface area.

$$\begin{aligned}\frac{\partial \phi}{\partial t} &= B e^{i\beta} D E(r) F(\theta) G(z) \frac{\partial H(t)}{\partial t} \\ &= B e^{i\beta} D E(r) F(\theta) G(z) \frac{\partial e^{-i\omega t}}{\partial t} \\ &= -i\omega B e^{i\beta} D E(r) F(\theta) G(z) H(t)\end{aligned} \tag{291}$$

$$\begin{aligned}\frac{\partial \phi}{\partial r} &= B e^{i\beta} D \frac{\partial E(r)}{\partial r} F(\theta) G(z) H(t) \\ &= B e^{i\beta} D \frac{\partial H_m^n(kr)}{\partial r} F(\theta) G(z) H(t) \\ &= B e^{i\beta} D \frac{k}{2}\left(J_{m-1}(kr) - J_{m+1}(kr) + i\left(Y_{m-1}(kr) - Y_{m+1}(kr)\right)\right) F(\theta) G(z) H(t) \\ &= \frac{k}{2} B e^{i\beta} D E'(r) F(\theta) G(z) H(t)\end{aligned} \tag{292}$$

Where $E'(r) = J_{m-1}(kr) - J_{m+1}(kr) + i\left(Y_{m-1}(kr) - Y_{m+1}(kr)\right)$

$$\begin{aligned}\frac{\partial \phi}{\partial \theta} &= B e^{i\beta} D E(r) \frac{\partial F(\theta)}{\partial \theta} G(z) H(t) \\ &= B e^{i\beta} D E(r) \frac{\partial \left(\cos(m\theta - \zeta)\right)}{\partial \theta} G(z) H(t) \\ &= -B e^{i\beta} D E(r) m \sin(m\theta - \zeta) G(z) H(t) \\ &= -m B e^{i\beta} D E(r) F'(\theta) G(z) H(t)\end{aligned} \tag{293}$$

Where $F'(\theta) = \sin(m\theta - \zeta)$

$$\begin{aligned}\frac{\partial \phi}{\partial z} &= B e^{i\beta} D E(r) F(\theta) \frac{\partial G(z)}{\partial z} H(t) \\ &= B e^{i\beta} D E(r) F(\theta) \frac{\partial \cosh(k(h+z))}{\partial z} H(t) \\ &= B e^{i\beta} D E(r) F(\theta) k \sinh(k(h+z)) H(t) \\ &= k B e^{i\beta} D E(r) F(\theta) G'(z) H(t)\end{aligned} \tag{294}$$

Where $G'(z) = \sinh(k(h+z))$

The time average value of two sinusoidal functions has the following property: If $f_1 = \Re\left(F_1 e^{-i\omega t}\right)$ and $f_2 = \Re\left(F_2 e^{-i\omega t}\right)$ then $\overline{f_1 f_2} = \frac{1}{2}\Re\left(F_1^* F_2\right) = \frac{1}{2}\Re\left(F_1 F_2^*\right)$ where F_1^* is the complex conjugate of F_1. This property allows us to evaluate the terms in Equation 288.

$$
\begin{aligned}
\overline{\frac{\partial \phi}{\partial t}\frac{\partial \phi}{\partial r}} &= \frac{1}{2}\Re\left(\left(-i\omega B e^{i\beta} D E(r) F(\theta) G(z)\right)^* \left(\frac{k}{2} B e^{i\beta} D E'(r) F(\theta) G(z)\right)\right) \\
&= \frac{\omega k B^2 D^2 F(\theta)^2 G(z)^2}{4}\Re\left(\left(-i e^{i\beta} E(r)\right)^* \left(e^{i\beta} E'(r)\right)\right) \\
&= \frac{\omega k B^2 D^2 F(\theta)^2 G(z)^2}{4}\Re\left(\left(e^{i\beta}\right)^* e^{i\beta}\left(-i E(r)\right)^* \left(E'(r)\right)\right) \\
&= \frac{\omega k B^2 D^2 F(\theta)^2 G(z)^2}{4}\Re\left(\left(i J_m(kr) + Y_m(kr)\right)\left(J_{m-1}(kr) - J_{m+1}(kr) + i\left(Y_{m-1}(kr) - Y_{m+1}(kr)\right)\right)\right) \\
&= \frac{\omega k B^2 D^2 F(\theta)^2 G(z)^2}{4}\Re\left(\left(Y_m(kr)\left(J_{m-1}(kr) - J_{m+1}(kr)\right) - J_m(kr)\left(Y_{m-1}(kr) - Y_{m+1}(kr)\right)\right)\right. \\
&\qquad \left. + i\left(J_m(kr)\left(J_{m-1}(kr) - J_{m+1}(kr)\right) + Y_m(kr)\left(Y_{m-1}(kr) - Y_{m+1}(kr)\right)\right)\right) \\
&= \frac{\omega k B^2 D^2 F(\theta)^2 G(z)^2}{4}\left(Y_m(kr)\left(J_{m-1}(kr) - J_{m+1}(kr)\right) - J_m(kr)\left(Y_{m-1}(kr) - Y_{m+1}(kr)\right)\right) \\
&= \frac{\omega k B^2 D^2 F(\theta)^2 G(z)^2}{4}\left(-\frac{4}{\pi k r}\right) \\
&= -\frac{\omega B^2 D^2 F(\theta)^2 G(z)^2}{\pi r}
\end{aligned}
\tag{295}
$$

$$
\begin{aligned}
\overline{\frac{1}{r}\frac{\partial \phi}{\partial t}\frac{\partial \phi}{\partial \theta}} &= \frac{1}{2}\Re\left(\left(-i\omega B e^{i\beta} D E(r) F(\theta) G(z)\right)^{*}\left(-B e^{i\beta} D E(r) m F'(\theta) G(z)\right)\right) \\
&= \frac{m\omega B^2 D^2 F(\theta) F'(\theta) G(z)^2}{2}\Re\left(\left(e^{i\beta}\right)^{*} e^{i\beta}\left(i E(r)\right)^{*} E(r)\right) \\
&= \frac{m\omega B^2 D^2 F(\theta) F'(\theta) G(z)^2}{2}\Re\left(\left(-i J_m(kr) - Y_m(kr)\right)\left(J_m(kr) + i Y_m(kr)\right)\right) \\
&= \frac{m\omega B^2 D^2 F(\theta) F'(\theta) G(z)^2}{2}\Re\left(Y_m(kr) J_m(kr) - Y_m(kr) J_m(kr) - i\left(J_m(kr)^2 + Y_m(kr)^2\right)\right) \\
&= -\frac{m\omega B^2 D^2 F(\theta) F'(\theta) G(z)^2}{2}\Re\left(i\left(J_m(kr)^2 + Y_m(kr)^2\right)\right) \\
&= 0
\end{aligned}
\tag{296}
$$

$$
\begin{aligned}
\overline{\frac{\partial \phi}{\partial t}\frac{\partial \phi}{\partial z}} &= \frac{1}{2}\Re\left(\left(-i\omega B e^{i\beta} D E(r) F(\theta) G(z)\right)^{*}\left(k B e^{i\beta} D E(r) F(\theta) G'(z)\right)\right) \\
&= \frac{k\omega B^2 D^2 F(\theta)^2 G(z) G'(z)^2}{2}\Re\left(\left(e^{i\beta}\right)^{*} e^{i\beta}\left(-i E(r)\right)^{*} E(r)\right) \\
&= 0 \qquad \left(\text{from the results for } \overline{\frac{1}{r}\frac{\partial \phi}{\partial t}\frac{\partial \phi}{\partial \theta}}\right)
\end{aligned}
\tag{297}
$$

Substitute the results from Equations 296, 297 and 298 into Equation 288.

$$\begin{aligned}\vec{\dot{E}} &= -\rho \int_{-h}^{0} \overline{\frac{\partial \phi}{\partial t}\frac{\partial \phi}{\partial r}}\, dz\, \hat{r} \\ &= \rho \int_{-h}^{0} \frac{\omega B^2 D^2 F(\theta)^2 G(z)^2}{\pi r}\, dz\, \hat{r}\end{aligned} \tag{298}$$

It is then possible to resolve the integral:

$$\begin{aligned}\vec{\dot{E}} &= \rho \int_{-h}^{0} \frac{\omega D^2 F(\theta)^2 G(z)^2}{\pi r}\, dz\, \hat{r} \\ &= \frac{\rho \omega D^2 F(\theta)^2}{\pi r} \int_{-h}^{0} G(z)^2\, dz\, \hat{r} \\ &= \frac{\rho \omega g^2 B^2 F(\theta)^2}{\omega^2 \cosh^2(k(h+z))\pi r} \int_{-h}^{0} \cosh^2(k(h+z))\, dz\, \hat{r} \\ &= \frac{\rho \omega g^2 B^2 F(\theta)^2}{g k \tanh(k h)\cosh^2(k h)\pi r} \int_{-h}^{0} \frac{1}{2}\left(\cosh(2k(h+z))+1\right) dz\, \hat{r} \\ &= \frac{\rho \omega g B^2 F(\theta)^2}{k \frac{\sinh(k h)}{\cosh(kh)}\cosh^2(k h)\pi r}\left[\frac{1}{2}\left(\frac{\sinh(2k(h+z))}{2k}+z\right)\right]_{-h}^{0} \hat{r}\end{aligned} \tag{299}$$

$$\begin{aligned}\vec{\dot{E}} &= \frac{\rho\,\omega\,g\,B^2\,F(\theta)^2}{2\pi\,k\,r\,\sinh(k\,h)\cosh(k\,h)}\left(\left(\frac{\sinh(2\,k\,h)}{2\,k}+0\right)-\left(\frac{\sinh(0)}{2\,k}-h\right)\right)\hat{r}\\ &= \frac{\rho\,\omega\,g\,B^2\,F(\theta)^2}{2\pi\,k\,r\,\frac{1}{2}\sinh(2\,k\,h)}\left(\frac{\sinh(2\,k\,h)}{2\,k}+h\right)\hat{r}\\ &= \frac{\rho\,\omega\,g\,B^2\,F(\theta)^2}{2\pi\,k^2\,r}\left(1+\frac{2\,k\,h}{\sinh(2\,k\,h)}\right)\hat{r}\end{aligned} \tag{299}$$

This gives a succinct expression for the rate of energy flux per unit surface area.

$$\vec{\dot{E}} = \frac{\rho\,\omega\,g\,B^2\cos^2(m\,\theta-\zeta)}{2\pi\,k^2\,r}\left(1+\frac{2\,k\,h}{\sinh(2\,k\,h)}\right)\hat{r} \tag{300}$$

A3.2 Calculating the Energy Density per Unit Surface Area

The next part of the puzzle is to calculate the Energy Density per unit surface area E_A.

$$\begin{aligned} E_{Total} &= Potential\ Energy + Kinetic\ Energy \\ &= \frac{\rho g}{2}\int\int\left(h^2+2h\eta+\eta^2\right)dx\,dy+\frac{\rho}{2}\int\int\int|\vec{V}|^2\,dx\,dy\,dz \end{aligned} \tag{301}$$

And therefore, assuming a flat seabed at $z=-h$ and infinitesimally small wave amplitudes:

$$E_A = \frac{\rho g}{2}\left(h^2+2h\eta+\eta^2\right)+\frac{\rho}{2}\int_{-h}^{0}|\vec{V}|^2\,dz \tag{302}$$

Because the wave fluctuates with time it will be useful to look at the time-averaged values. This excludes the static and sinusoidal terms in the equation.

$$\overline{E}_A = \frac{\rho g}{2}\overline{\eta^2}+\frac{\rho}{2}\int_{-h}^{0}\overline{|\vec{V}|^2}\,dz \tag{303}$$

Equation 289 can be used to determine the displacement function η for outgoing radial waves.

$$\begin{aligned}\eta &= -iBe^{i\beta}\cos(m\theta-\zeta)\left(J_m(kr)+iY_m(kr)\right)e^{-i\omega t} \\ &= -iBe^{i\beta}E(r)F(\theta)H(t)\end{aligned} \tag{304}$$

And:

$$\begin{aligned}\overline{\eta^2} &= \frac{1}{2}\Re\left(\left(-iBe^{i\beta}E(r)F(\theta)\right)^*\left(-iBe^{i\beta}E(r)F(\theta)\right)\right) \\ &= \frac{B^2F(\theta)^2}{2}\Re\left(\left(e^{i\beta}\right)^*e^{i\beta}\left(-iE(r)\right)^*\left(-iE(r)\right)\right) \\ &= \frac{B^2F(\theta)^2}{2}\Re\left(\left(iJ_m(kr)+Y_m(kr)\right)\left(-iJ_m(kr)+Y_m(kr)\right)\right) \\ &= \frac{B^2F(\theta)^2}{2}\Re\left(J_m(kr)^2+Y_m(kr)^2+i\left(J_m(kr)Y_m(kr)-Y_m(kr)J_m(kr)\right)\right) \\ &= \frac{B^2F(\theta)^2}{2}\Re\left(J_m(kr)^2+Y_m(kr)^2\right) \\ &= \frac{B^2F(\theta)^2}{2}\left(J_m(kr)^2+Y_m(kr)^2\right)\end{aligned} \tag{305}$$

The time-averaged value of square of the velocity $\vec{V}$ can be expressed in terms of the cylindrical coordinates gradient.

$$\overline{|\vec{V}|^2} = \overline{\left(\frac{\partial \phi}{\partial r}\right)^2} + \overline{\left(\frac{1}{r}\frac{\partial \phi}{\partial \theta}\right)^2} + \overline{\left(\frac{\partial \phi}{\partial z}\right)^2} \tag{306}$$

From Equation 292:

$$\begin{aligned}
\overline{\left(\frac{\partial \phi}{\partial r}\right)^2} &= \frac{1}{2}\Re\left(\left(\frac{k}{2}B e^{i\beta} D E'(r) F(\theta) G(z)\right)^* \left(\frac{k}{2}B e^{i\beta} D E'(r) F(\theta) G(z)\right)\right) \\
&= \frac{k^2 B^2 D^2 F(\theta)^2 G(z)^2}{8}\Re\left(\left(e^{i\beta}\right)^* e^{i\beta}\left(J_{m-1}(kr) - J_{m+1}(kr) - i\left(Y_{m-1}(kr) - Y_{m+1}(kr)\right)\right)\right. \\
&\qquad \left.\times\left(J_{m-1}(kr) - J_{m+1}(kr) + i\left(Y_{m-1}(kr) - Y_{m+1}(kr)\right)\right)\right) \\
&= \frac{k^2 B^2 D^2 F(\theta)^2 G(z)^2}{8}\Re\left(\left(J_{m-1}(kr) - J_{m+1}(kr)\right)^2 + \left(Y_{m-1}(kr) - Y_{m+1}(kr)\right)^2\right. \\
&\qquad \left. + i\left(J_{m-1}(kr) - J_{m+1}(kr)\right)\left(Y_{m-1}(kr) - Y_{m+1}(kr)\right) - i\left(Y_{m-1}(kr) - Y_{m+1}(kr)\right)\left(J_{m-1}(kr) - J_{m+1}(kr)\right)\right) \\
&= \frac{k^2 B^2 D^2 F(\theta)^2 G(z)^2}{8}\Re\left(\left(J_{m-1}(kr) - J_{m+1}(kr)\right)^2 + \left(Y_{m-1}(kr) - Y_{m+1}(kr)\right)^2\right) \\
&= \frac{k^2 B^2 D^2 F(\theta)^2 G(z)^2}{8}\left(\left(J_{m-1}(kr) - J_{m+1}(kr)\right)^2 + \left(Y_{m-1}(kr) - Y_{m+1}(kr)\right)^2\right)
\end{aligned} \tag{307}$$

From Equation 293:

$$
\begin{aligned}
\overline{\left(\frac{1}{r}\frac{\partial \phi}{\partial \theta}\right)^2} &= \frac{1}{2}\Re\left(\left(-\frac{m}{r}B e^{i\beta} D E(r) F'(\theta) G(z)\right)^* \times\left(-\frac{m}{r}B e^{i\beta} D E(r) F'(\theta) G(z)\right)\right) \\
&= \frac{m^2 B^2 D^2 F'(\theta)^2 G(z)^2}{2r^2}\Re\left(\left(e^{i\beta}\right)^* e^{i\beta}\left(E(r)\right)^*\left(E(r)\right)\right) \\
&= \frac{m^2 B^2 D^2 F'(\theta)^2 G(z)^2}{2r^2}\Re\left(\left(J_m(kr)-i\,Y_m(kr)\right)\left(J_m(kr)+i\,Y_m(kr)\right)\right) \\
&= \frac{m^2 B^2 D^2 F'(\theta)^2 G(z)^2}{2r^2}\Re\left(J_m(kr)^2+Y_m(kr)^2-i\left(J_m(kr)\,Y_m(kr)-Y_m(kr)\,J_m(kr)\right)\right) \\
&= \frac{m^2 B^2 D^2 F'(\theta)^2 G(z)^2}{2r^2}\Re\left(J_m(kr)^2+Y_m(kr)^2\right) \\
&= \frac{m^2 B^2 D^2 F'(\theta)^2 G(z)^2}{2r^2}\left(J_m(kr)^2+Y_m(kr)^2\right)
\end{aligned}
\tag{308}
$$

From Equation 294:

$$
\begin{aligned}
\overline{\left(\frac{\partial \phi}{\partial z}\right)^2} &= \frac{1}{2}\Re\left(\left(k\,B e^{i\beta} D E(r) F(\theta) G'(z)\right)^*\left(k\,B e^{i\beta} D E(r) F(\theta) G'(z)\right)\right) \\
&= \frac{k^2 B^2 D^2 F(\theta)^2 G'(z)^2}{2}\Re\left(\left(e^{i\beta}\right)^* e^{i\beta}\left(E(r)\right)^*\left(E(r)\right)\right) \\
&= \frac{k^2 B^2 D^2 F(\theta)^2 G'(z)^2}{2}\left(J_m(kr)^2+Y_m(kr)^2\right)
\end{aligned}
\tag{309}
$$

Combining Equations 296, 297 and 298 the left most term of Equation 303 becomes:

$$\begin{aligned}
\frac{\rho}{2}\int_{-h}^{0}\overline{|\vec{V}|^2}\,dz &= \frac{\rho}{2}\int_{-h}^{0}\overline{\left(\frac{\partial\phi}{\partial r}\right)^2}+\overline{\left(\frac{1}{r}\frac{\partial\phi}{\partial\theta}\right)^2}+\overline{\left(\frac{\partial\phi}{\partial z}\right)^2}\,dz \\
&= \frac{\rho}{2}\int_{-h}^{0}\left(\frac{k^2B^2D^2F(\theta)^2G(z)^2}{8}\left(\left|J_{m-1}(kr)-J_{m+1}(kr)\right|^2+\left|Y_{m-1}(kr)-Y_{m+1}(kr)\right|^2\right)\right. \\
&\qquad \left.+\frac{m^2B^2D^2F'(\theta)^2G(z)^2}{2r^2}\left(J_m(kr)^2+Y_m(kr)^2\right)+\frac{k^2B^2D^2F(\theta)^2G'(z)^2}{2}\left(J_m(kr)^2+Y_m(kr)^2\right)\right)dz \\
&= \frac{\rho k^2B^2D^2F(\theta)^2}{16}\left(\left|J_{m-1}(kr)-J_{m+1}(kr)\right|^2+\left|Y_{m-1}(kr)-Y_{m+1}(kr)\right|^2\right)\int_{-h}^{0}G(z)^2\,dz \\
&\qquad +\frac{\rho m^2B^2D^2F'(\theta)^2}{4r^2}\left(J_m(kr)^2+Y_m(kr)^2\right)\int_{-h}^{0}G(z)^2\,dz+\frac{\rho k^2B^2D^2F(\theta)^2}{4}\left(J_m(kr)^2+Y_m(kr)^2\right)\int_{-h}^{0}G'(z)^2\,dz \qquad (310)\ 1\text{ of }2 \\
&= \left(\frac{\rho k^2B^2D^2F(\theta)^2}{16}\left(\left|J_{m-1}(kr)-J_{m+1}(kr)\right|^2+\left|Y_{m-1}(kr)-Y_{m+1}(kr)\right|^2\right)\right. \\
&\qquad \left.+\frac{\rho m^2B^2D^2F'(\theta)^2}{4r^2}\left(J_m(kr)^2+Y_m(kr)^2\right)\right)\int_{-h}^{0}G(z)^2\,dz+\frac{\rho k^2B^2D^2F(\theta)^2}{4}\left(J_m(kr)^2+Y_m(kr)^2\right)\int_{-h}^{0}G'(z)^2\,dz \\
&= \left(\frac{\rho k^2B^2D^2F(\theta)^2}{16}\left(\left|J_{m-1}(kr)-J_{m+1}(kr)\right|^2+\left|Y_{m-1}(kr)-Y_{m+1}(kr)\right|^2\right)+\frac{\rho m^2B^2D^2F'(\theta)^2}{4r^2}\left(J_m(kr)^2+Y_m(kr)^2\right)\right) \\
&\qquad \times\int_{-h}^{0}\cosh(k(h+z))^2\,dz+\frac{\rho k^2B^2D^2F(\theta)^2}{4}\left(J_m(kr)^2+Y_m(kr)^2\right)\int_{-h}^{0}\sinh(k(h+z))^2\,dz
\end{aligned}$$

$$\begin{aligned}\frac{\rho}{2}\int_{-h}^{0}\left|\overline{\vec{V}}\right|^2 dz &= \left(\frac{\rho\, k\, g\, B^2 F(\theta)^2}{8\sinh(2\,k\,h)}\left(\left(J_{m-1}(kr)-J_{m+1}(kr)\right)^2+\left(Y_{m-1}(kr)-Y_{m+1}(kr)\right)^2\right)\right.\\ &\left.+\frac{\rho\, g\, m^2 B^2 F'(\theta)^2}{2\,k\,r^2\sinh(2\,k\,h)}\left(J_m(kr)^2+Y_m(kr)^2\right)\right)\frac{1}{2}\left(\frac{\sinh(2\,k\,h)}{2\mathrm{k}}+h\right)+\frac{\rho\, g\, B^2 k\, F(\theta)^2}{2\sinh(2\,k\,h)}\left(J_m(kr)^2+Y_m(kr)^2\right)\frac{1}{2}\left(\frac{\sinh(2\,k\,h)}{2\mathrm{k}}-h\right)\\ &= \left(\frac{\rho\, g\, B^2 F(\theta)^2}{32}\left(\left(J_{m-1}(kr)-J_{m+1}(kr)\right)^2+\left(Y_{m-1}(kr)-Y_{m+1}(kr)\right)^2\right)\right.\\ &\left.+\frac{\rho\, g\, m^2 B^2 F'(\theta)^2}{8\,k^2 r^2}\left(J_m(kr)^2+Y_m(kr)^2\right)\right)\left(1+\frac{2\,k\,h}{\sinh(2\,k\,h)}\right)+\frac{\rho\, g\, B^2 F(\theta)^2}{8}\left(J_m(kr)^2+Y_m(kr)^2\right)\left(1-\frac{2\,k\,h}{\sinh(2\,k\,h)}\right)\end{aligned} \tag{310}$$

2 of 2

This result can be combined Equations 303 and 305 to give the full expression for the energy density per unit surface area.

$$\begin{aligned}\overline{E}_A &= \frac{\rho\, g}{2}\left(\overline{\eta^2}\right)+\frac{\rho}{2}\int_{-h}^{0}\left|\overline{\vec{V}}\right|^2 dz\\ &= \frac{\rho\, g}{2}\frac{B^2 F(\theta)^2}{2}\left(J_m(k\,r)^2+Y_m(k\,r)^2\right)+\left(\frac{\rho\, g\, B^2 F(\theta)^2}{32}\left(\left(J_{m-1}(kr)-J_{m+1}(kr)\right)^2+\left(Y_{m-1}(kr)-Y_{m+1}(kr)\right)^2\right)\right.\\ &\left.+\frac{\rho\, g\, m^2 B^2 F'(\theta)^2}{8\,k^2 r^2}\left(J_m(kr)^2+Y_m(kr)^2\right)\right)\left(1+\frac{2\,k\,h}{\sinh(2\,k\,h)}\right)+\frac{\rho\, g\, B^2 F(\theta)^2}{8}\left(J_m(kr)^2+Y_m(kr)^2\right)\left(1-\frac{2\,k\,h}{\sinh(2\,k\,h)}\right)\end{aligned} \tag{311}$$

1 of 2

$$\overline{E}_A = \frac{\rho g B^2}{8}\left(\left(\frac{F(\theta)^2}{4}\left(\left(J_{m-1}(kr)-J_{m+1}(kr)\right)^2+\left(Y_{m-1}(kr)-Y_{m+1}(kr)\right)^2\right)+\frac{m^2 F'(\theta)^2}{k^2 r^2}\left(J_m(kr)^2+Y_m(kr)^2\right)\right)\left(1+\frac{2kh}{\sinh(2kh)}\right)\right.$$
$$\left.+F(\theta)^2\left(J_m(kr)^2+Y_m(kr)^2\right)\left(3-\frac{2kh}{\sinh(2kh)}\right)\right) \quad (311)$$
2 of 2

The result from Equation 311 is the energy density per unit area expressed in cylindrical coordinates.

A3.3 Calculating the Group Velocity for Radial Waves

Group velocity, c_g, is defined as the velocity at which a wave transports energy. It can be expressed in terms of the rate of energy flux per unit surface area and the energy density per unit surface area. This leads to the general expression for the group velocity of a single radiated wave:

$$
\begin{aligned}
c_g &= \frac{\vec{\dot{E}}}{\overline{E}_A} \\
&= \frac{\dfrac{\rho\,\omega\,g\,B^2\,F(\theta)^2}{2\,\pi\,k^2\,r}\left(1+\dfrac{2\,k\,h}{\sinh(2\,k\,h)}\right)\hat{r}}{\left(\dfrac{\rho\,g\,B^2}{8}\left(\left(\dfrac{F(\theta)^2}{4}\left(\left(J_{m-1}(kr)-J_{m+1}(kr)\right)^2+\left(Y_{m-1}(kr)-Y_{m+1}(kr)\right)^2\right)+\dfrac{m^2\,F'(\theta)^2}{k^2\,r^2}\left(J_m(kr)^2+Y_m(kr)^2\right)\right)\left(1+\dfrac{2\,k\,h}{\sinh(2\,k\,h)}\right)\right.\right. \\
\left.\left.+F(\theta)^2\left(J_m(kr)^2+Y_m(kr)^2\right)\left(3-\dfrac{2\,k\,h}{\sinh(2\,k\,h)}\right)\right)\right)} \\
&= \frac{\dfrac{4\,\omega\,F(\theta)^2}{\pi\,k^2\,r}\left(1+\dfrac{2\,k\,h}{\sinh(2\,k\,h)}\right)\hat{r}}{\left(\dfrac{F(\theta)^2}{4}\left(\left(J_{m-1}(kr)-J_{m+1}(kr)\right)^2+\left(Y_{m-1}(kr)-Y_{m+1}(kr)\right)^2\right)+\dfrac{m^2\,F'(\theta)^2}{k^2\,r^2}\left(J_m(kr)^2+Y_m(kr)^2\right)\right)\left(1+\dfrac{2\,k\,h}{\sinh(2\,k\,h)}\right)} \\
&\qquad\left.+F(\theta)^2\left(J_m(kr)^2+Y_m(kr)^2\right)\left(3-\dfrac{2\,k\,h}{\sinh(2\,k\,h)}\right)\right)
\end{aligned}
\tag{312}
$$

Further to the general solution, it is also possible to determine the expression for the group velocity at large a large distance from the origin.

As $kr \to \infty$ the expressions in Equation 312 involving Bessel functions can be simplified. Note:

$$\left(\left(J_{m-1}(kr)-J_{m+1}(kr)\right)^2+\left(Y_{m-1}(kr)-Y_{m+1}(kr)\right)^2\right)\to\frac{8}{\pi k r} \quad \text{as} \quad k r\to\infty \tag{313}$$

And:

$$\left(J_m(kr)^2+Y_m(kr)^2\right)\to\frac{2}{\pi k r} \quad \text{as} \quad k r\to\infty \tag{314}$$

So:

$$\begin{aligned} c_g &\to \frac{\frac{4\omega F(\theta)^2}{\pi k^2 r}\left(1+\frac{2kh}{\sinh(2kh)}\right)\hat{r}}{\left(\left(\frac{F(\theta)^2}{4}\frac{8}{\pi k r}+\frac{m^2F'(\theta)^2}{k^2r^2}\frac{2}{\pi k r}\right)\left(1+\frac{2kh}{\sinh(2kh)}\right)+F(\theta)^2\frac{2}{\pi k r}\left(3-\frac{2kh}{\sinh(2kh)}\right)\right)} \quad \text{as} \quad kr\to\infty \\ &\to \frac{\frac{4\omega F(\theta)^2}{\pi k^2 r}\left(1+\frac{2kh}{\sinh(2kh)}\right)\hat{r}}{\left(\left(\frac{2F(\theta)^2}{\pi k r}+\frac{2m^2F'(\theta)^2}{\pi k^3 r^3}\right)\left(1+\frac{2kh}{\sinh(2kh)}\right)+\frac{2F(\theta)^2}{\pi k r}\left(3-\frac{2kh}{\sinh(2kh)}\right)\right)} \quad \text{as} \quad kr\to\infty \end{aligned} \tag{315}$$

$$c_g \rightarrow \frac{\frac{2\omega}{k}\left(1+\frac{2kh}{\sinh(2kh)}\right)\hat{r}}{\left(\left(1+\frac{m^2F'(\theta)^2}{k^2r^2F(\theta)^2}\right)\left(1+\frac{2kh}{\sinh(2kh)}\right)+\left(3-\frac{2kh}{\sinh(2kh)}\right)\right)} \quad \text{as} \quad kr\rightarrow\infty$$

$$\rightarrow \frac{\frac{2\omega}{k}\left(1+\frac{2kh}{\sinh(2kh)}\right)\hat{r}}{\left(4+\frac{m^2\tan^2(m\theta-\zeta)}{k^2r^2}\left(1+\frac{2kh}{\sinh(2kh)}\right)\right)} \quad \text{as} \quad kr\rightarrow\infty \tag{315}$$

If it is assumed that the circular wave is a theoretical heave wave (i.e. $m=0$) then:

$$c_{g\infty}\Big|_{m=0} \rightarrow \frac{\frac{2\omega}{k}\left(1+\frac{2kh}{\sinh(2kh)}\right)\hat{r}}{\left(4+\frac{0^20^2}{k^2r^2}\left(1+\frac{2kh}{\sinh(2kh)}\right)\right)} \quad \text{as} \quad kr\rightarrow\infty$$

$$\rightarrow \frac{\omega}{2k}\left(1+\frac{2kh}{\sinh(2kh)}\right)\hat{r} \quad \text{as} \quad kr\rightarrow\infty \tag{316}$$

Equation 316 is almost same expression as derived for plane waves. The only difference is that the velocity is not directed in the direction of incidence but radially outward from the source This means that as a radial wave radiates out further and further the group velocity tends toward that of plane wave. If $m \neq 0$ and providing $m\theta - \zeta$ does not tend to $\frac{\pi}{2} + a\pi$, where $a \in \mathbb{Z}$, then:

$$c_{g\infty}\Big|_{m\neq 0 \;\; (m\theta-\zeta)\neq\left(\frac{\pi}{2}+a\pi\right)} \;\rightarrow\; \frac{\omega}{2k}\left(1+\frac{2kh}{\sinh(2kh)}\right)\hat{r} \quad \text{as} \quad kr\rightarrow\infty \tag{317}$$

However, as $m\theta - \gamma \rightarrow \frac{\pi}{2} + a\pi$, then the term $\frac{m^2\tan^2(m\theta-\zeta)}{k^2r^2}\rightarrow\infty$ and $c_{g\infty}\rightarrow 0$. This means that, for circular waves with orders greater than zero, the group velocity tends towards the plane wave group velocity for that wavelength except in the areas where there is no surface displacement. In these areas the group velocity tends to zero.

Appendix 4: Circular Waves and the Sommerfeld Radiation Condition

This appendix applies the Sommerfeld radiation condition to circular waves to determine the conditions under which circular waves represent scattered waves. The Sommerfeld radiation condition is given in Section 5.6.2 from [22]:

$$\lim_{r\to\infty}\sqrt{(r)}\left(\frac{\partial}{\partial r}\pm i\lambda\right)\phi_s=0 \tag{318}$$

Where ϕ_s is the scattering potential, λ is an eigenvalue and the sign associated with λ depends on the sign of the time harmonic i.e. $+i\lambda$ if $e^{i\omega t}$ is used and $-i\lambda$ for $e^{-i\omega t}$. Note that $\lambda>0$ [78].

Assuming the circular wave velocity potential is given by Eqn 158 and $D=\frac{g}{\omega\cosh(k\,h)}$:

$$\phi=B\,e^{i\beta}\,D\,H_m(kr)\cos(m\theta-\zeta)\cosh(k(h+z))e^{-i\omega t} \tag{319}$$

Then:

$$\frac{\partial\phi}{\partial r}\;=\;\frac{k}{2}B\,e^{i\beta}\,D\cos(m\theta-\zeta)\left(H_{m-1}(kr)-H_{m+1}(kr)\right)\cosh(k(h+z))\,e^{-i\omega t} \tag{320}$$

It is assumed that the Hankel function in Eqn 158 is of the first kind (see Section 4.1.4). Note that:

$$\lim_{r\to\infty} H_m(kr) \approx \sqrt{\frac{2}{\pi k r}}\, e^{i\left(kr-\frac{(2m+1)\pi}{4}\right)} \tag{321}$$

Substituting Eqns 320 and 321 into 318:

$$\begin{aligned}
\lim_{r\to\infty}\sqrt{r}\left(\frac{\partial}{\partial r}-i\lambda\right)\phi_s &= \lim_{r\to\infty} B e^{i\beta} D\cosh(k(h+z))\cos(m\theta-\zeta)\sqrt{r}\left(\frac{k}{2}\left(H_{m-1}(kr)-H_{m+1}(kr)\right)-i\lambda H_m(kr)\right)e^{-i\omega t} \\
&= B e^{i\beta} D\cosh(k(h+z))\cos(m\theta-\zeta)\sqrt{r}\left(\frac{k}{2}\left(\sqrt{\frac{2}{\pi k r}}e^{i\left(kr-\frac{(2(m-1)+1)\pi}{4}\right)}-\sqrt{\frac{2}{\pi k r}}e^{i\left(kr-\frac{(2(m+1)+1)\pi}{4}\right)}\right)\right. \\
&\qquad \left.-i\lambda\sqrt{\frac{2}{\pi k r}}e^{i\left(kr-\frac{(2m+1)\pi}{4}\right)}\right)e^{-i\omega t} \\
&= B e^{i\beta} D\cosh(k(h+z))\cos(m\theta-\zeta)\sqrt{\frac{2}{\pi k}}\left(\frac{k}{2}\left(e^{i\left(kr-\frac{m}{2}\pi+\frac{1}{4}\pi\right)}-e^{i\left(kr-\frac{m}{2}\pi-\frac{3}{4}\pi\right)}\right)-i\lambda e^{i\left(kr-\frac{m}{2}\pi+\frac{1}{4}\pi\right)}\right)e^{-i\omega t} \\
&= B e^{i\beta} D\cosh(k(h+z))\sqrt{\frac{2}{\pi k}}B e^{i\left(kr-\frac{m}{2}\pi\right)}\cos(m\theta-\zeta)\left(\frac{k}{2}\left(e^{i\frac{1}{4}\pi}-e^{-i\frac{3}{4}\pi}\right)-i\lambda e^{-i\frac{1}{4}\pi}\right)e^{-i\omega t} \\
&= B e^{i\beta} D\cosh(k(h+z))\sqrt{\frac{2}{\pi k}}B e^{i\left(kr-\frac{2m-1}{4}\pi\right)}\cos(m\theta-\zeta)\left(\frac{k}{2}\left(e^{i0}-e^{-i\pi}\right)-i\lambda e^{-i\frac{1}{2}\pi}\right)e^{-i\omega t} \\
&= B e^{i\beta} D\cosh(k(h+z))\sqrt{\frac{2}{\pi k}}B e^{i\left(kr-\frac{2m-1}{4}\pi\right)}\cos(m\theta-\zeta)\left(\frac{k}{2}(1+1)-\lambda\right)e^{-i\omega t}
\end{aligned} \tag{322}$$

$$\lim_{r\to\infty}\sqrt{r}\left(\frac{\partial}{\partial r}-i\lambda\right)\phi_s = B e^{i\beta} D\cosh(k(h+z))\sqrt{\frac{2}{\pi k}} B e^{i\left(kr-\frac{2m-1}{4}\pi\right)}\cos(m\theta-\zeta)(k-\lambda)e^{-i\omega t} \quad (322)$$
2 of 2

For the Sommerfeld radiation condition to be fulfilled for Hankel functions of the first kind the eigenvalue, λ, must equal k. Hence, when the time harmonic is defined by $e^{-i\omega t}$, any circular waves defined by Hankel functions of the first kind are radiated waves.

The situation can also be examined for Hankel functions of the second kind. Then:

$$\lim_{r\to\infty} H_m^2(kr)\approx\sqrt{\frac{2}{\pi k r}}e^{-i\left(kr-\frac{(2m+1)\pi}{4}\right)} \quad (323)$$

Substituting Eqns 320 and 323 into 318:

$$\begin{aligned}\lim_{r\to\infty}\sqrt{r}\left(\frac{\partial}{\partial r}-i\lambda\right)\phi_s &= \lim_{r\to\infty} B e^{i\beta} D\cosh(k(h+z))\cos(m\theta-\zeta)\sqrt{r}\left(\frac{k}{2}\left(H_{m-1}^2(kr)-H_{m+1}^2(kr)\right)-i\lambda H_m^2(kr)\right)e^{-i\omega t}\\ &= B e^{i\beta} D\cosh(k(h+z))\cos(m\theta-\zeta)\sqrt{r}\left(\frac{k}{2}\left(\sqrt{\frac{2}{\pi k r}}e^{-i\left(kr-\frac{(2(m-1)+1)\pi}{4}\right)}-\sqrt{\frac{2}{\pi k r}}e^{-i\left(kr-\frac{(2(m+1)+1)\pi}{4}\right)}\right)\right.\\ &\qquad \left.-i\lambda\sqrt{\frac{2}{\pi k r}}e^{-i\left(kr-\frac{(2m+1)\pi}{4}\right)}\right)e^{-i\omega t}\end{aligned} \quad (324)$$
1 of 2

$$
\begin{aligned}
\lim_{r\to\infty}\sqrt{r}\left(\frac{\partial}{\partial r}-i\lambda\right)\phi_s &= B e^{i\beta} D\cosh(k(h+z))\cos(m\theta-\zeta)\sqrt{\frac{2}{\pi k}}\left(\frac{k}{2}\left(e^{-i\left(kr-\frac{m}{2}\pi+\frac{1}{4}\pi\right)}-e^{-i\left(kr-\frac{m}{2}\pi-\frac{3}{4}\pi\right)}\right)-i\lambda e^{-i\left(kr-\frac{m}{2}\pi+\frac{1}{4}\pi\right)}\right)e^{-i\omega t} \\
&= B e^{i\beta} D\cosh(k(h+z))\sqrt{\frac{2}{\pi k}} B e^{i\left(kr-\frac{m}{2}\pi\right)}\cos(m\theta-\zeta)\left(\frac{k}{2}\left(e^{-i\frac{1}{4}\pi}-e^{i\frac{3}{4}\pi}\right)-i\lambda e^{i\frac{1}{4}\pi}\right)e^{-i\omega t} \\
&= B e^{i\beta} D\cosh(k(h+z))\sqrt{\frac{2}{\pi k}} B e^{i\left(kr-\frac{2m+1}{4}\pi\right)}\cos(m\theta-\zeta)\left(\frac{k}{2}\left(e^{i0}-e^{i\pi}\right)-i\lambda e^{i\frac{1}{2}\pi}\right)e^{-i\omega t} \\
&= B e^{i\beta} D\cosh(k(h+z))\sqrt{\frac{2}{\pi k}} B e^{i\left(kr-\frac{2m-1}{4}\pi\right)}\cos(m\theta-\zeta)\left(\frac{k}{2}(1+1)+\lambda\right)e^{-i\omega t} \\
&= B e^{i\beta} D\cosh(k(h+z))\sqrt{\frac{2}{\pi k}} B e^{i\left(kr-\frac{2m-1}{4}\pi\right)}\cos(m\theta-\zeta)(k+\lambda)e^{-i\omega t}
\end{aligned}
\tag{324}
$$

For the Sommerfeld radiation condition to be fulfilled for Hankel functions of the second kind the eigenvalue, λ, must equal $-k$. As, by definition, the eigenvalue can only be positive, the Sommerfeld radiation condition cannot be met for all values of r, θ, z and t. Hence, in the case where the harmonic function is defined as $e^{-i\omega t}$, circular waves defined by Hankel functions of the second kind are not radiated waves.

Appendix 5: Radiated Power for Combinations of Plane and Circular Waves

The power radiated by the combination of plane and circular waves is derived below. The case studied is the general case where any number of plane waves of different frequencies, orientations amplitudes and phases may interact with any number of circular waves of different frequencies, modes, orientations, amplitudes and phases.

The expression for power can be written in a number of forms. One of the forms that is useful to fluids is:

$$\begin{aligned} Power &= Force \cdot Velocity \\ &= Pressure \cdot Area \cdot Velocity \end{aligned} \tag{325}$$

In the context of circular waves and complex velocity potentials pressure, assuming the particle velocities are small, can be expressed as:

$$Pressure = -\rho g z + \rho \frac{\partial \phi}{\partial t} \tag{326}$$

The velocity is given by:

$$Velocity = \vec{V} = -\nabla \phi \tag{327}$$

The area depends on the situation being examined. For instance, if a plane wave was being examined, an area perpendicular to the plane wave extending to the sea floor and infinitely wide would be appropriate. However, if a circular wave was being examined a cylindrical surface of a given radius may give more information. To simplify the calculation assume that the Area is constant with time.

Now, because of the cyclic nature of waves examining the elemental change in time-averaged power, $d\overline{P}$, is useful. So:

$$d\overline{P} = \overline{-\rho g z \nabla \phi \, d\vec{A}_r} - \overline{\rho \frac{\partial \phi}{\partial t} \nabla \phi \, d\vec{A}_r} \tag{328}$$

The time average power of a single sine or cosine function is zero. This means that the $\overline{-\rho g z \Delta \phi}$ term equals zero as all of the velocities are time harmonic. Therefore in circular cylindrical coordinates. Note it is assumed that the definition of the area does not oscillate with time. So:

$$\begin{aligned} d\overline{P} &= -\overline{\rho \frac{\partial \phi}{\partial t} \nabla \phi \, d\vec{A}_r} \\ &= -\overline{\rho \frac{\partial \phi}{\partial t} \left(\frac{\partial \phi}{\partial r} \hat{r} + \frac{1}{r} \frac{\partial \phi}{\partial \theta} \hat{\theta} + \frac{\partial \phi}{\partial z} \hat{z} \right) d\vec{A}_r} \\ &= -\rho \left(\overline{\frac{\partial \phi}{\partial t} \frac{\partial \phi}{\partial r}} \hat{r} + \overline{\frac{\partial \phi}{\partial t} \frac{1}{r} \frac{\partial \phi}{\partial \theta}} \hat{\theta} + \overline{\frac{\partial \phi}{\partial t} \frac{\partial \phi}{\partial z}} \hat{z} \right) d\vec{A}_r \end{aligned} \tag{329}$$

If it is assumed that ϕ is some combination of plane waves and circular waves and that all the circular waves are centred on a single point then ϕ can be expressed by the following equation:

$$\phi = \sum_{a=1}^{a_a}\sum_{b=1}^{b_a}\sum_{c=1}^{c_{ab}} A_{abc} e^{i\alpha_{abc}} D_a G_a e^{ik_a r\cos(\theta-\gamma_{ab})} e^{-i\omega_a t} + \sum_{a=1}^{a_a}\sum_{d=1}^{d_d}\sum_{e=1}^{e_{ad}}\sum_{f=1}^{f_{ade}} B_{adef} e^{i\beta_{adef}} D_a H_{m_d}^{(1)}(k_a r) F_{de} G_a e^{-i\omega_a t} \quad (330)$$

Note: implicit in this definition is that there is only one direction of incident wave for each wavelength, amplitude and phase.

Note in general: that r, θ, z and t are the three spacial cylindrical coordinate variables and time.

The subscripts for variables have been attributed as follows. Waves of a_a different wave numbers (k_a) have been introduced to the wave field. Each wave number has a group of plane waves with b_a different orientations (γ_{ab}). Each orientation has c_{ab} different phases (α_{abc}) and a corresponding amplitude (A_{abc}). Similarly, each wave number has a group of circular waves with d_a different orders (m_{ad}). Each order has e_{ad} different orientations (ζ_{ade}). Each orientation has f_{ade} different phases (β_{adef}) and a corresponding amplitude (B_{adef}). During the calculation, products of the velocity potentials arise. To preserve the different combinations of velocity potentials a second set of subscripts are required. Hence $n \in (b_{1,} b_2 \ldots b_a)$, $o \in (c_{11,} c_{12} \ldots c_{ab})$, $p \in (d_{1,} d_2 \ldots d_a)$, $q \in (e_{11,} e_{12} \ldots e_{ad})$ and $s \in (f_{111,} f_{112} \ldots f_{ade})$.

Note that: for each wave number (k_a) there is an associated phase velocity, (ω_a) given by the relationship $\omega^2 = g\,k \tanh(k\,h)$, that $H_{m_d}^{(1)}(k_a r)$ is the Hankel function of the first kind of order m and is equal to $J_{m_d}(k_a r) + i\,Y_{m_d}(k_a r)$, that $D_a = \dfrac{g}{\omega_a \cosh(k_a h)}$, that $G_a = \cosh(k_a(h+z))$, and that $F_{de} = \cos(m_d \theta - \zeta_{de})$.

Note for ζ: If $m=0$ then $\zeta=0$ so that $\cos(\zeta)=1$, if $m=1,2,3....$ then $\cos(m\theta-\zeta)$ allows ζ to have a rotating effect, and if $m\neq 0,1,2,3....$ then $\zeta=n\pi$ to satisfy first order continuity and second order continuity cannot be satisfied.

Mei, Stiassnie and Yue [17] define the time-average value of two harmonic functions, $f_1=F_1 e^{i\omega_1 t}$ and $f_2=F_2 e^{i\omega_2 t}$, where F_1 and F_2 are complex and $\omega_1=\omega_2$ as:

$$\overline{f_1 f_2} = \frac{1}{2}\Re\left(F_1^* F_2\right) \tag{331}$$

Also note that if $\omega_1\neq\omega_2$ then $\overline{f_1 f_2}=0$. Given ϕ is defined by Equation 330 and it is possible to calculate each term in Equation 329. Starting with the time derivative term:

$$\frac{\partial\phi}{\partial t} = \sum_{a=1}^{a_a}\sum_{b=1}^{b_a}\sum_{c=1}^{c_{ab}} -i\omega_a A_{abc} e^{i\alpha_{abc}} D_a G_a e^{i k_a r\cos(\theta-\gamma_{ab})} e^{-i\omega_a t} + \sum_{a=1}^{a_a}\sum_{d=1}^{d_d}\sum_{e=1}^{e_{ad}}\sum_{f=1}^{f_{ade}} -i\omega_a B_{adef} e^{i\beta_{adef}} D_a H_{m_d}^{(1)}(k_a r) F_{de} G_a e^{-i\omega_a t} \tag{332}$$

A useful quantity for calculating the time-averaged power is:

$$
\begin{aligned}
\left(\frac{\partial \phi}{\partial t}\frac{1}{e^{-i\omega_a t}}\right)^* &= \left(\sum_{a=1}^{a_a}\sum_{b=1}^{b_a}\sum_{c=1}^{c_{ab}} \omega_a A_{abc} D_a G_a \left(-i\cos(k_a r\cos(\theta-\gamma_{ab})+\alpha_{abc})+\sin(k_a r\cos(\theta-\gamma_{ab})+\alpha_{abc})\right)\right. \\
&\qquad \left. +\sum_{a=1}^{a_a}\sum_{d=1}^{d_d}\sum_{e=1}^{e_{ad}}\sum_{f=1}^{f_{ade}} \omega_a D_a F_{de} G_a B_{adef}\left(\sin(\beta_{adef})-i\cos(\beta_{adef})\right)\left(J_{m_d}(k_a r)+iY_{m_d}(k_a r)\right)\right)^* \\
&= \left(\sum_{a=1}^{a_a}\sum_{b=1}^{b_a}\sum_{c=1}^{c_{ab}} \omega_a A_{abc} D_a G_a \left(-i\cos(k_a r\cos(\theta-\gamma_{ab})+\alpha_{abc})+\sin(k_a r\cos(\theta-\gamma_{ab})+\alpha_{abc})\right)\right. \\
&\qquad +\sum_{a=1}^{a_a}\sum_{d=1}^{d_d}\sum_{e=1}^{e_{ad}}\sum_{f=1}^{f_{ade}} \omega_a D_a F_{de} G_a B_{adef}\left(J_{m_d}(k_a r)\sin(\beta_{adef})-iJ_{m_d}(k_a r)\cos(\beta_{adef})\right. \\
&\qquad \left.\left. +iY_{m_d}(k_a r)\sin(\beta_{adef})+Y_{m_d}(k_a r)\cos(\beta_{adef})\right)\right)^* \\
&= \left(\sum_{a=1}^{a_a}\sum_{b=1}^{b_a}\sum_{c=1}^{c_{ab}} \omega_a A_{abc} D_a G_a \sin(k_a r\cos(\theta-\gamma_{ab})+\alpha_{abc})\right. \\
&\qquad +\sum_{a=1}^{a_a}\sum_{d=1}^{d_d}\sum_{e=1}^{e_{ad}}\sum_{f=1}^{f_{ade}} \omega_a D_a F_{de} G_a B_{adef}\left(J_{m_d}(k_a r)\sin(\beta_{adef})+Y_{m_d}(k_a r)\cos(\beta_{adef})\right) \\
&\qquad +i\left(\sum_{a=1}^{a_a}\sum_{b=1}^{b_a}\sum_{c=1}^{c_{ab}} -\omega_a A_{abc} D_a G_a \cos(k_a r\cos(\theta-\gamma_{ab})+\alpha_{abc})\right. \\
&\qquad \left.\left.\left. +\sum_{a=1}^{a_a}\sum_{d=1}^{d_d}\sum_{e=1}^{e_{ad}}\sum_{f=1}^{f_{ade}} \omega_a D_a F_{de} G_a B_{adef}\left(Y_{m_d}(k_a r)\sin(\beta_{adef})-J_{m_d}(k_a r)\cos(\beta_{adef})\right)\right)\right)^*
\end{aligned}
$$

(333)
1 of 2

$$\left(\frac{\partial \phi}{\partial t}\frac{1}{e^{-i\omega_a t}}\right)^* = \sum_{a=1}^{a_a}\sum_{b=1}^{b_a}\sum_{c=1}^{c_{ab}} \omega_a A_{abc} D_a G_a \sin\left(k_a r\cos(\theta-\gamma_{ab})+\alpha_{abc}\right)$$
$$+\sum_{a=1}^{a_a}\sum_{d=1}^{d_d}\sum_{e=1}^{e_{ad}}\sum_{f=1}^{f_{ade}} \omega_a D_a F_{de} G_a B_{adef}\left(J_{m_d}(k_a r)\sin(\beta_{adef})+Y_{m_d}(k_a r)\cos(\beta_{adef})\right)$$
$$+i\left(\sum_{a=1}^{a_a}\sum_{b=1}^{b_a}\sum_{c=1}^{c_{ab}} \omega_a A_{abc} D_a G_a \cos\left(k_a r\cos(\theta-\gamma_{ab})+\alpha_{abc}\right)\right. \quad (333)$$
$$\left.+\sum_{a=1}^{a_a}\sum_{d=1}^{d_d}\sum_{e=1}^{e_{ad}}\sum_{f=1}^{f_{ade}} \omega_a D_a F_{de} G_a B_{adef}\left(J_{m_d}(k_a r)\cos(\beta_{adef})-Y_{m_d}(k_a r)\sin(\beta_{adef})\right)\right) \quad 2 \text{ of } 2$$
$$= \sum_{a=1}^{a_a}\sum_{b=1}^{b_a}\sum_{c=1}^{c_{ab}} T_1+\sum_{a=1}^{a_a}\sum_{d=1}^{d_d}\sum_{e=1}^{e_{ad}}\sum_{f=1}^{f_{ade}} T_2+i\left(\sum_{a=1}^{a_a}\sum_{b=1}^{b_a}\sum_{c=1}^{c_{ab}} T_3+\sum_{a=1}^{a_a}\sum_{d=1}^{d_d}\sum_{e=1}^{e_{ad}}\sum_{f=1}^{f_{ade}} T_4\right)$$

The derivative of ϕ with respect to r is:

$$\frac{\partial \phi}{\partial r} = \sum_{a=1}^{a_a}\sum_{b=1}^{b_a}\sum_{c=1}^{c_{ab}} i k_a \cos(\theta-\gamma_{ab}) A_{abc} e^{i\alpha_{abc}} D_a G_a e^{i k_a r\cos(\theta-\gamma_{ab})} e^{-i\omega_a t}$$
$$+\sum_{a=1}^{a_a}\sum_{d=1}^{d_d}\sum_{e=1}^{e_{ad}}\sum_{f=1}^{f_{ade}} \frac{k_a}{2} B_{adef} e^{i\beta_{adef}} D_a\left(J_{m_d-1}(k_a r)-J_{m_d+1}(k_a r)+i\left(Y_{m_d-1}(k_a r)-Y_{m_d+1}(k_a r)\right)\right) F_{de} G_a e^{-i\omega_a t} \quad (334)$$

Another useful quantity to calculate is:

$$\begin{aligned}
\frac{\partial \phi}{\partial r}\frac{1}{e^{-i\omega_a t}} &= \sum_{a=1}^{a_a}\sum_{b=1}^{b_a}\sum_{c=1}^{c_{ab}} i k_a \cos(\theta-\gamma_{ab}) A_{abc} D_a G_a e^{i\left(k_a r\cos(\theta-\gamma_{ab})+\alpha_{abc}\right)} \\
&\qquad + \sum_{a=1}^{a_a}\sum_{d=1}^{d_d}\sum_{e=1}^{e_{ad}}\sum_{f=1}^{f_{ade}} \frac{k_a}{2} B_{adef} e^{i\beta_{adef}} D_a F_{de} G_a \left(J_{m_d-1}(k_a r)-J_{m_d+1}(k_a r)+i\left(Y_{m_d-1}(k_a r)-Y_{m_d+1}(k_a r)\right)\right) \\
&= \sum_{a=1}^{a_a}\sum_{b=1}^{b_a}\sum_{c=1}^{c_{ab}} k_a \cos(\theta-\gamma_{ab}) A_{abc} D_a G_a \left(i\cos(k_a r\cos(\theta-\gamma_{ab})+\alpha_{abc})-\sin(k_a r\cos(\theta-\gamma_{ab})+\alpha_{abc})\right) \\
&\qquad + \sum_{a=1}^{a_a}\sum_{d=1}^{d_d}\sum_{e=1}^{e_{ad}}\sum_{f=1}^{f_{ade}} \frac{k_a}{2} B_{adef} D_a F_{de} G_a \left(\cos(\beta_{adef})+i\sin(\beta_{adef})\right)\left(J_{m_d-1}(k_a r)-J_{m_d+1}(k_a r)+i\left(Y_{m_d-1}(k_a r)-Y_{m_d+1}(k_a r)\right)\right) \\
&= \sum_{a=1}^{a_a}\sum_{b=1}^{b_a}\sum_{c=1}^{c_{ab}} k_a \cos(\theta-\gamma_{ab}) A_{abc} D_a G_a \left(i\cos(k_a r\cos(\theta-\gamma_{ab})+\alpha_{abc})-\sin(k_a r\cos(\theta-\gamma_{ab})+\alpha_{abc})\right) \\
&\qquad + \sum_{a=1}^{a_a}\sum_{d=1}^{d_d}\sum_{e=1}^{e_{ad}}\sum_{f=1}^{f_{ade}} \left(\frac{k_a}{2} B_{adef} D_a F_{de} G_a \left(i\cos(\beta_{adef})\left(Y_{m_d-1}(k_a r)-Y_{m_d+1}(k_a r)\right)-\sin(\beta_{adef})\left(Y_{m_d-1}(k_a r)-Y_{m_d+1}(k_a r)\right)\right.\right. \\
&\qquad \left.\left. +\cos(\beta_{adef})\left(J_{m_d-1}(k_a r)-J_{m_d+1}(k_a r)\right)+i\sin(\beta_{adef})\left(J_{m_d-1}(k_a r)-J_{m_d+1}(k_a r)\right)\right)\right)
\end{aligned} \tag{335}$$

1 of 2

$$
\begin{aligned}
&= \sum_{a=1}^{a_a}\sum_{b=1}^{b_a}\sum_{c=1}^{c_{ab}} -k_a\cos(\theta-\gamma_{ab})\,A_{abc}\,D_a\,G_a\sin(k_a r\cos(\theta-\gamma_{ab})+\alpha_{abc}) \\
&\quad +\sum_{a=1}^{a_a}\sum_{d=1}^{d_d}\sum_{e=1}^{e_{ad}}\sum_{f=1}^{f_{ade}}\frac{k_a}{2}B_{adef}\,D_a\,F_{de}\,G_a\Big(\cos(\beta_{adef})\big(J_{m_d-1}(k_a r)-J_{m_d+1}(k_a r)\big)-\sin(\beta_{adef})\big(Y_{m_d-1}(k_a r)-Y_{m_d+1}(k_a r)\big)\Big) \\
&\quad +i\left(\sum_{a=1}^{a_a}\sum_{b=1}^{b_a}\sum_{c=1}^{c_{ab}} k_a\cos(\theta-\gamma_{ab})\,A_{abc}\,D_a\,G_a\cos(k_a r\cos(\theta-\gamma_{ab})+\alpha_{abc})\right. \\
&\quad \left.+\sum_{a=1}^{a_a}\sum_{d=1}^{d_d}\sum_{e=1}^{e_{ad}}\sum_{f=1}^{f_{ade}}\frac{k_a}{2}B_{adef}\,D_a\,F_{de}\,G_a\Big(\cos(\beta_{adef})\big(Y_{m_d-1}(k_a r)-Y_{m_d+1}(k_a r)\big)+\sin(\beta_{adef})\big(J_{m_d-1}(k_a r)-J_{m_d+1}(k_a r)\big)\Big)\right) \\
&= \sum_{a=1}^{a_a}\sum_{b=1}^{b_a}\sum_{c=1}^{c_{ab}} -T_5+\sum_{a=1}^{a_a}\sum_{d=1}^{d_d}\sum_{e=1}^{e_{ad}}\sum_{f=1}^{f_{ade}} T_6+i\left(\sum_{a=1}^{a_a}\sum_{b=1}^{b_a}\sum_{c=1}^{c_{ab}} T_7+\sum_{a=1}^{a_a}\sum_{d=1}^{d_d}\sum_{e=1}^{e_{ad}}\sum_{f=1}^{f_{ade}} T_8\right)
\end{aligned}
\tag{335}
$$

2 of 2

The derivative of ϕ with respect to θ is:

$$
\begin{aligned}
\frac{\partial\phi}{\partial\theta} &= \sum_{a=1}^{a_a}\sum_{b=1}^{b_a}\sum_{c=1}^{c_{ab}} -i\,k_a r\sin(\theta-\gamma_{ab})\,A_{abc}\,e^{i\alpha_{abc}}\,D_a\,G_a\,e^{i\,k_a r\cos(\theta-\gamma_{ab})}\,e^{-i\omega_a t} \\
&\quad +\sum_{a=1}^{a_a}\sum_{d=1}^{d_d}\sum_{e=1}^{e_{ad}}\sum_{f=1}^{f_{ade}} -m_d\sin(m_d\theta-\zeta_e)\,B_{adef}\,e^{i\beta_{adef}}\,D_a\,H_{m_d}^{(1)}(k_a r)\,G_a\,e^{-i\omega_a t}
\end{aligned}
\tag{336}
$$

And:

$$
\begin{aligned}
\frac{\partial \phi}{\partial \theta}\frac{1}{e^{-i\omega_a t}} &= \sum_{a=1}^{a_a}\sum_{b=1}^{b_a}\sum_{c=1}^{c_{ab}} -i\,k_a r\sin(\theta-\gamma_{ab})\,A_{abc}\,D_a\,G_a\,e^{i\left(k_a r\cos(\theta-\gamma_{ab})+\alpha_{abc}\right)} \\
&\quad +\sum_{a=1}^{a_a}\sum_{d=1}^{d_d}\sum_{e=1}^{e_{ad}}\sum_{f=1}^{f_{ade}} -m_d\sin(m_d\theta-\zeta_e)\,B_{adef}\,D_a\,G_a\left(\cos(\beta_{adef})+i\sin(\beta_{adef})\right)\left(J_{m_d}(k_a r)+i\,Y_{m_d}(k_a r)\right) \\
&= \sum_{a=1}^{a_a}\sum_{b=1}^{b_a}\sum_{c=1}^{c_{ab}} -k_a r\sin(\theta-\gamma_{ab})\,A_{abc}\,D_a\,G_a\left(i\cos\left(k_a r\cos(\theta-\gamma_{ab})+\alpha_{abc}\right)-\sin\left(k_a r\cos(\theta-\gamma_{ab})+\alpha_{abc}\right)\right) \\
&\quad +\sum_{a=1}^{a_a}\sum_{d=1}^{d_d}\sum_{e=1}^{e_{ad}}\sum_{f=1}^{f_{ade}}\left(-m_d\sin(m_d\theta-\zeta_e)\,B_{adef}\,D_a\,G_a\left(J_{m_d}(k_a r)\cos(\beta_{adef})+i\,J_{m_d}(k_a r)\sin(\beta_{adef})\right.\right. \\
&\quad \left.\left.+i\,Y_{m_d}(k_a r)\cos(\beta_{adef})-Y_{m_d}(k_a r)\sin(\beta_{adef})\right)\right) \\
&= \sum_{a=1}^{a_a}\sum_{b=1}^{b_a}\sum_{c=1}^{c_{ab}} k_a r\sin(\theta-\gamma_{ab})\,A_{abc}\,D_a\,G_a\sin\left(k_a r\cos(\theta-\gamma_{ab})+\alpha_{abc}\right) \\
&\quad +\sum_{a=1}^{a_a}\sum_{d=1}^{d_d}\sum_{e=1}^{e_{ad}}\sum_{f=1}^{f_{ade}} -m_d\sin(m_d\theta-\zeta_e)\,B_{adef}\,D_a\,G_a\left(J_{m_d}(k_a r)\cos(\beta_{adef})-Y_{m_d}(k_a r)\sin(\beta_{adef})\right) \\
&\quad +i\left(\sum_{a=1}^{a_a}\sum_{b=1}^{b_a}\sum_{c=1}^{c_{ab}} -k_a r\sin(\theta-\gamma_{ab})\,A_{abc}\,D_a\,G_a\cos\left(k_a r\cos(\theta-\gamma_{ab})+\alpha_{abc}\right)\right. \\
&\quad \left.+\sum_{a=1}^{a_a}\sum_{d=1}^{d_d}\sum_{e=1}^{e_{ad}}\sum_{f=1}^{f_{ade}} -m_d\sin(m_d\theta-\zeta_e)\,B_{adef}\,D_a\,G_a\left(J_{m_d}(k_a r)\sin(\beta_{adef})+Y_{m_d}(k_a r)\cos(\beta_{adef})\right)\right) \\
&= \sum_{a=1}^{a_a}\sum_{b=1}^{b_a}\sum_{c=1}^{c_{ab}} T_9+\sum_{a=1}^{a_a}\sum_{d=1}^{d_d}\sum_{e=1}^{e_{ad}}\sum_{f=1}^{f_{ade}} -T_{10}+i\left(\sum_{a=1}^{a_a}\sum_{b=1}^{b_a}\sum_{c=1}^{c_{ab}} -T_{11}+\sum_{a=1}^{a_a}\sum_{d=1}^{d_d}\sum_{e=1}^{e_{ad}}\sum_{f=1}^{f_{ade}} -T_{12}\right)
\end{aligned}
\tag{337}
$$

Finally, the derivative of ϕ with respect to z:

$$\frac{\partial \phi}{\partial z} = \sum_{a=1}^{a_a}\sum_{b=1}^{b_a}\sum_{c=1}^{c_{ab}} k_a A_{abc} e^{i\alpha_{abc}} D_a \sinh(k_a(h+z)) e^{i k_a r \cos(\theta-\gamma_{ab})} e^{-i\omega_a t} + \sum_{a=1}^{a_a}\sum_{d=1}^{d_d}\sum_{e=1}^{e_{ad}}\sum_{f=1}^{f_{ade}} k_a B_{adef} e^{i\beta_{adef}} D_a H_{m_d}^{(1)}(k_a r) F_{de} \sinh(k_a(h+z)) e^{-i\omega_a t} \quad (338)$$

And:

$$\begin{aligned}\frac{\partial \phi}{\partial z}\frac{1}{e^{-i\omega_a t}} &= \sum_{a=1}^{a_a}\sum_{b=1}^{b_a}\sum_{c=1}^{c_{ab}} k_a A_{abc} D_a \sinh(k_a(h+z)) e^{i\left(k_a r\cos(\theta-\gamma_{ab})+\alpha_{abc}\right)} \\ &\quad + \sum_{a=1}^{a_a}\sum_{d=1}^{d_d}\sum_{e=1}^{e_{ad}}\sum_{f=1}^{f_{ade}} k_a B_{adef} D_a \cos(m_d\theta-\zeta_e)\sinh(k_a(h+z))\left(\cos(\beta_{adef})+i\sin(\beta_{adef})\right)\left(J_{m_d}(k_a r)+i\,Y_{m_d}(k_a r)\right) \\ &= \sum_{a=1}^{a_a}\sum_{b=1}^{b_a}\sum_{c=1}^{c_{ab}} k_a A_{abc} D_a \sinh(k_a(h+z))\left(\cos(k_a r\cos(\theta-\gamma_{ab})+\alpha_{abc})+i\sin(k_a r\cos(\theta-\gamma_{ab})+\alpha_{abc})\right) \\ &\quad + \sum_{a=1}^{a_a}\sum_{d=1}^{d_d}\sum_{e=1}^{e_{ad}}\sum_{f=1}^{f_{ade}} \Big(k_a B_{adef} D_a F_{de} \sinh(k_a(h+z))\left(J_{m_d}(k_a r)\cos(\beta_{adef})+i\,J_{m_d}(k_a r)\sin(\beta_{adef})\right. \\ &\quad \left. + i\,Y_{m_d}(k_a r)\cos(\beta_{adef})-Y_{m_d}(k_a r)\sin(\beta_{adef})\right)\Big)\end{aligned} \quad (339)$$

$$\begin{aligned}\frac{\partial \phi}{\partial z}\frac{1}{e^{-i\omega_a t}} &= \sum_{a=1}^{a_a}\sum_{b=1}^{b_a}\sum_{c=1}^{c_{ab}} k_a A_{abc} D_a \sinh(k_a(h+z))\cos(k_a r\cos(\theta-\gamma_{ab})+\alpha_{abc}) \\ &\quad +\sum_{a=1}^{a_a}\sum_{d=1}^{d_d}\sum_{e=1}^{e_{ad}}\sum_{f=1}^{f_{ade}} k_a B_{adef} D_a F_{de} \sinh(k_a(h+z))\left(J_{m_d}(k_a r)\cos(\beta_{adef})-Y_{m_d}(k_a r)\sin(\beta_{adef})\right) \\ &\quad +i\left(\sum_{a=1}^{a_a}\sum_{b=1}^{b_a}\sum_{c=1}^{c_{ab}} k_a A_{abc} D_a \sinh(k_a(h+z))\sin(k_a r\cos(\theta-\gamma_{ab})+\alpha_{abc})\right. \\ &\quad \left.+\sum_{a=1}^{a_a}\sum_{d=1}^{d_d}\sum_{e=1}^{e_{ad}}\sum_{f=1}^{f_{ade}} k_a B_{adef} D_a F_{de} \sinh(k_a(h+z))\left(J_{m_d}(k_a r)\sin(\beta_{adef})+Y_{m_d}(k_a r)\cos(\beta_{adef})\right)\right) \\ &= \sum_{a=1}^{a_a}\sum_{b=1}^{b_a}\sum_{c=1}^{c_{ab}} T_{13}+\sum_{a=1}^{a_a}\sum_{d=1}^{d_d}\sum_{e=1}^{e_{ad}}\sum_{f=1}^{f_{ade}} T_{14}+i\left(\sum_{a=1}^{a_a}\sum_{b=1}^{b_a}\sum_{c=1}^{c_{ab}} T_{15}+\sum_{a=1}^{a_a}\sum_{d=1}^{d_d}\sum_{e=1}^{e_{ad}}\sum_{f=1}^{f_{ade}} T_{16}\right)\end{aligned} \tag{339}$$

2 of 2

Using the shortened T_n notation it is possible to minimise the number of terms required to calculate the components of Equation 329. Starting with the left most term in the brackets on the right-hand side of the Equation 329.

$$\begin{aligned}\overline{\frac{\partial \phi}{\partial t}\frac{\partial \phi}{\partial r}} &= \frac{1}{2}\Re\left(\left(\sum_{a=1}^{a_a}\sum_{b=1}^{b_a}\sum_{c=1}^{c_{ab}} T_1+\sum_{a=1}^{a_a}\sum_{d=1}^{d_d}\sum_{e=1}^{e_{ad}}\sum_{f=1}^{f_{ade}} T_2+i\left(\sum_{a=1}^{a_a}\sum_{b=1}^{b_a}\sum_{c=1}^{c_{ab}} T_3+\sum_{a=1}^{a_a}\sum_{d=1}^{d_d}\sum_{e=1}^{e_{ad}}\sum_{f=1}^{f_{ade}} T_4\right)\right)\right. \\ &\quad \left.\times\left(\sum_{a=1}^{a_a}\sum_{b=1}^{b_a}\sum_{c=1}^{c_{ab}} -T_5+\sum_{a=1}^{a_a}\sum_{d=1}^{d_d}\sum_{e=1}^{e_{ad}}\sum_{f=1}^{f_{ade}} T_6+i\left(\sum_{a=1}^{a_a}\sum_{b=1}^{b_a}\sum_{c=1}^{c_{ab}} T_7+\sum_{a=1}^{a_a}\sum_{d=1}^{d_d}\sum_{e=1}^{e_{ad}}\sum_{f=1}^{f_{ade}} T_8\right)\right)\right)\end{aligned} \tag{340}$$

Because the time-averaged products of terms with different frequencies is zero, the $\sum_{a=1}^{a_a}$ can be moved to the front of the equation. Equation 340 can be rewritten:

$$\begin{aligned}
\overline{\frac{\partial \phi}{\partial t}\frac{\partial \phi}{\partial r}} &= \frac{1}{2}\Re\left(\left(\sum_{a=1}^{a_a}\sum_{b=1}^{b_a}\sum_{c=1}^{c_{ab}} T_1+\sum_{a=1}^{a_a}\sum_{d=1}^{d_d}\sum_{e=1}^{e_{ad}}\sum_{f=1}^{f_{ade}} T_2+i\left(\sum_{a=1}^{a_a}\sum_{b=1}^{b_a}\sum_{c=1}^{c_{ab}} T_3+\sum_{a=1}^{a_a}\sum_{d=1}^{d_d}\sum_{e=1}^{e_{ad}}\sum_{f=1}^{f_{ade}} T_4\right)\right)\right. \\
&\quad \left.\times\left(\sum_{a=1}^{a_a}\sum_{b=1}^{b_a}\sum_{c=1}^{c_{ab}} -T_5+\sum_{a=1}^{a_a}\sum_{d=1}^{d_d}\sum_{e=1}^{e_{ad}}\sum_{f=1}^{f_{ade}} T_6+i\left(\sum_{a=1}^{a_a}\sum_{b=1}^{b_a}\sum_{c=1}^{c_{ab}} T_7+\sum_{a=1}^{a_a}\sum_{d=1}^{d_d}\sum_{e=1}^{e_{ad}}\sum_{f=1}^{f_{ade}} T_8\right)\right)\right) \\
&= \frac{1}{2}\Re\left(\left(\sum_{a=1}^{a_a}\sum_{b=1}^{b_a}\sum_{c=1}^{c_{ab}} T_1+\sum_{a=1}^{a_a}\sum_{d=1}^{d_d}\sum_{e=1}^{e_{ad}}\sum_{f=1}^{f_{ade}} T_2\right)\left(\sum_{a=1}^{a_a}\sum_{b=1}^{b_a}\sum_{c=1}^{c_{ab}} -T_5+\sum_{a=1}^{a_a}\sum_{d=1}^{d_d}\sum_{e=1}^{e_{ad}}\sum_{f=1}^{f_{ade}} T_6\right)\right. \\
&\quad +i\left(\sum_{a=1}^{a_a}\sum_{b=1}^{b_a}\sum_{c=1}^{c_{ab}} T_3+\sum_{a=1}^{a_a}\sum_{d=1}^{d_d}\sum_{e=1}^{e_{ad}}\sum_{f=1}^{f_{ade}} T_4\right)\left(\sum_{a=1}^{a_a}\sum_{b=1}^{b_a}\sum_{c=1}^{c_{ab}} -T_5+\sum_{a=1}^{a_a}\sum_{d=1}^{d_d}\sum_{e=1}^{e_{ad}}\sum_{f=1}^{f_{ade}} T_6\right) \\
&\quad +i\left(\sum_{a=1}^{a_a}\sum_{b=1}^{b_a}\sum_{c=1}^{c_{ab}} T_1+\sum_{a=1}^{a_a}\sum_{d=1}^{d_d}\sum_{e=1}^{e_{ad}}\sum_{f=1}^{f_{ade}} T_2\right)\left(\sum_{a=1}^{a_a}\sum_{b=1}^{b_a}\sum_{c=1}^{c_{ab}} T_7+\sum_{a=1}^{a_a}\sum_{d=1}^{d_d}\sum_{e=1}^{e_{ad}}\sum_{f=1}^{f_{ade}} T_8\right) \\
&\quad \left.-\left(\sum_{a=1}^{a_a}\sum_{b=1}^{b_a}\sum_{c=1}^{c_{ab}} T_3+\sum_{a=1}^{a_a}\sum_{d=1}^{d_d}\sum_{e=1}^{e_{ad}}\sum_{f=1}^{f_{ade}} T_4\right)\left(\sum_{a=1}^{a_a}\sum_{b=1}^{b_a}\sum_{c=1}^{c_{ab}} T_7+\sum_{a=1}^{a_a}\sum_{d=1}^{d_d}\sum_{e=1}^{e_{ad}}\sum_{f=1}^{f_{ade}} T_8\right)\right)
\end{aligned} \tag{341}$$

$$\overline{\frac{\partial \phi}{\partial t}\frac{\partial \phi}{\partial r}} = \frac{1}{2}\left(\left(\sum_{a=1}^{a_a}\sum_{b=1}^{b_a}\sum_{c=1}^{c_{ab}} T_1 + \sum_{a=1}^{a_a}\sum_{d=1}^{d_d}\sum_{e=1}^{e_{ad}}\sum_{f=1}^{f_{ade}} T_2\right)\left(\sum_{a=1}^{a_a}\sum_{b=1}^{b_a}\sum_{c=1}^{c_{ab}} - T_5 + \sum_{a=1}^{a_a}\sum_{d=1}^{d_d}\sum_{e=1}^{e_{ad}}\sum_{f=1}^{f_{ade}} T_6\right)\right.$$
$$\left. - \left(\sum_{a=1}^{a_a}\sum_{b=1}^{b_a}\sum_{c=1}^{c_{ab}} T_3 + \sum_{a=1}^{a_a}\sum_{d=1}^{d_d}\sum_{e=1}^{e_{ad}}\sum_{f=1}^{f_{ade}} T_4\right)\left(\sum_{a=1}^{a_a}\sum_{b=1}^{b_a}\sum_{c=1}^{c_{ab}} T_7 + \sum_{a=1}^{a_a}\sum_{d=1}^{d_d}\sum_{e=1}^{e_{ad}}\sum_{f=1}^{f_{ade}} T_8\right)\right) \quad (341)$$
$$= \frac{1}{2}\sum_{a=1}^{a_a}\left(\left(\sum_{b=1}^{b_a}\sum_{c=1}^{c_{ab}} T_1 + \sum_{d=1}^{d_d}\sum_{e=1}^{e_{ad}}\sum_{f=1}^{f_{ade}} T_2\right)\left(\sum_{b=1}^{b_a}\sum_{c=1}^{c_{ab}} - T_5 + \sum_{d=1}^{d_d}\sum_{e=1}^{e_{ad}}\sum_{f=1}^{f_{ade}} T_6\right) - \left(\sum_{b=1}^{b_a}\sum_{c=1}^{c_{ab}} T_3 + \sum_{d=1}^{d_d}\sum_{e=1}^{e_{ad}}\sum_{f=1}^{f_{ade}} T_4\right)\left(\sum_{b=1}^{b_a}\sum_{c=1}^{c_{ab}} T_7 + \sum_{d=1}^{d_d}\sum_{e=1}^{e_{ad}}\sum_{f=1}^{f_{ade}} T_8\right)\right)$$

2 of 2

Also, to preserve the combination of terms it is necessary to introduce five new terms n, o, p, q and s such that each term has the same range as b, c, d, e and f respectively but vary independently. Using these new variables it is possible to create a relatively short notation for all of the terms involved:

$$\overline{\frac{\partial \phi}{\partial t}\frac{\partial \phi}{\partial r}} = \frac{1}{2}\sum_{a=1}^{a_a}\left(\left(\sum_{b=1}^{b_a}\sum_{c=1}^{c_{ab}} T_{1\mathrm{bc}} + \sum_{d=1}^{d_d}\sum_{e=1}^{e_{ad}}\sum_{f=1}^{f_{ade}} T_{2\mathrm{def}}\right)\left(\sum_{n=1}^{n_a}\sum_{o=1}^{o_{an}} - T_{5\mathrm{no}} + \sum_{p=1}^{p_p}\sum_{q=1}^{q_{ap}}\sum_{s=1}^{s_{apq}} T_{6\mathrm{pqs}}\right)\right.$$
$$\left. - \left(\sum_{b=1}^{b_a}\sum_{c=1}^{c_{ab}} T_{3\mathrm{bc}} + \sum_{d=1}^{d_d}\sum_{e=1}^{e_{ad}}\sum_{f=1}^{f_{ade}} T_{4\mathrm{def}}\right)\left(\sum_{n=1}^{n_a}\sum_{o=1}^{o_{an}} T_{7\mathrm{no}} + \sum_{p=1}^{p_p}\sum_{q=1}^{q_{ap}}\sum_{s=1}^{s_{apq}} T_{8\mathrm{pqs}}\right)\right) \quad (342)$$

1 of 2

$$\begin{aligned}
\overline{\frac{\partial \phi}{\partial t}\frac{\partial \phi}{\partial r}} &= \frac{1}{2}\sum_{a=1}^{a_a}\left(\sum_{b=1}^{b_a}\sum_{c=1}^{c_{ab}}\sum_{n=1}^{n_a}\sum_{o=1}^{o_{an}} -T_{1\text{bc}}T_{5\text{no}} + \sum_{d=1}^{d_d}\sum_{e=1}^{e_{ad}}\sum_{f=1}^{f_{ade}}\sum_{n=1}^{n_a}\sum_{o=1}^{o_{an}} -T_{2\text{def}}T_{5\text{no}} + \sum_{b=1}^{b_a}\sum_{c=1}^{c_{ab}}\sum_{p=1}^{p_p}\sum_{q=1}^{q_{ap}}\sum_{s=1}^{s_{apq}} T_{1\text{bc}}T_{6\text{pqs}} + \sum_{d=1}^{d_d}\sum_{e=1}^{e_{ad}}\sum_{f=1}^{f_{ade}}\sum_{p=1}^{p_p}\sum_{q=1}^{q_{ap}}\sum_{s=1}^{s_{apq}} T_{2\text{def}}T_{6\text{pqs}}\right. \\
&\qquad \left. -\left(\sum_{b=1}^{b_a}\sum_{c=1}^{c_{ab}}\sum_{n=1}^{n_a}\sum_{o=1}^{o_{an}} T_{3\text{bc}}T_{7\text{no}} + \sum_{d=1}^{d_d}\sum_{e=1}^{e_{ad}}\sum_{f=1}^{f_{ade}}\sum_{n=1}^{n_a}\sum_{o=1}^{o_{an}} T_{4\text{def}}T_{7\text{no}} + \sum_{b=1}^{b_a}\sum_{c=1}^{c_{ab}}\sum_{p=1}^{p_p}\sum_{q=1}^{q_{ap}}\sum_{s=1}^{s_{apq}} T_{3\text{bc}}T_{8\text{pqs}} + \sum_{d=1}^{d_d}\sum_{e=1}^{e_{ad}}\sum_{f=1}^{f_{ade}}\sum_{p=1}^{p_p}\sum_{q=1}^{q_{ap}}\sum_{s=1}^{s_{apq}} T_{4\text{def}}T_{8\text{pqs}}\right)\right) \\
&= \frac{1}{2}\sum_{a=1}^{a_a}\left(\sum_{b=1}^{b_a}\sum_{c=1}^{c_{ab}}\sum_{n=1}^{n_a}\sum_{o=1}^{o_{an}} -T_{1\text{bc}}T_{5\text{no}} - T_{3\text{bc}}T_{7\text{no}} + \sum_{b=1}^{b_a}\sum_{c=1}^{c_{ab}}\sum_{d=1}^{d_d}\sum_{e=1}^{e_{ad}}\sum_{f=1}^{f_{ade}} T_{1\text{bc}}T_{6\text{def}} - T_{2\text{def}}T_{5\text{bc}} - T_{4\text{def}}T_{7\text{dc}} - T_{3\text{dc}}T_{8\text{def}}\right. \\
&\qquad \left. + \sum_{d=1}^{d_d}\sum_{e=1}^{e_{ad}}\sum_{f=1}^{f_{ade}}\sum_{p=1}^{p_p}\sum_{q=1}^{q_{ap}}\sum_{s=1}^{s_{apq}} T_{2\text{def}}T_{6\text{pqs}} - T_{4\text{def}}T_{8\text{pqs}}\right)
\end{aligned} \tag{342}$$

(342) 2 of 2

Each of the summed groups can then be calculated:

$$\begin{aligned}
-T_{1\text{bc}}T_{5\text{no}} - T_{3\text{bc}}T_{7\text{no}} &= -\left(\omega_a A_{abc} D_a G_a \sin\left(k_a r\cos(\theta-\gamma_{ab})+\alpha_{abc}\right)\right) \text{ x } \left(k_a\cos(\theta-\gamma_{an}) A_{ano} D_a G_a \sin\left(k_a r\cos(\theta-\gamma_{an})+\alpha_{ano}\right)\right) \\
&\quad -\left(\omega_a A_{abc} D_a G_a \cos\left(k_a r\cos(\theta-\gamma_{ab})+\alpha_{abc}\right)\right) \text{ x } \left(k_a\cos(\theta-\gamma_{an}) A_{ano} D_a G_a \cos\left(k_a r\cos(\theta-\gamma_{an})+\alpha_{ano}\right)\right) \\
&= -k_a \omega_a D_a^2 G_a^2 A_{abc} A_{ano}\cos(\theta-\gamma_{an})\left(\sin\left(k_a r\cos(\theta-\gamma_{ab})+\alpha_{abc}\right)\sin\left(k_a r\cos(\theta-\gamma_{an})+\alpha_{ano}\right)\right. \\
&\qquad \left. -\cos\left(k_a r\cos(\theta-\gamma_{ab})+\alpha_{abc}\right)\cos\left(k_a r\cos(\theta-\gamma_{an})+\alpha_{ano}\right)\right) \\
&= -k_a \omega_a D_a^2 G_a^2 A_{abc} A_{ano}\cos(\theta-\gamma_{an})\left(\cos\left(k_a r\cos(\theta-\gamma_{ab})+\alpha_{abc}-\left(k_a r\cos(\theta-\gamma_{an})+\alpha_{ano}\right)\right)\right) \\
&= -k_a \omega_a D_a^2 G_a^2 A_{abc} A_{ano}\cos(\theta-\gamma_{an})\cos\left(k_a r\left(\cos(\theta-\gamma_{ab})-\cos(\theta-\gamma_{an})\right)+\alpha_{abc}-\alpha_{ano}\right)
\end{aligned} \tag{343}$$

$$
\begin{aligned}
&T_{1\mathrm{bc}}T_{6\mathrm{def}}-T_{2\mathrm{def}}T_{5\mathrm{bc}}-T_{4\mathrm{def}}T_{7\mathrm{dc}}-T_{3\mathrm{dc}}T_{8\mathrm{def}}\\
&=\left(\omega_a A_{abc} D_a G_a \sin\left(k_a r\cos(\theta-\gamma_{ab})+\alpha_{abc}\right)\right)\\
&\qquad\times\left(\frac{k_a}{2}B_{adef}D_a F_{de}G_a\left(\cos(\beta_{adef})\left(J_{m_d-1}(k_a r)-J_{m_d+1}(k_a r)\right)-\sin(\beta_{adef})\left(Y_{m_d-1}(k_a r)-Y_{m_d+1}(k_a r)\right)\right)\right)\\
&\quad-\left(\omega_a D_a F_{de}G_a B_{adef}\left(J_{m_d}(k_a r)\sin(\beta_{adef})+Y_{m_d}(k_a r)\cos(\beta_{adef})\right)\right)\ \mathrm{x}\ \left(k_a\cos(\theta-\gamma_{ab})A_{abc}D_a G_a\sin\left(k_a r\cos(\theta-\gamma_{ab})+\alpha_{abc}\right)\right)\\
&\quad-\left(\omega_a D_a F_{de}G_a B_{adef}\left(J_{m_d}(k_a r)\cos(\beta_{adef})-Y_{m_d}(k_a r)\sin(\beta_{adef})\right)\right)\ \mathrm{x}\ \left(k_a\cos(\theta-\gamma_{ab})A_{abc}D_a G_a\cos\left(k_a r\cos(\theta-\gamma_{ab})+\alpha_{abc}\right)\right)\\
&\qquad-\left(\omega_a A_{abc}D_a G_a\cos\left(k_a r\cos(\theta-\gamma_{ab})+\alpha_{abc}\right)\right)\\
&\qquad\times\left(\frac{k_a}{2}B_{adef}D_a F_{de}G_a\left(\cos(\beta_{adef})\left(Y_{m_d-1}(k_a r)-Y_{m_d+1}(k_a r)\right)+\sin(\beta_{adef})\left(J_{m_d-1}(k_a r)-J_{m_d+1}(k_a r)\right)\right)\right)\\
&=\frac{A_{abc}B_{adef}}{2}k_a\omega_a D_a^2 F_{de}G_a^2\left(\left(J_{m_d-1}(k_a r)-J_{m_d+1}(k_a r)\right)\cos(\beta_{adef})\sin\left(k_a r\cos(\theta-\gamma_{ab})+\alpha_{abc}\right)\right.\\
&\qquad\left.-\left(Y_{m_d-1}(k_a r)-Y_{m_d+1}(k_a r)\right)\sin(\beta_{adef})\sin\left(k_a r\cos(\theta-\gamma_{ab})+\alpha_{abc}\right)\right)-A_{abc}B_{adef}\cos(\theta-\gamma_{ab})k_a\omega_a D_a^2 F_{de}G_a^2\\
&\qquad\times\left(J_{m_d}(k_a r)\sin(\beta_{adef})\sin\left(k_a r\cos(\theta-\gamma_{ab})+\alpha_{abc}\right)+Y_{m_d}(k_a r)\cos(\beta_{adef})\sin\left(k_a r\cos(\theta-\gamma_{ab})+\alpha_{abc}\right)\right)\\
&\qquad-A_{abc}B_{adef}\cos(\theta-\gamma_{ab})k_a\omega_a D_a^2 F_{de}G_a^2\\
&\qquad\times\left(J_{m_d}(k_a r)\cos(\beta_{adef})\cos\left(k_a r\cos(\theta-\gamma_{ab})+\alpha_{abc}\right)-Y_{m_d}(k_a r)\sin(\beta_{adef})\cos\left(k_a r\cos(\theta-\gamma_{ab})+\alpha_{abc}\right)\right)\\
&\quad-\frac{A_{abc}B_{adef}}{2}k_a\omega_a D_a^2 F_{de}G_a^2\left(\left(Y_{m_d-1}(k_a r)-Y_{m_d+1}(k_a r)\right)\cos(\beta_{adef})\cos\left(k_a r\cos(\theta-\gamma_{ab})+\alpha_{abc}\right)+\left(J_{m_d-1}(k_a r)-J_{m_d+1}(k_a r)\right)\right.\\
&\qquad\left.\times\sin(\beta_{adef})\cos\left(k_a r\cos(\theta-\gamma_{ab})+\alpha_{abc}\right)\right)
\end{aligned}
\tag{344}
$$

$$
\begin{aligned}
&T_{1\mathrm{bc}}T_{6\mathrm{def}}-T_{2\mathrm{def}}T_{5\mathrm{bc}}-T_{4\mathrm{def}}T_{7\mathrm{dc}}-T_{3\mathrm{dc}}T_{8\mathrm{def}}\\
&= k_a\omega_a D_a^2 F_{de} G_a^2\Bigg(\frac{A_{abc}B_{adef}}{2}\Big(\big(J_{m_d-1}(k_a r)-J_{m_d+1}(k_a r)\big)\\
&\qquad\times\big(\cos(\beta_{adef})\sin(k_a r\cos(\theta-\gamma_{ab})+\alpha_{abc})-\sin(\beta_{adef})\cos(k_a r\cos(\theta-\gamma_{ab})+\alpha_{abc})\big)\\
&\qquad-\big(Y_{m_d-1}(k_a r)-Y_{m_d+1}(k_a r)\big)\big(\sin(\beta_{adef})\sin(k_a r\cos(\theta-\gamma_{ab})+\alpha_{abc})+\cos(\beta_{adef})\cos(k_a r\cos(\theta-\gamma_{ab})+\alpha_{abc})\big)\Big)\\
&\quad-A_{abc}B_{adef}\cos(\theta-\gamma_{ab})\Big(J_{m_d}(k_a r)\big(\sin(\beta_{adef})\sin(k_a r\cos(\theta-\gamma_{ab})+\alpha_{abc})+\cos(\beta_{adef})\cos(k_a r\cos(\theta-\gamma_{ab})+\alpha_{abc})\big)\\
&\qquad+Y_{m_d}(k_a r)\big(\cos(\beta_{adef})\sin(k_a r\cos(\theta-\gamma_{ab})+\alpha_{abc})-\sin(\beta_{adef})\cos(k_a r\cos(\theta-\gamma_{ab})+\alpha_{abc})\big)\Big)\Bigg)\\
&= k_a\omega_a D_a^2 F_{de} G_a^2\Bigg(\frac{A_{abc}B_{adef}}{2}\Big(\big(J_{m_d-1}(k_a r)-J_{m_d+1}(k_a r)\big)\sin(k_a r\cos(\theta-\gamma_{ab})+\alpha_{abc}-\beta_{adef})\\
&\qquad-\big(Y_{m_d-1}(k_a r)-Y_{m_d+1}(k_a r)\big)\cos(k_a r\cos(\theta-\gamma_{ab})+\alpha_{abc}-\beta_{adef})\Big)\\
&\quad-A_{abc}B_{adef}\cos(\theta-\gamma_{ab})\Big(J_{m_d}(k_a r)\cos(k_a r\cos(\theta-\gamma_{ab})+\alpha_{abc}-\beta_{adef})+Y_{m_d}(k_a r)\sin(k_a r\cos(\theta-\gamma_{ab})+\alpha_{abc}-\beta_{adef})\Big)\Bigg)\\
&= k_a\omega_a D_a^2 F_{de} G_a^2 A_{abc}B_{adef}\Bigg(\Bigg(\frac{1}{2}\big(J_{m_d-1}(k_a r)-J_{m_d+1}(k_a r)\big)-Y_{m_d}(k_a r)\cos(\theta-\gamma_{ab})\Bigg)\sin(k_a r\cos(\theta-\gamma_{ab})+\alpha_{abc}-\beta_{adef})\\
&\qquad-\Bigg(\frac{1}{2}\big(Y_{m_d-1}(k_a r)-Y_{m_d+1}(k_a r)\big)+J_{m_d}(k_a r)\cos(\theta-\gamma_{ab})\Bigg)\cos(k_a r\cos(\theta-\gamma_{ab})+\alpha_{abc}-\beta_{adef})\Bigg)
\end{aligned}
\tag{344}
$$

And:

$$
\begin{aligned}
&T_{2\mathrm{def}}T_{6\mathrm{pqs}}-T_{4\mathrm{def}}T_{8\mathrm{pqs}}\\
&=\left(\omega_a D_a F_{de} G_a B_{adef}\left(J_{m_d}(k_a r)\sin(\beta_{adef})+Y_{m_d}(k_a r)\cos(\beta_{adef})\right)\right)\\
&\qquad\times\left(\frac{k_a}{2}B_{apqs}D_a F_{pq} G_a\left(\cos(\beta_{apqs})\left(J_{m_p-1}(k_a r)-J_{m_p+1}(k_a r)\right)-\sin(\beta_{apqs})\left(Y_{m_p-1}(k_a r)-Y_{m_p+1}(k_a r)\right)\right)\right)\\
&\qquad-\left(\omega_a D_a F_{de} G_a B_{adef}\left(J_{m_d}(k_a r)\cos(\beta_{adef})-Y_{m_d}(k_a r)\sin(\beta_{adef})\right)\right)\\
&\qquad\times\left(\frac{k_a}{2}B_{apqs}D_a F_{pq} G_a\left(\cos(\beta_{apqs})\left(Y_{m_p-1}(k_a r)-Y_{m_p+1}(k_a r)\right)+\sin(\beta_{apqs})\left(J_{m_p-1}(k_a r)-J_{m_p+1}(k_a r)\right)\right)\right)\\
&=\frac{1}{2}k_a\omega_a D_a^2 F_{de}F_{pq}G_a^2 B_{adef}B_{apqs}\left(\left(J_{m_d}(k_a r)\sin(\beta_{adef})+Y_{m_d}(k_a r)\cos(\beta_{adef})\right)\right.\\
&\qquad\times\left(\cos(\beta_{apqs})\left(J_{m_p-1}(k_a r)-J_{m_p+1}(k_a r)\right)-\sin(\beta_{apqs})\left(Y_{m_p-1}(k_a r)-Y_{m_p+1}(k_a r)\right)\right)\\
&\qquad-\left(J_{m_d}(k_a r)\cos(\beta_{adef})-Y_{m_d}(k_a r)\sin(\beta_{adef})\right)\\
&\qquad\left.\times\left(\cos(\beta_{apqs})\left(Y_{m_p-1}(k_a r)-Y_{m_p+1}(k_a r)\right)+\sin(\beta_{apqs})\left(J_{m_p-1}(k_a r)-J_{m_p+1}(k_a r)\right)\right)\right)\\
&=\frac{1}{2}k_a\omega_a D_a^2 F_{de}F_{pq}G_a^2 B_{adef}B_{apqs}\\
&\qquad\times\left(J_{m_d}(k_a r)\sin(\beta_{adef})\cos(\beta_{apqs})\left(J_{m_p-1}(k_a r)-J_{m_p+1}(k_a r)\right)+Y_{m_d}(k_a r)\cos(\beta_{adef})\cos(\beta_{apqs})\left(J_{m_p-1}(k_a r)-J_{m_p+1}(k_a r)\right)\right.\\
&\qquad-J_{m_d}(k_a r)\sin(\beta_{adef})\sin(\beta_{apqs})\left(Y_{m_p-1}(k_a r)-Y_{m_p+1}(k_a r)\right)-Y_{m_d}(k_a r)\cos(\beta_{adef})\sin(\beta_{apqs})\left(Y_{m_p-1}(k_a r)-Y_{m_p+1}(k_a r)\right)\\
&\qquad-J_{m_d}(k_a r)\cos(\beta_{adef})\cos(\beta_{apqs})\left(Y_{m_p-1}(k_a r)-Y_{m_p+1}(k_a r)\right)+Y_{m_d}(k_a r)\sin(\beta_{adef})\cos(\beta_{apqs})\left(Y_{m_p-1}(k_a r)-Y_{m_p+1}(k_a r)\right)\\
&\qquad\left.-J_{m_d}(k_a r)\cos(\beta_{adef})\sin(\beta_{apqs})\left(J_{m_p-1}(k_a r)-J_{m_p+1}(k_a r)\right)+Y_{m_d}(k_a r)\sin(\beta_{adef})\sin(\beta_{apqs})\left(J_{m_p-1}(k_a r)-J_{m_p+1}(k_a r)\right)\right)
\end{aligned}
\tag{345}
$$

$$
\begin{aligned}
&T_{2\mathrm{def}}\,T_{6\mathrm{pqs}}-T_{4\mathrm{def}}\,T_{8\mathrm{pqs}}\\
&=\ \frac{1}{2}k_a\omega_a D_a^2 F_{de}F_{pq}G_a^2 B_{adef}B_{apqs}\\
&\qquad\times\Big(J_{m_d}(k_a r)\Big(J_{m_p-1}(k_a r)-J_{m_p+1}(k_a r)\Big)\Big(\sin(\beta_{adef})\cos(\beta_{apqs})-\cos(\beta_{adef})\sin(\beta_{apqs})\Big)\\
&\qquad+Y_{m_d}(k_a r)\Big(J_{m_p-1}(k_a r)-J_{m_p+1}(k_a r)\Big)\Big(\cos(\beta_{adef})\cos(\beta_{apqs})+\sin(\beta_{adef})\sin(\beta_{apqs})\Big)\\
&\qquad-J_{m_d}(k_a r)\Big(Y_{m_p-1}(k_a r)-Y_{m_p+1}(k_a r)\Big)\Big(\sin(\beta_{adef})\sin(\beta_{apqs})+\cos(\beta_{adef})\cos(\beta_{apqs})\Big)\\
&\qquad-Y_{m_d}(k_a r)\Big(Y_{m_p-1}(k_a r)-Y_{m_p+1}(k_a r)\Big)\Big(\cos(\beta_{adef})\sin(\beta_{apqs})-\sin(\beta_{adef})\cos(\beta_{apqs})\Big)\Big)\\
&=\ \frac{1}{2}k_a\omega_a D_a^2 F_{de}F_{pq}G_a^2 B_{adef}B_{apqs}\Big(\Big(J_{m_d}(k_a r)\Big(J_{m_p-1}(k_a r)-J_{m_p+1}(k_a r)\Big)-Y_{m_d}(k_a r)\Big(Y_{m_p-1}(k_a r)-Y_{m_p+1}(k_a r)\Big)\Big)\sin(\beta_{adef}-\beta_{apqs})\\
&\qquad+\Big(Y_{m_d}(k_a r)\Big(J_{m_p-1}(k_a r)-J_{m_p+1}(k_a r)\Big)-J_{m_d}(k_a r)\Big(Y_{m_p-1}(k_a r)-Y_{m_p+1}(k_a r)\Big)\Big)\cos(\beta_{adef}-\beta_{apqs})\Big)
\end{aligned}
\tag{345}
$$

This gives the first term of Equation 329 to be:

$$\overline{\frac{\partial \phi}{\partial t}\frac{\partial \phi}{\partial r}} = \frac{1}{2}\sum_{a=1}^{a_a}\left(\sum_{b=1}^{b_a}\sum_{c=1}^{c_{ab}}\sum_{n=1}^{n_a}\sum_{o=1}^{o_{an}} -T_{1\mathrm{bc}}T_{5\mathrm{no}} - T_{3\mathrm{bc}}T_{7\mathrm{no}} + \sum_{b=1}^{b_a}\sum_{c=1}^{c_{ab}}\sum_{d=1}^{d_d}\sum_{e=1}^{e_{ad}}\sum_{f=1}^{f_{ade}} T_{1\mathrm{bc}}T_{6\mathrm{def}} - T_{2\mathrm{def}}T_{5\mathrm{bc}} - T_{4\mathrm{def}}T_{7\mathrm{dc}} - T_{3\mathrm{dc}}T_{8\mathrm{def}} \right.$$

$$\left. + \sum_{d=1}^{d_d}\sum_{e=1}^{e_{ad}}\sum_{f=1}^{f_{ade}}\sum_{p=1}^{p_p}\sum_{q=1}^{q_{ap}}\sum_{s=1}^{s_{apq}} T_{2\mathrm{def}}T_{6\mathrm{pqs}} - T_{4\mathrm{def}}T_{8\mathrm{pqs}}\right)$$

$$= \frac{1}{2}\sum_{a=1}^{a_a}\left(\sum_{b=1}^{b_a}\sum_{c=1}^{c_{ab}}\sum_{n=1}^{n_a}\sum_{o=1}^{o_{an}} -k_a\omega_a D_a^2 G_a^2 A_{abc}A_{ano}\cos(\theta-\gamma_{an})\cos(k_a r(\cos(\theta-\gamma_{ab})-\cos(\theta-\gamma_{an}))+\alpha_{abc}-\alpha_{ano}) \right.$$

$$+\sum_{b=1}^{b_a}\sum_{c=1}^{c_{ab}}\sum_{d=1}^{d_d}\sum_{e=1}^{e_{ad}}\sum_{f=1}^{f_{ade}} k_a\omega_a D_a^2 F_{de} G_a^2 A_{abc} B_{adef}$$

$$\times\left(\left(\frac{1}{2}\left(J_{m_d-1}(k_a r)-J_{m_d+1}(k_a r)\right)-Y_{m_d}(k_a r)\cos(\theta-\gamma_{ab})\right)\sin(k_a r\cos(\theta-\gamma_{ab})+\alpha_{abc}-\beta_{adef})\right.$$

$$\left.-\left(\frac{1}{2}\left(Y_{m_d-1}(k_a r)-Y_{m_d+1}(k_a r)\right)+J_{m_d}(k_a r)\cos(\theta-\gamma_{ab})\right)\cos(k_a r\cos(\theta-\gamma_{ab})+\alpha_{abc}-\beta_{adef})\right)$$

$$+\sum_{d=1}^{d_d}\sum_{e=1}^{e_{ad}}\sum_{f=1}^{f_{ade}}\sum_{p=1}^{p_p}\sum_{q=1}^{q_{ap}}\sum_{s=1}^{s_{apq}}\frac{1}{2}k_a\omega_a D_a^2 F_{de}F_{pq}G_a^2 B_{adef}B_{apqs}$$

$$\times\left(\left(J_{m_d}(k_a r)\left(J_{m_p-1}(k_a r)-J_{m_p+1}(k_a r)\right)-Y_{m_d}(k_a r)\left(Y_{m_p-1}(k_a r)-Y_{m_p+1}(k_a r)\right)\right)\sin(\beta_{adef}-\beta_{apqs})\right.$$

$$\left.+\left(Y_{m_d}(k_a r)\left(J_{m_p-1}(k_a r)-J_{m_p+1}(k_a r)\right)-J_{m_d}(k_a r)\left(Y_{m_p-1}(k_a r)-Y_{m_p+1}(k_a r)\right)\right)\cos(\beta_{adef}-\beta_{apqs})\right)\right)$$

(346)
1 of 2

$$\begin{aligned}\overline{\frac{\partial\phi}{\partial t}\frac{\partial\phi}{\partial r}} &= \frac{1}{2}\sum_{a=1}^{a_a} k_a\omega_a D_a^2 G_a^2\Bigg(\sum_{b=1}^{b_a}\sum_{c=1}^{c_{ab}}\sum_{n=1}^{n_a}\sum_{o=1}^{o_{an}} -A_{abc}A_{ano}\cos(\theta-\gamma_{an})\cos\left(k_a r(\cos(\theta-\gamma_{ab})-\cos(\theta-\gamma_{an}))+\alpha_{abc}-\alpha_{ano}\right)\\ &+\sum_{b=1}^{b_a}\sum_{c=1}^{c_{ab}}\sum_{d=1}^{d_d}\sum_{e=1}^{e_{ad}}\sum_{f=1}^{f_{ade}} F_{de}A_{abc}B_{adef}\Bigg(\left(\frac{1}{2}\left(J_{m_d-1}(k_a r)-J_{m_d+1}(k_a r)\right)-Y_{m_d}(k_a r)\cos(\theta-\gamma_{ab})\right)\sin\left(k_a r\cos(\theta-\gamma_{ab})+\alpha_{abc}-\beta_{adef}\right)\\ &-\left(\frac{1}{2}\left(Y_{m_d-1}(k_a r)-Y_{m_d+1}(k_a r)\right)+J_{m_d}(k_a r)\cos(\theta-\gamma_{ab})\right)\cos\left(k_a r\cos(\theta-\gamma_{ab})+\alpha_{abc}-\beta_{adef}\right)\Bigg)\\ &+\sum_{d=1}^{d_d}\sum_{e=1}^{e_{ad}}\sum_{f=1}^{f_{ade}}\sum_{p=1}^{p_p}\sum_{q=1}^{q_{ap}}\sum_{s=1}^{s_{apq}}\frac{1}{2}F_{de}F_{pq}B_{adef}B_{apqs}\\ &\times\Big(\left(J_{m_d}(k_a r)\left(J_{m_p-1}(k_a r)-J_{m_p+1}(k_a r)\right)-Y_{m_d}(k_a r)\left(Y_{m_p-1}(k_a r)-Y_{m_p+1}(k_a r)\right)\right)\sin\left(\beta_{adef}-\beta_{apqs}\right)\\ &+\left(Y_{m_d}(k_a r)\left(J_{m_p-1}(k_a r)-J_{m_p+1}(k_a r)\right)-J_{m_d}(k_a r)\left(Y_{m_p-1}(k_a r)-Y_{m_p+1}(k_a r)\right)\right)\cos\left(\beta_{adef}-\beta_{apqs}\right)\Big)\end{aligned} \quad (346)$$

The middle term in the brackets on the right-hand side of the Equation 329 is:

$$\begin{aligned}\overline{\frac{\partial\phi}{\partial t}\frac{1}{r}\frac{\partial\phi}{\partial\theta}} &= \frac{1}{2r}\Re\Bigg(\Bigg(\sum_{a=1}^{a_a}\sum_{b=1}^{b_a}\sum_{c=1}^{c_{ab}}T_1+\sum_{a=1}^{a_a}\sum_{d=1}^{d_d}\sum_{e=1}^{e_{ad}}\sum_{f=1}^{f_{ade}}T_2+i\left(\sum_{a=1}^{a_a}\sum_{b=1}^{b_a}\sum_{c=1}^{c_{ab}}T_3+\sum_{a=1}^{a_a}\sum_{d=1}^{d_d}\sum_{e=1}^{e_{ad}}\sum_{f=1}^{f_{ade}}T_4\right)\Bigg)\\ &\times\left(\sum_{a=1}^{a_a}\sum_{b=1}^{b_a}\sum_{c=1}^{c_{ab}}T_9+\sum_{a=1}^{a_a}\sum_{d=1}^{d_d}\sum_{e=1}^{e_{ad}}\sum_{f=1}^{f_{ade}}-T_{10}+i\left(\sum_{a=1}^{a_a}\sum_{b=1}^{b_a}\sum_{c=1}^{c_{ab}}-T_{11}+\sum_{a=1}^{a_a}\sum_{d=1}^{d_d}\sum_{e=1}^{e_{ad}}\sum_{f=1}^{f_{ade}}-T_{12}\right)\right)\Bigg)\end{aligned} \quad (347)$$

Because the time-averaged products of terms with different frequencies is zero, the $\sum_{a=1}^{a_a}$ can be moved to the front of the equation. Equation 347 can be re written:

$$\begin{aligned}
\overline{\frac{\partial \phi}{\partial t}\frac{1}{r}\frac{\partial \phi}{\partial \theta}} &= \frac{1}{2r}\Re\left(\left(\sum_{a=1}^{a_a}\sum_{b=1}^{b_a}\sum_{c=1}^{c_{ab}} T_1+\sum_{a=1}^{a_a}\sum_{d=1}^{d_d}\sum_{e=1}^{e_{ad}}\sum_{f=1}^{f_{ade}} T_2+i\left(\sum_{a=1}^{a_a}\sum_{b=1}^{b_a}\sum_{c=1}^{c_{ab}} T_3+\sum_{a=1}^{a_a}\sum_{d=1}^{d_d}\sum_{e=1}^{e_{ad}}\sum_{f=1}^{f_{ade}} T_4\right)\right)\right. \\
&\qquad \left.\times\left(\sum_{a=1}^{a_a}\sum_{b=1}^{b_a}\sum_{c=1}^{c_{ab}} T_9+\sum_{a=1}^{a_a}\sum_{d=1}^{d_d}\sum_{e=1}^{e_{ad}}\sum_{f=1}^{f_{ade}} -T_{10}+i\left(\sum_{a=1}^{a_a}\sum_{b=1}^{b_a}\sum_{c=1}^{c_{ab}} -T_{11}+\sum_{a=1}^{a_a}\sum_{d=1}^{d_d}\sum_{e=1}^{e_{ad}}\sum_{f=1}^{f_{ade}} -T_{12}\right)\right)\right) \\
&= \frac{1}{2r}\Re\left(\left(\sum_{a=1}^{a_a}\sum_{b=1}^{b_a}\sum_{c=1}^{c_{ab}} T_1+\sum_{a=1}^{a_a}\sum_{d=1}^{d_d}\sum_{e=1}^{e_{ad}}\sum_{f=1}^{f_{ade}} T_2\right)\left(\sum_{a=1}^{a_a}\sum_{b=1}^{b_a}\sum_{c=1}^{c_{ab}} T_9+\sum_{a=1}^{a_a}\sum_{d=1}^{d_d}\sum_{e=1}^{e_{ad}}\sum_{f=1}^{f_{ade}} -T_{10}\right)\right. \\
&\qquad +i\left(\sum_{a=1}^{a_a}\sum_{b=1}^{b_a}\sum_{c=1}^{c_{ab}} T_3+\sum_{a=1}^{a_a}\sum_{d=1}^{d_d}\sum_{e=1}^{e_{ad}}\sum_{f=1}^{f_{ade}} T_4\right)\left(\sum_{a=1}^{a_a}\sum_{b=1}^{b_a}\sum_{c=1}^{c_{ab}} T_9+\sum_{a=1}^{a_a}\sum_{d=1}^{d_d}\sum_{e=1}^{e_{ad}}\sum_{f=1}^{f_{ade}} -T_{10}\right) \\
&\qquad +i\left(\sum_{a=1}^{a_a}\sum_{b=1}^{b_a}\sum_{c=1}^{c_{ab}} T_1+\sum_{a=1}^{a_a}\sum_{d=1}^{d_d}\sum_{e=1}^{e_{ad}}\sum_{f=1}^{f_{ade}} T_2\right)\left(\sum_{a=1}^{a_a}\sum_{b=1}^{b_a}\sum_{c=1}^{c_{ab}} -T_{11}+\sum_{a=1}^{a_a}\sum_{d=1}^{d_d}\sum_{e=1}^{e_{ad}}\sum_{f=1}^{f_{ade}} -T_{12}\right) \\
&\qquad \left.-\left(\sum_{a=1}^{a_a}\sum_{b=1}^{b_a}\sum_{c=1}^{c_{ab}} T_3+\sum_{a=1}^{a_a}\sum_{d=1}^{d_d}\sum_{e=1}^{e_{ad}}\sum_{f=1}^{f_{ade}} T_4\right)\left(\sum_{a=1}^{a_a}\sum_{b=1}^{b_a}\sum_{c=1}^{c_{ab}} -T_{11}+\sum_{a=1}^{a_a}\sum_{d=1}^{d_d}\sum_{e=1}^{e_{ad}}\sum_{f=1}^{f_{ade}} -T_{12}\right)\right)
\end{aligned} \tag{348}$$

1 of 2

$$\begin{aligned}\overline{\frac{\partial\phi}{\partial t}\frac{1}{r}\frac{\partial\phi}{\partial\theta}} &= \frac{1}{2r}\left(\left(\sum_{a=1}^{a_a}\sum_{b=1}^{b_a}\sum_{c=1}^{c_{ab}} T_1+\sum_{a=1}^{a_a}\sum_{d=1}^{d_d}\sum_{e=1}^{e_{ad}}\sum_{f=1}^{f_{ade}} T_2\right)\left(\sum_{a=1}^{a_a}\sum_{b=1}^{b_a}\sum_{c=1}^{c_{ab}} T_9+\sum_{a=1}^{a_a}\sum_{d=1}^{d_d}\sum_{e=1}^{e_{ad}}\sum_{f=1}^{f_{ade}} -T_{10}\right)\right. \\ &\quad \left.-\left(\sum_{a=1}^{a_a}\sum_{b=1}^{b_a}\sum_{c=1}^{c_{ab}} T_3+\sum_{a=1}^{a_a}\sum_{d=1}^{d_d}\sum_{e=1}^{e_{ad}}\sum_{f=1}^{f_{ade}} T_4\right)\left(\sum_{a=1}^{a_a}\sum_{b=1}^{b_a}\sum_{c=1}^{c_{ab}} -T_{11}+\sum_{a=1}^{a_a}\sum_{d=1}^{d_d}\sum_{e=1}^{e_{ad}}\sum_{f=1}^{f_{ade}} -T_{12}\right)\right) \\ &= \frac{1}{2r}\sum_{a=1}^{a_a}\left(\left(\sum_{b=1}^{b_a}\sum_{c=1}^{c_{ab}} T_1+\sum_{d=1}^{d_d}\sum_{e=1}^{e_{ad}}\sum_{f=1}^{f_{ade}} T_2\right)\left(\sum_{b=1}^{b_a}\sum_{c=1}^{c_{ab}} T_9+\sum_{d=1}^{d_d}\sum_{e=1}^{e_{ad}}\sum_{f=1}^{f_{ade}} -T_{10}\right)\right. \\ &\quad \left.-\left(\sum_{b=1}^{b_a}\sum_{c=1}^{c_{ab}} T_3+\sum_{d=1}^{d_d}\sum_{e=1}^{e_{ad}}\sum_{f=1}^{f_{ade}} T_4\right)\left(\sum_{b=1}^{b_a}\sum_{c=1}^{c_{ab}} -T_{11}+\sum_{d=1}^{d_d}\sum_{e=1}^{e_{ad}}\sum_{f=1}^{f_{ade}} -T_{12}\right)\right)\end{aligned} \quad (348)$$

2 of 2

Using the n, o, p, q and s variables it is possible to reduce Equation 348 further:

$$\begin{aligned}\overline{\frac{\partial\phi}{\partial t}\frac{1}{r}\frac{\partial\phi}{\partial\theta}} &= \frac{1}{2r}\sum_{a=1}^{a_a}\left(\left(\sum_{b=1}^{b_a}\sum_{c=1}^{c_{ab}} T_{1\mathrm{bc}}+\sum_{d=1}^{d_d}\sum_{e=1}^{e_{ad}}\sum_{f=1}^{f_{ade}} T_{2\mathrm{def}}\right)\left(\sum_{n=1}^{n_a}\sum_{o=1}^{o_{an}} T_{9\mathrm{no}}+\sum_{p=1}^{p_p}\sum_{q=1}^{q_{ap}}\sum_{s=1}^{s_{apq}} -T_{10\mathrm{pqs}}\right)\right. \\ &\quad \left.-\left(\sum_{b=1}^{b_a}\sum_{c=1}^{c_{ab}} T_{3\mathrm{bc}}+\sum_{d=1}^{d_d}\sum_{e=1}^{e_{ad}}\sum_{f=1}^{f_{ade}} T_{4\mathrm{def}}\right)\left(\sum_{n=1}^{n_a}\sum_{o=1}^{o_{an}} -T_{11\mathrm{no}}+\sum_{p=1}^{p_p}\sum_{q=1}^{q_{ap}}\sum_{s=1}^{s_{apq}} -T_{12\mathrm{pqs}}\right)\right)\end{aligned} \quad (349)$$

1 of 2

$$\overline{\frac{\partial \phi}{\partial t}\frac{1}{r}\frac{\partial \phi}{\partial \theta}} = \frac{1}{2r}\sum_{a=1}^{a_a}\left(\sum_{b=1}^{b_a}\sum_{c=1}^{c_{ab}}\sum_{n=1}^{n_a}\sum_{o=1}^{o_{an}} T_{1\mathrm{bc}}T_{9\mathrm{no}} + \sum_{d=1}^{d_d}\sum_{e=1}^{e_{ad}}\sum_{f=1}^{f_{ade}}\sum_{n=1}^{n_a}\sum_{o=1}^{o_{an}} T_{2\mathrm{def}}T_{9\mathrm{no}} + \sum_{b=1}^{b_a}\sum_{c=1}^{c_{ab}}\sum_{p=1}^{p_p}\sum_{q=1}^{q_{ap}}\sum_{s=1}^{s_{apq}} -T_{1\mathrm{bc}}T_{10\mathrm{pqs}}\right.$$
$$+\sum_{d=1}^{d_d}\sum_{e=1}^{e_{ad}}\sum_{f=1}^{f_{ade}}\sum_{p=1}^{p_p}\sum_{q=1}^{q_{ap}}\sum_{s=1}^{s_{apq}} -T_{2\mathrm{def}}T_{10\mathrm{pqs}} - \left(\sum_{b=1}^{b_a}\sum_{c=1}^{c_{ab}}\sum_{n=1}^{n_a}\sum_{o=1}^{o_{an}} -T_{3\mathrm{bc}}T_{11\mathrm{no}} + \sum_{d=1}^{d_d}\sum_{e=1}^{e_{ad}}\sum_{f=1}^{f_{ade}}\sum_{n=1}^{n_a}\sum_{o=1}^{o_{an}} -T_{4\mathrm{def}}T_{11\mathrm{no}}\right.$$
$$\left.\left. +\sum_{b=1}^{b_a}\sum_{c=1}^{c_{ab}}\sum_{p=1}^{p_p}\sum_{q=1}^{q_{ap}}\sum_{s=1}^{s_{apq}} -T_{3\mathrm{bc}}T_{12\mathrm{pqs}} + \sum_{d=1}^{d_d}\sum_{e=1}^{e_{ad}}\sum_{f=1}^{f_{ade}}\sum_{p=1}^{p_p}\sum_{q=1}^{q_{ap}}\sum_{s=1}^{s_{apq}} -T_{4\mathrm{def}}T_{12\mathrm{pqs}}\right)\right) \quad (349)$$
2 of 2

$$= \frac{1}{2r}\sum_{a=1}^{a_a}\left(\sum_{b=1}^{b_a}\sum_{c=1}^{c_{ab}}\sum_{n=1}^{n_a}\sum_{o=1}^{o_{an}} T_{1\mathrm{bc}}T_{9\mathrm{no}} + T_{3\mathrm{bc}}T_{11\mathrm{no}} + \sum_{b=1}^{b_a}\sum_{c=1}^{c_{ab}}\sum_{d=1}^{d_d}\sum_{e=1}^{e_{ad}}\sum_{f=1}^{f_{ade}} -T_{1\mathrm{bc}}T_{10\mathrm{def}} + T_{2\mathrm{def}}T_{9\mathrm{bc}} + T_{4\mathrm{def}}T_{11\mathrm{bc}} + T_{3\mathrm{bc}}T_{12\mathrm{def}}\right.$$
$$\left. +\sum_{d=1}^{d_d}\sum_{e=1}^{e_{ad}}\sum_{f=1}^{f_{ade}}\sum_{p=1}^{p_p}\sum_{q=1}^{q_{ap}}\sum_{s=1}^{s_{apq}} -T_{2\mathrm{def}}T_{10\mathrm{pqs}} + T_{4\mathrm{def}}T_{12\mathrm{pqs}}\right)$$

Each group of terms can be further reduced:

$$\begin{aligned} T_{1\mathrm{bc}}T_{9\mathrm{no}} + T_{3\mathrm{bc}}T_{11\mathrm{no}} &= \left(\omega_a A_{abc} D_a G_a \sin(k_a r\cos(\theta-\gamma_{ab})+\alpha_{abc})\right) \text{ x } \left(k_a r \sin(\theta-\gamma_{an}) A_{ano} D_a G_a \sin\left(k_a r\cos(\theta-\gamma_{an})+\alpha_{ano}\right)\right) \\ &\quad +\left(\omega_a A_{abc} D_a G_a \cos(k_a r\cos(\theta-\gamma_{ab})+\alpha_{abc})\right) \text{ x } \left(k_a r \sin(\theta-\gamma_{an}) A_{ano} D_a G_a \cos\left(k_a r\cos(\theta-\gamma_{an})+\alpha_{ano}\right)\right) \\ &= k_a \omega_a D_a^2 G_a^2 r \sin(\theta-\gamma_{an}) A_{abc} A_{ano}\left(\sin(k_a r\cos(\theta-\gamma_{ab})+\alpha_{abc})\sin\left(k_a r\cos(\theta-\gamma_{an})+\alpha_{ano}\right)\right. \\ &\quad \left. +\cos(k_a r\cos(\theta-\gamma_{ab})+\alpha_{abc})\cos\left(k_a r\cos(\theta-\gamma_{an})+\alpha_{ano}\right)\right) \\ &= k_a \omega_a D_a^2 G_a^2 r \sin(\theta-\gamma_{an}) A_{abc} A_{ano} \cos(k_a r\left(\cos(\theta-\gamma_{ab})-\cos(\theta-\gamma_{an})\right)+\alpha_{abc}-\alpha_{ano}) \end{aligned} \quad (350)$$

And:

$$
\begin{aligned}
&-T_{1\mathrm{bc}}T_{10\mathrm{def}}+T_{2\mathrm{def}}T_{9\mathrm{bc}}+T_{4\mathrm{def}}T_{11\mathrm{dc}}+T_{3\mathrm{dc}}T_{12\mathrm{def}} \\
&= -\left(\omega_a A_{abc} D_a G_a \sin\left(k_a r\cos(\theta-\gamma_{ab})+\alpha_{abc}\right)\right) \mathrm{x}\ \left(m_d \sin(m_d\theta-\zeta_e)\, B_{adef} D_a G_a\left(J_{m_d}(k_a r)\cos(\beta_{adef})-Y_{m_d}(k_a r)\sin(\beta_{adef})\right)\right) \\
&\quad +\left(\omega_a D_a F_{de} G_a B_{adef}\left(J_{m_d}(k_a r)\sin(\beta_{adef})+Y_{m_d}(k_a r)\cos(\beta_{adef})\right)\right) \mathrm{x}\ \left(k_a r\sin(\theta-\gamma_{ab})\, A_{abc} D_a G_a \sin\left(k_a r\cos(\theta-\gamma_{ab})+\alpha_{abc}\right)\right) \\
&\quad +\left(\omega_a D_a F_{de} G_a B_{adef}\left(J_{m_d}(k_a r)\cos(\beta_{adef})-Y_{m_d}(k_a r)\sin(\beta_{adef})\right)\right) \mathrm{x}\ \left(k_a r\sin(\theta-\gamma_{ab})\, A_{abc} D_a G_a \cos\left(k_a r\cos(\theta-\gamma_{ab})+\alpha_{abc}\right)\right) \\
&\quad +\left(\omega_a A_{abc} D_a G_a \cos\left(k_a r\cos(\theta-\gamma_{ab})+\alpha_{abc}\right)\right) \mathrm{x}\ \left(m_d \sin(m_d\theta-\zeta_e) B_{adef} D_a G_a\left(J_{m_d}(k_a r)\sin(\beta_{adef})+Y_{m_d}(k_a r)\cos(\beta_{adef})\right)\right) \\
&= \omega_a D_a^2 G_a^2 A_{abc} B_{adef}\Big(-\Big(\sin\left(k_a r\cos(\theta-\gamma_{ab})+\alpha_{abc}\right) m_d \sin(m_d\theta-\zeta_e)\left(J_{m_d}(k_a r)\cos(\beta_{adef})-Y_{m_d}(k_a r)\sin(\beta_{adef})\right)\Big) \\
&\qquad +\left(F_{de}\left(J_{m_d}(k_a r)\sin(\beta_{adef})+Y_{m_d}(k_a r)\cos(\beta_{adef})\right) k_a r\sin(\theta-\gamma_{ab})\sin\left(k_a r\cos(\theta-\gamma_{ab})+\alpha_{abc}\right)\right) \\
&\qquad +\left(F_{de}\left(J_{m_d}(k_a r)\cos(\beta_{adef})-Y_{m_d}(k_a r)\sin(\beta_{adef})\right) k_a r\sin(\theta-\gamma_{ab})\cos\left(k_a r\cos(\theta-\gamma_{ab})+\alpha_{abc}\right)\right) \\
&\qquad +\left(\cos\left(k_a r\cos(\theta-\gamma_{ab})+\alpha_{abc}\right) m_d \sin(m_d\theta-\zeta_e)\left(J_{m_d}(k_a r)\sin(\beta_{adef})+Y_{m_d}(k_a r)\cos(\beta_{adef})\right)\right)\Big) \qquad (351) \\
&= \omega_a D_a^2 G_a^2 A_{abc} B_{adef} \qquad \text{1 of 2} \\
&\qquad \times\Big(m_d \sin(m_d\theta-\zeta_e)\Big(J_{m_d}(k_a r)\sin(\beta_{adef})\cos\left(k_a r\cos(\theta-\gamma_{ab})+\alpha_{abc}\right)+Y_{m_d}(k_a r)\cos(\beta_{adef})\cos\left(k_a r\cos(\theta-\gamma_{ab})+\alpha_{abc}\right) \\
&\qquad\quad -J_{m_d}(k_a r)\cos(\beta_{adef})\sin\left(k_a r\cos(\theta-\gamma_{ab})+\alpha_{abc}\right)+Y_{m_d}(k_a r)\sin(\beta_{adef})\sin\left(k_a r\cos(\theta-\gamma_{ab})+\alpha_{abc}\right)\Big) \\
&\qquad +k_a F_{de} r\sin(\theta-\gamma_{ab})\Big(J_{m_d}(k_a r)\sin(\beta_{adef})\sin\left(k_a r\cos(\theta-\gamma_{ab})+\alpha_{abc}\right)+Y_{m_d}(k_a r)\cos(\beta_{adef})\sin\left(k_a r\cos(\theta-\gamma_{ab})+\alpha_{abc}\right) \\
&\qquad\quad +J_{m_d}(k_a r)\cos(\beta_{adef})\cos\left(k_a r\cos(\theta-\gamma_{ab})+\alpha_{abc}\right)-Y_{m_d}(k_a r)\sin(\beta_{adef})\cos\left(k_a r\cos(\theta-\gamma_{ab})+\alpha_{abc}\right)\Big)\Big) \\
&= \omega_a D_a^2 G_a^2 A_{abc} B_{adef} \\
&\qquad \times\Big(m_d \sin(m_d\theta-\zeta_e)\Big(-J_{m_d}(k_a r)\sin\left(k_a r\cos(\theta-\gamma_{ab})+\alpha_{abc}-\beta_{adef}\right)+Y_{m_d}(k_a r)\cos\left(k_a r\cos(\theta-\gamma_{ab})+\alpha_{abc}-\beta_{adef}\right)\Big) \\
&\qquad +k_a F_{de} r\sin(\theta-\gamma_{ab})\Big(J_{m_d}(k_a r)\cos\left(k_a r\cos(\theta-\gamma_{ab})+\alpha_{abc}-\beta_{adef}\right)+Y_{m_d}(k_a r)\sin\left(k_a r\cos(\theta-\gamma_{ab})+\alpha_{abc}-\beta_{adef}\right)\Big)\Big)
\end{aligned}
$$

$$
\begin{aligned}
&-T_{1\text{bc}}T_{10\text{def}}+T_{2\text{def}}T_{9\text{bc}}+T_{4\text{def}}T_{11\text{dc}}+T_{3\text{dc}}T_{12\text{def}} \\
&= \omega_a D_a^2 G_a^2 A_{abc} B_{adef}\Big(\Big(k_a F_{de} r\sin(\theta-\gamma_{ab}) J_{m_d}(k_a r)+m_d\sin(m_d\theta-\zeta_e) Y_{m_d}(k_a r)\Big)\cos\Big(k_a r\cos(\theta-\gamma_{ab})+\alpha_{abc}-\beta_{adef}\Big) \quad \text{stack\{} \\
&\qquad +\Big(k_a F_{de} r\sin(\theta-\gamma_{ab}) Y_{m_d}(k_a r)-m_d\sin(m_d\theta-\zeta_e) J_{m_d}(k_a r)\Big)\sin\Big(k_a r\cos(\theta-\gamma_{ab})+\alpha_{abc}-\beta_{adef}\Big)\Big)
\end{aligned} \tag{351}
$$

stack{ 2 of 2

And:

$$
\begin{aligned}
&-T_{2\text{def}}T_{10\text{pqs}}+T_{4\text{def}}T_{12\text{pqs}} \\
&= -\Big(\omega_a D_a F_{de} G_a B_{adef}\Big(J_{m_d}(k_a r)\sin(\beta_{adef})+Y_{m_d}(k_a r)\cos(\beta_{adef})\Big)\Big) \\
&\qquad \times\Big(m_p\sin(m_p\theta-\zeta_q) B_{apqs} D_a G_a\Big(J_{m_p}(k_a r)\cos(\beta_{apqs})-Y_{m_p}(k_a r)\sin(\beta_{apqs})\Big)\Big) \\
&\qquad +\Big(\omega_a D_a F_{de} G_a B_{adef}\Big(J_{m_d}(k_a r)\cos(\beta_{adef})-Y_{m_d}(k_a r)\sin(\beta_{adef})\Big)\Big) \\
&\qquad \times\Big(m_p\sin(m_p\theta-\zeta_q) B_{apqs} D_a G_a\Big(J_{m_p}(k_a r)\sin(\beta_{apqs})+Y_{m_p}(k_a r)\cos(\beta_{apqs})\Big)\Big) \\
&= \omega_a D_a^2 F_{de} G_a^2 B_{adef} B_{apqs} m_p\sin(m_p\theta-\zeta_q)\Big(-\Big(J_{m_d}(k_a r)\sin(\beta_{adef})+Y_{m_d}(k_a r)\cos(\beta_{adef})\Big)\Big(J_{m_p}(k_a r)\cos(\beta_{apqs})-Y_{m_p}(k_a r)\sin(\beta_{apqs})\Big) \\
&\qquad +\Big(J_{m_d}(k_a r)\cos(\beta_{adef})-Y_{m_d}(k_a r)\sin(\beta_{adef})\Big)\Big(J_{m_p}(k_a r)\sin(\beta_{apqs})+Y_{m_p}(k_a r)\cos(\beta_{apqs})\Big)\Big) \\
&= \omega_a D_a^2 F_{de} G_a^2 B_{adef} B_{apqs} m_p\sin(m_p\theta-\zeta_q)\Big(-J_{m_d}(k_a r) J_{m_p}(k_a r)\cos(\beta_{apqs})\sin(\beta_{adef})-Y_{m_d}(k_a r) J_{m_p}(k_a r)\cos(\beta_{apqs})\cos(\beta_{adef}) \\
&\qquad +J_{m_d}(k_a r) Y_{m_p}(k_a r)\sin(\beta_{apqs})\sin(\beta_{adef})+Y_{m_d}(k_a r) Y_{m_p}(k_a r)\sin(\beta_{apqs})\cos(\beta_{adef}) \\
&\qquad +J_{m_d}(k_a r) J_{m_p}(k_a r)\sin(\beta_{apqs})\cos(\beta_{adef})-Y_{m_d}(k_a r) J_{m_p}(k_a r)\sin(\beta_{apqs})\sin(\beta_{adef}) \\
&\qquad +J_{m_d}(k_a r) Y_{m_p}(k_a r)\cos(\beta_{apqs})\cos(\beta_{adef})-Y_{m_d}(k_a r) Y_{m_p}(k_a r)\cos(\beta_{apqs})\sin(\beta_{adef})\Big)
\end{aligned} \tag{352}
$$

$$
\begin{aligned}
&-T_{2\mathrm{def}}T_{10\mathrm{pqs}}+T_{4\mathrm{def}}T_{12\mathrm{pqs}}\\
&= \omega_a D_a^2 F_{de} G_a^2 B_{adef} B_{apqs} m_p \sin(m_p\theta-\zeta_q)\Big(J_{m_d}(k_a r)J_{m_p}(k_a r)\big(\sin(\beta_{apqs})\cos(\beta_{adef})-\cos(\beta_{apqs})\sin(\beta_{adef})\big)\\
&\quad -Y_{m_d}(k_a r)J_{m_p}(k_a r)\big(\sin(\beta_{apqs})\sin(\beta_{adef})+\cos(\beta_{apqs})\cos(\beta_{adef})\big)+J_{m_d}(k_a r)Y_{m_p}(k_a r)\big(\sin(\beta_{apqs})\sin(\beta_{adef})+\cos(\beta_{apqs})\cos(\beta_{adef})\big)\\
&\quad +Y_{m_d}(k_a r)Y_{m_p}(k_a r)\big(\sin(\beta_{apqs})\cos(\beta_{adef})-\cos(\beta_{apqs})\sin(\beta_{adef})\big)\Big)\\
&= \omega_a D_a^2 F_{de} G_a^2 B_{adef} B_{apqs} m_p \sin(m_p\theta-\zeta_q)\Big(-J_{m_d}(k_a r)J_{m_p}(k_a r)\big(\sin(\beta_{adef}-\beta_{apqs})\big)-Y_{m_d}(k_a r)J_{m_p}(k_a r)\big(\cos(\beta_{adef}-\beta_{apqs})\big)\\
&\quad +J_{m_d}(k_a r)Y_{m_p}(k_a r)\big(\cos(\beta_{adef}-\beta_{apqs})\big)-Y_{m_d}(k_a r)Y_{m_p}(k_a r)\big(\sin(\beta_{adef}-\beta_{apqs})\big)\Big)\\
&= \omega_a D_a^2 F_{de} G_a^2 B_{adef} B_{apqs} m_p \sin(m_p\theta-\zeta_q)\Big(\big(J_{m_d}(k_a r)Y_{m_p}(k_a r)-Y_{m_d}(k_a r)J_{m_p}(k_a r)\big)\big(\cos(\beta_{adef}-\beta_{apqs})\big)\\
&\quad -\big(J_{m_d}(k_a r)J_{m_p}(k_a r)+Y_{m_d}(k_a r)Y_{m_p}(k_a r)\big)\big(\sin(\beta_{adef}-\beta_{apqs})\big)\Big)
\end{aligned}
\tag{352}
$$

2 of 2

Substituting Equations 350, 351 and 352 into Equation 349:

$$
\begin{aligned}
\overline{\frac{\partial\phi}{\partial t}\frac{1}{r}\frac{\partial\phi}{\partial\theta}} &= \frac{1}{2r}\sum_{a=1}^{a_a}\Bigg(\sum_{b=1}^{b_a}\sum_{c=1}^{c_{ab}}\sum_{n=1}^{n_a}\sum_{o=1}^{o_{an}} T_{1\mathrm{bc}}T_{9\mathrm{no}}+T_{3\mathrm{bc}}T_{11\mathrm{no}}+\sum_{b=1}^{b_a}\sum_{c=1}^{c_{ab}}\sum_{d=1}^{d_d}\sum_{e=1}^{e_{ad}}\sum_{f=1}^{f_{ade}} -T_{1\mathrm{bc}}T_{10\mathrm{def}}+T_{2\mathrm{def}}T_{9\mathrm{dc}}+T_{4\mathrm{def}}T_{11\mathrm{dc}}+T_{3\mathrm{dc}}T_{12\mathrm{def}}\\
&\quad +\sum_{d=1}^{d_d}\sum_{e=1}^{e_{ad}}\sum_{f=1}^{f_{ade}}\sum_{p=1}^{p_p}\sum_{q=1}^{q_{ap}}\sum_{s=1}^{s_{apq}} -T_{2\mathrm{def}}T_{10\mathrm{pqs}}+T_{4\mathrm{def}}T_{12\mathrm{pqs}}\Bigg)
\end{aligned}
\tag{353}
$$

1 of 2

$$\overline{\frac{\partial \phi}{\partial t}\frac{1}{r}\frac{\partial \phi}{\partial \theta}} = \frac{1}{2r}\sum_{a=1}^{a_a}\left(\sum_{b=1}^{b_a}\sum_{c=1}^{c_{ab}}\sum_{n=1}^{n_a}\sum_{o=1}^{o_{an}} k_a \omega_a D_a^2 G_a^2 r \sin(\theta-\gamma_{an}) A_{abc} A_{ano} \cos\left(k_a r\left(\cos(\theta-\gamma_{ab})-\cos(\theta-\gamma_{an})\right)+\alpha_{abc}-\alpha_{ano}\right)\right.$$

$$+\sum_{b=1}^{b_a}\sum_{c=1}^{c_{ab}}\sum_{d=1}^{d_d}\sum_{e=1}^{e_{ad}}\sum_{f=1}^{f_{ade}} \omega_a D_a^2 G_a^2 A_{abc} B_{adef}\left(\left(k_a F_{de} r \sin(\theta-\gamma_{ab}) J_{m_d}(k_a r)+m_d \sin(m_d\theta-\zeta_e) Y_{m_d}(k_a r)\right)\cos\left(k_a r\cos(\theta-\gamma_{ab})+\alpha_{abc}-\beta_{adef}\right)\right.$$

$$\left.+\left(k_a F_{de} r \sin(\theta-\gamma_{ab}) Y_{m_d}(k_a r)-m_d \sin(m_d\theta-\zeta_e) J_{m_d}(k_a r)\right)\sin\left(k_a r\cos(\theta-\gamma_{ab})+\alpha_{abc}-\beta_{adef}\right)\right)$$

$$+\sum_{d=1}^{d_d}\sum_{e=1}^{e_{ad}}\sum_{f=1}^{f_{ade}}\sum_{p=1}^{p_p}\sum_{q=1}^{q_{ap}}\sum_{s=1}^{s_{apq}} \omega_a D_a^2 F_{de} G_a^2 B_{adef} B_{apqs} m_p \sin(m_p\theta-\zeta_e)\left(\left(J_{m_d}(k_a r) Y_{m_p}(k_a r)-Y_{m_d}(k_a r) J_{m_p}(k_a r)\right)\cos(\beta_{adef}-\beta_{apqs})\right.$$

$$\left.-\left(J_{m_d}(k_a r) J_{m_p}(k_a r)+Y_{m_d}(k_a r) Y_{m_p}(k_a r)\right)\sin(\beta_{adef}-\beta_{apqs})\right)$$

(353)
2 of 2

$$= \frac{1}{2}\sum_{a=1}^{a_a} k_a \omega_a D_a^2 G_a^2\left(\sum_{b=1}^{b_a}\sum_{c=1}^{c_{ab}}\sum_{n=1}^{n_a}\sum_{o=1}^{o_{an}} \sin(\theta-\gamma_{an}) A_{abc} A_{ano} \cos\left(k_a r\left(\cos(\theta-\gamma_{ab})-\cos(\theta-\gamma_{an})\right)+\alpha_{abc}-\alpha_{ano}\right)\right.$$

$$+\sum_{b=1}^{b_a}\sum_{c=1}^{c_{ab}}\sum_{d=1}^{d_d}\sum_{e=1}^{e_{ad}}\sum_{f=1}^{f_{ade}} A_{abc} B_{adef}\left(\left(F_{de}\sin(\theta-\gamma_{ab}) J_{m_d}(k_a r)+\frac{m_d \sin(m_d\theta-\zeta_e)}{k_a r} Y_{m_d}(k_a r)\right)\cos\left(k_a r\cos(\theta-\gamma_{ab})+\alpha_{abc}-\beta_{adef}\right)\right.$$

$$\left.+\left(F_{de}\sin(\theta-\gamma_{ab}) Y_{m_d}(k_a r)-\frac{m_d \sin(m_d\theta-\zeta_e)}{k_a r} J_{m_d}(k_a r)\right)\sin\left(k_a r\cos(\theta-\gamma_{ab})+\alpha_{abc}-\beta_{adef}\right)\right)$$

$$+\sum_{d=1}^{d_d}\sum_{e=1}^{e_{ad}}\sum_{f=1}^{f_{ade}}\sum_{p=1}^{p_p}\sum_{q=1}^{q_{ap}}\sum_{s=1}^{s_{apq}} \frac{F_{de} B_{adef} B_{apqs} m_p \sin(m_p\theta-\zeta_q)}{k_a r}\left(\left(J_{m_d}(k_a r) Y_{m_p}(k_a r)-Y_{m_d}(k_a r) J_{m_p}(k_a r)\right)\left(\cos(\beta_{adef}-\beta_{apqs})\right)\right.$$

$$\left.\left.-\left(J_{m_d}(k_a r) J_{m_p}(k_a r)+Y_{m_d}(k_a r) Y_{m_p}(k_a r)\right)\left(\sin(\beta_{adef}-\beta_{apqs})\right)\right)\right)$$

Finally the right most term in the brackets on the right-hand side of the Equation 329.

$$\overline{\frac{\partial \phi}{\partial t}\frac{\partial \phi}{\partial z}} = \frac{1}{2}\Re\left(\left(\sum_{a=1}^{a_a}\sum_{b=1}^{b_a}\sum_{c=1}^{c_{ab}} T_1 + \sum_{a=1}^{a_a}\sum_{d=1}^{d_d}\sum_{e=1}^{e_{ad}}\sum_{f=1}^{f_{ade}} T_2 + i\left(\sum_{a=1}^{a_a}\sum_{b=1}^{b_a}\sum_{c=1}^{c_{ab}} T_3 + \sum_{a=1}^{a_a}\sum_{d=1}^{d_d}\sum_{e=1}^{e_{ad}}\sum_{f=1}^{f_{ade}} T_4\right)\right)\right.$$
$$\left.\times\left(\sum_{a=1}^{a_a}\sum_{b=1}^{b_a}\sum_{c=1}^{c_{ab}} T_{13} + \sum_{a=1}^{a_a}\sum_{d=1}^{d_d}\sum_{e=1}^{e_{ad}}\sum_{f=1}^{f_{ade}} T_{14} + i\left(\sum_{a=1}^{a_a}\sum_{b=1}^{b_a}\sum_{c=1}^{c_{ab}} T_{15} + \sum_{a=1}^{a_a}\sum_{d=1}^{d_d}\sum_{e=1}^{e_{ad}}\sum_{f=1}^{f_{ade}} T_{16}\right)\right)\right) \quad (354)$$

Because the time-averaged products of terms with different frequencies is zero, the $\sum_{a=1}^{a_a}$ can be moved to the front of the equation. Equation 354 can be re written:

$$\overline{\frac{\partial \phi}{\partial t}\frac{\partial \phi}{\partial z}} = \frac{1}{2}\Re\left(\left(\sum_{a=1}^{a_a}\sum_{b=1}^{b_a}\sum_{c=1}^{c_{ab}} T_1 + \sum_{a=1}^{a_a}\sum_{d=1}^{d_d}\sum_{e=1}^{e_{ad}}\sum_{f=1}^{f_{ade}} T_2 + i\left(\sum_{a=1}^{a_a}\sum_{b=1}^{b_a}\sum_{c=1}^{c_{ab}} T_3 + \sum_{a=1}^{a_a}\sum_{d=1}^{d_d}\sum_{e=1}^{e_{ad}}\sum_{f=1}^{f_{ade}} T_4\right)\right)\right.$$
$$\left.\times\left(\sum_{a=1}^{a_a}\sum_{b=1}^{b_a}\sum_{c=1}^{c_{ab}} T_{13} + \sum_{a=1}^{a_a}\sum_{d=1}^{d_d}\sum_{e=1}^{e_{ad}}\sum_{f=1}^{f_{ade}} T_{14} + i\left(\sum_{a=1}^{a_a}\sum_{b=1}^{b_a}\sum_{c=1}^{c_{ab}} T_{15} + \sum_{a=1}^{a_a}\sum_{d=1}^{d_d}\sum_{e=1}^{e_{ad}}\sum_{f=1}^{f_{ade}} T_{16}\right)\right)\right) \quad (355)$$

$$\overline{\frac{\partial \phi}{\partial t}\frac{\partial \phi}{\partial z}} = \frac{1}{2}\Re\left(\left(\sum_{a=1}^{a_a}\sum_{b=1}^{b_a}\sum_{c=1}^{c_{ab}} T_1 + \sum_{a=1}^{a_a}\sum_{d=1}^{d_d}\sum_{e=1}^{e_{ad}}\sum_{f=1}^{f_{ade}} T_2\right)\left(\sum_{a=1}^{a_a}\sum_{b=1}^{b_a}\sum_{c=1}^{c_{ab}} T_{13} + \sum_{a=1}^{a_a}\sum_{d=1}^{d_d}\sum_{e=1}^{e_{ad}}\sum_{f=1}^{f_{ade}} T_{14}\right)\right.$$
$$+i\left(\sum_{a=1}^{a_a}\sum_{b=1}^{b_a}\sum_{c=1}^{c_{ab}} T_3 + \sum_{a=1}^{a_a}\sum_{d=1}^{d_d}\sum_{e=1}^{e_{ad}}\sum_{f=1}^{f_{ade}} T_4\right)\left(\sum_{a=1}^{a_a}\sum_{b=1}^{b_a}\sum_{c=1}^{c_{ab}} T_{13} + \sum_{a=1}^{a_a}\sum_{d=1}^{d_d}\sum_{e=1}^{e_{ad}}\sum_{f=1}^{f_{ade}} T_{14}\right)$$
$$+i\left(\sum_{a=1}^{a_a}\sum_{b=1}^{b_a}\sum_{c=1}^{c_{ab}} T_1 + \sum_{a=1}^{a_a}\sum_{d=1}^{d_d}\sum_{e=1}^{e_{ad}}\sum_{f=1}^{f_{ade}} T_2\right)\left(\sum_{a=1}^{a_a}\sum_{b=1}^{b_a}\sum_{c=1}^{c_{ab}} T_{15} + \sum_{a=1}^{a_a}\sum_{d=1}^{d_d}\sum_{e=1}^{e_{ad}}\sum_{f=1}^{f_{ade}} T_{16}\right)$$
$$\left.-\left(\sum_{a=1}^{a_a}\sum_{b=1}^{b_a}\sum_{c=1}^{c_{ab}} T_3 + \sum_{a=1}^{a_a}\sum_{d=1}^{d_d}\sum_{e=1}^{e_{ad}}\sum_{f=1}^{f_{ade}} T_4\right)\left(\sum_{a=1}^{a_a}\sum_{b=1}^{b_a}\sum_{c=1}^{c_{ab}} T_{15} + \sum_{a=1}^{a_a}\sum_{d=1}^{d_d}\sum_{e=1}^{e_{ad}}\sum_{f=1}^{f_{ade}} T_{16}\right)\right) \quad (355)$$
2 of 2

$$= \frac{1}{2}\left(\left(\sum_{a=1}^{a_a}\sum_{b=1}^{b_a}\sum_{c=1}^{c_{ab}} T_1 + \sum_{a=1}^{a_a}\sum_{d=1}^{d_d}\sum_{e=1}^{e_{ad}}\sum_{f=1}^{f_{ade}} T_2\right)\left(\sum_{a=1}^{a_a}\sum_{b=1}^{b_a}\sum_{c=1}^{c_{ab}} T_{13} + \sum_{a=1}^{a_a}\sum_{d=1}^{d_d}\sum_{e=1}^{e_{ad}}\sum_{f=1}^{f_{ade}} T_{14}\right)\right.$$
$$\left.-\left(\sum_{a=1}^{a_a}\sum_{b=1}^{b_a}\sum_{c=1}^{c_{ab}} T_3 + \sum_{a=1}^{a_a}\sum_{d=1}^{d_d}\sum_{e=1}^{e_{ad}}\sum_{f=1}^{f_{ade}} T_4\right)\left(\sum_{a=1}^{a_a}\sum_{b=1}^{b_a}\sum_{c=1}^{c_{ab}} T_{15} + \sum_{a=1}^{a_a}\sum_{d=1}^{d_d}\sum_{e=1}^{e_{ad}}\sum_{f=1}^{f_{ade}} T_{16}\right)\right)$$

$$= \frac{1}{2}\sum_{a=1}^{a_a}\left(\left(\sum_{b=1}^{b_a}\sum_{c=1}^{c_{ab}} T_1 + \sum_{d=1}^{d_d}\sum_{e=1}^{e_{ad}}\sum_{f=1}^{f_{ade}} T_2\right)\left(\sum_{b=1}^{b_a}\sum_{c=1}^{c_{ab}} T_{13} + \sum_{d=1}^{d_d}\sum_{e=1}^{e_{ad}}\sum_{f=1}^{f_{ade}} T_{14}\right)-\left(\sum_{b=1}^{b_a}\sum_{c=1}^{c_{ab}} T_3 + \sum_{d=1}^{d_d}\sum_{e=1}^{e_{ad}}\sum_{f=1}^{f_{ade}} T_4\right)\left(\sum_{b=1}^{b_a}\sum_{c=1}^{c_{ab}} T_{15} + \sum_{d=1}^{d_d}\sum_{e=1}^{e_{ad}}\sum_{f=1}^{f_{ade}} T_{16}\right)\right)$$

Also, to preserve the combination of terms it is necessary to introduce five new terms n, o, p, q and s such that each term has the same range as b, c, d, e and f respectively but vary independently. Using these new variables it is possible to create a relatively short notation for all of the terms involved:

$$
\begin{aligned}
\overline{\frac{\partial \phi}{\partial t}\frac{\partial \phi}{\partial z}} &= \frac{1}{2}\sum_{a=1}^{a_a}\left(\left(\sum_{b=1}^{b_a}\sum_{c=1}^{c_{ab}} T_{1\mathrm{bc}} + \sum_{d=1}^{d_d}\sum_{e=1}^{e_{ad}}\sum_{f=1}^{f_{ade}} T_{2\mathrm{def}}\right)\left(\sum_{n=1}^{n_a}\sum_{o=1}^{o_{an}} T_{13\mathrm{no}} + \sum_{p=1}^{p_p}\sum_{q=1}^{q_{ap}}\sum_{s=1}^{s_{apq}} T_{14\mathrm{pqs}}\right)\right. \\
&\qquad \left. -\left(\sum_{b=1}^{b_a}\sum_{c=1}^{c_{ab}} T_{3\mathrm{bc}} + \sum_{d=1}^{d_d}\sum_{e=1}^{e_{ad}}\sum_{f=1}^{f_{ade}} T_{4\mathrm{def}}\right)\left(\sum_{n=1}^{n_a}\sum_{o=1}^{o_{an}} T_{15\mathrm{no}} + \sum_{p=1}^{p_p}\sum_{q=1}^{q_{ap}}\sum_{s=1}^{s_{apq}} T_{16\mathrm{pqs}}\right)\right) \\
&= \frac{1}{2}\sum_{a=1}^{a_a}\left(\sum_{b=1}^{b_a}\sum_{c=1}^{c_{ab}}\sum_{n=1}^{n_a}\sum_{o=1}^{o_{an}} T_{1\mathrm{bc}}T_{13\mathrm{no}} + \sum_{d=1}^{d_d}\sum_{e=1}^{e_{ad}}\sum_{f=1}^{f_{ade}}\sum_{n=1}^{n_a}\sum_{o=1}^{o_{an}} T_{2\mathrm{def}}T_{13\mathrm{no}} + \sum_{b=1}^{b_a}\sum_{c=1}^{c_{ab}}\sum_{p=1}^{p_q}\sum_{q=1}^{q_{ap}}\sum_{s=1}^{s_{apq}} T_{1\mathrm{bc}}T_{14\mathrm{pqs}} + \sum_{d=1}^{d_d}\sum_{e=1}^{e_{ad}}\sum_{f=1}^{f_{ade}}\sum_{p=1}^{p_p}\sum_{q=1}^{q_{aq}}\sum_{s=1}^{s_{apq}} T_{2\mathrm{def}}T_{14\mathrm{pqs}}\right. \\
&\qquad \left. -\left(\sum_{b=1}^{b_a}\sum_{c=1}^{c_{ab}}\sum_{n=1}^{n_a}\sum_{o=1}^{o_{an}} T_{3\mathrm{bc}}T_{15\mathrm{no}} + \sum_{d=1}^{d_d}\sum_{e=1}^{e_{ad}}\sum_{f=1}^{f_{ade}}\sum_{n=1}^{n_a}\sum_{o=1}^{o_{an}} T_{4\mathrm{def}}T_{15\mathrm{no}} + \sum_{b=1}^{b_a}\sum_{c=1}^{c_{ab}}\sum_{p=1}^{p_p}\sum_{q=1}^{q_{ap}}\sum_{s=1}^{s_{apq}} T_{3\mathrm{bc}}T_{16\mathrm{pqs}} + \sum_{d=1}^{d_d}\sum_{e=1}^{e_{ad}}\sum_{f=1}^{f_{ade}}\sum_{p=1}^{p_p}\sum_{q=1}^{q_{ap}}\sum_{s=1}^{s_{apq}} T_{4\mathrm{def}}T_{16\mathrm{pqs}}\right)\right) \\
&= \frac{1}{2}\sum_{a=1}^{a_a}\left(\sum_{b=1}^{b_a}\sum_{c=1}^{c_{ab}}\sum_{n=1}^{n_a}\sum_{o=1}^{o_{an}} T_{1\mathrm{bc}}T_{13\mathrm{no}} - T_{3\mathrm{bc}}T_{15\mathrm{no}} + \sum_{b=1}^{b_a}\sum_{c=1}^{c_{ab}}\sum_{d=1}^{d_d}\sum_{e=1}^{e_{ad}}\sum_{f=1}^{f_{ade}} T_{1\mathrm{bc}}T_{14\mathrm{def}} + T_{2\mathrm{def}}T_{13\mathrm{bc}} - T_{4\mathrm{def}}T_{15\mathrm{dc}} - T_{3\mathrm{dc}}T_{16\mathrm{def}}\right. \\
&\qquad \left. + \sum_{d=1}^{d_d}\sum_{e=1}^{e_{ad}}\sum_{f=1}^{f_{ade}}\sum_{p=1}^{p_p}\sum_{q=1}^{q_{ap}}\sum_{s=1}^{s_{apq}} T_{2\mathrm{def}}T_{14\mathrm{pqs}} - T_{4\mathrm{def}}T_{16\mathrm{pqs}}\right)
\end{aligned}
\tag{356}
$$

Each group of terms can be further reduced:

$$
\begin{aligned}
T_{1\mathrm{bc}}T_{13\mathrm{no}}-T_{3\mathrm{bc}}T_{15\mathrm{no}} &= \left(\omega_a A_{abc} D_a G_a \sin\left(k_a r\cos(\theta-\gamma_{ab})+\alpha_{abc}\right)\right) \text{ x } \left(k_a A_{ano} D_a \sinh\left(k_a(h+z)\right)\cos\left(k_a r\cos(\theta-\gamma_{an})+\alpha_{ano}\right)\right) \\
&\quad -\left(\omega_a A_{abc} D_a G_a \cos\left(k_a r\cos(\theta-\gamma_{ab})+\alpha_{abc}\right)\right) \text{ x } \left(k_a A_{ano} D_a \sinh\left(k_a(h+z)\right)\sin\left(k_a r\cos(\theta-\gamma_{an})+\alpha_{ano}\right)\right) \\
&= k_a \omega_a D_a^2 G_a A_{abc} A_{ano} \sinh\left(k_a(h+z)\right)\left(\left(\sin\left(k_a r\cos(\theta-\gamma_{ab})+\alpha_{abc}\right)\cos\left(k_a r\cos(\theta-\gamma_{an})+\alpha_{ano}\right)\right)\right. \\
&\quad \left. -\left(\cos\left(k_a r\cos(\theta-\gamma_{ab})+\alpha_{abc}\right)\sin\left(k_a r\cos(\theta-\gamma_{an})+\alpha_{ano}\right)\right)\right) \\
&= k_a \omega_a D_a^2 G_a A_{abc} A_{ano} \sinh\left(k_a(h+z)\right)\sin\left(k_a r\left(\cos(\theta-\gamma_{ab})-\cos(\theta-\gamma_{an})\right)+\alpha_{abc}-\alpha_{ano}\right)
\end{aligned} \tag{357}
$$

And:

$$
\begin{aligned}
&T_{1\mathrm{bc}}T_{14\mathrm{def}}+T_{2\mathrm{def}}T_{13\mathrm{bc}}-T_{4\mathrm{def}}T_{15\mathrm{dc}}-T_{3\mathrm{dc}}T_{16\mathrm{def}} \\
&= \left(\omega_a A_{abc} D_a G_a \sin\left(k_a r\cos(\theta-\gamma_{ab})+\alpha_{abc}\right)\right)\times\left(k_a B_{adef} D_a F_{de} \sinh\left(k_a(h+z)\right)\left(J_{m_d}(k_a r)\cos(\beta_{adef})-Y_{m_d}(k_a r)\sin(\beta_{adef})\right)\right) \\
&\quad +\left(\omega_a D_a F_{de} G_a B_{adef}\left(J_{m_d}(k_a r)\sin(\beta_{adef})+Y_{m_d}(k_a r)\cos(\beta_{adef})\right)\right)\times\left(k_a A_{abc} D_a \sinh\left(k_a(h+z)\right)\cos\left(k_a r\cos(\theta-\gamma_{ab})+\alpha_{abc}\right)\right) \\
&\quad -\left(\omega_a D_a F_{de} G_a B_{adef}\left(J_{m_d}(k_a r)\cos(\beta_{adef})-Y_{m_d}(k_a r)\sin(\beta_{adef})\right)\right)\times\left(k_a A_{abc} D_a \sinh\left(k_a(h+z)\right)\sin\left(k_a r\cos(\theta-\gamma_{ab})+\alpha_{abc}\right)\right) \\
&\quad -\left(\omega_a A_{abc} D_a G_a \cos\left(k_a r\cos(\theta-\gamma_{ab})+\alpha_{abc}\right)\right)\times\left(k_a B_{adef} D_a F_{de} \sinh\left(k_a(h+z)\right)\left(J_{m_d}(k_a r)\sin(\beta_{adef})+Y_{m_d}(k_a r)\cos(\beta_{adef})\right)\right) \\
&= k_a \omega_a D_a^2 F_{de} G_a A_{abc} B_{adef} \sinh\left(k_a(h+z)\right)\left(\left(\sin\left(k_a r\cos(\theta-\gamma_{ab})+\alpha_{abc}\right)\left(J_{m_d}(k_a r)\cos(\beta_{adef})-Y_{m_d}(k_a r)\sin(\beta_{adef})\right)\right)\right. \\
&\quad +\left(\left(J_{m_d}(k_a r)\sin(\beta_{adef})+Y_{m_d}(k_a r)\cos(\beta_{adef})\right)\cos\left(k_a r\cos(\theta-\gamma_{ab})+\alpha_{abc}\right)\right) \\
&\quad -\left(\left(J_{m_d}(k_a r)\cos(\beta_{adef})-Y_{m_d}(k_a r)\sin(\beta_{adef})\right)\sin\left(k_a r\cos(\theta-\gamma_{ab})+\alpha_{abc}\right)\right) \\
&\quad \left. -\left(\cos\left(k_a r\cos(\theta-\gamma_{ab})+\alpha_{abc}\right)\left(J_{m_d}(k_a r)\sin(\beta_{adef})+Y_{m_d}(k_a r)\cos(\beta_{adef})\right)\right)\right) \\
&= k_a \omega_a D_a^2 F_{de} G_a A_{abc} B_{adef} \sinh\left(k_a(h+z)\right)(0) \\
&= 0
\end{aligned} \tag{358}
$$

And:

$$
\begin{aligned}
&T_{2\mathrm{def}}T_{14\mathrm{pqs}}-T_{4\mathrm{def}}T_{16\mathrm{pqs}}\\
&=\left(\omega_a D_a F_{de} G_a B_{adef}\left(J_{m_d}(k_a r)\sin(\beta_{adef})+Y_{m_d}(k_a r)\cos(\beta_{adef})\right)\right)\\
&\qquad\times\left(k_a B_{apqs} D_a F_{pq}\sinh(k_a(h+z))\left(J_{m_p}(k_a r)\cos(\beta_{apqs})-Y_{m_p}(k_a r)\sin(\beta_{apqs})\right)\right)\\
&\qquad-\left(\omega_a D_a F_{de} G_a B_{adef}\left(J_{m_d}(k_a r)\cos(\beta_{adef})-Y_{m_d}(k_a r)\sin(\beta_{adef})\right)\right)\\
&\qquad\times\left(k_a B_{apqs} D_a F_{pq}\sinh(k_a(h+z))\left(J_{m_p}(k_a r)\sin(\beta_{apqs})+Y_{m_p}(k_a r)\cos(\beta_{apqs})\right)\right)\\
&=k_a\omega_a D_a^2 F_{de}F_{pq}G_a B_{adef}B_{apqs}\sinh(k_a(h+z))\\
&\qquad\times\left(\left(\left(J_{m_d}(k_a r)\sin(\beta_{adef})+Y_{m_d}(k_a r)\cos(\beta_{adef})\right)\left(J_{m_p}(k_a r)\cos(\beta_{apqs})-Y_{m_p}(k_a r)\sin(\beta_{apqs})\right)\right)\right.\\
&\qquad\left.-\left(\left(J_{m_d}(k_a r)\cos(\beta_{adef})-Y_{m_d}(k_a r)\sin(\beta_{adef})\right)\left(J_{m_p}(k_a r)\sin(\beta_{apqs})+Y_{m_p}(k_a r)\cos(\beta_{apqs})\right)\right)\right)\\
&=k_a\omega_a D_a^2 F_{de}F_{pq}G_a B_{adef}B_{apqs}\sinh(k_a(h+z))\left(J_{m_d}(k_a r)J_{m_p}(k_a r)\cos(\beta_{apqs})\sin(\beta_{adef})+Y_{m_d}(k_a r)J_{m_p}(k_a r)\cos(\beta_{apqs})\cos(\beta_{adef})\right.\\
&\qquad-J_{m_d}(k_a r)Y_{m_p}(k_a r)\sin(\beta_{apqs})\sin(\beta_{adef})-Y_{m_d}(k_a r)Y_{m_p}(k_a r)\sin(\beta_{apqs})\cos(\beta_{adef})\\
&\qquad-J_{m_d}(k_a r)J_{m_p}(k_a r)\sin(\beta_{apqs})\cos(\beta_{adef})+Y_{m_d}(k_a r)J_{m_p}(k_a r)\sin(\beta_{apqs})\sin(\beta_{adef})\\
&\qquad\left.-J_{m_d}(k_a r)Y_{m_p}(k_a r)\cos(\beta_{apqs})\cos(\beta_{adef})+Y_{m_d}(k_a r)Y_{m_p}(k_a r)\cos(\beta_{apqs})\sin(\beta_{adef})\right)\\
&=k_a\omega_a D_a^2 F_{de}F_{pq}G_a B_{adef}B_{apqs}\sinh(k_a(h+z))\\
&\times\left(J_{m_d}(k_a r)J_{m_p}(k_a r)\left(\cos(\beta_{apqs})\sin(\beta_{adef})-\sin(\beta_{apqs})\cos(\beta_{adef})\right)+Y_{m_d}(k_a r)J_{m_p}(k_a r)\left(\cos(\beta_{apqs})\cos(\beta_{adef})+\sin(\beta_{apqs})\sin(\beta_{adef})\right)\right.\\
&\left.-J_{m_d}(k_a r)Y_{m_p}(k_a r)\left(\sin(\beta_{apqs})\sin(\beta_{adef})+\cos(\beta_{apqs})\cos(\beta_{adef})\right)+Y_{m_d}(k_a r)Y_{m_p}(k_a r)\left(\cos(\beta_{apqs})\sin(\beta_{adef})-\sin(\beta_{apqs})\cos(\beta_{adef})\right)\right)\\
&=k_a\omega_a D_a^2 F_{de}F_{pq}G_a B_{adef}B_{apqs}\sinh(k_a(h+z))\left(J_{m_d}(k_a r)J_{m_p}(k_a r)\sin(\beta_{adef}-\beta_{apqs})+Y_{m_d}(k_a r)J_{m_p}(k_a r)\cos(\beta_{adef}-\beta_{apqs})\right.\\
&\qquad\left.-J_{m_d}(k_a r)Y_{m_p}(k_a r)\cos(\beta_{adef}-\beta_{apqs})+Y_{m_d}(k_a r)Y_{m_p}(k_a r)\sin(\beta_{adef}-\beta_{apqs})\right)
\end{aligned}
\tag{359}
$$

1 of 2

$$
\begin{aligned}
&T_{2\mathrm{def}}\,T_{14\mathrm{pqs}}-T_{4\mathrm{def}}\,T_{16\mathrm{pqs}}\\
&\quad=\;k_a\omega_a D_a^2 F_{de}F_{pq}G_a B_{adef}B_{apqs}\sinh\left(k_a(h+z)\right)\Big(\left(J_{m_d}(k_a r)J_{m_p}(k_a r)+Y_{m_d}(k_a r)\,Y_{m_p}(k_a r)\right)\sin\left(\beta_{adef}-\beta_{apqs}\right)\\
&\qquad\qquad+\left(Y_{m_d}(k_a r)\,J_{m_p}(k_a r)-J_{m_d}(k_a r)\,Y_{m_p}(k_a r)\right)\cos\left(\beta_{adef}-\beta_{apqs}\right)\Big)
\end{aligned}
\tag{359}
$$

2 of 2

And finally:

$$
\begin{aligned}
\overline{\frac{\partial\phi}{\partial t}\frac{\partial\phi}{\partial z}}\;&=\;\frac{1}{2}\sum_{a=1}^{a_a}\Bigg(\sum_{b=1}^{b_a}\sum_{c=1}^{c_{ab}}\sum_{n=1}^{n_a}\sum_{o=1}^{o_{an}}T_{1\mathrm{bc}}T_{13\mathrm{no}}-T_{3\mathrm{bc}}T_{15\mathrm{no}}+\sum_{b=1}^{b_a}\sum_{c=1}^{c_{ab}}\sum_{d=1}^{d_d}\sum_{e=1}^{e_{ad}}\sum_{f=1}^{f_{ade}}T_{1\mathrm{bc}}T_{14\mathrm{def}}+T_{2\mathrm{def}}T_{13\mathrm{bc}}-T_{4\mathrm{def}}T_{15\mathrm{dc}}-T_{3\mathrm{dc}}T_{16\mathrm{def}}\\
&\qquad+\sum_{d=1}^{d_d}\sum_{e=1}^{e_{ad}}\sum_{f=1}^{f_{ade}}\sum_{p=1}^{p_p}\sum_{q=1}^{q_{ap}}\sum_{s=1}^{s_{apq}}T_{2\mathrm{def}}T_{14\mathrm{pqs}}-T_{4\mathrm{def}}T_{16\mathrm{pqs}}\Bigg)\\
&=\;\frac{1}{2}\sum_{a=1}^{a_a}\Bigg(\sum_{b=1}^{b_a}\sum_{c=1}^{c_{ab}}\sum_{n=1}^{n_a}\sum_{o=1}^{o_{an}}k_a\omega_a D_a^2 G_a A_{abc}A_{ano}\sinh\left(k_a(h+z)\right)\sin\left(k_a r\left(\cos(\theta-\gamma_{ab})-\cos(\theta-\gamma_{an})\right)+\alpha_{abc}-\alpha_{ano}\right)\\
&\qquad+\sum_{b=1}^{b_a}\sum_{c=1}^{c_{ab}}\sum_{d=1}^{d_d}\sum_{e=1}^{e_{ad}}\sum_{f=1}^{f_{ade}}0+\sum_{d=1}^{d_d}\sum_{e=1}^{e_{ad}}\sum_{f=1}^{f_{ade}}\sum_{p=1}^{p_p}\sum_{q=1}^{q_{ap}}\sum_{s=1}^{s_{apq}}k_a\omega_a D_a^2 F_{de}F_{pq}G_a B_{adef}B_{apqs}\sinh\left(k_a(h+z)\right)\\
&\quad\times\Big(\left(J_{m_d}(k_a r)J_{m_p}(k_a r)+Y_{m_d}(k_a r)Y_{m_p}(k_a r)\right)\sin\left(\beta_{adef}-\beta_{apqs}\right)+\left(Y_{m_d}(k_a r)J_{m_p}(k_a r)-J_{m_d}(k_a r)Y_{m_p}(k_a r)\right)\cos\left(\beta_{adef}-\beta_{apqs}\right)\Big)
\end{aligned}
\tag{360}
$$

1 of 2

$$\overline{\frac{\partial \phi}{\partial t}\frac{\partial \phi}{\partial z}} = \frac{1}{2}\sum_{a=1}^{a_a} k_a \omega_a D_a^2 G_a \sinh(k_a(h+z))\left(\sum_{b=1}^{b_a}\sum_{c=1}^{c_{ab}}\sum_{n=1}^{n_a}\sum_{o=1}^{o_{an}} A_{abc}A_{ano}\sin\left(k_a r\left(\cos(\theta-\gamma_{ab})-\cos(\theta-\gamma_{an})\right)+\alpha_{abc}-\alpha_{ano}\right)\right.$$
$$+\sum_{d=1}^{d_d}\sum_{e=1}^{e_{ad}}\sum_{f=1}^{f_{ade}}\sum_{p=1}^{p_p}\sum_{q=1}^{q_{ap}}\sum_{s=1}^{s_{apq}} F_{de}F_{pq}B_{adef}B_{apqs}\left(\left(J_{m_d}(k_a r)J_{m_p}(k_a r)+Y_{m_d}(k_a r)Y_{m_p}(k_a r)\right)\sin(\beta_{adef}-\beta_{apqs})\right. \quad (360)$$
$$\left.\left.+\left(Y_{m_d}(k_a r)J_{m_p}(k_a r)-J_{m_d}(k_a r)Y_{m_p}(k_a r)\right)\cos(\beta_{adef}-\beta_{apqs})\right)\right) \quad 2 \text{ of } 2$$

The term in Equation 360 that results from the multiplication of purely plane wave terms is the $\hat{z}$ plane wave term. The core of the term from Equation 360 is:

$$\sum_{b=1}^{b_a}\sum_{c=1}^{c_{ab}}\sum_{n=1}^{n_a}\sum_{o=1}^{o_{an}} A_{abc}A_{ano}\sin\left(k_a r\left(\cos(\theta-\gamma_{ab})-\cos(\theta-\gamma_{an})\right)+\alpha_{abc}-\alpha_{ano}\right) \quad (361)$$

By examining the properties of this core set of terms it is possible to make a substantial simplification. Due to the summing of variables there are two different cases that arise. The first case is when $b=n$ and $c=o$. In this case a single term is generated and the following reduction can be made.

$$A_{abc}^2\sin\left(k_a r\left(\cos(\theta-\gamma_{ab})-\cos(\theta-\gamma_{ab})\right)+\alpha_{abc}-\alpha_{abc}\right) = 0 \quad (362)$$

The second case is if either of the following statements are true: $b\neq n$ or $c\neq o$. In this case the sums generate two terms that can be reduced as follows:

$$\begin{aligned} & A_{abc}A_{ano}\sin\left(k_a r\left(\cos(\theta-\gamma_{ab})-\cos(\theta-\gamma_{an})\right)+\alpha_{abc}-\alpha_{ano}\right)+A_{ano}A_{abc}\sin\left(k_a r\left(\cos(\theta-\gamma_{an})-\cos(\theta-\gamma_{ab})\right)+\alpha_{ano}-\alpha_{abc}\right) \\ &= A_{abc}A_{ano}\sin\left(k_a r\left(\cos(\theta-\gamma_{ab})-\cos(\theta-\gamma_{an})\right)+\alpha_{abc}-\alpha_{ano}\right)-A_{ano}A_{abc}\sin\left(k_a r\left(\cos(\theta-\gamma_{ab})-\cos(\theta-\gamma_{an})\right)+\alpha_{abc}-\alpha_{ano}\right) \\ &= 0 \end{aligned} \tag{363}$$

This means that in all cases the $\hat{z}$ plane wave term is equal to zero.

$$\sum_{b=1}^{b_a}\sum_{c=1}^{c_{ab}}\sum_{n=1}^{n_a}\sum_{o=1}^{o_{an}} A_{abc}A_{ano}\sin\left(k_a r\left(\cos(\theta-\gamma_{ab})-\cos(\theta-\gamma_{an})\right)+\alpha_{abc}-\alpha_{ano}\right) = 0 \tag{364}$$

The term from Equation 360 that results as the product of the purely circular waves is the $\hat{z}$ circular term. The core of the term from Equation 360 is:

$$\begin{aligned} \sum_{d=1}^{d_d}\sum_{e=1}^{e_{ad}}\sum_{f=1}^{f_{ade}}\sum_{p=1}^{p_p}\sum_{q=1}^{q_{ap}}\sum_{s=1}^{s_{apq}} F_{de}F_{pq}B_{adef}B_{apqs}\Big(&\left(J_{m_d}(k_a r)J_{m_p}(k_a r)+Y_{m_d}(k_a r)Y_{m_p}(k_a r)\right)\sin(\beta_{adef}-\beta_{apqs}) \\ &+\left(Y_{m_d}(k_a r)J_{m_p}(k_a r)-J_{m_d}(k_a r)Y_{m_p}(k_a r)\right)\cos(\beta_{adef}-\beta_{apqs})\Big) \end{aligned} \tag{365}$$

By examining the properties of this core set of terms it is possible to make a substantial simplification. Due to the summing of variables there are two different cases that arise. The first case is when $d=p$, $e=q$ and $f=s$. In this case a single term is generated and the following reduction can be made.

$$F_{de}^2 B_{adef}^2\left(\left(J_{m_d}(k_a r)^2+Y_{m_d}(k_a r)^2\right)\sin(\beta_{adef}-\beta_{adef})+\left(Y_{m_d}(k_a r)J_{m_d}(k_a r)-J_{m_d}(k_a r)Y_{m_d}(k_a r)\right)\cos(\beta_{adef}-\beta_{adef})\right) = 0 \tag{366}$$

The second case is if any of the following statements are true: $d \neq p$, $e \neq q$ or $f \neq s$. In this case the sums generate two terms that can be reduced as follows:

$$\begin{aligned}
& F_{de} F_{pq} B_{adef} B_{apqs} \Big(\Big(J_{m_d}(k_a r) J_{m_p}(k_a r) + Y_{m_d}(k_a r) Y_{m_p}(k_a r) \Big) \sin(\beta_{adef} - \beta_{apqs}) \\
& \qquad + \Big(Y_{m_d}(k_a r) J_{m_p}(k_a r) - J_{m_d}(k_a r) Y_{m_p}(k_a r) \Big) \cos(\beta_{adef} - \beta_{apqs}) \Big) \\
& \qquad + F_{pq} F_{de} B_{apqs} B_{adef} \Big(\Big(J_{m_p}(k_a r) J_{m_d}(k_a r) + Y_{m_p}(k_a r) Y_{m_d}(k_a r) \Big) \sin(\beta_{apqs} - \beta_{adef}) \\
& \qquad + \Big(Y_{m_p}(k_a r) J_{m_d}(k_a r) - J_{m_p}(k_a r) Y_{m_d}(k_a r) \Big) \cos(\beta_{apqs} - \beta_{adef}) \Big) \\
= \; & F_{de} F_{pq} B_{adef} B_{apqs} \Big(\Big(J_{m_d}(k_a r) J_{m_p}(k_a r) + Y_{m_d}(k_a r) Y_{m_p}(k_a r) \Big) \sin(\beta_{adef} - \beta_{apqs}) \\
& \qquad + \Big(Y_{m_d}(k_a r) J_{m_p}(k_a r) - J_{m_d}(k_a r) Y_{m_p}(k_a r) \Big) \cos(\beta_{adef} - \beta_{apqs}) \Big) \\
& \qquad + F_{pq} F_{de} B_{apqs} B_{adef} \Big(- \Big(J_{m_p}(k_a r) J_{m_d}(k_a r) + Y_{m_p}(k_a r) Y_{m_d}(k_a r) \Big) \sin(\beta_{adef} - \beta_{apqs}) \\
& \qquad + \Big(Y_{m_p}(k_a r) J_{m_d}(k_a r) - J_{m_p}(k_a r) Y_{m_d}(k_a r) \Big) \cos(\beta_{adef} - \beta_{apqs}) \Big) \\
= \; & 0
\end{aligned} \tag{367}$$

This means that in all cases the $\hat{z}$ circular term is equal to zero.

$$\begin{aligned}
\sum_{d=1}^{d_d} \sum_{e=1}^{e_{ad}} \sum_{f=1}^{f_{ade}} \sum_{p=1}^{p_p} \sum_{q=1}^{q_{ap}} \sum_{s=1}^{s_{apq}} & F_{de} F_{pq} B_{adef} B_{apqs} \Big(\Big(J_{m_d}(k_a r) J_{m_p}(k_a r) + Y_{m_d}(k_a r) Y_{m_p}(k_a r) \Big) \sin(\beta_{adef} - \beta_{apqs}) \\
& + \Big(Y_{m_d}(k_a r) J_{m_p}(k_a r) - J_{m_d}(k_a r) Y_{m_p}(k_a r) \Big) \cos(\beta_{adef} - \beta_{apqs}) \Big) \\
& = 0
\end{aligned} \tag{368}$$

These results for the $\hat{z}$ plane wave and $\hat{z}$ circular wave, show that no matter how the plane waves and circular waves are combined, energy cannot be radiated in the $\hat{z}$ direction.

The results from Equations 346, 353, 360, 364 and 368 can be substituted into 329 to give the general solution to the elemental change of the time-averaged power for the interaction of plane waves and circular waves:

$$d\overline{P} = -\frac{1}{2}\rho\sum_{a=1}^{a_a} k_a \omega_a D_a^2 G_a^2 \left(\left(T_{17a}+T_{18a}+T_{19a}\right)\hat{r}+\left(T_{20a}+T_{21a}+T_{22a}\right)\hat{\theta}\right) d\vec{A}_r \tag{369}$$

Where:

$$T_{17a} = \sum_{b=1}^{b_a}\sum_{c=1}^{c_{ab}}\sum_{n=1}^{n_a}\sum_{o=1}^{o_{an}} -A_{abc}A_{ano}\cos(\theta-\gamma_{an})\cos(k_a r(\cos(\theta-\gamma_{ab})-\cos(\theta-\gamma_{an}))+\alpha_{abc}-\alpha_{ano}) \tag{370}$$

$$\begin{aligned} T_{18a} = \sum_{b=1}^{b_a}\sum_{c=1}^{c_{ab}}\sum_{d=1}^{d_d}\sum_{e=1}^{e_{ad}}\sum_{f=1}^{f_{ade}} F_{de}A_{abc}B_{adef}\Bigg(&\left(\frac{1}{2}\left(J_{m_d-1}(k_a r)-J_{m_d+1}(k_a r)\right)-Y_{m_d}(k_a r)\cos(\theta-\gamma_{ab})\right)\sin(k_a r\cos(\theta-\gamma_{ab})+\alpha_{abc}-\beta_{adef}) \\ &-\left(\frac{1}{2}\left(Y_{m_d-1}(k_a r)-Y_{m_d+1}(k_a r)\right)+J_{m_d}(k_a r)\cos(\theta-\gamma_{ab})\right)\cos(k_a r\cos(\theta-\gamma_{ab})+\alpha_{abc}-\beta_{adef})\Bigg) \end{aligned} \tag{371}$$

$$T_{19a} = \sum_{d=1}^{d_d}\sum_{e=1}^{e_{ad}}\sum_{f=1}^{f_{ade}}\sum_{p=1}^{p_p}\sum_{q=1}^{q_{ap}}\sum_{s=1}^{s_{apq}}\frac{1}{2}F_{de}F_{pq}B_{adef}B_{apqs} \times\Big(\Big(J_{m_d}(k_a r)\Big(J_{m_p-1}(k_a r)-J_{m_p+1}(k_a r)\Big)-Y_{m_d}(k_a r)\Big(Y_{m_p-1}(k_a r)-Y_{m_p+1}(k_a r)\Big)\Big)\sin(\beta_{adef}-\beta_{apqs}) +\Big(Y_{m_d}(k_a r)\Big(J_{m_p-1}(k_a r)-J_{m_p+1}(k_a r)\Big)-J_{m_d}(k_a r)\Big(Y_{m_p-1}(k_a r)-Y_{m_p+1}(k_a r)\Big)\Big)\cos(\beta_{adef}-\beta_{apqs})\Big) \tag{372}$$

$$T_{20a} = \sum_{b=1}^{b_a}\sum_{c=1}^{c_{ab}}\sum_{n=1}^{n_a}\sum_{o=1}^{o_{an}}\sin(\theta-\gamma_{an})A_{abc}A_{ano}\cos(k_a r\big(\cos(\theta-\gamma_{ab})-\cos(\theta-\gamma_{an})\big)+\alpha_{abc}-\alpha_{ano}) \tag{373}$$

$$T_{21a} = \sum_{b=1}^{b_a}\sum_{c=1}^{c_{ab}}\sum_{d=1}^{d_d}\sum_{e=1}^{e_{ad}}\sum_{f=1}^{f_{ade}}A_{abc}B_{adef}\Bigg(\Bigg(F_{de}\sin(\theta-\gamma_{ab})J_{m_d}(k_a r)+\frac{m_d\sin(m_d\theta-\zeta_e)}{k_a r}Y_{m_d}(k_a r)\Bigg)\cos\big(k_a r\cos(\theta-\gamma_{ab})+\alpha_{abc}-\beta_{adef}\big) +\Bigg(F_{de}\sin(\theta-\gamma_{ab})Y_{m_d}(k_a r)-\frac{m_d\sin(m_d\theta-\zeta_e)}{k_a r}J_{m_d}(k_a r)\Bigg)\sin\big(k_a r\cos(\theta-\gamma_{ab})+\alpha_{abc}-\beta_{adef}\big)\Bigg) \tag{374}$$

$$T_{22a} = \sum_{d=1}^{d_d}\sum_{e=1}^{e_{ad}}\sum_{f=1}^{f_{ade}}\sum_{p=1}^{p_p}\sum_{q=1}^{q_{ap}}\sum_{s=1}^{s_{apq}}\frac{F_{de}B_{adef}B_{apqs}m_p\sin(m_p\theta-\zeta_q)}{k_a r}\Big(\big(J_{m_d}(k_a r)Y_{m_p}(k_a r)-Y_{m_d}(k_a r)J_{m_p}(k_a r)\big)\big(\cos(\beta_{adef}-\beta_{apqs})\big) -\big(J_{m_d}(k_a r)J_{m_p}(k_a r)+Y_{m_d}(k_a r)Y_{m_p}(k_a r)\big)\big(\sin(\beta_{adef}-\beta_{apqs})\big)\Big) \tag{375}$$

Appendix 6: Time-Averaged Power for a Plane Wave

The general solution for time-averaged power given by Equations 369 to 375 in Appendix 5. If it is assumed that only a single monochromatic plane wave is present then the following substitutions can be made:

$$\begin{array}{lll} a_a = 1 & k_a = k & A_{abc} = A_{ano} = A \\ b_a = n_a = 1 & \omega_a = \omega & B_{adef} = B_{apqs} = 0 \\ c_{ab} = o_{an} = 1 & D_a = D & \alpha_{abc} - \alpha_{ano} = 0 \\ & G_a = G & \gamma_{ab} = \gamma_{an} = \gamma \end{array} \tag{376}$$

Which gives:

$$\begin{aligned} d\overline{P} = & -\frac{1}{2}\rho k_a \omega_a D_a^2 G_a^2 \\ & \times\left(\left(\cos(\theta-\gamma_{an})\cos(k_a r(\cos(\theta-\gamma_{ab})-\cos(\theta-\gamma_{an}))+\alpha_{abc}-\alpha_{ano})+\sum_{b=1}^{b_a}\sum_{c=1}^{c_{ab}}\sum_{d=1}^{d_d}\sum_{e=1}^{e_{ad}}\sum_{f=1}^{f_{ade}} 0+\sum_{d=1}^{d_d}\sum_{e=1}^{e_{ad}}\sum_{f=1}^{f_{ade}}\sum_{p=1}^{p_p}\sum_{q=1}^{q_{ap}}\sum_{s=1}^{s_{apq}} 0\right)\hat{r}\right. \\ & \left.+\left(\sin(\theta-\gamma_{an})A_{abc}A_{ano}\cos(k_a r\left|\cos(\theta-\gamma_{ab})-\cos(\theta-\gamma_{an})\right|+\alpha_{abc}-\alpha_{ano})+\sum_{b=1}^{b_a}\sum_{c=1}^{c_{ab}}\sum_{d=1}^{d_d}\sum_{e=1}^{e_{ad}}\sum_{f=1}^{f_{ade}} 0+\sum_{d=1}^{d_d}\sum_{e=1}^{e_{ad}}\sum_{f=1}^{f_{ade}}\sum_{p=1}^{p_p}\sum_{q=1}^{q_{ap}}\sum_{s=1}^{s_{apq}} 0\right)\hat{\theta}\right)d\vec{A}_r \end{aligned} \tag{377}$$

Which reduces to:

$$\begin{aligned} d\overline{P} &= -\frac{1}{2}\rho k\omega D^2 G^2\left(-A^2\cos(\theta-\gamma)\cos(k\,r(\cos(\theta-\gamma)-\cos(\theta-\gamma))+\alpha-\alpha)\hat{r}\right. \\ &\qquad \left.+\sin(\theta-\gamma)\,A^2\cos(k\,r\left|\cos(\theta-\gamma)-\cos(\theta-\gamma)\right|+\alpha-\alpha)\hat{\theta}\right) d\,\vec{A}_r \\ &= -\frac{1}{2}\rho k\omega A^2 D^2 G^2\left(-\cos(\theta-\gamma)\hat{r}+\sin(\theta-\gamma)\hat{\theta}\right) d\,\vec{A}_r \end{aligned} \tag{378}$$

A6.1 Time-Averaged Power Through a Planar Surface

It is possible to describe an area that is parallel to the wave front and with a length of 1 by defining the area with $r_1 \le r \le r_2$ where $r_2 - r_1 = 1$, $\theta = \gamma - \frac{\pi}{2}$ and $-h \le z \le \eta$. By this definition the $\hat{\theta}$ becomes the $\hat{y}$ vector and the $\hat{r}$ vector is $\widehat{\perp\gamma}$. Assuming that $\eta \approx 0$ the power crossing an area of unit length parallel with the wave front is:

$$
\begin{aligned}
\overline{P}_{\gamma lm} &= -\frac{1}{2}\rho k \omega A^2 D^2 \int_{-h}^{0} G^2 dz \int_{r_1}^{r_2} \left(-\cos(\gamma - \frac{\pi}{2} - \gamma)\, \widehat{\perp\gamma} \cdot \hat{\gamma} + \sin(\gamma - \frac{\pi}{2} - \gamma)\, \hat{\gamma} \cdot \hat{\gamma} \right) dr \\
&= -\frac{1}{2}\rho k \omega A^2 D^2 \int_{-h}^{0} G^2 dz \int_{r_1}^{r_2} -1\, dr \\
&= \frac{1}{2}\rho k \omega A^2 D^2 \int_{-h}^{0} G^2 dz \left[r \right]_{r_1}^{r_2} \\
&= \frac{1}{2}\rho k \omega A^2 D^2 \int_{-h}^{0} G^2 dz \left(r_2 - r_1 \right) \\
&= \frac{1}{2}\rho k \omega A^2 D^2 \int_{-h}^{0} G^2 dz
\end{aligned}
\tag{379}
$$

The alternative definition, using $\theta = \gamma + \frac{\pi}{2}$, will yield an identical result. Note that to keep the plane in the same orientation the order of integration must also be reversed hence the integral becomes $\int_{r_2}^{r_1} dr$ for this case. Substituting Equation 282 into Equation 384 along with the definition of D:

$$\begin{aligned}\overline{P}_{y/m} &= \frac{1}{2}\frac{\rho g^2 k \omega A^2}{\omega^2 \cosh^2(k h)}\frac{1}{2}\left(\frac{\sinh(2 k h)}{2 k}+h\right)\\ &= \frac{1}{4}\frac{\rho g^2 k \omega A^2}{g k \tanh(k h)\cosh^2(k h)}\left(\frac{\sinh(2 k h)}{2 k}+h\right)\\ &= \frac{1}{2}\frac{\rho g \omega A^2}{\sinh(2 k h)}\left(\frac{\sinh(2 k h)}{2 k}+h\right)\\ &= \frac{1}{4}\frac{\rho g \omega A^2}{k}\left(1+\frac{2 k h}{\sinh(2 k h)}\right)\end{aligned} \tag{380}$$

The end result is that the power traversing a through a plane perpendicular to the wave crest and with unit width. As a note no power is transmitted across the wave front.

A6.2 Time-Averaged Power Through a Circular Area

If the area A_r is taken to be a circular cylinder the same height as the water depth h then an element of the area becomes:

$$d\vec{A}_r = r\, d\theta\, dz \tag{381}$$

And:

$$\int_A d\,\vec{A}_r = \int_{-h}^{\eta}\int_{-\pi}^{\pi} r\,d\,\theta\,dz\,\hat{r} \tag{382}$$

And so Equation 50 becomes:

$$\begin{aligned}
\overline{P}_{r\ p} &= -\frac{1}{2}\rho\,k\,\omega\,D^2\,A^2\,r\int_{-h}^{\eta} G^2\,dz\int_{-\pi}^{\pi}\left(-\cos(\theta-\gamma)\hat{r}\cdot\hat{r}+\sin(\theta-\gamma)\hat{\theta}\cdot\hat{r}\right)d\,\theta \\
&= -\frac{1}{2}\rho\,k\,\omega\,D^2\,A^2\,r\int_{-h}^{\eta} G^2\,dz\left[-\sin(\theta-\gamma)\right]_{-\pi}^{\pi} \\
&= -\frac{1}{2}\rho\,k\,\omega\,D^2\,A^2\,r\int_{-h}^{\eta} G^2\,dz\left(-\left(\sin(\pi-\gamma)-\sin(-\pi-\gamma)\right)\right) \\
&= 0
\end{aligned} \tag{383}$$

This result makes a good deal of sense as for a single, monochromatic plane wave of any incident angle there should be as much power entering the cylinder's surface as exiting independent of the radius of the cylinder.

Appendix 7: Time-Averaged Power for a Plane Wave and a Circular Wave

The general solution for time-averaged power given by Equations 369 to 375 in Appendix 5. If it is assumed that only a single monochromatic plane wave is present then the following substitutions can be made: single monochromatic plane wave interacts with a single monochromatic radial wave of exactly the same wavelength then the following substitutions can be made:

$$\begin{aligned} a_a &= 1 \\ b_a &= n_a = 1 \\ c_{ab} &= o_{an} = 1 \\ d_d &= p_p = 1 \\ e_{ad} &= q_{ap} = 1 \\ f_{ade} &= s_{apq} = 1 \end{aligned} \qquad \begin{aligned} k_a &= k \\ \omega_a &= \omega \\ D_a &= D \\ G_a &= G \\ F_{de} &= F_{pq} = F \end{aligned} \qquad \begin{aligned} A_{abc} &= A_{ano} = A \\ \alpha_{abc} &= \alpha_{ano} = \alpha \\ B_{adef} &= B_{apqs} = B \\ \beta_{adef} &= \beta_{apqs} = \beta \\ \zeta_e &= \zeta_q = \zeta \\ m_d &= m_p = m \end{aligned} \tag{384}$$

Noting that the area, A_r, is defined from $\int_A d\vec{A}_r = \int_{-h}^{\eta}\int_{-\pi}^{\pi} r\, d\theta\, dz\hat{r}$, the dot product reduces the $\overline{P}$ to a function in only the $\hat{r}$ direction. This means that all of the $\hat{\theta}$ terms of Equation 369 can be ignored. Hence:

$$
\begin{aligned}
\overline{P} \;=\; -\frac{1}{2}\rho\, r\, k\, \omega\, D^2 \int_{-h}^{\eta} G^2\, dz \int_{-\pi}^{\pi} \Big(& -A^2 \cos(\theta-\gamma)\cos(k\,r(\cos(\theta)-\cos(\theta))+\alpha-\alpha) \\
& + F\,A\,B\left(\left(\frac{1}{2}\left(J_{m-1}(k\,r)-J_{m+1}(k\,r)\right)-Y_m(k\,r)\cos(\theta-\gamma)\right)\sin(k\,r\cos(\theta-\gamma)+\alpha-\beta)\right. \\
& \left. -\left(\frac{1}{2}\left(Y_{m-1}(k\,r)-Y_{m+1}(k\,r)\right)+J_m(k\,r)\cos(\theta-\gamma)\right)\cos(k\,r\cos(\theta-\gamma)+\alpha-\beta)\right) \\
& + F^2 B^2\Big(\left(J_m(k\,r)\left(J_{m-1}(k\,r)-J_{m+1}(k\,r)\right)-Y_m(k\,r)\left(Y_{m-1}(k\,r)-Y_{m+1}(k\,r)\right)\right)\sin(\beta-\beta) \\
& + \left(Y_m(k\,r)\left(J_{m-1}(k\,r)-J_{m+1}(k\,r)\right)-J_m(k\,r)\left(Y_{m-1}(k\,r)-Y_{m+1}(k\,r)\right)\right)\cos(\beta-\beta)\Big)\Big)\, d\theta \\
= \; -\frac{1}{2}\rho\, r\, k\, \omega\, D^2 \int_{-h}^{\eta} G^2\, dz \int_{-\pi}^{\pi} \Bigg(& -A^2\cos(\theta-\gamma) + F\,A\,B\left(\left(\frac{1}{2}\left(J_{m-1}(k\,r)-J_{m+1}(k\,r)\right)-Y_m(k\,r)\cos(\theta-\gamma)\right)\sin(k\,r\cos(\theta-\gamma)+\alpha-\beta)\right. \\
& \left. -\left(\frac{1}{2}\left(Y_{m-1}(k\,r)-Y_{m+1}(k\,r)\right)+J_m(k\,r)\cos(\theta-\gamma)\right)\cos(k\,r\cos(\theta-\gamma)+\alpha-\beta)\right) \\
& + F^2 B^2\Big(Y_m(k\,r)\left(J_{m-1}(k\,r)-J_{m+1}(k\,r)\right)-J_m(k\,r)\left(Y_{m-1}(k\,r)-Y_{m+1}(k\,r)\right)\Big)\Bigg)\, d\theta
\end{aligned}
\tag{385}
$$

For reference the naming of the terms is as follows:

$$
\textit{plane wave } \hat{r} \textit{ term} \;=\; \frac{1}{2}\rho\, A_r\, k\, \omega\, D^2 G^2 A^2 \cos(\theta-\gamma) \tag{386}
$$

$$\begin{aligned} \textit{combined } \hat{r} \textit{ term } = -\frac{1}{2}\rho A_r k\omega D^2 G^2 F A B\Bigg(\Bigg(\frac{1}{2}\left(J_{m-1}(kr)-J_{m+1}(kr)\right)-Y_m(kr)\cos(\theta-\gamma)\Bigg)\sin(kr\cos(\theta-\gamma)+\alpha-\beta) \\ -\Bigg(\frac{1}{2}\left(Y_{m-1}(kr)-Y_{m+1}(kr)\right)+J_m(kr)\cos(\theta-\gamma)\Bigg)\cos(kr\cos(\theta-\gamma)+\alpha-\beta)\Bigg) \end{aligned} \tag{387}$$

$$\textit{circular } \hat{r} \textit{ term } = -\frac{1}{2}\rho A_r k\omega D^2 G^2 F^2 B^2\left(Y_m(kr)\left(J_{m-1}(kr)-J_{m+1}(kr)\right)-J_m(kr)\left(Y_{m-1}(kr)-Y_{m+1}(kr)\right)\right) \tag{388}$$

Section A6.2 deals with the terms derived from the plane wave $\hat{r}$ terms. Appendix 5 deals with the term derived from the circular $\hat{r}$ term. As the combined $\hat{r}$ term has not yet been resolved it bears further investigation. Collecting the θ terms:

$$\begin{aligned} \textit{combined } \hat{r} \textit{ term } &= -\frac{1}{2}\rho A_r k\omega D^2 G^2 F A B\Bigg(\Bigg(\frac{1}{2}\left(J_{m-1}(kr)-J_{m+1}(kr)\right)-Y_m(kr)\cos(\theta-\gamma)\Bigg)\sin(kr\cos(\theta-\gamma)+\alpha-\beta) \\ &\quad -\Bigg(\frac{1}{2}\left(Y_{m-1}(kr)-Y_{m+1}(kr)\right)+J_m(kr)\cos(\theta-\gamma)\Bigg)\cos(kr\cos(\theta-\gamma)+\alpha-\beta)\Bigg) \\ &= -\frac{1}{2}\rho A_r k\omega D^2 G^2 A B\Bigg(\Bigg(\frac{1}{2}\left(J_{m-1}(kr)-J_{m+1}(kr)\right)\cos(m\theta-\zeta)\sin(kr\cos(\theta-\gamma)+\alpha-\beta) \\ &\quad -Y_m(kr)\cos(m\theta-\zeta)\cos(\theta-\gamma)\sin(kr\cos(\theta-\gamma)+\alpha-\beta)\Big) \\ &\quad -\Bigg(\frac{1}{2}\left(Y_{m-1}(kr)-Y_{m+1}(kr)\right)\cos(m\theta-\zeta)\cos(kr\cos(\theta-\gamma)+\alpha-\beta) \\ &\quad +J_m(kr)\cos(m\theta-\zeta)\cos(\theta-\gamma)\cos(kr\cos(\theta-\gamma)+\alpha-\beta)\Big)\Bigg) \end{aligned} \tag{389}$$

For reference the naming of terms is as follows:

$$\begin{aligned} T_{AB1} &= \cos(m\theta-\zeta)\sin(kr\cos(\theta-\gamma)+\alpha-\beta) & \qquad T_{AB3} &= \cos(m\theta-\zeta)\cos(\theta-\gamma)\sin(kr\cos(\theta-\gamma)+\alpha-\beta) \\ T_{AB2} &= \cos(m\theta-\zeta)\cos(kr\cos(\theta-\gamma)+\alpha-\beta) & \qquad T_{AB4} &= \cos(m\theta-\zeta)\cos(\theta-\gamma)\cos(kr\cos(\theta-\gamma)+\alpha-\beta) \end{aligned} \tag{390}$$

Each term can be reduced in turn. Beginning with T_{AB1} :

$$\begin{aligned} T_{AB1} &= \cos(m\theta-\zeta)\sin(kr\cos(\theta-\gamma)+\alpha-\beta) \\ &= \left(\cos(m\theta)\cos(\zeta)+\sin(m\theta)\sin(\zeta)\right)\left(\sin(kr\cos(\theta-\gamma))\cos(\alpha-\beta)+\cos(kr\cos(\theta-\gamma))\sin(\alpha-\beta)\right) \\ &= \cos(m\theta)\cos(\zeta)\sin(kr\cos(\theta-\gamma))\cos(\alpha-\beta)+\cos(m\theta)\cos(\zeta)\cos(kr\cos(\theta-\gamma))\sin(\alpha-\beta) \\ &\quad +\sin(m\theta)\sin(\zeta)\sin(kr\cos(\theta-\gamma))\cos(\alpha-\beta)+\sin(m\theta)\sin(\zeta)\cos(kr\cos(\theta-\gamma))\sin(\alpha-\beta) \\ &= \frac{1}{2}\Big(\cos(\zeta)\cos(\alpha-\beta)\left(\sin(kr\cos(\theta-\gamma)+m\theta)+\sin(kr\cos(\theta-\gamma)-m\theta)\right) \\ &\qquad +\cos(\zeta)\sin(\alpha-\beta)\left(\cos(kr\cos(\theta-\gamma)+m\theta)+\cos(kr\cos(\theta-\gamma)-m\theta)\right) \\ &\qquad +\sin(\zeta)\cos(\alpha-\beta)\left(-\cos(kr\cos(\theta-\gamma)+m\theta)+\cos(kr\cos(\theta-\gamma)-m\theta)\right) \\ &\qquad +\sin(\zeta)\sin(\alpha-\beta)\left(\sin(kr\cos(\theta-\gamma)+m\theta)-\sin(kr\cos(\theta-\gamma)-m\theta)\right)\Big) \\ &= \frac{1}{2}\Big(\sin(kr\cos(\theta-\gamma)+m\theta)\left(\cos(\zeta)\cos(\alpha-\beta)+\sin(\zeta)\sin(\alpha-\beta)\right) \\ &\qquad +\sin(kr\cos(\theta-\gamma)-m\theta)\left(\cos(\zeta)\cos(\alpha-\beta)-\sin(\zeta)\sin(\alpha-\beta)\right) \\ &\qquad \cos(kr\cos(\theta-\gamma)+m\theta)\left(\cos(\zeta)\sin(\alpha-\beta)-\sin(\zeta)\cos(\alpha-\beta)\right) \\ &\qquad +\cos(kr\cos(\theta-\gamma)-m\theta)\left(\cos(\zeta)\sin(\alpha-\beta)+\sin(\zeta)\cos(\alpha-\beta)\right)\Big) \end{aligned} \tag{391}$$

$$T_{AB1} = \frac{1}{2}\left(\sin(kr\cos(\theta-\gamma)+m\theta)\cos(\alpha-\beta-\zeta)+\sin(kr\cos(\theta-\gamma)-m\theta)\cos(\alpha-\beta+\zeta)\right.$$
$$\left.+\cos(kr\cos(\theta-\gamma)+m\theta)\sin(\alpha-\beta-\zeta)+\cos(kr\cos(\theta-\gamma)-m\theta)\sin(\alpha-\beta+\zeta)\right) \quad (391)$$

As the four terms (T_{AB1} , T_{AB2} , T_{AB3} and T_{AB4}) are independent of z and all other terms in the combined $\hat{r}$ term are independent of θ it is possible to separate out the integrals and determine, for instance, $\int_{-\pi}^{\pi} T_{AB1}\,d\theta$.

The following identities will be useful in the following working:

$$\int_{-\pi}^{\pi} \sin(kr\cos(\theta-\gamma)+m\theta)\,d\theta = 2\pi\sin(m\gamma+m\frac{\pi}{2})J_m(kr) \quad (392)$$

$$\int_{-\pi}^{\pi} \cos(kr\cos(\theta-\gamma)+m\theta)\,d\theta = 2\pi\cos(m\gamma+m\frac{\pi}{2})J_m(kr) \quad (393)$$

Utilising the identities from Equations 392 and 393:

$$\begin{aligned}
\int_{-\pi}^{\pi} T_{AB1}\, d\theta \;&=\; \frac{1}{2}\left(\int_{-\pi}^{\pi} \sin(k r\cos(\theta-\gamma)+m\theta)\, d\theta \cos(\alpha-\beta-\zeta)+\int_{-\pi}^{\pi} \sin(k r\cos(\theta-\gamma)-m\theta)\, d\theta \cos(\alpha-\beta+\zeta)\right.\\
&\qquad\left.+\int_{-\pi}^{\pi} \cos(k r\cos(\theta-\gamma)+m\theta)\, d\theta \sin(\alpha-\beta-\zeta)+\int_{-\pi}^{\pi} \cos(k r\cos(\theta-\gamma)-m\theta)\, d\theta \sin(\alpha-\beta+\zeta)\right)\\
&=\; \frac{1}{2}\left(2\pi \sin(m\gamma+m\frac{\pi}{2}) J_m(k r)\cos(\alpha-\beta-\zeta)+2\pi \sin(-m\gamma-m\frac{\pi}{2}) J_{-m}(k r)\cos(\alpha-\beta+\zeta)\right.\\
&\qquad\left.+2\pi \cos(m\gamma+m\frac{\pi}{2}) J_m(k r)\sin(\alpha-\beta-\zeta)+2\pi \cos(-m\gamma-m\frac{\pi}{2}) J_{-m}(k r)\sin(\alpha-\beta+\zeta)\right) \qquad (394)\\
&=\; \pi\left(\left(\sin(m\gamma+m\frac{\pi}{2})\cos(\alpha-\beta-\zeta)+\cos(m\gamma+m\frac{\pi}{2})\sin(\alpha-\beta-\zeta)\right) J_m(k r)\right.\\
&\qquad\left.+\left(\cos(m\gamma+m\frac{\pi}{2})\sin(\alpha-\beta+\zeta)-\sin(m\gamma+m\frac{\pi}{2})\cos(\alpha-\beta+\zeta)\right) J_{-m}(k r)\right]\\
&=\; \pi\left(\sin(\alpha-\beta-\zeta+m\gamma+m\frac{\pi}{2}) J_m(k r)+\sin(\alpha-\beta+\zeta-m\gamma-m\frac{\pi}{2}) J_{-m}(k r)\right)
\end{aligned}$$

And, as $J_{-m}(k r) \;=\; -1^{m} J_m(k r)$, when m is even:

$$\begin{aligned}\int_{-\pi}^{\pi} T_{AB1}\,d\theta\Big|_{even\ m} &= \pi\left(\sin(\alpha-\beta-\zeta+m\gamma+m\frac{\pi}{2})J_m(kr)+\sin(\alpha-\beta+\zeta-m\gamma-m\frac{\pi}{2})J_{-m}(kr)\right)\\ &= \pi\left(\sin(\alpha-\beta-\zeta+m\gamma+m\frac{\pi}{2})+\sin(\alpha-\beta+\zeta-m\gamma-m\frac{\pi}{2})\right)J_m(kr)\\ &= 2\pi\sin(\alpha-\beta)\cos(m\gamma+m\frac{\pi}{2}-\zeta)J_m(kr)\end{aligned} \tag{395}$$

And when m is odd:

$$\begin{aligned}\int_{-\pi}^{\pi} T_{AB1}\,d\theta\Big|_{odd\ m} &= \pi\left(\sin(\alpha-\beta-\zeta+m\gamma+m\frac{\pi}{2})J_m(kr)+\sin(\alpha-\beta+\zeta-m\gamma-m\frac{\pi}{2})J_{-m}(kr)\right)\\ &= \pi\left(\sin(\alpha-\beta-\zeta+m\gamma+m\frac{\pi}{2})-\sin(\alpha-\beta+\zeta-m\gamma-m\frac{\pi}{2})\right)J_m(kr)\\ &= 2\pi\cos(\alpha-\beta)\sin(m\gamma+m\frac{\pi}{2}-\zeta)J_m(kr)\end{aligned} \tag{396}$$

Examining term T_{AB2} :

$$\begin{aligned}
T_{AB2} &= \cos(m\theta-\zeta)\cos(kr\cos(\theta-\gamma)+\alpha-\beta) \\
&= \left(\cos(m\theta)\cos(\zeta)+\sin(m\theta)\sin(\zeta)\right)\left(\cos(kr\cos(\theta-\gamma))\cos(\alpha-\beta)-\sin(kr\cos(\theta-\gamma))\sin(\alpha-\beta)\right) \\
&= \cos(m\theta)\cos(\zeta)\cos(kr\cos(\theta-\gamma))\cos(\alpha-\beta)-\cos(m\theta)\cos(\zeta)\sin(kr\cos(\theta-\gamma))\sin(\alpha-\beta) \\
&\quad +\sin(m\theta)\sin(\zeta)\cos(kr\cos(\theta-\gamma))\cos(\alpha-\beta)-\sin(m\theta)\sin(\zeta)\sin(kr\cos(\theta-\gamma))\sin(\alpha-\beta) \\
&= \frac{1}{2}\Big(\cos(\zeta)\cos(\alpha-\beta)\left(\cos(kr\cos(\theta-\gamma)+m\theta)+\cos(kr\cos(\theta-\gamma)-m\theta)\right) \\
&\qquad -\cos(\zeta)\sin(\alpha-\beta)\left(\sin(kr\cos(\theta-\gamma)+m\theta)+\sin(kr\cos(\theta-\gamma)-m\theta)\right) \\
&\qquad +\sin(\zeta)\cos(\alpha-\beta)\left(\sin(kr\cos(\theta-\gamma)+m\theta)-\sin(kr\cos(\theta-\gamma)-m\theta)\right) \\
&\qquad -\sin(\zeta)\sin(\alpha-\beta)\left(-\cos(kr\cos(\theta-\gamma)+m\theta)+\cos(kr\cos(\theta-\gamma)-m\theta)\right)\Big) \\
&= \frac{1}{2}\Big(\sin(kr\cos(\theta-\gamma)+m\theta)\left(-\cos(\zeta)\sin(\alpha-\beta)+\sin(\zeta)\cos(\alpha-\beta)\right) \\
&\qquad +\sin(kr\cos(\theta-\gamma)-m\theta)\left(-\cos(\zeta)\sin(\alpha-\beta)-\sin(\zeta)\cos(\alpha-\beta)\right) \\
&\qquad +\cos(kr\cos(\theta-\gamma)+m\theta)\left(\cos(\zeta)\cos(\alpha-\beta)+\sin(\zeta)\sin(\alpha-\beta)\right) \\
&\qquad +\cos(kr\cos(\theta-\gamma)-m\theta)\left(\cos(\zeta)\cos(\alpha-\beta)-\sin(\zeta)\sin(\alpha-\beta)\right)\Big) \\
&= \frac{1}{2}\Big(\sin(kr\cos(\theta-\gamma)+m\theta)\sin(\zeta-(\alpha-\beta))-\sin(kr\cos(\theta-\gamma)-m\theta)\sin(\zeta+(\alpha-\beta)) \\
&\qquad +\cos(kr\cos(\theta-\gamma)+m\theta)\cos(\zeta-(\alpha-\beta))+\cos(kr\cos(\theta-\gamma)-m\theta)\cos(\zeta+(\alpha-\beta))\Big)
\end{aligned} \tag{397}$$

Utilising the identities from Equations 392 and 393:

$$\begin{aligned}
\int_{-\pi}^{\pi} T_{AB2}\, d\theta &= \frac{1}{2}\left(\int_{-\pi}^{\pi} \sin(kr\cos(\theta-\gamma)+m\theta)\, d\theta \sin(\zeta-(\alpha-\beta)) - \int_{-\pi}^{\pi} \sin(kr\cos(\theta-\gamma)-m\theta)\, d\theta \sin(\zeta+(\alpha-\beta))\right. \\
&\quad \left. + \int_{-\pi}^{\pi} \cos(kr\cos(\theta-\gamma)+m\theta)\, d\theta \cos(\zeta-(\alpha-\beta)) + \int_{-\pi}^{\pi} \cos(kr\cos(\theta-\gamma)-m\theta)\, d\theta \cos(\zeta+(\alpha-\beta))\right) \\
&= \frac{1}{2}\left(2\pi \sin(m\gamma+m\frac{\pi}{2}) J_m(kr) \sin(\zeta-(\alpha-\beta)) - 2\pi \sin(-m\gamma-m\frac{\pi}{2}) J_{-m}(kr) \sin(\zeta+(\alpha-\beta))\right. \\
&\quad \left. + ¿ 2\pi \cos(m\gamma+m\frac{\pi}{2}) J_m(kr) \cos(\zeta-(\alpha-\beta)) + 2\pi \cos(-m\gamma-m\frac{\pi}{2}) J_{-m}(kr) \cos(\zeta+(\alpha-\beta))\right) \qquad (398) \\
&= \pi\left(\left(\sin(m\gamma+m\frac{\pi}{2})\sin(\zeta-(\alpha-\beta)) + \cos(m\gamma+m\frac{\pi}{2})\cos(\zeta-(\alpha-\beta))\right) J_m(kr)\right. \\
&\quad \left. + \left(\sin(m\gamma+m\frac{\pi}{2})\sin(\zeta+(\alpha-\beta)) + \cos(m\gamma+m\frac{\pi}{2})\cos(\zeta+(\alpha-\beta))\right) J_{-m}(kr)\right) \\
&= \pi\left(\cos((\alpha-\beta)-\zeta+m\gamma+m\frac{\pi}{2}) J_m(kr) + \cos((\alpha-\beta)+\zeta-m\gamma-m\frac{\pi}{2}) J_{-m}(kr)\right)
\end{aligned}$$

And, as $J_{-m}(kr) = -1^m J_m(kr)$, when m is even:

$$\begin{aligned}\int_{-\pi}^{\pi} T_{AB2}\, d\theta\Big|_{even\ m} &= \pi\left(\cos((\alpha-\beta)-\zeta+m\gamma+m\frac{\pi}{2})J_m(kr)+\cos((\alpha-\beta)+\zeta-m\gamma-m\frac{\pi}{2})J_{-m}(kr)\right)\\ &= \pi\left(\cos((\alpha-\beta)-\zeta+m\gamma+m\frac{\pi}{2})+\cos((\alpha-\beta)+\zeta-m\gamma-m\frac{\pi}{2})\right)J_m(kr)\\ &= 2\pi\cos(\alpha-\beta)\cos(m\gamma+m\frac{\pi}{2}-\zeta)J_m(kr)\end{aligned} \tag{399}$$

And when m is odd:

$$\begin{aligned}\int_{-\pi}^{\pi} T_{AB2}\, d\theta\Big|_{odd\ m} &= \pi\left(\cos((\alpha-\beta)-\zeta+m\gamma+m\frac{\pi}{2})J_m(kr)+\cos((\alpha-\beta)+\zeta-m\gamma-m\frac{\pi}{2})J_{-m}(kr)\right)\\ &= \pi\left(\cos((\alpha-\beta)-\zeta+m\gamma+m\frac{\pi}{2})-\cos((\alpha-\beta)+\zeta-m\gamma-m\frac{\pi}{2})\right)J_m(kr)\\ &= -2\pi\sin(\alpha-\beta)\sin(m\gamma+m\frac{\pi}{2}-\zeta)J_m(kr)\end{aligned} \tag{400}$$

Examining term T_{AB3} :

$$\begin{aligned}
T_{AB3} &= \cos(m\theta-\zeta)\cos(\theta-\gamma)\sin(kr\cos(\theta-\gamma)+\alpha-\beta) \\
&= \left(\cos(m\theta)\cos(\zeta)+\sin(m\theta)\sin(\zeta)\right)\left(\cos(\theta)\cos(\gamma)+\sin(\theta)\sin(\gamma)\right)\sin(kr\cos(\theta-\gamma)+\alpha-\beta) \\
&= \big(\cos(\theta)\cos(m\theta)\cos(\zeta)\cos(\gamma)+\sin(\theta)\cos(m\theta)\cos(\zeta)\sin(\gamma)+\cos(\theta)\sin(m\theta)\sin(\zeta)\cos(\gamma) \\
&\qquad +\sin(\theta)\sin(m\theta)\sin(\zeta)\sin(\gamma)\big)\sin(kr\cos(\theta-\gamma)+\alpha-\beta) \\
&= \frac{1}{2}\big(\cos(\zeta)\cos(\gamma)\cos((m+1)\theta)+\cos(\zeta)\cos(\gamma)\cos((m-1)\theta)+\cos(\zeta)\sin(\gamma)\sin((m+1)\theta)-\cos(\zeta)\sin(\gamma)\sin((m-1)\theta) \\
&\qquad +\sin(\zeta)\cos(\gamma)\sin((m+1)\theta)+\sin(\zeta)\cos(\gamma)\sin((m-1)\theta)-\sin(\zeta)\sin(\gamma)\cos((m+1)\theta)+\sin(\zeta)\sin(\gamma)\cos((m-1)\theta)\big) \\
&\qquad \times\sin(kr\cos(\theta-\gamma)+\alpha-\beta) \\
&= \frac{1}{2}\big(\left(\cos(\zeta)\cos(\gamma)-\sin(\zeta)\sin(\gamma)\right)\cos((m+1)\theta)+\left(\cos(\zeta)\cos(\gamma)+\sin(\zeta)\sin(\gamma)\right)\cos((m-1)\theta) \\
&\qquad +\left(\cos(\zeta)\sin(\gamma)+\sin(\zeta)\cos(\gamma)\right)\sin((m+1)\theta)+\left(\sin(\zeta)\cos(\gamma)-\cos(\zeta)\sin(\gamma)\right)\sin((m-1)\theta)\big) \\
&\qquad \times\sin(kr\cos(\theta-\gamma)+\alpha-\beta) \\
&= \frac{1}{2}\big(\cos(\gamma+\zeta)\cos((m+1)\theta)+\cos(\gamma-\zeta)\cos((m-1)\theta)+\sin(\gamma+\zeta)\sin((m+1)\theta) \\
&\qquad -\sin(\gamma-\zeta)\sin((m-1)\theta)\big)\left(\sin(kr\cos(\theta-\gamma))\cos(\alpha-\beta)+\cos(kr\cos(\theta-\gamma))\sin(\alpha-\beta)\right) \\
&= \frac{1}{2}\big(\cos(\gamma+\zeta)\cos(\alpha-\beta)\sin(kr\cos(\theta-\gamma))\cos((m+1)\theta)+\cos(\gamma-\zeta)\cos(\alpha-\beta)\sin(kr\cos(\theta-\gamma))\cos((m-1)\theta) \\
&\qquad +\sin(\gamma+\zeta)\cos(\alpha-\beta)\sin(kr\cos(\theta-\gamma))\sin((m+1)\theta)-\sin(\gamma-\zeta)\cos(\alpha-\beta)\sin(kr\cos(\theta-\gamma))\sin((m-1)\theta) \\
&\qquad +\cos(\gamma+\zeta)\sin(\alpha-\beta)\cos(kr\cos(\theta-\gamma))\cos((m+1)\theta)+\cos(\gamma-\zeta)\sin(\alpha-\beta)\cos(kr\cos(\theta-\gamma))\cos((m-1)\theta) \\
&\qquad +\sin(\gamma+\zeta)\sin(\alpha-\beta)\cos(kr\cos(\theta-\gamma))\sin((m+1)\theta)-\sin(\gamma-\zeta)\sin(\alpha-\beta)\cos(kr\cos(\theta-\gamma))\sin((m-1)\theta)\big)
\end{aligned}$$

(401)
1 of 3

$$
\begin{aligned}
T_{AB3} \;=\; & \frac{1}{4}\big(\cos(\gamma+\zeta)\cos(\alpha-\beta)\big(\sin(k\,r\cos(\theta-\gamma)+(m+1)\theta)+\sin(k\,r\cos(\theta-\gamma)-(m+1)\theta)\big) \\
& +\cos(\gamma-\zeta)\cos(\alpha-\beta)\big(\sin(k\,r\cos(\theta-\gamma)+(m-1)\theta)+\sin(k\,r\cos(\theta-\gamma)-(m-1)\theta)\big) \\
& +\sin(\gamma+\zeta)\cos(\alpha-\beta)\big(\cos(k\,r\cos(\theta-\gamma)-(m+1)\theta)-\cos(k\,r\cos(\theta-\gamma)+(m+1)\theta)\big) \\
& -\sin(\gamma-\zeta)\cos(\alpha-\beta)\big(\cos(k\,r\cos(\theta-\gamma)-(m-1)\theta)-\cos(k\,r\cos(\theta-\gamma)+(m-1)\theta)\big) \\
& +\cos(\gamma+\zeta)\sin(\alpha-\beta)\big(\cos(k\,r\cos(\theta-\gamma)+(m+1)\theta)+\cos(k\,r\cos(\theta-\gamma)-(m+1)\theta)\big) \\
& +\cos(\gamma-\zeta)\sin(\alpha-\beta)\big(\cos(k\,r\cos(\theta-\gamma)+(m-1)\theta)+\cos(k\,r\cos(\theta-\gamma)-(m-1)\theta)\big) \\
& +\sin(\gamma+\zeta)\sin(\alpha-\beta)\big(\sin(k\,r\cos(\theta-\gamma)+(m+1)\theta)-\sin(k\,r\cos(\theta-\gamma)-(m+1)\theta)\big) \\
& -\sin(\gamma-\zeta)\sin(\alpha-\beta)\big(\sin(k\,r\cos(\theta-\gamma)+(m-1)\theta)-\sin(k\,r\cos(\theta-\gamma)-(m-1)\theta)\big)\big) \\
= \; & \frac{1}{4}\big(\sin(k\,r\cos(\theta-\gamma)+(m+1)\theta)\big(\cos(\gamma+\zeta)\cos(\alpha-\beta)+\sin(\gamma+\zeta)\sin(\alpha-\beta)\big) \\
& +\sin(k\,r\cos(\theta-\gamma)-(m+1)\theta)\big(\cos(\gamma+\zeta)\cos(\alpha-\beta)-\sin(\gamma+\zeta)\sin(\alpha-\beta)\big) \\
& +\sin(k\,r\cos(\theta-\gamma)+(m-1)\theta)\big(\cos(\gamma-\zeta)\cos(\alpha-\beta)-\sin(\gamma-\zeta)\sin(\alpha-\beta)\big) \\
& +\sin(k\,r\cos(\theta-\gamma)-(m-1)\theta)\big(\cos(\gamma-\zeta)\cos(\alpha-\beta)+\sin(\gamma-\zeta)\sin(\alpha-\beta)\big) \\
& +\cos(k\,r\cos(\theta-\gamma)+(m+1)\theta)\big(\cos(\gamma+\zeta)\sin(\alpha-\beta)-\sin(\gamma+\zeta)\cos(\alpha-\beta)\big) \\
& +\cos(k\,r\cos(\theta-\gamma)-(m+1)\theta)\big(\cos(\gamma+\zeta)\sin(\alpha-\beta)+\sin(\gamma+\zeta)\cos(\alpha-\beta)\big) \\
& +\cos(k\,r\cos(\theta-\gamma)+(m-1)\theta)\big(\cos(\gamma-\zeta)\sin(\alpha-\beta)+\sin(\gamma-\zeta)\cos(\alpha-\beta)\big) \\
& +\cos(k\,r\cos(\theta-\gamma)-(m-1)\theta)\big(\cos(\gamma-\zeta)\sin(\alpha-\beta)-\sin(\gamma-\zeta)\cos(\alpha-\beta)\big)\big]
\end{aligned}
\qquad (401)
$$

2 of 3

$$
\begin{aligned}
T_{AB3} \;=\; \frac{1}{4}\big(&\sin(k\,r\cos(\theta-\gamma)+(m+1)\theta)\cos(\gamma+\zeta-(\alpha-\beta))+\sin(k\,r\cos(\theta-\gamma)-(m+1)\theta)\cos(\gamma+\zeta+(\alpha-\beta))\\
&+\sin(k\,r\cos(\theta-\gamma)+(m-1)\theta)\cos(\gamma-\zeta+(\alpha-\beta))+\sin(k\,r\cos(\theta-\gamma)-(m-1)\theta)\cos(\gamma-\zeta-(\alpha-\beta))\\
&-\cos(k\,r\cos(\theta-\gamma)+(m+1)\theta)\sin(\gamma+\zeta-(\alpha-\beta))+\cos(k\,r\cos(\theta-\gamma)-(m+1)\theta)\sin(\gamma+\zeta+(\alpha-\beta))\\
&+\cos(k\,r\cos(\theta-\gamma)+(m-1)\theta)\sin(\gamma-\zeta+(\alpha-\beta))-\cos(k\,r\cos(\theta-\gamma)-(m-1)\theta)\sin(\gamma-\zeta-(\alpha-\beta))\big)
\end{aligned}
\tag{401}
$$

3 of 3

Utilising the identities from Equations 392 and 393:

$$
\begin{aligned}
\int_{-\pi}^{\pi} T_{AB3}\,d\theta \;=\; \frac{1}{4}\int_{-\pi}^{\pi}\big(&\sin(k\,r\cos(\theta-\gamma)+(m+1)\theta)\cos(\gamma+\zeta-(\alpha-\beta))+\sin(k\,r\cos(\theta-\gamma)-(m+1)\theta)\cos(\gamma+\zeta+(\alpha-\beta))\\
&+\sin(k\,r\cos(\theta-\gamma)+(m-1)\theta)\cos(\gamma-\zeta+(\alpha-\beta))+\sin(k\,r\cos(\theta-\gamma)-(m-1)\theta)\cos(\gamma-\zeta-(\alpha-\beta))\\
&-\cos(k\,r\cos(\theta-\gamma)+(m+1)\theta)\sin(\gamma+\zeta-(\alpha-\beta))+\cos(k\,r\cos(\theta-\gamma)-(m+1)\theta)\sin(\gamma+\zeta+(\alpha-\beta))\\
&+\cos(k\,r\cos(\theta-\gamma)+(m-1)\theta)\sin(\gamma-\zeta+(\alpha-\beta))-\cos(k\,r\cos(\theta-\gamma)-(m-1)\theta)\sin(\gamma-\zeta-(\alpha-\beta))\big]\,d\theta\\
=\; \frac{1}{4}\Big(&2\pi\sin((m+1)(\gamma+\tfrac{\pi}{2}))J_{m+1}(k\,r)\cos(\gamma+\zeta-(\alpha-\beta))+2\pi\sin(-(m+1)(\gamma+\tfrac{\pi}{2}))J_{-(m+1)}(k\,r)\cos(\gamma+\zeta+(\alpha-\beta))\\
&+2\pi\sin((m-1)(\gamma+\tfrac{\pi}{2}))J_{m-1}(k\,r)\cos(\gamma-\zeta+(\alpha-\beta))+2\pi\sin(-(m-1)(\gamma+\tfrac{\pi}{2}))J_{-(m-1)}(k\,r)\cos(\gamma-\zeta-(\alpha-\beta))\\
&-2\pi\cos((m+1)(\gamma+\tfrac{\pi}{2}))J_{m+1}(k\,r)\sin(\gamma+\zeta-(\alpha-\beta))+2\pi\cos(-(m+1)(\gamma+\tfrac{\pi}{2}))J_{-(m+1)}(k\,r)\sin(\gamma+\zeta+(\alpha-\beta))\\
&+2\pi\cos((m-1)(\gamma+\tfrac{\pi}{2}))J_{m-1}(k\,r)\sin(\gamma-\zeta+(\alpha-\beta))-2\pi\cos(-(m-1)(\gamma+\tfrac{\pi}{2}))J_{-(m-1)}(k\,r)\sin(\gamma-\zeta-(\alpha-\beta))\Big)
\end{aligned}
\tag{402}
$$

1 of 3

$$
\begin{aligned}
\int_{-\pi}^{\pi} T_{AB3}\, d\theta \;=\; & \frac{\pi}{2}\Bigg(\Bigg(\sin((m+1)(\gamma+\frac{\pi}{2}))\cos(\gamma+\zeta-(\alpha-\beta))-\cos((m+1)(\gamma+\frac{\pi}{2}))\sin(\gamma+\zeta-(\alpha-\beta))\Bigg)J_{m+1}(k\,r) \\
& +\Bigg(\cos((m+1)(\gamma+\frac{\pi}{2}))\sin(\gamma+\zeta+(\alpha-\beta))-\sin((m+1)(\gamma+\frac{\pi}{2}))\cos(\gamma+\zeta+(\alpha-\beta))\Bigg)J_{-(m+1)}(k\,r) \\
& +\Bigg(\sin((m-1)(\gamma+\frac{\pi}{2}))\cos(\gamma-\zeta+(\alpha-\beta))+\cos((m-1)(\gamma+\frac{\pi}{2}))\sin(\gamma-\zeta+(\alpha-\beta))\Bigg)J_{m-1}(k\,r) \\
& -\Bigg(\sin((m-1)(\gamma+\frac{\pi}{2}))\cos(\gamma-\zeta-(\alpha-\beta))+\cos((m-1)(\gamma+\frac{\pi}{2}))\sin(\gamma-\zeta-(\alpha-\beta))\Bigg)J_{-(m-1)}(k\,r)\Bigg) \\
= \; & \frac{\pi}{2}\Bigg(\Bigg(\sin((m+1)(\gamma+\frac{\pi}{2}))\cos(\gamma+\zeta-(\alpha-\beta))-\cos((m+1)(\gamma+\frac{\pi}{2}))\sin(\gamma+\zeta-(\alpha-\beta))\Bigg)J_{m+1}(k\,r) \\
& +\Bigg(\cos((m+1)(\gamma+\frac{\pi}{2}))\sin(\gamma+\zeta+(\alpha-\beta))-\sin((m+1)(\gamma+\frac{\pi}{2}))\cos(\gamma+\zeta+(\alpha-\beta))\Bigg)J_{-(m+1)}(k\,r) \\
& +\Bigg(\sin((m-1)(\gamma+\frac{\pi}{2}))\cos(\gamma-\zeta+(\alpha-\beta))+\cos((m-1)(\gamma+\frac{\pi}{2}))\sin(\gamma-\zeta+(\alpha-\beta))\Bigg)J_{m-1}(k\,r) \\
& -\Bigg(\sin((m-1)(\gamma+\frac{\pi}{2}))\cos(\gamma-\zeta-(\alpha-\beta))+\cos((m-1)(\gamma+\frac{\pi}{2}))\sin(\gamma-\zeta-(\alpha-\beta))\Bigg)J_{-(m-1)}(k\,r)\Bigg) \\
= \; & \frac{\pi}{2}\Bigg(\sin((m+1)(\gamma+\frac{\pi}{2})-\gamma-\zeta+(\alpha-\beta))J_{m+1}(k\,r)-\sin((m+1)(\gamma+\frac{\pi}{2})-\gamma-\zeta-(\alpha-\beta))J_{-(m+1)}(k\,r) \\
& +\sin((m-1)(\gamma+\frac{\pi}{2})+\gamma-\zeta+(\alpha-\beta))J_{m-1}(k\,r)-\sin((m-1)(\gamma+\frac{\pi}{2})+\gamma-\zeta-(\alpha-\beta))J_{-(m-1)}(k\,r)\Bigg)
\end{aligned}
\tag{402}
$$

$$\int_{-\pi}^{\pi} T_{AB3}\,d\theta = \frac{\pi}{2}\left(\cos(m\gamma+m\frac{\pi}{2}-\zeta+(\alpha-\beta))J_{m+1}(kr)-\cos(m\gamma+m\frac{\pi}{2}-\zeta-(\alpha-\beta))J_{-(m+1)}(kr)\right.$$
$$\left.-\cos(m\gamma+m\frac{\pi}{2}-\zeta+(\alpha-\beta))J_{m-1}(kr)+\cos(m\gamma+m\frac{\pi}{2}-\zeta-(\alpha-\beta))J_{-(m-1)}(kr)\right) \quad (402)$$

And, as $J_{-m}(kr) = -1^{m}J_{m}(kr)$, when m is even:

$$\begin{aligned}\int_{-\pi}^{\pi} T_{AB3}\,d\theta\Big|_{even\ m} &= \frac{\pi}{2}\left(\cos(m\gamma+m\frac{\pi}{2}-\zeta+(\alpha-\beta))J_{m+1}(kr)-\cos(m\gamma+m\frac{\pi}{2}-\zeta-(\alpha-\beta))J_{-(m+1)}(kr)\right.\\ &\quad\left.-\cos(m\gamma+m\frac{\pi}{2}-\zeta+(\alpha-\beta))J_{m-1}(kr)+\cos(m\gamma+m\frac{\pi}{2}-\zeta-(\alpha-\beta))J_{-(m-1)}(kr)\right)\\ &= \frac{\pi}{2}\left(\left(\cos(m\gamma+m\frac{\pi}{2}-\zeta+(\alpha-\beta))+\cos(m\gamma+m\frac{\pi}{2}-\zeta-(\alpha-\beta))\right)J_{m+1}(kr)\right.\\ &\quad\left.-\left(\cos(m\gamma+m\frac{\pi}{2}-\zeta+(\alpha-\beta))+\cos(m\gamma+m\frac{\pi}{2}-\zeta-(\alpha-\beta))\right)J_{m-1}(kr)\right)\\ &= -\pi\cos(\alpha-\beta)\cos(m\gamma+m\frac{\pi}{2}-\zeta)\left(J_{m-1}(kr)-J_{m+1}(kr)\right)\end{aligned} \quad (403)$$

And when m is odd:

$$\begin{aligned}
\int_{-\pi}^{\pi} T_{AB3}\,d\theta\Big|_{odd\ m} &= \frac{\pi}{2}\Big(\cos(m\gamma+m\frac{\pi}{2}-\zeta+(\alpha-\beta))J_{m+1}(kr)-\cos(m\gamma+m\frac{\pi}{2}-\zeta-(\alpha-\beta))J_{-(m+1)}(kr)\\
&\quad -\cos(m\gamma+m\frac{\pi}{2}-\zeta+(\alpha-\beta))J_{m-1}(kr)+\cos(m\gamma+m\frac{\pi}{2}-\zeta-(\alpha-\beta))J_{-(m-1)}(kr)\Big)\\
&= \frac{\pi}{2}\Big(\Big(\cos(m\gamma+m\frac{\pi}{2}-\zeta+(\alpha-\beta))-\cos(m\gamma+m\frac{\pi}{2}-\zeta-(\alpha-\beta))\Big)J_{m+1}(kr)\\
&\quad -\Big(\cos(m\gamma+m\frac{\pi}{2}-\zeta+(\alpha-\beta))-\cos(m\gamma+m\frac{\pi}{2}-\zeta-(\alpha-\beta))\Big)J_{m-1}(kr)\Big)\\
&= \pi\sin(\alpha-\beta)\sin(m\gamma+m\frac{\pi}{2}-\zeta)\big(J_{m-1}(kr)-J_{m+1}(kr)\big)
\end{aligned} \tag{404}$$

Examining term T_{AB4} :

$$\begin{aligned}
T_{AB4} &= \cos(m\theta-\zeta)\cos(\theta-\gamma)\cos(kr\cos(\theta-\gamma)+\alpha-\beta)\\
&= \big(\cos(m\theta)\cos(\zeta)+\sin(m\theta)\sin(\zeta)\big)\big(\cos(\theta)\cos(\gamma)+\sin(\theta)\sin(\gamma)\big)\cos(kr\cos(\theta-\gamma)+\alpha-\beta)\\
&= \big(\cos(\theta)\cos(m\theta)\cos(\zeta)\cos(\gamma)+\sin(\theta)\cos(m\theta)\cos(\zeta)\sin(\gamma)+\cos(\theta)\sin(m\theta)\sin(\zeta)\cos(\gamma)\\
&\qquad +\sin(\theta)\sin(m\theta)\sin(\zeta)\sin(\gamma)\big)\cos(kr\cos(\theta-\gamma)+\alpha-\beta)\\
&= \big(\cos(\zeta)\cos(\gamma)\cos((m+1)\theta)+\cos(\zeta)\cos(\gamma)\cos((m-1)\theta)+\cos(\zeta)\sin(\gamma)\sin((m+1)\theta)\\
&\qquad -\cos(\zeta)\sin(\gamma)\sin((m-1)\theta)+\sin(\zeta)\cos(\gamma)\sin((m+1)\theta)+\sin(\zeta)\cos(\gamma)\sin((m-1)\theta)\\
&\qquad -\sin(\zeta)\sin(\gamma)\cos((m+1)\theta)+\sin(\zeta)\sin(\gamma)\cos((m-1)\theta)\big)\cos(kr\cos(\theta-\gamma)+\alpha-\beta)
\end{aligned} \tag{405}$$

$$
\begin{aligned}
T_{AB4} &= \big(\big(\cos(\zeta)\cos(\gamma)-\sin(\zeta)\sin(\gamma)\big)\cos((m+1)\theta)+\big(\sin(\zeta)\cos(\gamma)+\cos(\zeta)\sin(\gamma)\big)\sin((m+1)\theta) \\
&\qquad +\big(\sin(\zeta)\cos(\gamma)-\cos(\zeta)\sin(\gamma)\big)\sin((m-1)\theta)+\big(\cos(\zeta)\cos(\gamma)+\sin(\zeta)\sin(\gamma)\big)\cos((m-1)\theta)\big) \\
&\qquad \times\cos(k\,r\cos(\theta-\gamma)+\alpha-\beta) \\
&= \frac{1}{2}\big(\big(\cos(\gamma+\zeta)\cos((m+1)\theta)+\sin(\gamma+\zeta)\sin((m+1)\theta)-\sin(\gamma-\zeta)\sin((m-1)\theta)+\cos(\gamma-\zeta)\cos((m-1)\theta)\big) \\
&\qquad \times\big(\cos(k\,r\cos(\theta-\gamma))\cos(\alpha-\beta)-\sin(k\,r\cos(\theta-\gamma))\sin(\alpha-\beta)\big)\big) \\
&= \frac{1}{2}\big(\cos(\gamma+\zeta)\cos(\alpha-\beta)\cos((m+1)\theta)\cos(k\,r\cos(\theta-\gamma))+\sin(\gamma+\zeta)\cos(\alpha-\beta)\sin((m+1)\theta)\cos(k\,r\cos(\theta-\gamma)) \\
&\qquad -\sin(\gamma-\zeta)\cos(\alpha-\beta)\sin((m-1)\theta)\cos(k\,r\cos(\theta-\gamma))+\cos(\gamma-\zeta)\cos(\alpha-\beta)\cos((m-1)\theta)\cos(k\,r\cos(\theta-\gamma)) \\
&\qquad -\cos(\gamma+\zeta)\sin(\alpha-\beta)\cos((m+1)\theta)\sin(k\,r\cos(\theta-\gamma))-\sin(\gamma+\zeta)\sin(\alpha-\beta)\sin((m+1)\theta)\sin(k\,r\cos(\theta-\gamma)) \\
&\qquad +\sin(\gamma-\zeta)\sin(\alpha-\beta)\sin((m-1)\theta)\sin(k\,r\cos(\theta-\gamma))-\cos(\gamma-\zeta)\sin(\alpha-\beta)\cos((m-1)\theta)\sin(k\,r\cos(\theta-\gamma))\big) \\
&= \frac{1}{4}\big(\cos(\gamma+\zeta)\cos(\alpha-\beta)\big(\cos(k\,r\cos(\theta-\gamma)+(m+1)\theta)+\cos(k\,r\cos(\theta-\gamma)-(m+1)\theta)\big) \\
&\qquad +\sin(\gamma+\zeta)\cos(\alpha-\beta)\big(\sin(k\,r\cos(\theta-\gamma)+(m+1)\theta)-\sin(k\,r\cos(\theta-\gamma)-(m+1)\theta)\big) \\
&\qquad -\sin(\gamma-\zeta)\cos(\alpha-\beta)\big(\sin(k\,r\cos(\theta-\gamma)+(m-1)\theta)-\sin(k\,r\cos(\theta-\gamma)-(m-1)\theta)\big) \\
&\qquad +\cos(\gamma-\zeta)\cos(\alpha-\beta)\big(\cos(k\,r\cos(\theta-\gamma)+(m-1)\theta)+\cos(k\,r\cos(\theta-\gamma)-(m-1)\theta)\big) \\
&\qquad -\cos(\gamma+\zeta)\sin(\alpha-\beta)\big(\sin(k\,r\cos(\theta-\gamma)+(m+1)\theta)+\sin(k\,r\cos(\theta-\gamma)-(m+1)\theta)\big) \\
&\qquad -\sin(\gamma+\zeta)\sin(\alpha-\beta)\big(-\cos(k\,r\cos(\theta-\gamma)+(m+1)\theta)+\cos(k\,r\cos(\theta-\gamma)-(m+1)\theta)\big) \\
&\qquad +\sin(\gamma-\zeta)\sin(\alpha-\beta)\big(-\cos(k\,r\cos(\theta-\gamma)+(m-1)\theta)+\cos(k\,r\cos(\theta-\gamma)-(m-1)\theta)\big) \\
&\qquad -\cos(\gamma-\zeta)\sin(\alpha-\beta)\big(\sin(k\,r\cos(\theta-\gamma)+(m-1)\theta)+\sin(k\,r\cos(\theta-\gamma)-(m-1)\theta)\big)\big)
\end{aligned}
\tag{405}
$$

2 of 3

$$
\begin{aligned}
T_{AB4} \;=\; \frac{1}{4}\Big(&\cos(k\,r\cos(\theta-\gamma)+(m+1)\theta)\big(\cos(\gamma+\zeta)\cos(\alpha-\beta)+\sin(\gamma+\zeta)\sin(\alpha-\beta)\big)\\
&+\cos(k\,r\cos(\theta-\gamma)-(m+1)\theta)\big(\cos(\gamma+\zeta)\cos(\alpha-\beta)-\sin(\gamma+\zeta)\sin(\alpha-\beta)\big)\\
&+\cos(k\,r\cos(\theta-\gamma)+(m-1)\theta)\big(\cos(\gamma-\zeta)\cos(\alpha-\beta)-\sin(\gamma-\zeta)\sin(\alpha-\beta)\big)\\
&+\cos(k\,r\cos(\theta-\gamma)-(m-1)\theta)\big(\cos(\gamma-\zeta)\cos(\alpha-\beta)+\sin(\gamma-\zeta)\sin(\alpha-\beta)\big)\\
&-\sin(k\,r\cos(\theta-\gamma)+(m+1)\theta)\big(\sin(\gamma+\zeta)\cos(\alpha-\beta)+\cos(\gamma+\zeta)\sin(\alpha-\beta)\big)\\
&+\sin(k\,r\cos(\theta-\gamma)-(m+1)\theta)\big(\sin(\gamma+\zeta)\cos(\alpha-\beta)+\cos(\gamma+\zeta)\sin(\alpha-\beta)\big)\\
&+\sin(k\,r\cos(\theta-\gamma)-(m-1)\theta)\big(\sin(\gamma-\zeta)\cos(\alpha-\beta)-\cos(\gamma-\zeta)\sin(\alpha-\beta)\big)\\
&-\sin(k\,r\cos(\theta-\gamma)+(m-1)\theta)\big(\sin(\gamma-\zeta)\cos(\alpha-\beta)+\cos(\gamma-\zeta)\sin(\alpha-\beta)\big)\Big)\\
=\; \frac{1}{4}\Big(&\cos(\gamma+\zeta-(\alpha-\beta))\cos(k\,r\cos(\theta-\gamma)+(m+1)\theta)+\cos(\gamma+\zeta+(\alpha-\beta))\cos(k\,r\cos(\theta-\gamma)-(m+1)\theta)\\
&+\cos(\gamma-\zeta+(\alpha-\beta))\cos(k\,r\cos(\theta-\gamma)+(m-1)\theta)+\cos(\gamma-\zeta-(\alpha-\beta))\cos(k\,r\cos(\theta-\gamma)-(m-1)\theta)\\
&+\sin(\gamma+\zeta-(\alpha-\beta))\sin(k\,r\cos(\theta-\gamma)+(m+1)\theta)-\sin(\gamma+\zeta+(\alpha-\beta))\sin(k\,r\cos(\theta-\gamma)-(m+1)\theta)\\
&-\sin(\gamma-\zeta+(\alpha-\beta))\sin(k\,r\cos(\theta-\gamma)+(m-1)\theta)+\sin(\gamma-\zeta-(\alpha-\beta))\sin(k\,r\cos(\theta-\gamma)-(m-1)\theta)\Big)
\end{aligned}
\tag{405}
$$

Utilising the identities from Equations 392 and 393:

$$
\begin{aligned}
\int_{-\pi}^{\pi} T_{AB4}\,d\theta \;=\; & \frac{1}{4}\int_{-\pi}^{\pi} \big(\cos(\gamma+\zeta-(\alpha-\beta))\cos(k\,r\cos(\theta-\gamma)+(m+1)\theta)+\cos(\gamma+\zeta+(\alpha-\beta))\cos(k\,r\cos(\theta-\gamma)-(m+1)\theta) \\
& +\cos(\gamma-\zeta+(\alpha-\beta))\cos(k\,r\cos(\theta-\gamma)+(m-1)\theta)+\cos(\gamma-\zeta-(\alpha-\beta))\cos(k\,r\cos(\theta-\gamma)-(m-1)\theta) \\
& +\sin(\gamma+\zeta-(\alpha-\beta))\sin(k\,r\cos(\theta-\gamma)+(m+1)\theta)-\sin(\gamma+\zeta+(\alpha-\beta))\sin(k\,r\cos(\theta-\gamma)-(m+1)\theta) \\
& -\sin(\gamma-\zeta+(\alpha-\beta))\sin(k\,r\cos(\theta-\gamma)+(m-1)\theta)+\sin(\gamma-\zeta-(\alpha-\beta))\sin(k\,r\cos(\theta-\gamma)-(m-1)\theta)\big)\,d\theta \\
= \; & \frac{1}{4}\Bigg(\cos(\gamma+\zeta-(\alpha-\beta))2\pi\cos((m+1)(\gamma+\tfrac{\pi}{2}))J_{m+1}(k\,r)+\cos(\gamma+\zeta+(\alpha-\beta))2\pi\cos(-(m+1)(\gamma+\tfrac{\pi}{2}))J_{-(m+1)}(k\,r) \\
& +\cos(\gamma-\zeta+(\alpha-\beta))2\pi\cos((m-1)(\gamma+\tfrac{\pi}{2}))J_{m-1}(k\,r)+\cos(\gamma-\zeta-(\alpha-\beta))2\pi\cos(-(m-1)(\gamma+\tfrac{\pi}{2}))J_{-(m-1)}(k\,r) \\
& +\sin(\gamma+\zeta-(\alpha-\beta))2\pi\sin((m+1)(\gamma+\tfrac{\pi}{2}))J_{m+1}(k\,r)-\sin(\gamma+\zeta+(\alpha-\beta))2\pi\sin(-(m+1)(\gamma+\tfrac{\pi}{2}))J_{-(m+1)}(k\,r) \\
& -\sin(\gamma-\zeta+(\alpha-\beta))2\pi\sin((m-1)(\gamma+\tfrac{\pi}{2}))J_{m-1}(k\,r)+\sin(\gamma-\zeta-(\alpha-\beta))2\pi\sin(-(m-1)(\gamma+\tfrac{\pi}{2}))J_{-(m-1)}(k\,r)\Bigg) \\
= \; & \frac{\pi}{2}\Bigg(\Big(\cos(\gamma+\zeta-(\alpha-\beta))\cos((m+1)(\gamma+\tfrac{\pi}{2}))+\sin(\gamma+\zeta-(\alpha-\beta))\sin((m+1)(\gamma+\tfrac{\pi}{2}))\Big)J_{m+1}(k\,r) \\
& +\Big(\cos(\gamma+\zeta+(\alpha-\beta))\cos((m+1)(\gamma+\tfrac{\pi}{2}))+\sin(\gamma+\zeta+(\alpha-\beta))\sin((m+1)(\gamma+\tfrac{\pi}{2}))\Big)J_{-(m+1)}(k\,r) \\
& +\Big(\cos(\gamma-\zeta+(\alpha-\beta))\cos((m-1)(\gamma+\tfrac{\pi}{2}))-\sin(\gamma-\zeta+(\alpha-\beta))\sin((m-1)(\gamma+\tfrac{\pi}{2}))\Big)J_{m-1}(k\,r) \\
& +\Big(\cos(\gamma-\zeta-(\alpha-\beta))\cos((m-1)(\gamma+\tfrac{\pi}{2}))-\sin(\gamma-\zeta-(\alpha-\beta))\sin((m-1)(\gamma+\tfrac{\pi}{2}))\Big)J_{-(m-1)}(k\,r)\Bigg)
\end{aligned}
\tag{406}
$$

1 of 2

$$\begin{aligned}\int_{-\pi}^{\pi} T_{AB4}\,d\theta &= \frac{\pi}{2}\Big(\cos((m+1)(\gamma+\frac{\pi}{2})-\gamma-\zeta+(\alpha-\beta))J_{m+1}(kr)+\cos((m+1)(\gamma+\frac{\pi}{2})-\gamma-\zeta-(\alpha-\beta))J_{-(m+1)}(kr)\\ &\quad+\cos((m-1)(\gamma+\frac{\pi}{2})+\gamma-\zeta+(\alpha-\beta))J_{m-1}(kr)+\cos((m-1)(\gamma+\frac{\pi}{2})+\gamma-\zeta-(\alpha-\beta))J_{-(m-1)}(kr)\Big)\\ &= \frac{\pi}{2}\Big(-\sin(m\gamma+m\frac{\pi}{2}-\zeta+(\alpha-\beta))J_{m+1}(kr)-\sin(m\gamma+m\frac{\pi}{2}-\zeta-(\alpha-\beta))J_{-(m+1)}(kr)\\ &\quad+\sin(m\gamma+m\frac{\pi}{2}-\zeta+(\alpha-\beta))J_{m-1}(kr)+\sin(m\gamma+m\frac{\pi}{2}-\zeta-(\alpha-\beta))J_{-(m-1)}(kr)\Big)\end{aligned} \tag{406}$$

And, as $J_{-m}(kr) = -1^{m}J_{m}(kr)$, when m is even:

$$\begin{aligned}\int_{-\pi}^{\pi} T_{AB4}\,d\theta\Big|_{even\ m} &= \frac{\pi}{2}\Big(-\sin(m\gamma+m\frac{\pi}{2}-\zeta+(\alpha-\beta))J_{m+1}(kr)-\sin(m\gamma+m\frac{\pi}{2}-\zeta-(\alpha-\beta))J_{-(m+1)}(kr)\\ &\quad+\sin(m\gamma+m\frac{\pi}{2}-\zeta+(\alpha-\beta))J_{m-1}(kr)+\sin(m\gamma+m\frac{\pi}{2}-\zeta-(\alpha-\beta))J_{-(m-1)}(kr)\Big)\\ &= \frac{\pi}{2}\Big(\Big(\sin(m\gamma+m\frac{\pi}{2}-\zeta+(\alpha-\beta))-\sin(m\gamma+m\frac{\pi}{2}-\zeta-(\alpha-\beta))\Big)J_{m-1}(kr)\\ &\quad-\Big(\sin(m\gamma+m\frac{\pi}{2}-\zeta+(\alpha-\beta))-\sin(m\gamma+m\frac{\pi}{2}-\zeta-(\alpha-\beta))\Big)J_{m+1}(kr)\Big)\\ &= \pi\sin(\alpha-\beta)\cos(m\gamma+m\frac{\pi}{2}-\zeta)\big(J_{m-1}(kr)-J_{m+1}(kr)\big)\end{aligned} \tag{407}$$

And when m is odd:

$$\begin{aligned}
\int_{-\pi}^{\pi} T_{AB4}\, d\theta \Big|_{odd\ m} &= \frac{\pi}{2}\Big(-\sin(m\gamma + m\frac{\pi}{2} - \zeta + (\alpha-\beta))J_{m+1}(kr) - \sin(m\gamma + m\frac{\pi}{2} - \zeta - (\alpha-\beta))J_{-(m+1)}(kr) \\
&\qquad + \sin(m\gamma + m\frac{\pi}{2} - \zeta + (\alpha-\beta))J_{m-1}(kr) + \sin(m\gamma + m\frac{\pi}{2} - \zeta - (\alpha-\beta))J_{-(m-1)}(kr)\Big) \\
&= \frac{\pi}{2}\Big(\Big(\sin(m\gamma + m\frac{\pi}{2} - \zeta + (\alpha-\beta)) + \sin(m\gamma + m\frac{\pi}{2} - \zeta - (\alpha-\beta))\Big)J_{m-1}(kr) \\
&\qquad - \Big(\sin(m\gamma + m\frac{\pi}{2} - \zeta + (\alpha-\beta)) + \sin(m\gamma + m\frac{\pi}{2} - \zeta - (\alpha-\beta))\Big)J_{m+1}(kr)\Big) \\
&= \pi\cos(\alpha-\beta)\sin(m\gamma + m\frac{\pi}{2} - \zeta)\big(J_{m-1}(kr) - J_{m+1}(kr)\big)
\end{aligned} \tag{408}$$

This completes the analysis for the components of the combined $\hat{r}$ term. The general solution can be resolved by examining the combined $\hat{r}$ term in the two special cases of m is even and m is odd.

For m is even, Equations 395, 399, 403 and 407 can be substituted into the expression for the combined $\hat{r}$ term in Equation 388:

$$
\begin{aligned}
&\textit{combined } \hat{r} \textit{ term}\big|_{\textit{even } m} \\
&= -\frac{1}{2}\rho k \omega D^2 \int_{-h}^{\eta} G^2 dz\, AB r \Bigg(\frac{1}{2}\left(J_{m-1}(kr) - J_{m+1}(kr)\right) 2\pi \sin(\alpha-\beta)\cos\left(m\gamma + m\frac{\pi}{2} - \zeta\right) J_m(kr) \\
&\qquad + Y_m(kr)\pi\cos(\alpha-\beta)\cos\left(m\gamma + m\frac{\pi}{2} - \zeta\right)\left(J_{m-1}(kr) - J_{m+1}(kr)\right) \\
&\qquad - \Bigg(\frac{1}{2}\left(Y_{m-1}(kr) - Y_{m+1}(kr)\right) 2\pi\cos(\alpha-\beta)\cos\left(m\gamma + m\frac{\pi}{2} - \zeta\right) J_m(kr) \\
&\qquad + J_m(kr)\pi\sin(\alpha-\beta)\cos\left(m\gamma + m\frac{\pi}{2} - \zeta\right)\left(J_{m-1}(kr) - J_{m+1}(kr)\right) \Bigg) \Bigg) \\
&= -\frac{\pi}{2}\rho k \omega D^2 \int_{-h}^{\eta} G^2 dz\, AB r \cos\left(m\gamma + m\frac{\pi}{2} - \zeta\right) \\
&\qquad \times \Big(\left(J_{m-1}(kr) - J_{m+1}(kr)\right)\sin(\alpha-\beta) J_m(kr) + Y_m(kr)\cos(\alpha-\beta)\left(J_{m-1}(kr) - J_{m+1}(kr)\right) \\
&\qquad - \left(Y_{m-1}(kr) - Y_{m+1}(kr)\right)\cos(\alpha-\beta) J_m(kr) - J_m(kr)\sin(\alpha-\beta)\left(J_{m-1}(kr) - J_{m+1}(kr)\right) \Big) \\
&= -\frac{\pi}{2}\rho k \omega D^2 \int_{-h}^{\eta} G^2 dz\, AB r \cos(\alpha-\beta)\cos\left(m\gamma + m\frac{\pi}{2} - \zeta\right)\left(Y_m(kr)\left(J_{m-1}(kr) - J_{m+1}(kr)\right) - \left(Y_{m-1}(kr) - Y_{m+1}(kr)\right) J_m(kr) \right) \\
&= -\frac{\pi}{2}\rho k \omega D^2 \int_{-h}^{\eta} G^2 dz\, AB r \cos(\alpha-\beta)\cos\left(m\gamma + m\frac{\pi}{2} - \zeta\right)\left(-\frac{4}{\pi k r} \right) \\
&= 2\rho\omega D^2 \int_{-h}^{\eta} G^2 dz\, AB \cos(\alpha-\beta)\cos\left(m\gamma + m\frac{\pi}{2} - \zeta\right)
\end{aligned}
\tag{409}
$$

For m is even, Equations 396, 400, 404 and 408 can be substituted into the expression for the combined $\hat{r}$ term in Equation 388:

$$
\begin{aligned}
&\textit{combined } \hat{r} \textit{ term}\big|_{\textit{odd } m} \\
&= -\frac{1}{2}\rho k \omega D^2 \int_{-h}^{\eta} G^2 dz\, A B r \Bigg(\frac{1}{2}\big(J_{m-1}(kr)-J_{m+1}(kr)\big) 2\pi \cos(\alpha-\beta)\sin\big(m\gamma+m\frac{\pi}{2}-\zeta\big) J_m(kr) \\
&\qquad\qquad -Y_m(kr)\pi\sin(\alpha-\beta)\sin\big(m\gamma+m\frac{\pi}{2}-\zeta\big)\big(J_{m-1}(kr)-J_{m+1}(kr)\big) \\
&\qquad -\Bigg(-\frac{1}{2}\big(Y_{m-1}(kr)-Y_{m+1}(kr)\big) 2\pi\sin(\alpha-\beta)\sin\big(m\gamma+m\frac{\pi}{2}-\zeta\big) J_m(kr) \\
&\qquad\qquad +J_m(kr)\pi\cos(\alpha-\beta)\sin\big(m\gamma+m\frac{\pi}{2}-\zeta\big)\big(J_{m-1}(kr)-J_{m+1}(kr)\big)\Bigg)\Bigg) \\
&= -\frac{\pi}{2}\rho k \omega D^2 \int_{-h}^{\eta} G^2 dz\, A B r \sin\big(m\gamma+m\frac{\pi}{2}-\zeta\big) \\
&\qquad\qquad \times\Big(\big(J_{m-1}(kr)-J_{m+1}(kr)\big)\cos(\alpha-\beta)J_m(kr)-Y_m(kr)\sin(\alpha-\beta)\big(J_{m-1}(kr)-J_{m+1}(kr)\big) \\
&\qquad\qquad +\big(Y_{m-1}(kr)-Y_{m+1}(kr)\big)\sin(\alpha-\beta)J_m(kr)-J_m(kr)\cos(\alpha-\beta)\big(J_{m-1}(kr)-J_{m+1}(kr)\big)\Big) \\
&= -\frac{\pi}{2}\rho k \omega D^2 \int_{-h}^{\eta} G^2 dz\, A B r \sin(\alpha-\beta)\sin\big(m\gamma+m\frac{\pi}{2}-\zeta\big)\Big(-Y_m(kr)\big(J_{m-1}(kr)-J_{m+1}(kr)\big)+\big(Y_{m-1}(kr)-Y_{m+1}(kr)\big)J_m(kr)\Big) \\
&= -\frac{\pi}{2}\rho k \omega D^2 \int_{-h}^{\eta} G^2 dz\, A B r \sin(\alpha-\beta)\sin\big(m\gamma+m\frac{\pi}{2}-\zeta\big)\left(\frac{4}{\pi k r}\right) \\
&= -2\rho\omega D^2 \int_{-h}^{\eta} G^2 dz\, A B \sin(\alpha-\beta)\sin\big(m\gamma+m\frac{\pi}{2}-\zeta\big)
\end{aligned}
\tag{410}
$$

And so, the combined $\hat{r}$ term can be shown to be:

$$\begin{aligned} \textit{combined } \hat{r} \textit{ term}\big|_{m\in\mathbb{Z}} &= 2\rho\omega D^2 \int_{-h}^{\eta} G^2 dz\, AB\cos(\alpha-\beta+m\frac{\pi}{2})\cos(m\gamma-\zeta) \\ &= \frac{\rho\omega g}{k^2}\left(1+\frac{2kh}{\sinh(kh)}\right) AB\cos(\alpha-\beta+m\frac{\pi}{2})\cos(m\gamma-\zeta) \end{aligned} \tag{411}$$

So the general solution for the total power for a combined plane and circular wave is can be found by substituting Equations 283, 383, 411 into Equation 385:

$$\begin{aligned} \overline{P}_{r\ \ p+m}\big|_{m\in\mathbb{Z}} &= \frac{\rho\omega g B^2}{2\pi k^2}\left(\pi+\frac{\sin(2m\pi)\cos(2\zeta)}{2m}\right)\left(1+\frac{2kh}{\sinh(2kh)}\right)+\frac{\rho\omega g}{k^2}\left(1+\frac{\sinh(2kh)}{2kh}\right) AB\cos(\alpha-\beta+m\frac{\pi}{2})\cos(m\gamma-\zeta) \\ &= \frac{\rho\omega g}{k^2}\left(1+\frac{2kh}{\sinh(2kh)}\right)\left(\frac{B^2}{2}\left(1+\frac{\sin(2m\pi)\cos(2\zeta)}{2m\pi}\right)+AB\cos(\alpha-\beta+m\frac{\pi}{2})\cos(m\gamma-\zeta)\right) \end{aligned} \tag{412}$$

Appendix 8: Time-averaged Power for Plane Wave and Three Circular Waves

The general solution for time-averaged power given by Equations 369 to 375 in Appendix 5. If it is assumed that a single monochromatic plane wave interacts with 3 radial waves of identical wavelength with each one of the radial waves representing either heave, surge and sway then the following substitutions can be made:

$$
\begin{array}{lll}
a_a = 1 & F_{11} = \cos(m_1\theta-\zeta_{11}) = 1 & \beta_{1111} = \beta_1 \\
b_a = n_a = 1 & F_{21} = \cos(m_2\theta-\zeta_{21}) = \cos(\theta) & \beta_{1211} = \beta_2 \\
c_{ab} = o_{an} = 1 & F_{31} = \cos(m_3\theta-\zeta_{31}) = \cos(\theta-\frac{\pi}{2}) & \beta_{1311} = \beta_3 \\
d_d = p_p = 3 & A_{abc} = A_{ano} = A & \zeta_{11} = 0 \\
e_{ad} = q_{ap} = 1 & \gamma_{ab} = \gamma_{an} = \gamma & \zeta_{21} = \zeta \\
f_{ade} = s_{apq} = 1 & \alpha_{abc} = \alpha_{ano} = \alpha & \zeta_{31} = \zeta+\frac{\pi}{2} \\
k_a = k & B_{1111} = B_1 & m_1 = 0 \\
\omega_a = \omega & B_{1211} = B_2 & m_2 = 1 \\
D_a = D & B_{1311} = B_3 & m_3 = 1 \\
G_a = G & &
\end{array}
\tag{413}
$$

Let:

$$
T_1 = \sum_{b=1}^{b_a}\sum_{c=1}^{c_{ab}}\sum_{n=1}^{n_a}\sum_{o=1}^{o_{an}} -A_{abc}A_{ano}\cos(\theta-\gamma_{an})\cos(k_a r(\cos(\theta-\gamma_{ab})-\cos(\theta-\gamma_{an}))+\alpha_{abc}-\alpha_{ano}) \tag{414}
$$

Substituting in the constraints gives the following:

$$\begin{aligned} T_1 &= -A^2\cos(\theta-\gamma)\cos(kr(\cos(\theta-\gamma)-\cos(\theta-\gamma))+0) \\ &= -A^2\cos(\theta-\gamma)\cos(0) \\ &= -A^2\cos(\theta-\gamma) \end{aligned} \tag{415}$$

Noting that the area, A_r, is defined from $\int_A d\vec{A}_r = \int_{-h}^{\eta}\int_{-\pi}^{\pi} r\,d\theta\,dz\hat{r}$, the dot product reduces the $\overline{P}$ to a function in only the $\hat{r}$ direction. This means that all of the $\hat{\theta}$ terms of Equation 369 can be ignored. Let:

$$\begin{aligned} T_{2\mathrm{d}} = \sum_{b=1}^{b_a}\sum_{c=1}^{c_{ab}}\sum_{d=1}^{d_d}\sum_{e=1}^{e_{ad}}\sum_{f=1}^{f_{ade}} F_{de}A_{abc}B_{adef}\Bigg(&\left(\frac{1}{2}\left(J_{m_d-1}(k_ar)-J_{m_d+1}(k_ar)\right)-Y_{m_d}(k_ar)\cos(\theta-\gamma_{ab})\right)\sin(k_ar\cos(\theta-\gamma_{ab})+\alpha_{abc}-\beta_{adef}) \\ &-\left(\frac{1}{2}\left(Y_{m_d-1}(k_ar)-Y_{m_d+1}(k_ar)\right)+J_{m_d}(k_ar)\cos(\theta-\gamma_{ab})\right)\cos(k_ar\cos(\theta-\gamma_{ab})+\alpha_{abc}-\beta_{adef})\Bigg) \end{aligned} \tag{416}$$

Substituting in the constraints generates three terms. They are as follows:

$$\begin{aligned} T_{21} = AB_1\Bigg(&\left(\frac{1}{2}\left(J_{-1}(kr)-J_1(kr)\right)-Y_0(kr)\cos(\theta-\gamma)\right)\sin(kr\cos(\theta-\gamma)+\alpha-\beta_1) \\ &-\left(\frac{1}{2}\left(Y_{-1}(kr)-Y_1(kr)\right)+J_0(kr)\cos(\theta-\gamma)\right)\cos(kr\cos(\theta-\gamma)+\alpha-\beta_1)\Bigg) \end{aligned} \tag{417}$$

$$T_{22} = \cos(\theta-\zeta)\,A\,B_2\left(\left(\frac{1}{2}\left(J_0(k\,r)-J_2(k\,r)\right)-Y_1(k\,r)\cos(\theta-\gamma)\right)\sin(k\,r\cos(\theta-\gamma)+\alpha-\beta_2)\right.$$
$$\left.-\left(\frac{1}{2}\left(Y_0(k\,r)-Y_2(k\,r)\right)+J_1(k\,r)\cos(\theta-\gamma)\right)\cos(k\,r\cos(\theta-\gamma)+\alpha-\beta_2)\right) \tag{418}$$

$$T_{23} = \sin(\theta-\zeta)\,A\,B_3\left(\left(\frac{1}{2}\left(J_0(k\,r)-J_2(k\,r)\right)-Y_1(k\,r)\cos(\theta-\gamma)\right)\sin(k\,r\cos(\theta-\gamma)+\alpha-\beta_3)\right.$$
$$\left.-\left(\frac{1}{2}\left(Y_0(k\,r)-Y_2(k\,r)\right)+J_1(k\,r)\cos(\theta-\gamma)\right)\cos(k\,r\cos(\theta-\gamma)+\alpha-\beta_3)\right) \tag{419}$$

From Appendix 7 it is possible to note that where $\int_A dA_r = \int_{-h}^{\eta}\int_{-\pi}^{\pi} r\,d\theta\,dz\hat{r}$:

$$-\frac{1}{2}\rho\,A_r\,k\,\omega\,D^2\,G^2\,T_2 = \frac{\rho\,\omega\,g}{k^2}\left(1+\frac{2\,k\,h}{\sinh(2\,k\,h)}\right)A\,B_1\cos(\alpha-\beta_1)-\frac{\rho\,\omega\,g}{k^2}\left(1+\frac{2\,k\,h}{\sinh(2\,k\,h)}\right)A\,B_2\sin(\alpha-\beta_2)\cos(\gamma-\zeta)$$
$$\frac{-\rho\,\omega\,g}{k^2}\left(1+\frac{2\,k\,h}{\sinh(2\,k\,h)}\right)A\,B_3\sin(\alpha-\beta_3)\sin(\gamma-\zeta) \tag{420}$$
$$= \frac{\rho\,\omega\,g}{k^2}\left(1+\frac{2\,k\,h}{\sinh(2\,k\,h)}\right)\left(A\,B_1\cos(\alpha-\beta_1)-A\,B_2\sin(\alpha-\beta_2)\cos(\gamma-\zeta)-A\,B_3\sin(\alpha-\beta_3)\sin(\gamma-\zeta)\right)$$

Let:

$$T_{3\mathrm{dp}} = \sum_{d=1}^{d_d}\sum_{e=1}^{e_{ad}}\sum_{f=1}^{f_{ade}}\sum_{p=1}^{p_p}\sum_{q=1}^{q_{ap}}\sum_{s=1}^{s_{apq}}\frac{1}{2}F_{de}F_{pq}B_{adef}B_{apqs} \times\Big(\Big(J_{m_d}(k_a r)\big(J_{m_p-1}(k_a r)-J_{m_p+1}(k_a r)\big)-Y_{m_d}(k_a r)\big(Y_{m_p-1}(k_a r)-Y_{m_p+1}(k_a r)\big)\Big)\sin(\beta_{adef}-\beta_{apqs}) +\Big(Y_{m_d}(k_a r)\big(J_{m_p-1}(k_a r)-J_{m_p+1}(k_a r)\big)-J_{m_d}(k_a r)\big(Y_{m_p-1}(k_a r)-Y_{m_p+1}(k_a r)\big)\Big)\cos(\beta_{adef}-\beta_{apqs})\Big) \quad (421)$$

Substituting in the constraints from Equation 413 generates nine terms. They are as follows:

$$\begin{aligned} T_{311} &= B_1^2\Big(\big(J_0(kr)\big(J_{-1}(kr)-J_1(kr)\big)-Y_0(kr)\big(Y_{-1}(kr)-Y_1(kr)\big)\big)\sin(0) \\ &\quad +\Big(Y_0(kr)\big(J_{-1}(kr)-J_1(kr)\big)-J_0(kr)\big(Y_{-1}(kr)-Y_1(kr)\big)\Big)\cos(0)\Big) \\ &= B_1^2\big(Y_0(kr)\big(J_{-1}(kr)-J_1(kr)\big)-J_0(kr)\big(Y_{-1}(kr)-Y_1(kr)\big)\big) \\ &= -\frac{4B_1^2}{\pi kr} \end{aligned} \quad (422)$$

$$\begin{aligned} T_{312} &= \cos(\theta-\zeta)B_1B_2\Big(\big(J_0(kr)\big(J_0(kr)-J_2(kr)\big)-Y_0(kr)\big(Y_0(kr)-Y_2(kr)\big)\big)\sin(\beta_1-\beta_2) \\ &\quad +\Big(Y_0(kr)\big(J_0(kr)-J_2(kr)\big)-J_0(kr)\big(Y_0(kr)-Y_2(kr)\big)\Big)\cos(\beta_1-\beta_2)\Big) \end{aligned} \quad (423)$$

$$\begin{aligned} T_{321} &= \cos(\theta-\zeta)B_2B_1\Big(\big(J_1(kr)\big(J_{-1}(kr)-J_1(kr)\big)-Y_1(kr)\big(Y_{-1}(kr)-Y_1(kr)\big)\big)\sin(\beta_2-\beta_1) \\ &\quad +\Big(Y_1(kr)\big(J_{-1}(kr)-J_1(kr)\big)-J_1(kr)\big(Y_{-1}(kr)-Y_1(kr)\big)\Big)\cos(\beta_2-\beta_1)\Big) \end{aligned} \quad (424)$$

$$T_{313} = \sin(\theta-\zeta)\,B_1 B_3\Big(\big(J_0(kr)\big(J_0(kr)-J_2(kr)\big)-Y_0(kr)\big(Y_0(kr)-Y_2(kr)\big)\big)\sin(\beta_1-\beta_3) + \big(Y_0(kr)\big(J_0(kr)-J_2(kr)\big)-J_0(kr)\big(Y_0(kr)-Y_2(kr)\big)\big)\cos(\beta_1-\beta_3)\Big) \tag{425}$$

$$T_{331} = \sin(\theta-\zeta)\,B_3 B_1\Big(\big(J_1(kr)\big(J_{-1}(kr)-J_1(kr)\big)-Y_1(kr)\big(Y_{-1}(kr)-Y_1(kr)\big)\big)\sin(\beta_3-\beta_1) + \big(Y_1(kr)\big(J_{-1}(kr)-J_1(kr)\big)-J_1(kr)\big(Y_{-1}(kr)-Y_1(kr)\big)\big)\cos(\beta_3-\beta_1)\Big) \tag{426}$$

It is useful to note at this point that terms T_{312}, T_{321}, T_{313} and T_{331} are a factor of either $\cos(\theta-\zeta)$ or $\sin(\theta-\zeta)$. When factors are combined with a cylindrical area, as described by $\int_A d\vec{A}_r = \int_{-h}^{\eta}\int_{-\pi}^{\pi} r\,d\theta\,dz\hat{r}$, the integral with respect to θ becomes:

$$\begin{aligned}\int_{-\pi}^{\pi}\cos(\theta-\zeta)\,d\theta &= \big[\sin(\theta-\zeta)\big]_{-\pi}^{\pi}\\ &= \big[\sin(\theta)\cos(\zeta)-\cos(\theta)\sin(\zeta)\big]_{-\pi}^{\pi}\\ &= \sin(\pi)\cos(\zeta)-\cos(\pi)\sin(\zeta)-\sin(-\pi)\cos(\zeta)+\cos(-\pi)\sin(\zeta)\\ &= 0+\sin(\zeta)-0-\sin(\zeta)\\ &= 0\end{aligned} \tag{427}$$

Or:

$$\int_{-\pi}^{\pi}\sin(\theta-\zeta)\,d\theta = 0 \tag{428}$$

This means that terms T_{312}, T_{321}, T_{313} and T_{331} have no bearing on the result and can be ignored.

$$\begin{aligned} T_{322} &= \cos^2(\theta-\zeta)\,B_2^2\Big(\big(J_1(kr)\big(J_0(kr)-J_2(kr)\big)-Y_1(kr)\big(Y_0(kr)-Y_2(kr)\big)\big)\sin(0) \\ &\qquad +\big(Y_1(kr)\big(J_0(kr)-J_2(kr)\big)-J_1(kr)\big(Y_0(kr)-Y_2(kr)\big)\big)\cos(0)\Big) \\ &= \cos^2(\theta-\zeta)\,B_2^2\big(Y_1(kr)\big(J_0(kr)-J_2(kr)\big)-J_1(kr)\big(Y_0(kr)-Y_2(kr)\big)\big) \\ &= -\frac{4\cos^2(\theta-\zeta)\,B_2^2}{\pi kr} \end{aligned} \tag{429}$$

$$\begin{aligned} T_{323} &= \cos(\theta-\zeta)\sin(\theta-\zeta)\,B_2B_3\Big(\big(J_1(kr)\big(J_0(kr)-J_2(kr)\big)-Y_1(kr)\big(Y_0(kr)-Y_2(kr)\big)\big)\sin(\beta_2-\beta_3) \\ &\qquad +\big(Y_1(kr)\big(J_0(kr)-J_2(kr)\big)-J_1(kr)\big(Y_0(kr)-Y_2(kr)\big)\big)\cos(\beta_2-\beta_3)\Big) \\ &= \cos(\theta-\zeta)\sin(\theta-\zeta)\,B_2B_3\left(\big(J_1(kr)\big(J_0(kr)-J_2(kr)\big)-Y_1(kr)\big(Y_0(kr)-Y_2(kr)\big)\big)\sin(\beta_2-\beta_3)-\left(\frac{4}{\pi kr}\right)\cos(\beta_2-\beta_3)\right) \end{aligned} \tag{430}$$

$$\begin{aligned} T_{332} &= \sin(\theta-\zeta)\cos(\theta-\zeta)\,B_3B_2\Big(\big(J_1(kr)\big(J_0(kr)-J_2(kr)\big)-Y_1(kr)\big(Y_0(kr)-Y_2(kr)\big)\big)\sin(\beta_3-\beta_2) \\ &\qquad +\big(Y_1(kr)\big(J_0(kr)-J_2(kr)\big)-J_1(kr)\big(Y_0(kr)-Y_2(kr)\big)\big)\cos(\beta_3-\beta_2)\Big) \\ &= \sin(\theta-\zeta)\cos(\theta-\zeta)\,B_3B_2\left(\big(J_1(kr)\big(J_0(kr)-J_2(kr)\big)-Y_1(kr)\big(Y_0(kr)-Y_2(kr)\big)\big)\sin(\beta_3-\beta_2)-\left(\frac{4}{\pi kr}\right)\cos(\beta_3-\beta_2)\right) \end{aligned} \tag{431}$$

Note: when T_{323} and T_{332} are added then the following results:

$$\begin{aligned}
T_{323}+T_{332} &= \cos(\theta-\zeta)\sin(\theta-\zeta)B_2B_3\left(\left(J_1(kr)\left(J_0(kr)-J_2(kr)\right)-Y_1(kr)\left(Y_0(kr)-Y_2(kr)\right)\right)\sin(\beta_2-\beta_3)-\left(\frac{4}{\pi kr}\right)\cos(\beta_2-\beta_3)\right)\\
&\quad+\sin(\theta-\zeta)\cos(\theta-\zeta)B_3B_2\left(\left(J_1(kr)\left(J_0(kr)-J_2(kr)\right)-Y_1(kr)\left(Y_0(kr)-Y_2(kr)\right)\right)\sin(\beta_3-\beta_2)-\left(\frac{4}{\pi kr}\right)\cos(\beta_3-\beta_2)\right)\\
&= \cos(\theta-\zeta)\sin(\theta-\zeta)B_2B_3\left(\left(J_1(kr)\left(J_0(kr)-J_2(kr)\right)-Y_1(kr)\left(Y_0(kr)-Y_2(kr)\right)\right)\sin(\beta_2-\beta_3)-\left(\frac{4}{\pi kr}\right)\cos(\beta_2-\beta_3)\right)\\
&\quad+\sin(\theta-\zeta)\cos(\theta-\zeta)B_3B_2\left(-\left(J_1(kr)\left(J_0(kr)-J_2(kr)\right)-Y_1(kr)\left(Y_0(kr)-Y_2(kr)\right)\right)\sin(\beta_2-\beta_3)-\left(\frac{4}{\pi kr}\right)\cos(\beta_2-\beta_3)\right) \qquad (432)\\
&= -\cos(\theta-\zeta)\sin(\theta-\zeta)B_2B_3\left(\frac{4}{\pi kr}\right)\cos(\beta_2-\beta_3)+\sin(\theta)\cos(\theta)B_3B_2\left(\frac{4}{\pi kr}\right)\cos(\beta_2-\beta_3)\\
&= -\frac{8B_2B_3}{\pi kr}\cos(\theta-\zeta)\sin(\theta-\zeta)\cos(\beta_2-\beta_3)\\
&= -\frac{4B_2B_3}{\pi kr}\sin(2\theta-2\zeta)\cos(\beta_2-\beta_3)
\end{aligned}$$

Although this term has simplified neatly it is useful to note that, as for the previous mixed T_{3xx} terms the integral of the θ component due to the choice of A_r results in this term reducing to zero. Hence it can be neglected in further calculations.

$$\begin{aligned} T_{333} &= \sin^2(\theta) B_3^2 \Big(\big(J1(kr) \big(J_0(kr) - J_2(kr) \big) - Y_1(kr) \big(Y_0(kr) - Y_2(kr) \big) \big) \sin(0) \\ &\qquad + \big(Y_1(kr) \big(J_0(kr) - J_2(kr) \big) - J_1(kr) \big(Y_0(kr) - Y_2(kr) \big) \big) \cos(0) \Big) \\ &= \sin^2(\theta) B_3^2 \big(Y_1(kr) \big(J_0(kr) - J_2(kr) \big) - J_1(kr) \big(Y_0(kr) - Y_2(kr) \big) \big) \\ &= -\frac{4 \sin^2(\theta) B_3^2}{\pi kr} \end{aligned} \tag{433}$$

Terms T_{311}, T_{322} and T_{333} have appeared in Appendix 7 when deriving the time-averaged power for the combination of a plane wave and a single radial wave. Hence:

$$\begin{aligned} -\frac{1}{2} \rho A_r k \omega D^2 G^2 T_3 &= \frac{\rho \omega g B_1^2}{k^2} \left(1 + \frac{2kh}{\sinh(2kh)} \right) + \frac{\rho \omega g B_2^2}{2k^2} \left(1 + \frac{2kh}{\sinh(2kh)} \right) + \frac{\rho \omega g B_3^2}{2k^2} \left(1 + \frac{2kh}{\sinh(2kh)} \right) \\ &= \frac{\rho \omega g}{k^2} \left(1 + \frac{2kh}{\sinh(2kh)} \right) \left(B_1^2 + \frac{B_2^2}{2} + \frac{B_3^2}{2} \right) \end{aligned} \tag{434}$$

Which gives the radial component of time-averaged power for a combined plane, heave, surge and sway wave field ($\overline{P}_{r\ p+h+sg+sw}$) as:

$$\begin{aligned}\overline{P}_{r\ p+h+sg+sw} &= \frac{\rho\omega g}{k^2}\left(1+\frac{2kh}{\sinh(2kh)}\right)\left(AB_1\cos(\alpha-\beta_1)-AB_2\sin(\alpha-\beta_2)\cos(\gamma-\zeta)-AB_3\sin(\alpha-\beta_3)\sin(\gamma-\zeta)\right) \\ &\quad +\frac{\rho\omega g}{k^2}\left(1+\frac{2kh}{\sinh(2kh)}\right)\left(B_1^2+\frac{B_2^2}{2}+\frac{B_3^2}{2}\right) \\ &= \frac{\rho\omega g}{k^2}\left(1+\frac{2kh}{\sinh(2kh)}\right)\left(B_1^2+AB_1\cos(\alpha-\beta_1)+\frac{B_2^2}{2}-AB_2\sin(\alpha-\beta_2)\cos(\gamma-\zeta)+\frac{B_3^2}{2}-AB_3\sin(\alpha-\beta_3)\sin(\gamma-\zeta)\right)\end{aligned} \quad (435)$$

Note that the time-averaged power of a plane wave combined with three circular waves is simply the sum of the time-averaged power of each circular wave combined with the plane wave.

Also note, that by the definition of surge and sway, $\zeta=\gamma$ and therefore:

$$\overline{P}_{r\ p+h+sg+sw} = \frac{\rho\omega g}{k^2}\left(1+\frac{2kh}{\sinh(2kh)}\right)\left(B_1^2+AB_1\cos(\alpha-\beta_1)+\frac{B_2^2}{2}-AB_2\sin(\alpha-\beta_2)+\frac{B_3^2}{2}\right) \quad (436)$$

So, in summary: Providing only one wave occurs in each given direction the time-averaged power of a number of circular waves combined with a single plane wave is simply the sum of individual circular waves combined with the plane wave.

Appendix 9: Derivation of Displaced Volumes

This appendix provides a reference for the derivation of the various formulae utilised in Chapter 9.

A9.1 Total mass flow through a Circular Cylindrical Volume

From Equation 221 the total mass flow through the control volume, $\dot{m}_t^{cv}$, is:

$$\dot{m}_t^{cv} = -\rho \int_{-h}^{\eta} \int_{-\pi}^{\pi} \nabla \phi \cdot r_r \hat{r} \, d\theta \, dz \tag{437}$$

The gradient of a velocity potential in circular cylindrical coordinates is:

$$\nabla \phi = \frac{\partial \phi}{\partial r} \hat{r} + \frac{1}{r} \frac{\partial \phi}{\partial \theta} \hat{\theta} + \frac{\partial \phi}{\partial z} \hat{z} \tag{438}$$

Hence Eqn 437 becomes:

$$\begin{aligned}\dot{m}_t^{cv} &= -\rho \int_{-h}^{\eta}\int_{-\pi}^{\pi}\left(\frac{\partial \phi}{\partial r}\hat{r}+\frac{1}{r}\frac{\partial \phi}{\partial \theta}\hat{\theta}+\frac{\partial \phi}{\partial z}\hat{z}\right)\cdot r_r \hat{r}\, d\theta\, dz \\ &= -\rho \int_{-h}^{\eta}\int_{-\pi}^{\pi}\frac{\partial \phi}{\partial r} r_r\, d\theta\, dz\end{aligned} \tag{439}$$

If ϕ is the velocity potential for a circular wave as defined by Eqn 158 then $\frac{\partial \phi}{\partial r}$ is given by Eqn 271. Further simplifications can be made by substituting the various terms into 271 and resolving the implicit real relationship for velocity potentials:

$$\frac{\partial \phi}{\partial r} = \frac{g\,k\,B\cos(m\theta-\zeta)\cosh(k(h+Z))}{2\,\omega\cosh(k\,h)}\Re\left(\left(J_{m-1}(k\,r)-J_{m+1}(k\,r)+i\left(Y_{m-1}(k\,r)-Y_{m+1}(k\,r)\right)\right)e^{i(\beta-\omega t)}\right) \tag{440}$$

And:

$$\begin{aligned}&\Re\left(\left(J_{m-1}(k\,r)-J_{m+1}(k\,r)+i\left(Y_{m-1}(k\,r)-Y_{m+1}(k\,r)\right)\right)e^{i(\beta-\omega t)}\right) \\ &= \Re\left(\left(J_{m-1}(k\,r)-J_{m+1}(k\,r)+i\left(Y_{m-1}(k\,r)-Y_{m+1}(k\,r)\right)\right)\left(\cos(\beta-\omega t)+i\sin(\beta-\omega t)\right)\right) \\ &= \Re\left(\left(J_{m-1}(k\,r)-J_{m+1}(k\,r)\right)\cos(\beta-\omega t)+i\left(Y_{m-1}(k\,r)-Y_{m+1}(k\,r)\right)\cos(\beta-\omega t)\right. \\ &\qquad \left.+i\left(J_{m-1}(k\,r)-J_{m+1}(k\,r)\right)\sin(\beta-\omega t)-\left(Y_{m-1}(k\,r)-Y_{m+1}(k\,r)\right)\sin(\beta-\omega t)\right) \\ &= \left(J_{m-1}(k\,r)-J_{m+1}(k\,r)\right)\cos(\omega t-\beta)+\left(Y_{m-1}(k\,r)-Y_{m+1}(k\,r)\right)\sin(\omega t-\beta)\end{aligned} \tag{441}$$

1 of 2

$$\Re\left(\left(J_{m-1}(k\,r)-J_{m+1}(k\,r)+i\left(Y_{m-1}(k\,r)-Y_{m+1}(k\,r)\right)\right)e^{i(\beta-\omega t)}\right) = R_m\cos(\omega t-\beta-\xi_m)$$

where

$$R_m = \sqrt{\left(J_{m-1}(k\,r)-J_{m+1}(k\,r)\right)^2+\left(Y_{m-1}(k\,r)-Y_{m+1}(k\,r)\right)^2}$$

$$\xi_m = atan\left(\frac{Y_{m-1}(k\,r)-Y_{m+1}(k\,r)}{J_{m-1}(k\,r)-J_{m+1}(k\,r)}\right)$$

(441)
2 of 2

Combining Eqns 439, 440 and 441:

$$\begin{aligned}\dot{m}_t^{cv} &= -\rho\int_{-h}^{\eta}\int_{-\pi}^{\pi}\frac{g\,k\,r\,B\cos(m\theta-\zeta)\cosh(k(h+Z))}{2\,\omega\cosh(k\,h)}R_m\cos(\omega t-\beta-\xi_m)\,d\theta\,dz \\ &= -\frac{\rho\,k\,r\,B}{2}R_m\cos(\omega t-\beta-\xi_m)\int_{-\pi}^{\pi}\cos(m\theta-\zeta)\,d\theta\int_{-h}^{\eta}\frac{g\cosh(k(h+Z))}{\omega\cosh(k\,h)}dz\end{aligned} \quad (442)$$

The z integral can be calculated:

$$\begin{aligned}\int_{-h}^{\eta}\frac{g\cosh(k(h+Z))}{\omega\cosh(k\,h)}dz &\approx \frac{g}{\omega\cosh(k\,h)}\int_{-h}^{0}\cosh(k(h+z))dz \\ &\approx \frac{g}{\omega\cosh(k\,h)}\left[\frac{\sinh(k(h+z))}{k}\right]_{-h}^{0}\end{aligned} \quad (443)$$
1 of 2

$$\begin{aligned}\int_{-h}^{\eta} \frac{g\cosh(k(h+Z))}{\omega\cosh(k\,h)}\,dz &\approx \frac{g\,\omega}{\omega^2\cosh(k\,h)}\left(\frac{\sinh(k\,h)}{k}-0\right)\\ &\approx \frac{g\,\omega\sinh(k\,h)}{g\,k^2\tanh(k\,h)\cosh(k\,h)}\\ &\approx \frac{\omega}{k^2}\end{aligned} \qquad (443)$$

2 of 2

Hence, combining Eqns 442 and 443, the total mass flow through the control volume, $\dot{m}_t^{cv}$, is:

$$\begin{aligned}\dot{m}_t^{cv} &= -\frac{\rho\,k\,r\,B}{2}R_m\cos(\omega\,t-\beta-\xi_m)\int_{-\pi}^{\pi}\cos(m\,\theta-\zeta)\,d\,\theta\,\frac{\omega}{k^2}\\ &= -\frac{\rho\,\omega\,r\,B}{2\,k}R_m\cos(\omega\,t-\beta-\xi_m)\int_{-\pi}^{\pi}\cos(m\,\theta-\zeta)\,d\,\theta\end{aligned} \qquad (444)$$

A9.1.1 Mass Flow Rate for a Higher Order Circular Wave

For $m>0$ the calculation of the mass flow rate must be limited to a specific region on the cylinder. The domain for the section of the cylindrical wall bounded by two nodal lines is $\theta\in\left[\frac{\zeta}{m}-\frac{\pi}{2\,m},\frac{\zeta}{m}+\frac{\pi}{2\,m}\right]$. Hence the θ integral from Eqn 444 becomes:

$$
\begin{aligned}
\int_{\frac{\zeta}{m}-\frac{\pi}{2m}}^{\frac{\zeta}{m}+\frac{\pi}{2m}} \cos(m\theta-\zeta)\,d\theta &= \left[\frac{\sin(m\theta-\zeta)}{m}\right]_{\frac{\zeta}{m}-\frac{\pi}{2m}}^{\frac{\zeta}{m}+\frac{\pi}{2m}} \\
&= \frac{\sin\left(m\left(\frac{\zeta}{m}+\frac{\pi}{2m}\right)-\zeta\right)}{m}-\frac{\sin\left(m\left(\frac{\zeta}{m}-\frac{\pi}{2m}\right)-\zeta\right)}{m} \\
&= \frac{\sin\left(\zeta+\frac{\pi}{2}-\zeta\right)}{m}-\frac{\sin\left(\zeta-\frac{\pi}{2}-\zeta\right)}{m} \\
&= \frac{\sin\left(\frac{\pi}{2}\right)}{m}-\frac{\sin\left(-\frac{\pi}{2}\right)}{m} \\
&= \frac{2}{m}
\end{aligned}
\tag{445}
$$

Hence, from Eqn 444, the mass flow rate through a section of the cylindrical control volume bounded by two nodal lines is:

$$\begin{aligned} \dot{m}_n^{cv} &= -\frac{\rho k r B}{2} R_n \cos(\omega t - \beta - \xi_m) \int_{\frac{\zeta}{n}-\frac{\pi}{2n}}^{\frac{\zeta}{n}+\frac{\pi}{2n}} \cos(n\theta - \zeta)\, d\theta \qquad for \quad n \in \mathbb{Z}, n \neq 0 \\ &= -\frac{\rho \omega r B}{n k} R_n \cos(\omega t - \beta - \xi_n) \end{aligned} \tag{446}$$

A9.2 Displaced Volume for a Heaving Sphere

The displaced volume of a sphere of radius R partially submerged to a depth h is:

$$V_{sub}^{s} = \frac{1}{3}\pi h^2 (3R - h) \tag{447}$$

For a half-submerged sphere oscillating with an amplitude a at frequency of ω and a phase of ε the submerged height becomes $h = R + a\sin(\omega t - \varepsilon)$. Hence the volume displaced by the motion of the sphere becomes:

$$
\begin{aligned}
\Delta V_0^s &= \frac{\pi}{3}(R+a\sin(\omega t-\varepsilon))^2\left(3R-(R+a\sin(\omega t-\varepsilon))\right)-\frac{2}{3}\pi R^3 \\
&= \frac{\pi}{3}\left(R+a\sin(\omega t-\varepsilon)\right)\left(R+a\sin(\omega t-\varepsilon)\right)\left(2R-a\sin(\omega t-\varepsilon)\right)-\frac{2}{3}\pi R^3 \\
&= \frac{\pi}{3}\left(R^2+2Ra\sin(\omega t-\varepsilon)+a^2\sin^2(\omega t-\varepsilon)\right)\left(2R-a\sin(\omega t-\varepsilon)\right)-\frac{2}{3}\pi R^3 \\
&= \frac{\pi}{3}\left(2R^3+4R^2a\sin(\omega t-\varepsilon)+2Ra^2\sin^2(\omega t-\varepsilon)-R^2a\sin(\omega t-\varepsilon)\right. \\
&\qquad\qquad \left.-2Ra^2\sin^2(\omega t-\varepsilon)-a^3\sin^3(\omega t-\varepsilon)\right)-\frac{2}{3}\pi R^3 \\
&= \frac{\pi}{3}\left(3R^2a\sin(\omega t-\varepsilon)-a^3\sin^3(\omega t-\varepsilon)\right) \\
&= \frac{\pi}{3}\left(3R^2a\sin(\omega t-\varepsilon)-a^3\sin(\omega t-\varepsilon)\frac{1}{2}\left(1-\cos\left(2(\omega t-\varepsilon)\right)\right)\right) \\
&= \frac{\pi}{3}\left(3R^2a\sin(\omega t-\varepsilon)-a^3\left(\frac{1}{2}\sin(\omega t-\varepsilon)-\frac{1}{2}\cos\left(2(\omega t-\varepsilon)\right)\sin(\omega t-\varepsilon)\right)\right) \\
&= \frac{\pi}{3}\left(3R^2a\sin(\omega t-\varepsilon)-a^3\left(\frac{1}{2}\sin(\omega t-\varepsilon)-\frac{1}{4}\left(\sin\left(3(\omega t-\varepsilon)\right)-\sin(\omega t-\varepsilon)\right)\right)\right) \\
&= \frac{\pi}{3}\left(3R^2a\sin(\omega t-\varepsilon)-a^3\left(\frac{3}{4}\sin(\omega t-\varepsilon)-\frac{1}{4}\sin\left(3(\omega t-\varepsilon)\right)\right)\right) \\
&= \pi a\left(R^2-\frac{a^2}{4}\right)\sin(\omega t-\varepsilon)+\frac{\pi a^3}{12}\sin\left(3(\omega t-\varepsilon)\right)
\end{aligned}
\tag{448}
$$

A9.3 Characteristic Cylinder Properties for a Surging Sphere

For a half submerged surging sphere the displaced volume is equal to:

$$\Delta V_1^s = \frac{\pi R^2 a}{2} \sin(\omega t - \varepsilon) \tag{449}$$

And the second moment of area for the cross section through the axis of symmetry of the submerged half of the sphere is:

$$I_1^s = \left(\frac{\pi}{8} - \frac{8}{9\pi}\right) R^4 \tag{450}$$

These values can be equated to the displaced volume and second moment of area of a surging characteristic cylinder:

$$\Delta V_1^{cc} = 2 r_c l_c a \sin(\omega t - \varepsilon) \tag{451}$$

$$I_1^{cc} = \frac{2 r_c l_c^3}{12} \tag{452}$$

Hence, from Eqns 449 and 451:

$$\begin{aligned} 2 r_c l_c a \sin(\omega t - \varepsilon) &= \frac{\pi R^2 a}{2} \sin(\omega t - \varepsilon) \\ \Rightarrow 2 r_c l_c &= \frac{\pi R^2}{2} \\ \Rightarrow r_c &= \frac{\pi R^2}{4 l_c} \end{aligned} \tag{453}$$

And from Eqns. 450, 452 and 453:

$$\begin{aligned} \frac{2 r_c l_c^3}{12} &= \left(\frac{\pi}{8} - \frac{8}{9\pi} \right) R^4 \\ \Rightarrow \frac{2 l_c^3}{12} \frac{\pi R^2}{4 l_c} &= \left(\frac{\pi}{8} - \frac{8}{9\pi} \right) R^4 \\ \Rightarrow \frac{\pi l_c^2}{24} &= \left(\frac{9\pi^2 - 64}{72\pi} \right) R^2 \\ \Rightarrow l_c^2 &= \frac{R^2}{\pi^2} \left(\frac{9\pi^2 - 64}{3} \right) \\ \Rightarrow l_c &= \frac{R}{\pi} \sqrt{\frac{9\pi^2 - 64}{3}} \end{aligned} \tag{454}$$

And:

$$\begin{aligned} r_c &= \frac{\pi R^2}{4 l_c} \\ \Rightarrow r_c &= \frac{\pi R^2}{4} \frac{\pi}{R} \sqrt{\frac{3}{9\pi^2 - 64}} \\ \Rightarrow r_c &= \frac{\pi^2 R}{4} \sqrt{\frac{3}{9\pi^2 - 64}} \end{aligned} \tag{455}$$

A9.4 Derivation of the Maximum Particle Acceleration for a Circular Wave

Assume that the potential for a radiated circular wave is:

$$\phi_r = \frac{g B \cos(m\theta - \zeta) \cosh(k(h+z))}{\omega \cosh(kh)} \Re\left(H_m^1(kr) e^{i(\beta - \omega t)} \right) \tag{456}$$

The vertical velocity, v_z is:

$$\begin{aligned} v_z &= -\frac{\partial \phi_r}{\partial z} \\ &= -\frac{g k B \cos(m\theta - \zeta) \sinh(k(h+z))}{\omega \cosh(kh)} \left(J_m(kr) \cos(\beta - \omega t) - Y_m(kr) \sin(\beta - \omega t) \right) \end{aligned} \tag{457}$$

The vertical acceleration, a_z, is:

$$\begin{aligned} a_z &= -\frac{\partial v_z}{\partial t} \\ &= -\frac{g\,k\,B\cos(m\theta-\zeta)\sinh(k(h+z))}{\cosh(k\,h)}\left(J_m(kr)\sin(\beta-\omega t)+Y_m(kr)\cos(\beta-\omega t)\right) \end{aligned} \tag{458}$$

The acceleration is a point of inflection when $\frac{\partial a_z}{\partial t}=0$. Note that:

$$\frac{\partial a_z}{\partial t} = \frac{g\,\omega\,k\,B\cos(m\theta-\zeta)\sinh(k(h+z))}{\cosh(k\,h)}\left(J_m(kr)\cos(\beta-\omega t)-Y_m(kr)\sin(\beta-\omega t)\right) \tag{459}$$

Therefore, the maximum and minimum acceleration occurs when:

$$\begin{aligned} \left(J_m(kr)\cos(\beta-\omega t)-Y_m(kr)\sin(\beta-\omega t)\right) &= 0 \\ \Rightarrow \beta-\omega t &= atan\left(\frac{J_m(kr)}{Y_m(kr)}\right) \end{aligned} \tag{460}$$

Noting the identities:

$$\cos\left(atan\left(\frac{J_m(kr)}{Y_m(kr)}\right)\right) = \frac{Y_m(kr)}{\sqrt{J_m(kr)^2+Y_m(kr)^2}} \tag{461}$$

And:

$$\sin\left(atan\left(\frac{J_m(kr)}{Y_m(kr)}\right)\right) = \frac{J_m(kr)}{\sqrt{J_m(kr)^2+Y_m(kr)^2}} \tag{462}$$

Substituting Equation 460 into Equation 458, using identities 461 and 462 and evaluating at $z=0$ and $\theta=\frac{\zeta}{m}$ gives the maximum vertical acceleration:

$$a_z^{max} = -g\,k\,B\tanh(k\,h)\sqrt{J_m(k\,r)^2+Y_m(k\,r)^2} \tag{463}$$

Appendix 10: Links to Digital Appendices

This section provides internet links to all of the digital appendices. Simply copy and paste the links into a web browser.

A10.1 Digital Appendix 1: Solidworks Model of the Radial Wave Generator

https://www.dropbox.com/s/ov41jhu1bjy9zjk/Digital%20Appendix%201%20-%20Solidworks%20Model%20of%20the%20Radial%20Wave%20Generator.zip

A10.2 Digital Appendix 2: LabVIEW Program

https://www.dropbox.com/s/309d8as9oqdulv3/Digital%20Appendix%202%20-%20LabVIEW%20Software.zip

A10.3 Digital Appendix 3: Experimental Data

https://www.dropbox.com/s/icz7aicwari8fq2/Digital%20Appendix%203%20-%20Experimental%20Data.zip

A10.4 Digital Appendix 4: MATLAB Files for Post-Processing and Matching

https://www.dropbox.com/s/9emstgnc1kp02n7/Digital%20Appendix%204%20-%20MATLAB%20Files%20for%20Post-Processing%20and%20Matching.zip

A10.5 Digital Appendix 5: Component Datasheets

https://www.dropbox.com/s/dlkw4ystteix9cg/Digital%20Appendix%205%20-%20Component%20Datasheets.zip

A10.6 Digital Appendix 6: Circular Wave Example Videos

https://www.dropbox.com/s/g2sv4miz8p6qpkp/Digital%20Appendix%206%20-%20Circular%20Wave%20Example%20Videos.zip

References

[1] International Energy Agency, *Key World Energy Statistics 2010*. International Energy Agency.

[2] M. T. Pontes, L. Cavaleri, and D. Mollison, “Ocean waves: Energy resource assessment,” *Marine Technology Society Journal*, vol. 36, no. 4, pp. 42–51, 2003.

[3] A. Muetze and J. G. Vining, “Ocean wave energy conversion - a survey,” in *Conference Record of the 2006 IEEE Industry Applications Conference Forty-First IAS Annual Meeting, 8-12 Oct. 2006*, Piscataway, NJ, USA, 2006, vol. 3, p. 8.

[4] M. E. McCormick, *Ocean Wave Energy Conversion*. Dover Publications, New York, 2007.

[5] P. R. Thies, “Is it a showstopper? Reliability assessment and criticality analysis afor wave energy converters,” in *Proceedings of the 8th European Wave and Tidal Energy Conference*, Uppsala, Sweden, 2009.

[6] The International Energy Agency, “Oil and Gas - Emergency Response of IEA contries - New Zealand 2010,” IEA, 2010.

[7] B. Metz, O. Davidson, P. Bosch, R. Dave, and L. Meyer, *Climate change 2007 - mitigation of climate change*. Cambridge University Press, New York, NY (United States), 2007.

[8] B. Holmes, K. Nielsen, and S. Barret, “Wave Energy Development & Evaluation Protocol,” in *Proceedings of the 8th European Wave and Tidal Energy Conference*, Porto, Portugal, 2007, p. 11.

[9] R. Bregman, R. H. Knapp, and P. K. Takahashi, “Design considerations for ocean energy resource systems,” in *`Challenges of Our Changing Global Environment’. Conference Proceedings. OCEANS ’95 MTS/IEEE*, New York, USA, 1995, vol. 2, pp. 1084–91.

[10] G. P. Harrison and A. R. Wallace, “Climate sensitivity of marine energy,” *Renewable Energy*, vol. 30, no. 12, pp. 1801–1817, 2005.

[11] S. A. Hughes, *Physical Models and Laboratory techniques in Coastal Engineering*, vol. 7, 7 vols. World Scientific Publishing Co. Pte. Ltd., 1993.

[12] J. Falnes and K. Budal, “Wave-power conversion by point absorbers.,” *Norway Maritime Resource*, vol. 6, no. 4, pp. 2–11, 1978.

[13] D. V. Evans, “A theory for wave-power absorption by oscillating bodies,” *Journal of Fluid Mechanics*, vol. 77, no. 1, pp. 1–25, 1976.

[14] J. Falnes, “A review of wave-energy extraction,” *Marine Structures*, vol. 20, no. 4, pp. 185–201, 2007.

[15] A. Gardiner, L. Le-Ngoc, and A. Caughley, “Wave Energy Converter,” U.S. Patent 20100140944.
[16] P. Moon and D. E. Spencer, *Field theory handbook*, 2nd ed. Springer, 1971.
[17] C. C. Mei, M. Stiassnie, and D. K.-P. Yue, *Theory and applications of ocean surface waves*. World Scientific, 2005.
[18] A. P. Trujillo and H. V. Thurman, *Essentials of oceanography*. Prentice Hall, 2010.
[19] Falnes, *Ocean Waves and Oscillating Systems*. Cambridge University Press, 2002.
[20] R. G. Dean and R. A. Dalrymple, *Water Wave Mechanics for Engineers and Scientists*, 1st ed., vol. 2. World Scientific Publishing Co. Pte. Ltd., 1991.
[21] R. M. Sorensen, *Basic wave mechanics: for coastal and ocean engineers*. Wiley-Interscience, 1993.
[22] M. Rahman, *Water Waves - Relating modern theory to advanced engineering practice*, 1st ed. Oxford University Press, 1994.
[23] M. E. McCormick, *Ocean Engineering Wave Mechanics*. John Wiley & Sons Inc, 1973.
[24] J. N. Newman, *Marine hydrodynamics*. MIT Press, 1977.
[25] J. V. Wehausen and E. V. Laitone, *Surface waves*. Springer, 1960.
[26] J. Cruz, *Ocean wave energy*. Springer, 2008.
[27] EMEC, “European Marine Energy Centre - Wave Energy Developers,” 2009. [Online]. Available: http://www.emec.org.uk/wave_energy_developers.asp. [Accessed: 27-Oct-2009].
[28] T. Whittaker, D. Collier, M. Folley, M. Osterried, A. Henry, and M. Crowley, “The development of Oyster – A shallow water surging wave energy converter,” in *Proceedings of the 8th European Wave and Tidal Energy Conference*, Porto, Portugal, 2007, p. 6.
[29] L. Le-Ngoc, A. I. Gardiner, R. J. Stuart, A. J. Caughley, and J. A. Huckerby, “Progress in the development of a multi-mode self-reacting wave energy converter,” in *OCEANS 2010 IEEE - Sydney*, 2010, pp. 1–7.
[30] D. P. Cashman, D. L. O’Sullivan, M. G. Egan, and J. G. Hayes, “Modelling and analysis of an offshore OWC WEC,” in *Proceedings of the 9th European Wave and Tidal Energy Conference*, Uppsala, Sweden, 2009, p. 10.
[31] J. Wolfram, “On assessing the reliability and availability of marine energy converters: the problems of a new technology,” *Proceedings of the Institution of Mechanical Engineers, Part O (Journal of Risk and Reliability)*, vol. 220, no. 1, pp. 55–68, Jun. 2006.

[32] S. Boots and A. Bisio, *Encyclopedia of energy technology and the environment*. Wiley, 1995.
[33] J. R. Chaplin, F. J. M. Farley, M. E. Prentice, R. C. T. Rainey, S. J. Rimmer, and A. T. Roach, “Development of the Anaconda all-rubber WEC,” in *Proceedings of the 8th European Wave and Tidal Energy Conference*, Porto, Portugal, 2007, p. 8.
[34] O. Reynolds, “On the rate of progression of groups of waves, and the rate at which energy is transmitted by waves,” *Nature*, vol. 16, no. 408, pp. 343–344, Aug. 1877.
[35] A. M. J. Davis, “A relation between the radiation and scattering of surface waves by axisymmetric bodies,” *Journal of Fluid Mechanics*, vol. 76, pp. 85–8, Jul. 1976.
[36] Sang-Ho Oh, N. Mizutani, Kyung-Duck Suh, and N. Hashimoto, “Experimental investigation of breaking criteria of deepwater wind waves under strong wind action,” *Applied Ocean Research*, vol. 27, no. 4–5, pp. 235–50, 2005.
[37] D. Yue, “MIT Open Course Ware - Marine Hydrodynamics.” [Online]. Available: http://ocw.mit.edu/courses/mechanical-engineering/2-20-marine-hydrodynamics-13-021-spring-2005/. [Accessed: 06-May-2012].
[38] G. Taylor, “An Experimental Study of Standing Waves,” *Proceedings of the Royal Society of London. Series A, Mathematical and Physical Sciences*, vol. 218, no. 1132, pp. 44–59, Jun. 1953.
[39] P. Stansell and C. MacFarlane, “Experimental Investigation of Wave Breaking Criteria Based on Wave Phase Speeds,” *Journal of Physical Oceanography*, vol. 32, no. 5, pp. 1269–1283, May 2002.
[40] M. L. Banner and D. H. Peregrine, “Wave breaking in deep water,” *Annual Review of Fluid Mechanics*, vol. 25, p. 373, 1993.
[41] M. S. Longuet-Higgins, “Generation of capillary waves by steep gravity waves,” *Journal of Fluid Mechanics*, vol. 16, no. Part 1, pp. 138–159, 1963.
[42] M. A. Srokosz, “On the probability of wave breaking in deep water,” *Journal of Physical Oceanography*, vol. 16, no. 2, pp. 382–5, Feb. 1986.
[43] M. K. Ochi and C.-H. Tsai, “Prediction of Occurrence of Breaking Waves in Deep Water,” *Journal of Physical Oceanography*, vol. 13, no. 11, pp. 2008–2019, Nov. 1983.
[44] J. Falnes and K. Budal, “Wave-power absorption by parallel rows of interacting oscillating bodies.,” *Applied Ocean Research*, vol. 4, no. 4, pp. 194–207, 1982.
[45] J. Falnes, “Radiation impedance matrix and optimum power absorption for interacting oscillators in surface waves,” *Applied Ocean Research*, vol. 2, no. 2, pp. 75–80, Apr. 1980.

[46] M. McIver, “Global relationships between two-dimensional water wave potentials,” *Journal of Fluid Mechanics*, vol. 312, pp. 299–309, Apr. 1996.
[47] T. F. Ogilvie, “First-and second-order forces on a cylinder submerged under a free surface,” *Journal of Fluid Mechanics*, vol. 16, no. 3, pp. 451–472, 1963.
[48] M. A. Srokosz, “Some relations for bodies in a canal, with an application to wave-power absorption,” *Journal of Fluid Mechanics*, vol. 99, pp. 145–62, Jul. 1980.
[49] D. V. Evans, “Power from water waves.,” *Annual Review of Fluid Mechanics*, vol. 13, pp. 157–187, 1981.
[50] P. McIver and D. V. Evans, “Occurrence of negative added mass in free-surface problems involving submerged oscillating bodies.,” *Journal of Engineering Mathematics*, vol. 18, no. 1, pp. 7–22, 1984.
[51] F. P. Lockett, “Mathematical modelling of wave energy systems,” *Renewable Energy*, vol. 9, pp. 1213–1217, 1996.
[52] C. C. Mei and J. N. Newman, “Wave power extraction by floating bodies.,” *Physics of Quantum Electronics*, pp. 1–28, 1980.
[53] J. N. Newman, “Exciting forces on fixed bodies in waves,” *Journal of Ship Research*, vol. 6, no. 3, pp. 10–17, 1962.
[54] M. D. Haskind and J. N. Newman, “The exciting forces and wetting of ships in waves.” 27-Oct-1998.
[55] J. N. Newman, “Expansion of the oscillatory source potential.,” *Applied Ocean Research*, vol. 6, no. 2, pp. 116–117, 1984.
[56] R. C. Thorne, “Multipole expansions in theory of surface waves,” *Cambridge Philosophical Society -- Proceedings*, vol. 49, no. Part 4, pp. 707–716, 1953.
[57] F. Ursell, “Surface Waves on Deep Water in the presence of a Submerged Circular Cylinder - 1,” *Mathematical Proceedings of the Cambridge Philosophical Society*, vol. 46, no. 01, pp. 141–152, 1950.
[58] H. Maeda and T. Kinoshita, “Fundamental study on ocean wave energy absorption,” *Report of the Institute of Industrial Science, The University of Tokyo*, vol. 33, no. 212, p. 48, 1986.
[59] N. Kuznetsov, V. Maz’ya, and B. Vainberg, *Linear Water Waves: A Mathematical Approach*, 1st ed. Cambridge University Press, 2002.
[60] K. Budal and J. Falnes, “A resonant point absorber of ocean-wave power.,” *Nature*, vol. 256, no. 5517, pp. 478 – 479, 1975.
[61] L. D. Mann, A. R. Burns, and M. E. Ottaviano, “CETO, a Carbon Free Wave Power Energy Provider of the Future,” *Burns*, 2007.
[62] J. Lucas, J. Cruz, S. H. Salter, J. Taylor, and I. G. Bryden, “Update on the modelling of a 1:33 scale model of a modified Edinburgh duck WEC,” in *Proceedings of the 8th European Wave and Tidal Energy Conference*, Porto, Portugal, 2007, p. 9.

[63] C.-H. Lee, *WAMIT theory manual*. Massachusetts Institute of Technology, Dept. of Ocean Engineering, 1995.
[64] G. S. Payne, J. R. M. Taylor, P. Parkin, and S. H. Salter, “Numerical modelling of the sloped ips buoy wave energy converter,” in *Proceedings of the International Offshore and Polar Engineering Conference*, 2006, pp. 396–402.
[65] M. J. French, “On the difficulty of inventing an economical sea wave energy converter: A personal view,” *Proceedings of the Institution of Mechanical Engineers Part M: Journal of Engineering for the Maritime Environment*, vol. 220, no. 3, pp. 149–155, 2006.
[66] J. Falnes, “Principals for capture of energy from ocean waves. Phase control and optimum oscillation.,” *Department of Physics, NTNU, N-7034 Trondheim, Norway*, 1997.
[67] J. Falnes, “Small is beautiful: How to make wave energy economic,” in *Proceeding of an International Symposium held in Edinburgh*, Edinburgh, 1993, vol. 1, pp. 367–372.
[68] D. C. Jeffrey, G. J. Keller, D. Mollison, D. J. E. Richmond, S. H. Salter, J. R. M. Taylor, and I. A. Young, “Study of mechanisms for extracting power from sea waves.” The University of Edinburgh, 1978.
[69] M. Alves and A. J. N. A. Sarmento, “Hydrodynamic Optimization of the Active surface of a heaving point absorber WEC,” in *Proceedings of the 9th European Wave and Tidal Energy Conference*, Uppsala, Sweden, 2009, p. 8.
[70] M. Alves, I. G. Traylor, H, and A. J. N. A. Sarmento, “Hydrodynamic optimization of a wave energy converter using a heave motion buoy,” in *Proceedings of the 8th European Wave and Tidal Energy Conference*, Porto, Portugal, 2007, p. 8.
[71] D. V. Evans, “Maximum wave-power absorption under motion constraints.,” *Applied Ocean Research*, vol. 3, no. 4, pp. 200–203, 1981.
[72] Y.-Y. Kuo and Y.-F. Chiu, “Transfer function between wave height and wave pressure for progressive waves,” *Coastal Engineering*, vol. 23, no. 1–2, pp. 81–93, 1994.
[73] C.-H. Tsai, M.-C. Huang, F.-J. Young, Y.-C. Lin, and H.-W. Li, “On the recovery of surface wave by pressure transfer function,” *Ocean Engineering*, vol. 32, no. 10, pp. 1247–1259, Jul. 2005.
[74] K. Nielsen, Ed., “Ocean Energy Systems Annex II report 2003.” IEA, 2003.
[75]“Recommended Practice DNV-RP-C205 - Environmental Conditions and Enviromental Loads.” DNV, Apr-2007.
[76] S. K. Chakrabarti, *Hydrodynamics of offshore structures*. Computational Mechanics, 1987.
[77] D. E. Hasselmann, M. Dunckel, and J. A. Ewing, “Directional Wave Spectra Observed during JONSWAP 1973,” *Journal of*

Physical Oceanography, vol. 10, no. 8, pp. 1264–1280, Aug. 1980.
[78] WikiWaves, “Sommerfeld Radiation Condition - WikiWaves,” *WikiWaves - Sommereld Radiation Condition*, 2011. [Online]. Available: http://www.wikiwaves.org/index.php/Sommerfeld_Radiation_Condition. [Accessed: 10-Apr-2011].
[79] K. Budal and J. Falnes, “Wave power conversion by point absorbers: a Norwegian project.,” *International Journal of Ambient Energy*, vol. 3, no. 2, pp. 59–67, 1982.
[80] S. H. Salter, “Wave power,” *Nature*, vol. 249, no. 5459, pp. 720–724, 1974.
[81] M. Abramowitz and I. A. Stegun, *Handbook of Mathematical Functions with Formulas*, 10th Printing. Dover Publications, New York, 1972.
[82] R. Stewart, “Introduction to Physical Oceanography,” *Texas A&M university*, 2005. [Online]. Available: http://oceanworld.tamu.edu/resources/ocng_textbook/contents.html. [Accessed: 13-Jan-2011].
[83] M. Wypych, L. Le-Ngoc, K. Alexander, and A. Gardner, “On the application of circular–cylindrical waves to ocean wave power absorption,” *Ocean Engineering*, vol. 40, no. 0, pp. 69–75, Feb. 2012.
[84] M. Wypych, “Derivation of Energy Flux and Group Velocity for Circular Waves,” Industrial Research Limited, Christchurch, NZ, 2547, Sep. 2011.
[85] M. Wypych, “General Solution for the Power Radiated by Combined Plane and Circular Waves,” Industrial Research Limited, Christchurch, NZ, 2546, Sep. 2011.
[86] M. T. Pontes, G. A. Athanassoulis, S. Barstow, L. Cavaleri, B. Holmes, D. Mollison, and H. Oliveira-Pires, “An Atlas of the Wave-Energy Resource in Europe,” *J. Offshore Mech. Arct. Eng.*, vol. 118, no. 4, pp. 307–309, Nov. 1996.
[87]“Apache OpenOffice - The Free and Open Productivity Suite.” [Online]. Available: http://www.openoffice.org/. [Accessed: 17-Nov-2012].
[88] Freescale, “Freescale Semiconductor.” [Online]. Available: http://www.freescale.com/. [Accessed: 22-Apr-2012].
[89]“Festo.” [Online]. Available: http://www.festo.com/net/startpage/. [Accessed: 22-Apr-2012].
[90] J. J. Sharp, *Hydraulic modelling*. Butterworths, 1981.
[91]“Hepco Motion.” [Online]. Available: http://www.hepcomotion.com/en/. [Accessed: 23-Apr-2012].

Glossary

Absorption gain. A dimensionless factor representing the scale of power absorption for the interaction of a plane wave and a circular wave.

Absorption length. The length of wave front absorbed by a WEC. The absorption length is calculated by dividing the power a WEC absorbs from the wave field by the power per meter wave front of the incident wave.

Added mass. The mass of water that must be accelerated and decelerated as a partially or fully submerged body oscillates.

Amplitude-phase envelope. A domain of amplitudes and phases for a circular wave that result in power absorption when the circular wave is combined with an incident plane wave.

Angle of incidence. The angle between the x-axis and the direction of travel for an incident plane wave.

Angle of radiation. The angle between the x-axis and the line of peak surface displacement for a non-symmetric radiated circular wave.

Antenna effect. The potential for a PAWEC to absorb more energy than is incident upon the physical extent of the PAWEC due to the properties of surface waves.

Attenuator. A device for capturing ocean wave energy that has a large physical extent (compared to the wave length of the incident wave) in the direction perpendicular to the incoming wave front.

Bessel function. The solutions to Bessel's differential equation which arises during solving the Laplace equation in circular cylindrical coordinates using separation of variables.

Bottom boundary. The physical floor supporting the body of fluid.

Capture width. See absorption length.

Capillary wave. A surface wave in which the dominant restoring force is surface tension.

Characteristic amplitude. The amplitude with which a characteristic cylinder oscillates.

Characteristic cylinder. A theoretical construct that represents the simplest form an axisymmetric body can take and still retain the same theoretical wave radiation properties. A characteristic cylinder is also an ideal radiator of circular waves.

Characteristic length. (1) The distance from the still water level to the bottom surface of a stationary characteristic cylinder. Also known as the characteristic draft. (2) The most significant dimension in determining a WEC's performance.

Characteristic radius. The radius of the characteristic cylinder.

Circular wave. A surface wave that arises from solving the Laplace equation in circular cylindrical coordinates for periodic functions using the principal of separation of variables.

Coefficient of determination. A measure of how certain a prediction made based upon a given model will be correct.

Compound motion generator. A component of the radial wave generator that oscillates a body in two independent degrees of freedom at exactly the same phase velocity.

Compound motion slide. A component of the compound motion generator that oscillates independently in two isolated degrees of freedom to which a body can be attached.

Conservative WEC. A WEC that absorbs energy from a wave field through the interaction of incident waves and radiated waves. A conservative WEC does not introduce any turbulence or dissipative effects into the wave field.

Deep water. The condition where the depth of the fluid means that the bottom boundary does not impact on the properties of a surface wave. For linear plane waves this typically occurs when the fluid depth is greater than half of the wavelength.

Displaced mass. The mass flowing into and out of a control volume during the period of a wave or oscillating body.

Displaced volume. The volume of fluid flowing into and out of a control volume during the period of a wave or oscillating body.

Dissipative WEC. A WEC that absorbs energy by introducing friction and turbulence into the wave field. A dissipative WEC may or may not radiate surface waves.

Dynamic reflector. A body oscillating in a fluid that reflects an incident wave without absorbing any wave power.

Dynamic wave breaking factor. A factor which, when multiplied by the acceleration of gravity, determines the maximum downward particle acceleration that can exist in a wave field before the onset of wave breaking.

Energy period. The period of a regular plane wave that has the same significant height and power density of a given spectral sea state.

Far-field coefficient. The complex potential function representing radiated waves at a large distance from the radiation source.

Free-field wave breaking limit. The maximum amplitude or power of wave that can exist in a wave field, excluding the limitations of localised effects caused by the interaction of the fluid with any boundaries.

Gravity wave. A surface wave in which the dominant restoring force is gravity.

Green's function. A mathematical construct used to solve inhomogeneous differential equations that are constrained by specific boundary conditions and initial states.

Group velocity. The speed at which two points with zero surface displacement and a constant distance of separation travel in the direction of propagation.

Hankel function. A complex linear combination of Bessel functions of the first and second kind used to model radiated and gravitated surface waves.

Haskind's relationship. A relationship that connects the forces and moments on a body with the far-field velocity potentials for forced oscillations of the body in calm water.

Heave. A vertical movement.

Heave wave. (1) An axisymmetric metric wave described by Hankel functions of the zeroth order. (2) The surface wave generated by a body moving vertically within a fluid.

Harmonic wave. A wave with a phase velocity which is a multiple of the phase velocity of the wave generating motion.

IRL. Industrial Research Limited.

Kochin function. A function utilised in wave-body interaction analysis and related to the far-field coefficient. The Kochin function has an order and varies with wave number and circular cylindrical variable θ.

Modified Bessel function. Non periodic solutions to the modified Bessel's equation.

Non-symmetric wave. A wave for which the surface displacement on one side of the point of generation is out of phase with the surface displacement on another.

PAWEC. See point absorbing wave energy converter.

Pitch. A rotation around an axis parallel to the incident wave front.

Phase angle. The phase offset for a wave at $t=0$.

Phase velocity. The angular velocity with which an oscillation occurs.

Pierson-Moskowitz Spectrum. A wave spectrum based on a fully developed, wind-generated sea state.

Plane wave. A monochromatic surface wave with an infinitely wide wave front.

Point absorbing wave energy converter. A device for capturing ocean wave energy that has a horizontal extent that is much smaller than the wave length of the incident wave.

Radial wave generator. A device designed to generate circular waves by oscillating a body in two independent degrees of freedom.

Radiated wave. A wave that propagates from a single point out to the bounds of the free surface.

Radiation resistance. The real component of the radiation impedance. This is associated with energy radiated by a surface wave.

Radiation reactance. The complex component of the radiation impedance. This is associated with energy stored in the fluid and returned to the body during a single oscillation.

Radiation impedance. The complex term that represents the real and reactive power flows associated with wave radiation in an oscillating system.

Radius of radiation. The radius at which the free surface of a fluid is no longer dominated by the effects of an oscillating body and radiated waves are free to propagate.

Required displaced volume limit. The maximum amplitude or power of a wave that can be radiated based upon the volume of fluid flowing into and out of a control volume during the period of a wave or oscillating body.

Roll. A rotation about an axis perpendicular to the incident wave front.

Significant wave height. The average wave height of the highest third of waves in a spectral sea state.

Shallow water. The condition where the depth of the fluid means that the bottom boundary determines the properties of the wave. For linear plane waves this typically occurs when the fluid depth is less than one-twentieth of the wavelength.

Small amplitude approximation. The assumption made as part of linear theory that the amplitude of the wave is small compared to both the wavelength of the wave and the depth of fluid over which the wave propagates.

Still water level. The level of the free surface when there are no waves upon the surface of the fluid.

Stokes drift. The mass transport that occurs in non-linear waves.

Surface displacement. The vertical distance of the deformed free surface from the still water level.

Surge. A horizontal movement parallel with the direction of propagation of the incident wave.

Surge wave. (1) An non-axisymmetric metric wave described by Hankel functions of the first order with an angle of radiation equal to angle of incidence of the incident wave. (2) The surface wave generated by a body oscillating horizontally and perpendicularly to the incoming wave front.

Sway. A horizontal movement perpendicular to the direction of propagation of the incident wave.

Sway wave. (1) An non-axisymmetric metric wave described by Hankel functions of the first order with an angle of radiation perpendicular to the angle of incidence of the incident wave. (2) The surface wave generated by a body oscillating horizontally and in parallel with the incoming wave front.

SWL. See still water level.

Symmetric wave. A wave for which the surface displacement on all sides of the point of generation are in phase.

Terminator. A device for capturing ocean wave energy that has a large physical extent (compared to the wave length of the incident wave) in the direction parallel with the incoming wave front.

Time-averaged. Averaged over the period of oscillation.

Time-averaged power. The power transmitted by an oscillating phenomenon when averaged over the period of oscillation.

Velocity potential. A scalar function defined in such a way that the gradient of the function is equal to the velocity at that point.

Wave amplitude. The distance from the still water level to the peak or trough of a wave.

Wave breaking. The non-linear phenomenon when a wave front can no longer support its own structure and spills, plunges or surges, dissipating energy.

Wave breaking limit. See free-field wave breaking limit.

Wave celerity. The speed at which a wave front propagates across the surface of the fluid.

Wave energy converter. A device designed to capture ocean wave energy and convert it into another form.

Wave front. An imaginary line representing the local maximum or minimum wave displacement in an area of the wave field at a given time.

Wave height. The vertical distance from a wave peak to a wave trough.

Wave number. A factor used for the characterisation of a wave and calculated by dividing two times the value of π by the wavelength of the wave.

Wave period. The time between two successive peaks or troughs passing a static point.

Wave radiation. The generation of radial waves.

Wavelength. The distance between two successive peaks or troughs in a wave.

WEC. See wave energy converter.

Wronskian. A determinant used in the study of differential equations and associated with linear independence sets of solutions.

Yaw. A rotation about a vertical axis.